



UNIVERSITY OF LEEDS

**Behaviour of Reinforced Concrete Beam-Column Joints
under Combined Loads Strengthened with CFRP Schemes
Applied to the Beam**

By

Sarmad Abdulsahab Ali

Submitted in accordance with the requirements for the degree of
Doctor of Philosophy

The University of Leeds
School of Civil Engineering

October, 2020

The candidate confirms that the work submitted is his own, except where work which has formed part of jointly-authored publications has been included. The contribution of the candidate and the other authors to this work has been explicitly indicated below. The candidate confirms that appropriate credit has been given within the thesis where reference has been made to the work of others.

The work presented in Chapters 4, 6 and 7 of this thesis has appeared in the following publication:

Ali, S.A. and Forth, J.P 2018. 'Behaviour of torsionally strengthened reinforced concrete beam-column joints with carbon fibre reinforced polymer sheets'. Proceedings of the 12th Fédération Internationale du béton (fib) International PhD Symposium 2018 being held at Prague, Czech Republic.

Ali, S.A. and Forth, J.P 2019. 'Numerical Investigation of Different Torsion Ratios on Behaviour of Reinforced Concrete Beam-Column Joints. Proceedings of PGR conference 2019, being held at University of Leeds, UK.

Ali, S.A. and Forth, J.P 2020. 'An Experimental and Analytical Investigation of Reinforced Concrete Beam-Column Joints Strengthened with a Range of CFRP Schemes Applied only to The Beam. In preparation to be submitted for publishing in the Advances in Structural Engineering, SAGE Journals.

The right of Sarmad Abdulsahab Ali to be identified as Author of this work has been asserted by him in accordance with the Copyright, Designs and Patents Act 1988.

Acknowledgements

*All gratitude to Allah for giving me the strength and capability to accomplish this research. I would like to express my sincere appreciation and gratitude to **Professor. John P. Forth** for his critical review and comments. His clear and constructive guidance have been invaluable throughout the duration of my research.*

*Special thanks also go to **Dr. Nikolaos NIKITAS** for his advices and comments which really improved the numerical studies .*

*I am truly indebted to the technical staff **Mr Norman Harmon, Mr Peter Flatt, Mr Marvin Wilman, Mr Robert Clarke** and **Mr Stephen Holmes** at the George Earl Laboratory for their continued support and assistance in accomplishment of the experimental work.*

I also wish to express my sincere thanks to the financial support given by The Ministry of Higher Education in Iraq for funding my studies.

My appreciation goes to the School of Civil Engineering staff, students and my fellow colleagues at University of Leeds for their support and encouragement.

Finally, I would like to extend my sincere thanks to my wonderful family, may parents, brothers, sisters, my wife and daughters for their support and encouragement, which have made this work possible.

Dedication

I dedicate this thesis to the people dearest to me in this world;

My beloved Parents

&

My lovely wife "Farah"

&

My beautiful and wonderful daughters

Warood, Yussor, and Lara

Abstract

This investigation concentrates on the behaviour of beam-column joints subjected to torque interacting with flexural and direct shear forces and in the presence of different Carbon Fibre Polymer (CFRP) strengthening wraps (applied only to the beam). These wrapping schemes have previously been determined by the research community as an effective method of enhancing the torsional capacities of simply supported reinforced concrete beams. Based on the literature and the lack of direct relevant research, an extensive experimental, analytical and numerical investigation has been performed. The experimental work involved a series of exterior reinforced concrete beam-column joints tested under short-term and long-term loads, combinations of which included torque.

The short-term tests performed under monotonically increasing loads illustrated the viability of using CFRP wrapping systems to enhance member capacities under torsional actions. The enhancement levels were affected by the fibre ratio, the confinement degree, and the fibre orientation. The ductility of the members was governed by the strength of the concrete struts. The rebars' strain readings confirmed the influence of the torsional forces; these forces increased the tensile stresses in the beam rebars, which affected the shear demand and distortion levels of the joints. The long-term tests (under sustained loads) illustrated a significant increase in the beam twist deformations due to the long-term torsional loads. Also, the sustained loads reduced the flexural stiffness; this corresponded to the level of the time-dependent deformations and the induced torsional cracks. The CFRP wraps considerably improved the time-dependent torsional stiffness compared to the unstrengthened specimens.

Formulas are proposed based on the space truss mechanism to evaluate the joint shear demand of beams wrapped in various ways, whilst also considering the interactions of torque with bending and direct shear. Further, an iterative model based on the average stress-strain method has been introduced to predict the joint's strength. The proposed analytical approaches showed good agreement with the experimental results. In addition, numerical models were developed in order to examine the influence of different torque to bending-shear ratios, multiple CFRP layers, and concrete strengths. These investigations revealed significant increases in the plastic strains, which exceeded those measured in the specimen under concentric loads. The high strength concrete models attained larger load capacities than the normal strength concrete models. The effectiveness of multiple CFRP wraps was limited to the concrete struts capacity. A considerable increase in the beam's time-dependent deflections was identified when compared with those predicted according to Eurocode-2.

Table of Contents

Acknowledgements.....	ii
Dedication.....	iii
Abstract.....	iv
Table of Contents.....	v
List of Tables.....	x
List of Figures	xii
Chapter 1 Introduction.....	1
1.1 Background.....	1
1.2 Research Problem	2
1.3 Aim and Objectives of the Research.....	4
1.4 Objectives.....	4
1.5 Structure of the Thesis.....	6
Chapter 2 Literature Review	9
2.1 Introduction.....	9
2.2 Torsion Analogy and Effects.....	10
2.2.1 Torsion Combined with Flexural, Direct Shear, Axial Forces	11
2.2.2 Interactions and Analytical Methods of Torsion and other Forces	13
2.2.3 Variable Angle Truss Model, MCFT and STM	17
2.3 Beam Torsional Strengthening with FRP.....	20
2.3.1 FRP Material	21
2.3.2 Torsional Fibre Schemes.....	22
2.3.2.1 Loads Combinations	26
2.3.3 Analytical Methods and Design Details for FRP Schemes ...	26
2.3.3.1 Softened Truss Method with FRP	30
2.4 Beam-Column Joints	32
2.4.1 Joint Forces and Transfer Mechanism	32
2.4.1.1 Concrete Compressive Strength.....	35
2.4.1.2 Transverse Reinforcements.....	35
2.4.1.3 Bond and Anchorage	36
2.4.1.4 Joint Aspect Ratio.....	37
2.4.1.5 Column Axial Load.....	38

2.4.2	Previous Research (beam-column joint with eccentric load and torsional moment).....	38
2.4.3	Codes Provisions.....	42
2.4.3.1	BS8110 (1997).....	42
2.4.3.2	Eurocode 2 (2004)	44
2.4.3.3	ACI-ASCE 352R-02 Committee (2002).....	45
2.4.3.4	NZS 3101 (2006)	46
2.5	Long-Term Behaviour of Reinforced Concrete Members under Sustained Torsional Loads	48
2.5.1	Creep.....	49
2.5.2	Shrinkage	52
2.5.3	Members under Sustained Torsional Load.....	54
2.6	Numerical Modelling of RC Sections under Torsional Forces.....	60
2.6.1	Introduction.....	60
2.6.2	Concrete Constitutive Models.....	60
2.6.3	Concrete Cracking.....	65
2.6.4	Previous Research Investigations Using Finite Elements Models.....	65
2.7	Conclusions	70
Chapter 3 Experimental programme.....		74
3.1	Introduction	74
3.2	Aim of Experimental Programme	74
3.3	Beam-Column Joint Details	75
3.4	Experimental Plan.....	77
3.5	Strengthening Schemes with CFRP	80
3.6	Casting Specimens.....	82
3.7	Material Properties.....	84
3.7.1	Concrete Properties.....	84
3.7.1.1	Coarse Aggregate.....	84
3.7.1.2	Cement	85
3.7.1.3	Fine Aggregate	86
3.7.1.4	Mixing Water.....	87
3.7.1.5	Compressive and Tensile Strength Tests	87
3.7.1.6	Concrete Modulus of Elasticity.....	90
3.7.1.7	Compressive Creep Test	91

3.7.1.8	Shrinkage Specimens	92
3.7.1.9	Tensile Creep Test.....	93
3.7.1.10	Time-dependent Tests Results	94
3.7.2	Steel Bars	97
3.7.3	CFRP Fabric and Epoxy Resin.....	98
3.8	Application of CFRP Jackets.	99
3.9	Test Procedure and Instrumentation.....	100
3.9.1	Short-Term Testing Procedure	100
3.9.2	Long-Term Testing Procedure.....	103
3.9.3	Electrical Resistance Strain (ERS) Gauges.....	106
3.9.4	LVDT's.....	108
3.9.5	DEMEC Points	110
3.10	Summary	111
Chapter 4	Short-Term Tests: Results and Discussion.....	112
4.1	Introduction	112
4.2	End Beam Deflection and Twist angle	112
4.2.1	Influence of Torsion	114
4.3	Effect of Torsional Strengthening Schemes.....	118
4.3.1	Full Continuous Wrapping Scheme	119
4.3.2	CFRP Strips (Hoops).....	122
4.3.3	45° CFRP Strips	124
4.3.4	Load -Twist Behaviour.....	127
4.4	Ductility Index	129
4.5	Strain Development in Steel and CFRP Reinforcement	131
4.5.1	Strain Levels in the Main Steel Reinforcement.....	131
4.5.2	Strain Level in Transverse Reinforcement.....	136
4.6	Joint Distortion and Cracks	140
4.7	Summary	143
Chapter 5	Long-Term Tests: Results and Discussion	146
5.1	Introduction	146
5.2	Time-Dependent Twisting and Deflection	146
5.2.1	Long-Term Twisting Behaviour.....	146
5.2.2	Long-Term Deflection	150
5.3	Observed Cracking	152

5.3.1	Crack Widths	154
5.4	Surface Strains Measurement	158
5.4.1	Evaluation of Surface Strain from the Beam's Curvature Based on Eurocode 2 (2004).....	159
5.4.2	Surface Strains for Specimens under a Single Stage Loading.....	160
5.4.3	Surface Strains for Specimen under Two Stages of Loading.....	173
5.5	Strain Development in the Steel Reinforcement	180
5.6	Summary	186
Chapter 6 Analytical Investigations.....		188
6.1	Introduction	188
6.2	Shear Demand and Concrete Strut Capacity.....	188
6.2.1	Concrete Strut Capacity	188
6.2.2	Joint Shear Demand.....	192
6.2.2.1	Shear Demand in Concrete Elements with Wrapping Schemes.....	194
6.3	Analytical Models of Beam-Column Joint	195
6.3.1	Review of Panel Truss Models	196
6.3.2	Model Derivation for Beam-Column Joint.....	201
6.4	Model Validation and Discussion	208
6.5	Summary	214
Chapter 7 Finite Element Modelling.....		216
7.1	Introduction	216
7.2	Modelling of Material.....	217
7.2.1	Concrete Modelling.....	217
7.2.1.1	Concrete in Tension.....	218
7.2.1.2	Concrete in Compression	220
7.2.1.3	Shear in Concrete.....	221
7.2.2	Steel Rebars Modelling	222
7.2.3	CFRP Modelling	222
7.3	Elements Types and Mesh Generation.....	223
7.4	Loads and Boundary Conditions.....	227
7.5	Verification of the Numerical Model	229
7.5.1	Short-Term Behaviour	229

7.5.2	Long-Term Behaviour.....	234
7.6	Influence of Different Ratios of Torsion to Bending-Shear Loads	238
7.7	Influence of Different CFRP Layers	244
7.8	Influence of High Compressive Strength of Concrete	246
7.9	Long-Term Behaviour for HSC and NSC under Various Loads Ratios	250
7.10	Summary	259
Chapter 8 Conclusions and recommendations		262
8.1	Conclusions	262
8.1.1	Findings from the Experimental Investigation (Short-Term Tests)	262
8.1.2	Findings from the Experimental Investigation (Long-Term Tests)	264
8.1.3	Conclusions Based on the Developed Analytical Approaches.	265
8.1.4	Conclusions Based on the Developed Numerical F.E. Approach	267
8.2	Recommendations for Future Research.	269
Bibliography		270
Appendix A Torsional Shear Flow and Truss Model.....		282
Appendix B The Frame Model Details		290
Appendix C Concentric Loading Test Setup		296

List of Tables

Table 2.1: A summary of the torsional configurations of beams and details of the fibres that have been experimentally tested.....	25
Table 2.2: Test results (Elshafiey et al., 2016)	42
Table 2.3: Summary of FE studies on RC sections under torsional forces	69
Table 3.1: Beam-column joint details	79
Table 3.2: CFRP schemes details	81
Table 3.3: Concrete samples details.....	82
Table 3.4: Concrete mix proportions.....	84
Table 3.5: Particle size distribution of coarse aggregate	85
Table 3.6: Chemical and physical properties of cement.....	86
Table 3.7: Particle size distribution of fine aggregates.....	87
Table 3.8: Experimental results of concrete compressive strength	88
Table 3.9: Experimental results of concrete tensile strength (f_t).....	89
Table 3.10: Concrete modulus of elasticity results	91
Table 3.11: Mechanical properties for steel bars.....	98
Table 3.12: Mechanical properties of the carbon fibre sheets	99
Table 4.1: CFRP contribution for all specimens.....	128
Table 4.2: Ductility index	130
Table 5.1: The increases in the instantaneous and time-dependent surface strains for the LN-U-C specimen.....	171
Table 5.2: The increases in the instantaneous and time-dependent surface strains for the LN-U-C-H specimen.....	172
Table 5.3: The increases in the time-dependent surface strains at end of stage-1 and stage-2 for the LN-U-S specimen.	179
Table 6.1: Predicted (designed) torsional capacity, strut angles in the beam sides, concrete strut capacity and ultimate strut stress...	209
Table 6.2: Comparison between experimental and predicted results using the developed model.....	211
Table 7.1: Predicted rebars strains to yield strains ratios and computed stresses to yield stresses ratios for the created models	241
Table 7.2 Comparison between HSC and NSC models results and observed damage for HSC models.....	249
Table 7.3: Creep coefficients and free shrinkage induced strain for HSC samples.	251

Table A.1: Area of shear flow calculation formulas	283
Table B.1: Predicted (designed) maximum applied beam's loads.....	295

List of Figures

Figure 1.1: a) Torque induced in spandrel beams b) Torque induced in peripheral beams under column removal scenarios	1
Figure 2.1: Actions of circulatory and warping torsion	10
Figure 2.2: Direct shear and torsion addition	12
Figure 2.3: Strain profiles in RC sections under flexural and torsional forces	13
Figure 2.4: Interaction diagrams a) Skew-bending method b) Truss model method.....	14
Figure 2.5: Interaction diagram, torsion-shear-bending	16
Figure 2.6: The MCFT equations.....	19
Figure 2.7: a) Panels and shear flow b) Shear flow summation c)Vertical shear distribution.....	20
Figure 2.8: Typical stress-strain curves of steel, CFRP,GFRP.....	21
Figure 2.9: Beams strengthening schemes (a) Full-continuous wrapping (b) FRP hoops (c) U-wrap (d) 45° inclined Strips (e) Horizontally oriented wrap	23
Figure 2.10: Effective strain of FRP composites in terms of $\epsilon_f \rho_f / f_{cm}^{2/3}$ (a) concrete shear failure with FRP de-bonding (b) concrete shear failure with (or followed by) the fracture of FRP ..	27
Figure 2.11: Space truss mechanism of strengthened RC beam with externally bonded FRP schemes.....	31
Figure 2.12: a) Acting forces on the beam and column b) joint shear forces c) column and joint bending moment.....	33
Figure 2.13: Joint forces transfer mechanism according to the strut-tie method.....	34
Figure 2.14 : a) Joint diagonal strut mechanism b) Joint truss mechanism	35
Figure 2.15: Bond stresses and the joint truss mechanism.....	37
Figure 2.16: Influence of biaxial loading on the joint strength.....	39
Figure 2.17: Test and specimen details (Elshafiey et al., 2016)	41
Figure 2.18: Creep strain under sustained load	49
Figure 2.19: Components of concrete strain under constant load	50
Figure 2.20: Components of shrinkage for (a) normal and (b) high strength concrete.....	53
Figure 2.21: Torsional creep and creep recovery for samples stored in water	55
Figure 2.22: Twist angle over time for the RC beams	56

Figure 2.23: Beam rotations, unloading, reloading and recovery with time for the beam with different stirrups spacings (120, 60, and 30 mm).	57
Figure 2.24: The ratio of the long-term rotation to the initial rotation for the tested beams	57
Figure 2.25: Twist angle-time curves for the plain concrete beams under different load values	58
Figure 2.26: Twist angle-time curves for the reinforced concrete beams under different load values	58
Figure 2.27: The rotations ratios (coefficient) for the beams under sustained torsion	59
Figure 2.28: Symmetry conditions in the orthotropic model.....	62
Figure 2.29: Concrete modelling in ANSYS	63
Figure 2.30: Concrete modelling in concrete damage plasticity (a) Tension (b) Compression.....	64
Figure 3.1: Frame Model	76
Figure 3.2: Reinforcement and section details for the scaled specimen	77
Figure 3.3: Experimental programme plan.....	78
Figure 3.4: Strengthening schemes, (a) Full wrapping, (b) Strip wrapping- hoops, (c) 45° inclined wrapping.	81
Figure 3.5: Casting of samples	83
Figure 3.6: Casting using the hand-held vibrator.....	83
Figure 3.7: Curing of the samples.....	83
Figure 3.8: Grading of coarse aggregate and BS 882 limits.....	85
Figure 3.9: Grading of fine aggregates and BS 882 limits	86
Figure 3.10: Testing Machines a) Compressive strength test b) Splitting tensile strength test c) Flexural test d) Direct tensile test.....	89
Figure 3.11: Test of modulus of elasticity	90
Figure 3.12: Compressive creep test.....	92
Figure 3.13: Shrinkage samples	93
Figure 3.14: 150 mm DEMEC gauge with calibration bars.....	93
Figure 3.15: Tensile creep test.....	94
Figure 3.16: Compressive creep strains developments with time	95
Figure 3.17: Compressive creep coefficients results.....	95
Figure 3.18: Developed shrinkage strains with time	96

Figure 3.19: Tensile creep strains developments with time	96
Figure 3.20: Reinforcements detailing the beam-column joints	98
Figure 3.21: Preparation and application of the CFRP sheets	100
Figure 3.22: Testing schematic diagrams	102
Figure 3.23: Test setup for two consecutive loading stages.....	105
Figure 3.24: Environmental conditions of the laboratory	106
Figure 3.25: Position of steel strain gauges	107
Figure 3.26: Strain gauge positions for long-term specimens.....	108
Figure 3.27: CFRP strain gauges	108
Figure 3.28: a) Schematic diagram of the joint deformation b) Diagonal LVDT's.....	109
Figure 3.29: DEMEC points on the beam's sides	110
Figure 3.30: DEMEC points on the beam's bottom and top	111
Figure 4.1: Load - end beam deflection (a) for SH-U-F sample (b) for SH-U-C sample.	116
Figure 4.2: SH-U-F and SH-U-C specimen failures (a) under flexural actions (b) under combined actions.....	117
Figure 4.3: Torque-twist diagram for SH-U-C specimen	118
Figure 4.4: Peak capacities (a) Ultimate bending moment (b) Ultimate Torque (c) Ultimate vertical shear (d) Cracking Torque	119
Figure 4.5: Load-end beam deflection for the SH-S-C-A sample	121
Figure 4.6: SH-S-C-A specimen failure under combined loads.....	121
Figure 4.7: Load-end beam deflection for the SH-S-C-H sample	123
Figure 4.8: SH-S-C-H specimen failure under combined loads.....	124
Figure 4.9: Load - end beam deflection for SH-S-C-I sample	125
Figure 4.10: SH-S-C-I specimen failure under combined loads	126
Figure 4.11: Torque-twist diagram for all specimens under torque actions	128
Figure 4.12: Ductility level, yield displacement of the reduced stiffness equivalent elasto-plastic system	131
Figure 4.13: Strain development in the beam main rebars at 100 mm from the column face, (a) for control specimens (b) for strengthened specimens (c) in the beam top rebars	134
Figure 4.14: (a) Column exterior bar steel strain at the top of the joint (b) Column exterior bar steel strain at the bottom of the joint (c) in the middle of the joints (beam's bottom rebars)	136

Figure 4.15: Strain development (a) in the beam stirrups at 200 mm from the column face (b) in the beam stirrups at 450 mm from the column face (c) in CFRP wraps at 250 mm from the column face (d) in CFRP wraps at 450 mm from the column face (e) in the column middle link at 145 mm from the column outer face..	139
Figure 4.16: Joint distortion angles and joint demands	141
Figure 4.17: Joint cracks (a) for the SH-U-F specimen (b) for the SH-S-C-A specimen (c) for the SH-S-C-I specimen (d) for the SH-U-C specimen (e) for the SH-S-C-H specimen.....	143
Figure 5.1: Developed end-beam twist angles with time for all specimens	149
Figure 5.2: Correlation between experimentally measured and predicted twist angle using hyperbolic functions.....	149
Figure 5.3: The increase in the long-term beam twist angles to instantaneous twisting with time.....	150
Figure 5.4: Developed end-beam deflection with time for LN-U-S specimen and Eurocode 2.....	151
Figure 5.5: Developed cracks in LN-U-S specimen (a) at the end of stage-1 (b) at the end of stage-2	152
Figure 5.6: Observed cracks on the beam's sides at the end of loading durations (a) for LN-U-C specimen (b) for LN-S-C-H specimen (c) for LN-U-S specimen.....	156
Figure 5.7: Developed crack widths over time (a) for LN-U-C specimen (b) for LN-S-C-H specimen (c) for LN-U-S specimen ..	157
Figure 5.8: DEMEC points rows across the beam's depth and sides	158
Figure 5.9: The developed surface strains at the beam's right and left sides for the LN-U-C specimen (a) Zone 1 (b) Zone 2 (c) Zone 3 (d) Zone 4 (e) Zone 5 (f) Zone 6 (g) Zone 7 (h) Zone 8.....	165
Figure 5.10: The developed surface strains at the beam's right and left sides for the LN-S-C-H specimen (a) Zone 2 (b) Zone 3 (c) Zone 4 (d) Zone 5 (e) Zone 6 (f) Zone 7 (g) Zone 8	168
Figure 5.11: The developed surface strains at the beam's top and bottom sides for the LN-U-C specimen (a) Zone 2 (b) Zone 3 (c) Zone 4 (d) Zone 5 (e) Zone 6 (f) Zone 7	170
Figure 5.12: The developed surface strains at the beam's right and left sides for the LN-U-S specimen (a) Zone 1 (b) Zone 2 (c) Zone 3 (d) Zone 4 (e) Zone 5 (f) Zone 6 (g) Zone 7	176
Figure 5.13: The developed surface strains at the beam's top and bottom sides for the LN-U-S specimen a) Zone 2 (b) Zone 3 (c) Zone 4 (d) Zone 5 (e) Zone 6 (f) Zone 7	178
Figure 5.14: Developed strains in the beam's main rebars for the LN-U-C specimen at 125 mm from the column face.....	182

Figure 5.15: Developed strains in the beam's main rebars for the LN-S-C-H specimen at 125 mm from the column face	182
Figure 5.16: Developed strains in the beam's main rebars for the LN-U-S specimen at 125 mm from the column face.....	183
Figure 5.17: Developed strains in the beam's main rebars for the LN-U-C specimen at 350 mm from the column face.....	183
Figure 5.18: Developed strains in the beam's main rebars for the LN-S-C-H specimen at 350 mm from the column face	184
Figure 5.19: Developed strains in the beam's main rebars for the LN-U-S specimen at 350 mm from the column face.....	184
Figure 5.20: Developed strains in the beam's main rebars for the LN-U-C specimen at 620 mm from the column face.....	185
Figure 5.21: Developed strains in the beam's main rebars for the LN-S-C-H specimen at 620 mm from the column face	185
Figure 5.22: Developed strains in the stirrups for all specimen at 310 mm from the column face	186
Figure 6.1: (a) Truss mechanism in the beam's sides (b) shear flow and section effective area	191
Figure 6.2: (a) Truss mechanism for inclined fibres (b) Space truss mechanism	192
Figure 6.3: (a) Concrete strut mechanism (b) The joint panel truss mechanism (c) Concrete biaxial strength represented by a 5 th degree parabola (Tsonos, 2008).	198
Figure 6.4: Stress equilibrium according to average stress-strain panel zone (a) Equilibrium of vertical force (b) Equilibrium of horizontal forces (Pantazopoulou and Bonacci, 1992)	200
Figure 6.5: (a) Stress variation along steel bars (b) kinematics of joints (c) forces and average stresses in the joint's section	202
Figure 6.6: Solution flow chart.....	207
Figure 6.7: Experimental versus predicated tensile stresses in the bottom beam chords by using the proposed method	209
Figure 6.8: A comparison between the design and peak torsional capacity (T_u) for strengthened specimens.....	210
Figure 6.9: Comparison between experimental and predicted maximum joint distortion angles	211
Figure 6.10: Comparison between experimental and predicted maximum joints forces (V_j)	212
Figure 6.11: Joint stress equilibrium in two orthogonal directions in the presence of steel and FRP reinforcement	214
Figure 7.1: Fixed and rotating crack models	218

Figure 7.2: Tensile behaviour of concrete based on Hordijk Model ...	219
Figure 7.3: Recommended crack band width according to element size (e) and type	220
Figure 7.4: Proposed softening models for concrete in compression	221
Figure 7.5 : Arrangement of fibres direction for transversely isotropic composite	223
Figure 7.6: Midas FEA elements types	224
Figure 7.7: Slip-bond models for FRP's-concrete interface	226
Figure 7.8: loads and support conditions in the F.E. models	228
Figure 7.9: Comparison between the experimental and F.E. results for twist angles due to torque action.	231
Figure 7.10: Comparison between the experimental and F.E. results for end-span deflection of the beams (a) all specimens (b) specimens under combined loads	232
Figure 7.11: Comparison between the experimental and F.E. result for the beams main rebars strains at 100 mm from the column face.....	232
Figure 7.12: Comparisons between the strains profiles obtained from F.E. models (short-term group) and observed damage from tests.....	234
Figure 7.13: Comparison between the experimental and F.E. results for long-term twist angles due to sustained loads.....	235
Figure 7.14: Time-dependent strains and cracks profiles for the LN-U-C model	236
Figure 7.15: Time-dependent strains and cracks profiles for the LN-S-C-H model.....	237
Figure 7.16: (a) Load-deflection curves for unstrengthened models (b) Twist-angle curves for unstrengthened models (c) Load-deflection curves for strengthened models (d) Twist-angle curves for strengthened models.....	242
Figure 7.17: Cracks profile for the unstrengthened models subjected to 1 and 0.5 T/M-S loads ratios.....	243
Figure 7.18: Predicted the beam rebars strains developments (a) for the unstrengthened models (b) the strengthened models	243
Figure 7.19: (a) Load-deflection curves for models with different CFRP layers(b) Twist-angle curves for models with different CFRP layers	245
Figure 7.20: (a) Load-deflection curves for HSC models (b) Twist-angle curves for HSC models	248

Figure 7.21: Developed end-beam twist angle with time under different ratios of sustained loads (a) Models created with NSC (b) Models created with HSC.....	255
Figure 7.22: Instantaneous and time-dependent principal tensile developed for the models created with NSC (a) under 1 T/M-S sustained loads ratio (b) under 0.5 T/M-S sustained loads ratio.	256
Figure 7.23: Instantaneous and time-dependent principal tensile developed for the models created with HSC (a) under 1.57 T/M-S sustained loads ratio (b) under 1 T/M-S sustained loads ratio (c) under 0.5 T/M-S sustained loads ratio.....	257
Figure 7.24: Developed end-beam deflection with time under different ratios of sustained loads (a) Models created with NSC (b) Models created with HSC.....	258
Figure A.1: Space truss model	285
Figure A.2: (a) Average strains in a cracked element (b) Mohr's Circle for Average Strains.	287
Figure B.1: (a) Plan details of the frame model (b) Side and front views for the frame model (c) Gravity Loads arrangement-type 1 (d) Gravity Loads arrangement-type 2	290
Figure C.1: Concentric test schematic diagrams.....	296

Chapter 1 Introduction

1.1 Background

Structural members in a reinforced concrete frame are subjected to various types and magnitudes of loads and forces. Accordingly, it is crucial to ensure structural integrity between the main members and provide robust load paths. These loads are typically one or more from the following - flexural, shear, axial, and torsional loads. Flexural and shear forces tend to govern the design of the structural members in buildings with symmetric layouts or concentric loadings. However, the effect of spandrel beams (Figure 1.1a), unequal spans or eccentric loadings, asymmetric building layouts, and an alternating loading pattern could induce significant torque. Further, the twisting at discontinuous edges produced from the slab hogging moment (Figure 1.1b) become substantially critical when an internal or external column damaged or removed (Pham et al., 2019). In a three-dimensional system, torsional cracking could, therefore, be promoted in beams, especially at exterior joints.

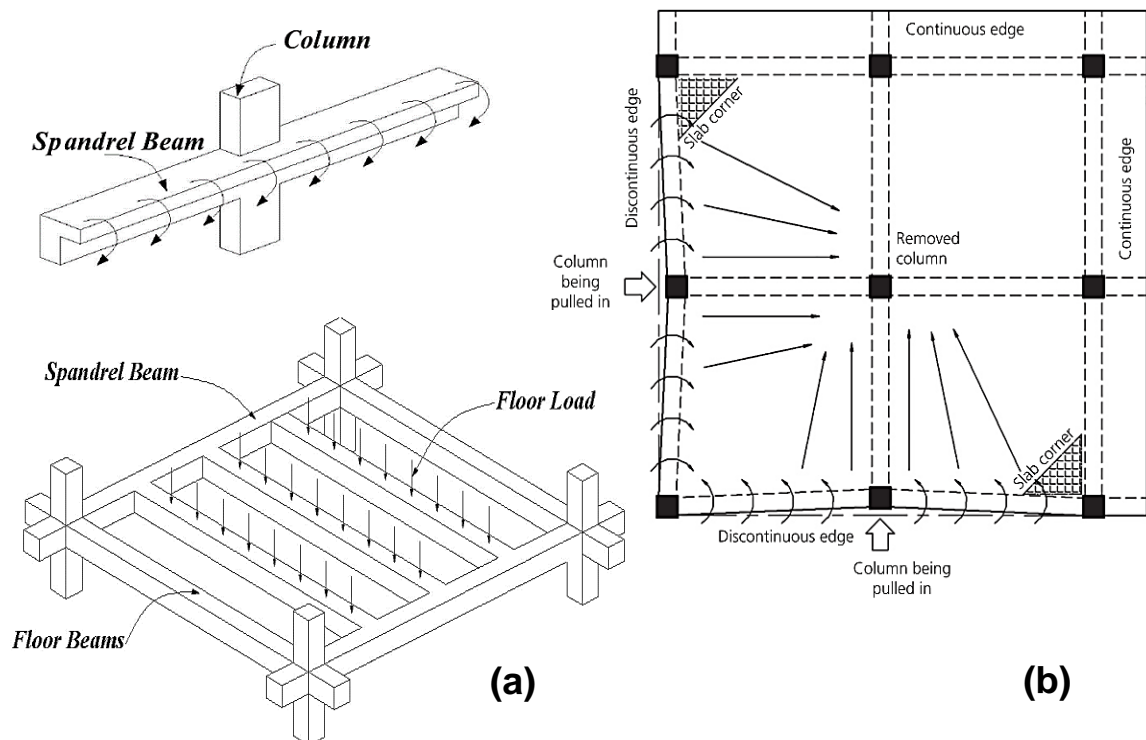


Figure 1.1: a) Torque induced in spandrel beams b) Torque induced in peripheral beams under column removal scenarios

a : (Prakash et al., 2010) b : (Pham et al., 2019)

The presence of torsional forces reduces the shear and flexural strength of RC members (Warwaruk, 1981), e.g., in the combination of the flexural and torsional forces, compression struts that result from torque action magnify the tension forces in the tension chords and alter the concrete compression zone. Also, in tests on RC cantilever walls, the imposed torsional forces affected the location of the plastic hinge and the flexural strength and ductility were substantially reduced (Peng and Wong, 2011). Previous work (Hsu and Wang, 2000; Hsu and Liang, 2003) has also shown that the torsional forces induced a reduction in the flexural capacity and member ductility of composite columns when applied simultaneously with bending moments. Work has also been conducted by Prakash et al. (2010) on the influence of torsion/bending ratio with shear on various RC column lengths. The test findings of these latter tests confirmed that shear stresses resulted from torsion and that the shear increases the strains in both the transverse and longitudinal reinforcement as well as degrading the cracking stiffness of the tested columns. Elfgren (1972) and Thurlimann (1979) used interaction curves based on the space truss mechanism; these curves indicated that the beam flexural capacity can be significantly affected by torsion. These observations clearly highlight the potential adverse effect of torque actions on RC members.

1.2 Research Problem

The role of the beam-column joint is important as it provides an efficient load path between the beam and column members. Poorly detailed or inadequately designed reinforced concrete (RC) beam-column joints lead to excessive deformations and increase in columns loads; ultimately, this may affect the stability of structure. Thus, a large number of tests have been carried out to investigate the behaviour of RC beam-column joints under monotonic or cyclic loading (i.e. short-term loading conditions up to failure). Generally, these tests involved the concentric loading of the beams and columns, i.e., Mostofinejad and Hajrasouliha (2019), Alavi-Dehkordi et al. (2019); Mostofinejad et al. (2018); Davood and Alireza (2017), Sasmal (2009), Triantafillou and Antonopoulos (2003), Hamil (2000b), Parker (1997), Sarsam and Phipps (1985). However, in practice, structural members can undergo a combination of loads including torsion during the construction stages and their working life. In comparison to concentrically loaded joints, much less research (given in Chapter 2) has investigated the effect of torsion on the beam-column joint behaviour. And most of this research has concentrated on the influence of the

eccentricity of the beam axis from the column axis where the beam's forces transfer into the joints away from the column's centroidal axis and induce a torque along the column height. Hence, further attention should be given to quantify the influence of torsion that can be developed in the beam region (i.e. floor loads) on the beam-column joint's behaviours and failure mechanisms.

The efficiency of Fibre Reinforced Polymers (FRP) external reinforcement systems (i.e. FRP wraps) for shear and flexural strengthening have driven a number of researchers to explore this system for torsion. Most of the proposed torsional strengthening schemes were investigated whilst strengthening beams rather than beam-column joints. As the tested beams were subjected to either pure torque or combined forces, details of these tests using FRP schemes are relevant and therefore described in Chapter 2. However, these torsional schemes can potentially increase beams capacities, stiffness, and levels of plastic deformations in beam's rebars to a sufficient level such that damage can occur in the column of the joint, negating the preferable strong column – weak beam behaviour. In addition, the performance of FRP wraps under sustained torsional forces did not investigated yet. Hence, there is a need to identify the influence of beam's wrapping on the failure types, joints forces (demands), and deformation levels.

Interestingly, the fib Model Code (2010b) and Eurocode 2 (2004) propose at the ultimate limit state that it is not necessary to consider torsion induced loading (by compatibility). To avoid excessive cracking, a minimum reinforcement should be incorporated by way of stirrups and longitudinal bars (fib Model Code, 2010b). Similar guidance is also provided in ACI Committee 318 (2014) for forces within the threshold limit; the threshold limit is defined as 25% of the torsional cracking moment. The general recommended design provisions for RC joints (ACI-ASCE 352R-02 Committee, 2002; Eurocode 2, 2004; NZS 3101, 2006; BS8110, 1997) do not provide guidelines to evaluate joint shear demand under combined actions including torsion. Also, it is important that the code provisions take into account the contribution of FRP wraps on increasing the beam's carrying loads and hence, the influence of the loads attained on the stresses developed in the steel rebars and concrete struts. Although, this appears that large plastic deformation in the beam's main rebars can arise from combined loads, while the corresponding beam-column joints design provisions for non-seismic regions do not consider strain hardening; i.e. ACI-ASCE 352R-02 Committee (2002) and Eurocode 2 (2004).

As mentioned above, very limited studies have attempted to address the effect of sustained torsional (long-term) loads on the time-dependent behaviour of RC beams. Certainly, the influence of combined loads and time-dependent developed strains on the beam-column joint behaviour was not examined even though significant time-dependent inclined cracks can be induced under long-term torsional loads (Allos and Rashid, 1989; Goode, 1975); these can affect the member's stiffness and durability.

1.3 Aim and Objectives of the Research

This research aims to identify the short and long-term influence of the beam torque combined with flexural and direct shear loads on exterior RC beam-column joints whilst considering the effects of previously developed beams torsional strengthening schemes using FRP's wraps.

To achieve this aim, determining the levels of induced stresses, strains, and damage due to the interaction between the combined loads is essential in order to define the failure mechanism and the joint's degree of distortion. This is achieved via experimental work and by introducing analytical and numerical models to quantify the joint forces and capacities; accordingly, this study presents the development of a number of formulas, proposed to evaluate the forces in the main rebars and compression struts under multiple actions and depending on the different wrapping orientations in the beam region – the intention is to develop guidance which will negate any risk of brittle failure in the compression struts. In addition, the intention is to achieve a better understanding of the behaviour of beam-column joints under sustained torsional forces combined with bending and shear, as well as investigating the long-term effectiveness of beam wrapping schemes.

1.4 Objectives

In order to achieve this aim, the following objectives were set:

1. Carry out a literature review of torsion effects on RC sections particularly the failure mechanisms that were observed during the beam tests and the performance of beam-column joints that eccentrically loaded; emphasis is given to:
 - The truss analogy and corresponding methods that were proposed to predict torsional behaviour of RC structures.

- The influences of the torsional beam wraps on the beam behaviour.
 - The behaviour of RC beams under sustained torsional forces and concrete time-dependent deformation.
 - The current state of knowledge on the behaviour of beam-column joints under eccentric loads and joint load transfer mechanisms, as well as the influential parameters relevant to the guidelines stated in the codes.
 - The proposed numerical models and corresponding concrete constitutive relationships for RC members under torsion.
2. To conduct experimental investigations on the beam-column joints, subjecting them to short and long-term loading series (i.e. monotonic and constant combined loads) in order to identify the following aspects:
- The effect of beam torque interacting with bending and direct shear loads on the failure mechanism and the carrying load capacities.
 - The variation in the attained loads, deformation and ductility levels, damaged zones and plastic hinge locations in respect to the wrapping schemes and loads attained.
 - The rise in the rebar strains due to the interaction between the imposed loads and the influence of the wraps used on the rebar forces.
 - The joint shear demands and distortion levels corresponding to the increase in the developed forces in the beam's main rebars.
 - The behaviour of the beam-column joint under constant loads; including the presence of beam torque and wraps.
 - Time-dependent deformations, cracks levels, and cracks patterns.
 - The developed time-dependent strains in the steel rebars and the concrete surfaces.
3. Propose analytical approaches for beam-column joints subjected to multiple loads, i.e.:
- Introduce rational formulas based on the truss analogy to evaluate the joint forces (demands) which account for the wrap orientations and the interaction between the combined forces acting on the beam.

- A design approach that limits the inclined compressive stresses induced from the shear-flow to the capacity of the concrete strut in order to avoid crushing of the concrete.
 - An analytical model to predict the joint strengths under multiple beam loads based on the concept of average stresses whilst considering various influential parameters that affect the RC joints.
4. To develop, by utilising non-linear finite element analysis, a three dimensional model approach which corresponds to the total strain crack constitutive model – this will be employed to simulate:
- The short and long-term behaviours of RC beam-column joints under combined load actions.
 - The influences of different load ratios (torque to bending-shear), concrete strengths, and multiple CFRP layers on the deformation levels, the strain development in the concrete and rebars, cracks and damage levels with respect to the loads attained and the wraps used.

1.5 Structure of the Thesis

The thesis consists of eight chapters:

Chapter 1 Introduction

This chapter provides the background to the research, highlights the research problem, and presents the aim and objectives of the research topic.

Chapter 2 Literature review

This chapter presents the methods and analogies identified in the literature which can be used to predict the behaviour of RC member's subjected to torsional and combined forces. Also, the studies that examined the RC beam-columns joints under eccentric loading conditions with the key factors that govern the force transfer mechanisms and joint strengths are discussed. A review of the joint design provisions stated in the major building codes is presented. A literature survey is also carried out to identify the beams and methods used to predict the beam's enhancement levels. This chapter also discusses the main findings identified in the literature with reference to the influence of sustained torsional forces and corresponding time-dependent deformation. The last section of this chapter reviews the research attempts

that numerically simulated the behaviours of RC Sections under torque actions; and a discussion of the developed constitutive models and cracking concepts for concrete is presented.

Chapter 3 Experimental programme

This chapter describes in detail the experimental program adopted to conduct two different sets of beam-column joint tests (i.e. short-term and long-term). Also, it provides the specimen geometries and details, the material properties, concrete mix, creep and shrinkage test details, and instrumentation used.

Chapter 4 Experimental results and discussion (short-term tests)

The results of the short-term beam-column joint tests using monotonically applied loads are presented here. The results have been analysed and discussed with a view to the thesis objectives.

Chapter 5 Experimental results and discussion (long-term tests)

The results of the long-term beam-column joint tests subjected to a sustained torsional load are included here. The long-term behaviour, developed strains and crack levels for the samples are discussed in relation to the time-dependent deformation of concrete (creep and Shrinkage).

Chapter 6 Analytical Models

This chapter proposes a number of formulas based on the truss mechanism intended to be used to quantify the joint forces and which consider the effects of combined loads and different wrapping schemes; further, it introduces a design approach which accounts for the level of developed compression forces due to shear-flow levels in order to prevent a concrete failure. It also develops a model according to the average stress concept, that can be used to predict the joint capacity.

Chapter 7 Finite elements modelling

The procedure used to develop the 3D models of the beam-column joints are provided; in addition to the constitutive models, loads applications, mesh and elements details, and constraints are provided. Validation of the models using experimental data is incorporated. Finally, this chapter presents a parametric study to examine the influences of different torque to bending-shear ratios, multiple CFRP layers, and concrete strengths; the analysis is carried out under monotonic and sustained loading conditions.

Chapter 8 Conclusion and recommendations

The main conclusions and findings drawn from this study are presented, as well as the recommendations for future research.

Chapter 2 Literature Review

2.1 Introduction

Torsional forces can significantly affect the RC members by increasing the level of cracks and altering the failure mode toward a brittle shear mode. Thus, it is important to recognise the mechanism and influences of torsional stresses combined with flexural and direct shear in order to identify the potential of the torsional configurations using Fibre Reinforced Polymers (FRPs) on both the beam and the joint behaviours. This chapter (Section 2.2) describes the methods and analogies developed in the literature to quantify the torque actions interacted with different loads on the member's behaviour. Moreover, a review of the studies that investigated the RC beam-columns joints under eccentric loading conditions with the most influential factors that affect the beam-column joint strengths and behaviour is conducted. In addition, the relevant design requirements and provisions according to the major building codes are also reviewed (e.g. ACI-ASCE 352R-02 Committee (2002); Eurocode 2 (2004); BS8110 (1997)).

The introduction of FRPs as an efficient strengthening material has driven many researchers to explore this material in the last 30 years. Hence, the use of externally bonded FRP composites for shear and flexural retrofitting for reinforced concrete (RC) structures has been studied extensively (e.g. Baggio et al., 2014; Gao et al., 2007; Täljsten and Elfgren, 2000; Triantafillou, 1998; Täljsten, 1997). Dry and wet lay-up methods of adhesively attaching FRP sheets or laminates on a member surface using thermoset resins are efficiently employed to improve the capacity of the structures. In contrast to the flexural and shear strengthening configurations, fewer studies have been conducted regarding torsional configurations; these configurations are reviewed in Section 2.3.

Section 2.5 considers the long-term behaviour of concrete members under sustained torsional loads, in which the main findings identified in the literature are discussed. Further, a discussion of the time-dependent characteristics and the effects of the creep and shrinkage of concrete is presented. The last section of this chapter (Section 2.6) discusses the numerical models that proposed in the literature to simulate the behaviour of RC sections under torque actions. Also, the developed constitutive models for concrete and the concepts of concrete cracking that adopted in the finite element analysis method are reviewed in this section.

2.2 Torsion Analogy and Effects

Twisting actions induce a shear stress that is distributed over the member section; these stresses vary from a maximum at the section's outer perimeter to zero at the section's centre, in accordance with the Saint Venant theory. Essentially, the solid prismatic concrete members resist the torsional shear stresses based on this aforementioned circulatory distribution of stresses theory. Prior to cracking, this analogy satisfies the principals of the theory of elasticity for sections with no warping prevention. Hsu (1968a) used the Saint Venant theory to predict the torsional cracking strength of plain concrete members assuming a homogenous linear-elastic behaviour of concrete before cracking. Further, Eurocode 2 (2004) suggests that the principal of Saint Venant can be applied to elastically predict the members' capacity of complex shaped concrete sections under pure torque actions. This can be performed by dividing the member's section into rectangular sub-sections. On the other hand, according to the assumption of the plastic distribution of circulatory stresses in concrete prior to failure, BS8110 (1997) and Hsu (1968) have utilised a sand heap analogy to determine the torsional shear strength of plain concrete.

In contrast to circulatory torsion (Figure 2.1), warping torsion can significantly affect open thin-walled section profiles with some warping restrictions (e.g. end restraint), which arise from the bending of the flanges (Elfgren, 1972; Timoshenko, 1940). Likewise, the Eurocode 2 (2004) and CEB-FIP (1991) model code stipulate that warping torsion predominates in open thin-walled cross sections, while for other section types (especially closed sections) it is satisfactory to design the members based on the circulatory torsion resisting mode. This work investigates the torque influences on the RC solid sections, wherein the analytical calculations correspond with the analogy of the circulatory action of torsional forces.

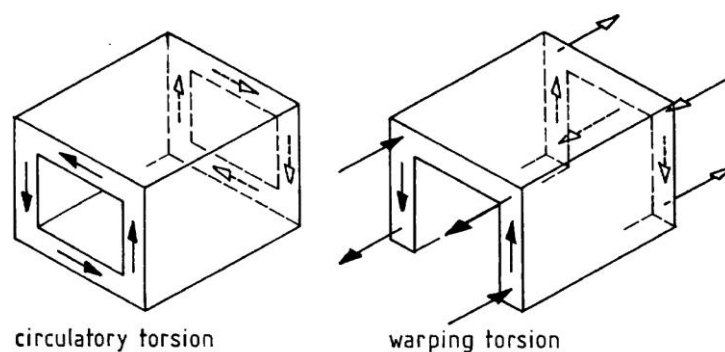


Figure 2.1: Actions of circulatory and warping torsion
(Fédération Internationale Du Béton, 1999)

2.2.1 Torsion Combined with Flexural, Direct Shear, Axial Forces

In practice, the occurrence of torsion with other forces, such as flexure, shear or axial loads is quite common. This combination produces a variation of strains around the cross section's perimeter and over the member's length. As the reinforcement strains, the direction and thickness of the compression zones differ (Leung and Schnobrich, 1987; Cocchi and Volpi, 1996). This is portrayed in a combination of flexural and torsional forces, as compression struts magnify the tension forces in the tension chords and alter the concrete compression zone. Lampert and Collins (1972) indicated that asymmetrical reinforcement affects the yielding of the longitudinal rebars and distributions of strain. Furthermore, Li (2012) reported that in unsymmetrically reinforced sections, the torsional shear stresses vary the section curvature (ϕ), as shown in Figure 2.3. However, an addition of flexural forces can enhance the torsional capacity of unsymmetrically reinforced sections (Warwaruk, 1981), where the flexural compressive stresses alleviate the tensile forces induced by the torque actions. Prakash et al. (2010) examined the influence of torsion/bending ratio with shear on various RC column lengths. The test findings confirmed that shear stresses resulted from both torsion and direct shear increase strains in both the transverse and longitudinal reinforcement. In addition, degradation in the cracking stiffness was observed. Hsu and Liang (2003), along with Hsu and Wang (2000), found a reduction in flexural capacity and member ductility when a torque was simultaneously applied to the experimental composite columns. Also, the combination of torsion and bending was studied by Tirasit and Kawashima (2007), whose experimental results showed that the presence of torsion with bending altered the location of the plastic hinge in RC columns, causing the damage to occur further from the flexural plastic zone.

Similarly, torsional effects combined with bending and shear on cantilever RC walls were investigated by Peng and Wong (2011). The test results also indicated the influence of torsion on the plastic hinge location - it moved further away from the fixed end, significantly so under a larger torsion/bending ratio, where a degradation in the torsional cracking strength was observed due to flexural-shear forces. Li et al. (2010) reported that a small ratio of torsion with

flexural forces would be lead to a yield of the transverse reinforcement. On the other hand, the effect of axial compressive forces with torsion has been investigated by Mondal and Prakash (2015); they found that the axial compressive forces increase the pre-cracking stiffness of RC columns by delaying the formation of tensile stresses induced from torsion, although this effect is not appreciable under the ultimate torsional strength.

The interaction between direct shear and torsional loads increases the shear stresses at the section side where the shear flow (q) resulted from adding torque and vertical shear (Figure 2.2). For this reason, the ACI Committee 318 (2014) and AASHTO LRFD (2010) limit the sum of shear and torsion stresses to the nominal shear and tensile strength of concrete, in order to reduce excessive cracks and reduce the crushing of concrete. However, for a favourable redistribution of shear stresses over a member's depth, a root-square summation of the direct shear and torsional forces has been recommended for concrete solid sections. Ewida and McMullen (1981) identified the influence of increases in the transverse reinforcement on the variation of the shear-torsion (S-T) interaction curve. Khaldoun and Michael (1995) found that with a larger concrete cover, a substantial increase in the shear and torsional capacity of RC beams was obtained, with various (S-T) ratios. In contrast, this caused increments in the crack's width.

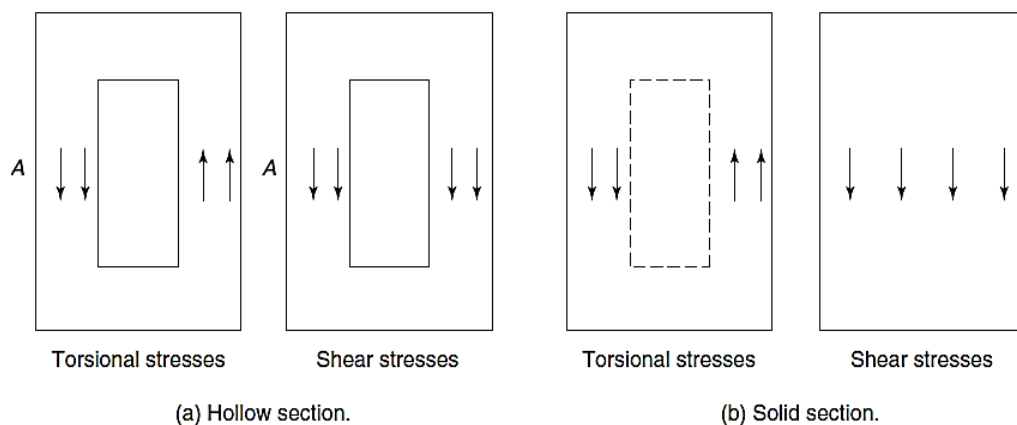


Figure 2.2: Direct shear and torsion addition

(Wight and MacGregor, 2012)

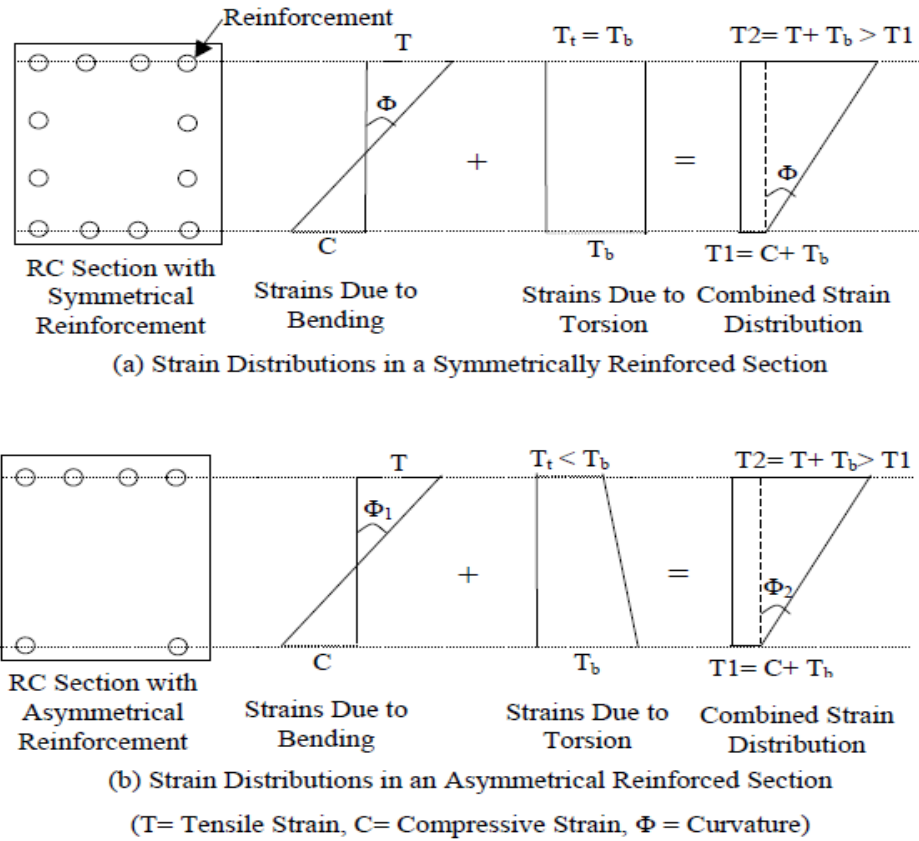


Figure 2.3: Strain profiles in RC sections under flexural and torsional forces

(Li, 2012)

2.2.2 Interactions and Analytical Methods of Torsion and other Forces

The earlier methods that were employed to identify the structural capacity of RC members under combined loading were skew-bending (Gvozdev et al., 1968; Hsu, 1968b; Elfgren et al., 1974; Ewida and McMullen, 1981) and truss model analogy, with a constant inclination angle. Both methods consider the condition of the force equilibrium condition and they can predict a member's capacity during its ultimate state. Lampert and Collins (1972) reported that the skew bending method predicts parabolic interaction curves that correspond closely with the truss method (Eq.2.1 a and b) for rectangular solid members under torsional and bending loads, as shown in Figure 2.4.a. However, due to the limitations of the skew-bending method in dealing with different types of

sections (e.g. box section), the modern codes of practice including the ACI 318 committee, utilise the truss method to design RC members with torsion.

$$r \left(\frac{T_u}{T_{uo}} \right)^2 + \frac{M_u}{M_{uo}} = 1 \quad \text{Eq.2.1a}$$

$$\left(\frac{T_u}{T_{uo}} \right)^2 - \frac{1}{r} \frac{M_u}{M_{uo}} = 1 \quad \text{Eq.2.1 b}$$

Where;

r = the ratio of the top to the bottom chord's yielding forces

$\frac{T_u}{T_{uo}}$ = the ratio of the applied torque to the nominal torsional capacity of a section under pure torsional loads

$\frac{M_u}{M_{uo}}$ = the ratio of the applied bending moment to the nominal bending capacity of a section under only bending loads

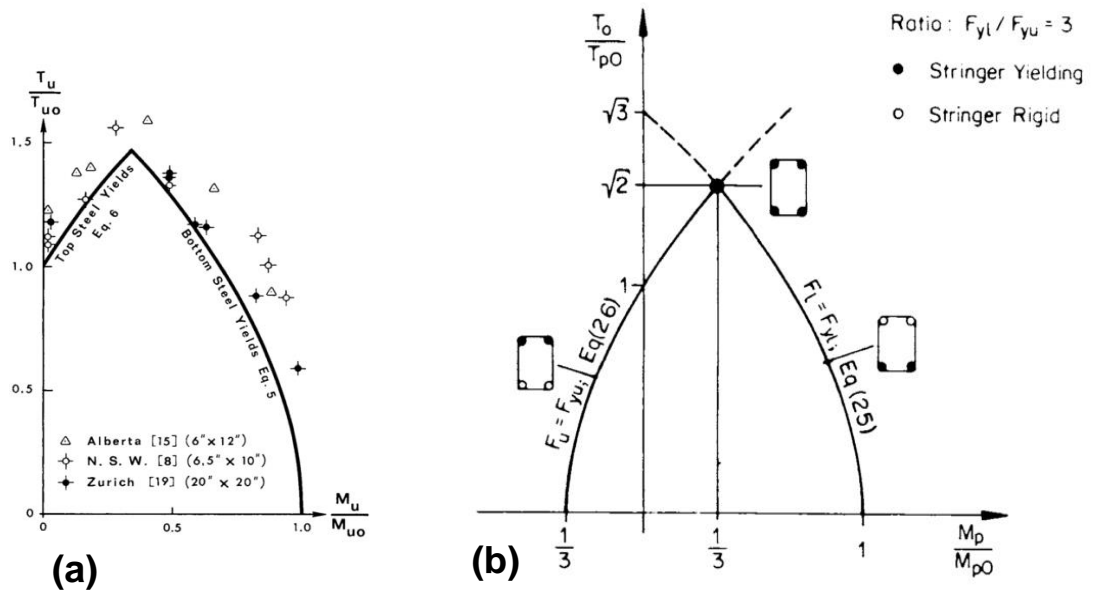


Figure 2.4: Interaction diagrams a) Skew-bending method b) Truss model method

a: (Lampert and Collins, 1972) b:(Thurlimann, 1979)

In using the truss model, Elfgren (1972), Thurlimann (1979), and Hsu (1993) have all introduced a set of interaction equations (Eq.2.2 a to c) of torsion, shear and bending loads. These satisfy the equilibrium equations by

considering the plasticity of reinforcement hoops and any of the main chords, where the yielding of bars can occur either in the section's bottom, top, one side, or all sides, depending on the ratio and direction of torsion when bending and direct shear are applied, as discussed in Section 2.2.1. For each failure mode, the equations are calculated using equilibrium, for example, the bottom yielding (1st Mode) expression is formulated directly by equating moments (external and internal) with the top chords. While the 2nd mode-Eq.2.2b is derived by equating moments with the bottom chords, where flexural compressive forces counter tensile forces produced by shear and torsion actions. Eq.2.2c (3rd Mode) neglects the influence of bending moment and it is formulated by taking moments about the beam side where the shear flow resulted from shear and torsion are subtractive. These rational equations show the influence of torsion combined with other forces on the interaction curves that are given in Figure 2.5. The increase in torsion reduces the flexural and shear capacity.

$$\left(\frac{M_u}{M_{uo}}\right) + \left(\frac{V_u}{V_{uo}}\right)^2 r + \left(\frac{T_u}{T_{uo}}\right)^2 r = 1 \quad (1^{\text{st}} \text{ Mode: bottom yielding}) \quad \text{Eq.2.2 a}$$

$$-\frac{1}{r} \left(\frac{M_u}{M_{uo}}\right) + \left(\frac{V_u}{V_{uo}}\right)^2 + \left(\frac{T_u}{T_{uo}}\right)^2 = 1 \quad (2^{\text{nd}} \text{ Mode: top yielding}) \quad \text{Eq.2.2 b}$$

$$\left(\frac{V_u}{V_{uo}}\right)^2 + \left(\frac{T_u}{T_{uo}}\right)^2 + 2 \left(\frac{V_u T_u}{V_{uo} T_{uo}}\right) \sqrt{\frac{2 dv}{p_o}} = \frac{1+r}{2r} \quad (3^{\text{rd}} \text{ Mode: side yielding}) \quad \text{Eq.2.2 c}$$

Where;

$\frac{V_u}{V_{uo}}$ = the ratio of the applied shear to the nominal shear capacity of a section under direct shear load only

dv = distance between top and bottom stringers c/c

With a view to evaluate member deformations and capacity throughout the loading stages, the diagonal Compression Field Theory (CFT) was proposed by Mitchell and Collins (1974) as a rational approach for determining the torsional stresses and strain developments within RC sections. CFT is based

on the truss analogy method (Appendix A), which satisfies the equilibrium and geometric conditions, in addition to the constitutive equations of concrete and steel. Rabbat and Collins (1978) introduced a truss model with variable inclination angles in order to identify members' behaviour with complex loading conditions. The Modified Compression Field Theory (MCFT) was developed as an extension of the original CFT by considering the softening of concrete, along with the tensile and shear stresses of cracked concrete. The MCFT (Vecchio and Collins, 1986) was initially derived to determine the responses of RC panels under in-plane shear and tensile forces, while in a later study conducted by Rahal and Collins (1995), MCFT was used to derive a model for sections subjected to combined loading. Meanwhile, Greene Jr and Belarbi (2009a) derived an analytical model based on the Softened Truss Model (STM) for RC sections under combined loads. The following sections briefly describe the variable truss model, MCFT, and STM.

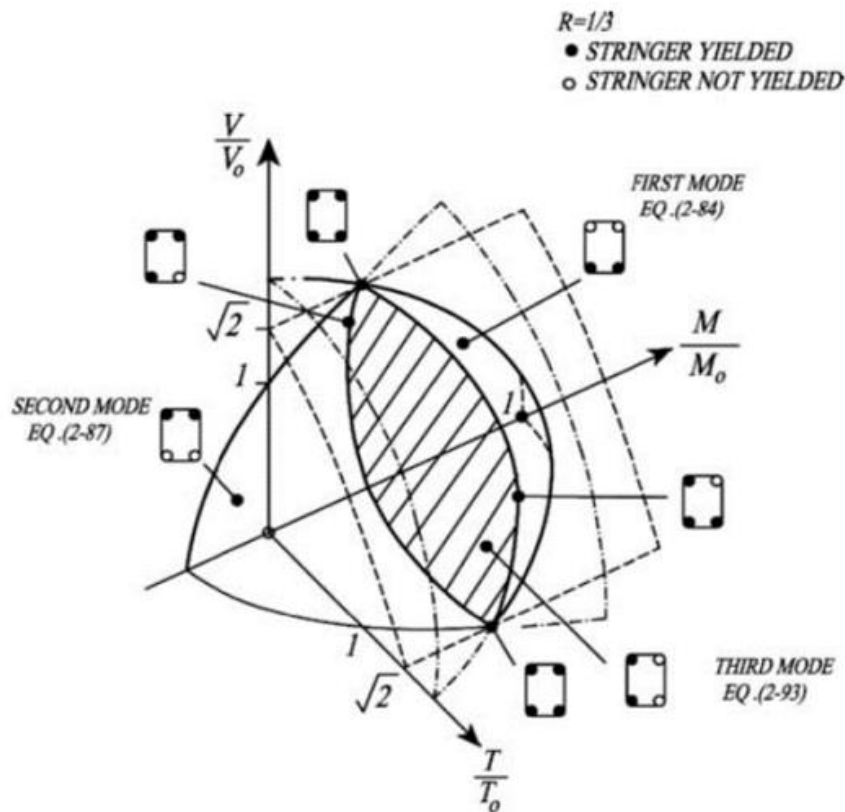


Figure 2.5: Interaction diagram, torsion-shear-bending
(Hsu, 1993)

2.2.3 Variable Angle Truss Model, MCFT and STM

According to the Variable Angle Truss model, the RC beam sections are idealised using four parallel chords representing the longitudinal steel ties and concrete blocks, located at the section's top and bottom corners. In addition, these chords are connected by the section's four walls, where each wall consists of a concrete strut and transverse ties (hoops). The equilibrium equations were derived under biaxial bending, axial, shear and torsional loads, while the geometry deformations correspond with Mohr's circle. The average shear flow resulted from superimposing the shear and torque, which is assumed to be a constant at each member's sides. The inclination angles at the section's faces were calculated according to the truss equations (Eq.A.1 to A.3 – Appendix A) and compatibility conditions. The model ignores the tensile strength of concrete and the tension stiffening effect, as it assumes a perfect bond between rebars and concrete ($\epsilon_s = \epsilon_c$).

In 1986, Vecchio and Collins developed the MCFT based on extensive biaxial tests of RC panels. The MCFT recognised the softening of concrete struts in correlation with the tensile strain (ϵ_1) of concrete. In addition to the softening of the constitutive equations, MCFT takes into account the concrete tensile stress (f_1) (tension stiffening) and shear stresses across cracks (v_{ci}). Where, shear stresses (v) on cracks depend on the following factors - the crack's width (ω), maximum aggregate size (a_g) and spacing between cracks (S), as shown in Figure 2.6. However, to determine the response of RC elements, a repetitive algorithm is required to satisfy the member's conditions.

Rahal and Collins (1995) introduced an analytical model for members under torsion, shear, biaxial bending and axial loads, based on the principals of MCFT. This aforementioned combination of forces is assumed to be resisted by two systems. The first system resists longitudinal forces resulting from axial, biaxial bending, and torsion. The second system consists of the section's walls that are subjected to shear stresses and the longitudinal strain from the first system that corresponds with the compatibility conditions. A computer program is employed to solve the model algorithm. The model results were verified with experimental tests. Selby and Vecchio (1991) developed a finite element formulation derived from MCFT in order to simulate the response of three-dimensional RC members. They defined the material stiffness matrix by considering the softening of concrete and steel stiffening according to the MCFT's constitutive equations.

Further research was conducted by Vecchio and Collins (1993) to properly determine the compression softening factor. A comparison between experimental tests and finite element results was carried out by employing various softening factors that were developed in the previous research. This demonstrates the influence of compression softening on the behaviour of cracked RC, and also confirms the major role of tensile strain on the degree of softening.

In a similar manner to CFT, with consideration of equilibrium, compatibility and material constitutive aspects, Hsu and Mo (1985b) introduced STM for members under torsional loads only. They included the softening of concrete by using Vecchio and Collins (1981) curves. Correspondingly, Belarbi and Hsu (1995); Belarbi et al. (1996) proposed constitutive formulas for cracked RC elements, based on the outcomes of biaxially tested panels (Eq.2.3a to c). Moreover, the STM correlates thickness of shear flow (t) with diagonal compressive strain at the section's surface (ϵ_d) and the curvature (Ψ), where $t = \epsilon_d / \Psi$; Hsu (1993) provides a solution algorithm to predict a full response for members subjected to torque actions.

$$\sigma_2 = \xi_{\sigma 0} f_c' \left[2 \left(\frac{\epsilon_2}{\xi_{\epsilon 0} \epsilon_o} \right) - \left(\frac{\epsilon_2}{\xi_{\epsilon 0} \epsilon_o} \right)^2 \right] \text{ if } \frac{\epsilon_2}{\xi_{\epsilon 0} \epsilon_o} \leq 1 \quad (\text{Eq.2.3 a})$$

$$\sigma_2 = \xi_{\sigma 0} f_c' \left[1 - \left(\frac{\frac{\epsilon_2}{\xi_{\epsilon 0} \epsilon_o} - 1}{\frac{2}{\xi_{\epsilon 0}} - 1} \right)^2 \right] \text{ if } \frac{\epsilon_2}{\xi_{\epsilon 0} \epsilon_o} > 1 \quad (\text{Eq.2.3 b})$$

$$\xi_{\sigma 0} = \frac{0.9}{\sqrt{1+400\epsilon_1}} \text{ and } \xi_{\epsilon 0} = \frac{1}{\sqrt{1+500\epsilon_1}} \quad (\text{Eq.2.3 c})$$

Where;

ϵ_o = compression strain at maximum stress in a uniaxial stress-strain curve of a concrete cylinder; can be taken as 0.002

σ^o = maximum compression stress of a concrete cylinder

ξ = softening coefficient

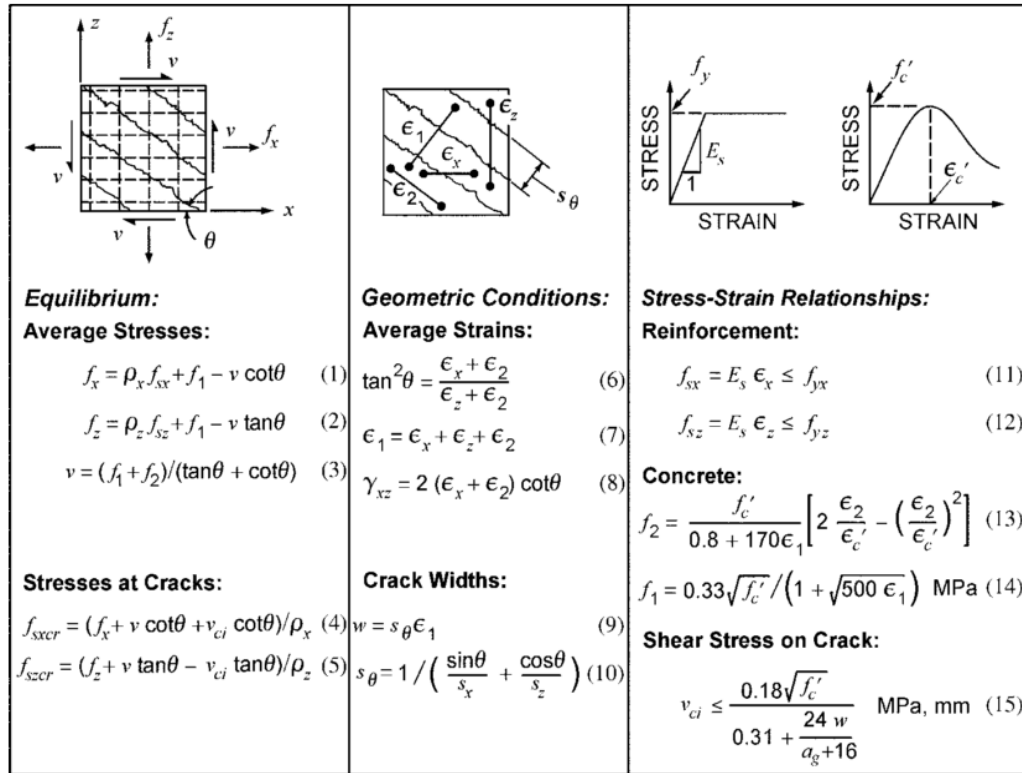


Figure 2.6: The MCFT equations.

(Bentz et al., 2006)

As mentioned in the previous section, Greene Jr and Belarbi (2009a) developed an analytical model related to STM to account for various load combinations in RC beams. The sections are assumed to be formed from panels with different thicknesses (Figure 2.7) that correspond to the magnitude of the shear flow zone at each face. The evaluation of the shear flow is based on the summation and directions of torsion and the direct shear of each panel, where a uniform distribution of shear stresses along the panel depth was assumed. The rotated crack method is employed to correlate and calculate the stresses in two orthogonal directions, along with the shear stresses and the principal stresses that represent the compressive strut and tensile stresses in a concrete panel, respectively. Moreover, three compatibility formulas for normal, shear and principal strains are included with other geometry variable equations (panel curvature, twisting angle, panel thickness, and surface strain). This model agrees with other models based on

MCFT and STM, where an iterative procedure is required to verify the variables assumption in order to solve the model's equations. However, these models (Greene Jr and Belarbi (2009a); Rahal and Collins 1995) were derived according to smeared stresses and strain distributions over a panel depth, which do not identify the force variations in the bottom and upper chords of each panel.

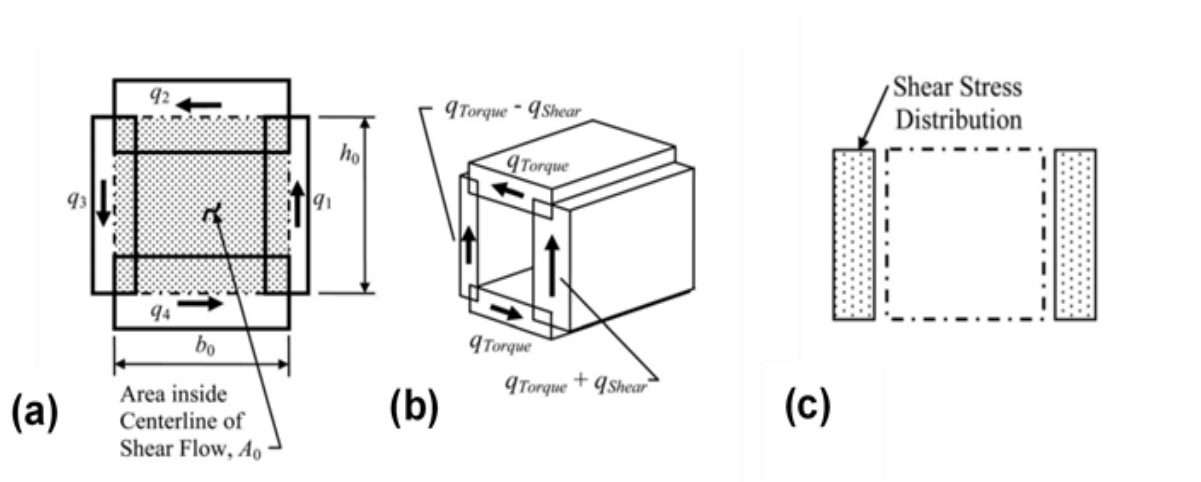


Figure 2.7: a) Panels and shear flow b) Shear flow summation c) Vertical shear distribution

(Greene Jr and Belarbi, 2009b)

2.3 Beam Torsional Strengthening with FRP

Since 2001, a number of studies have been conducted with a view to strengthen and increase the torsional capacity of RC beams with FRP composites. The simplicity of installation and superior physical characteristics of FRP wraps give advantages over conventional retrofitting materials, such as steel and concrete. Several fibre configurations have been investigated, consisting of both full and partial sectional wrapping. Additionally, analytical approaches that commonly correspond to the truss method have been proposed to predict the torsional behaviour of strengthened RC beams. Most of the available studies have investigated the efficiency of torsional arrangements on RC beam members, which the following sections review in detail.

2.3.1 FRP Material

The literature shows that FRP fabrics have been used extensively in beams tests with distinctive torsional strengthening schemes. These fabrics are typically made of high strength carbon or glass fibres. Recently, Al-Bayati et al. (2018) investigated CFRP laminate strips and ropes mounted inside the beam's covers by using the 'near surface mounted' technique in order to enhance torsional capacities for RC beams. Atta and El-Shafiey (2014) combined CFRP laminate strips with CFRP hoops glued to a beam surface. Figure 2.8 shows the typical stress-strain curves for carbon and glass fibres with steel, indicating the superior strength of carbon fibres and the brittle nature of FRPs.

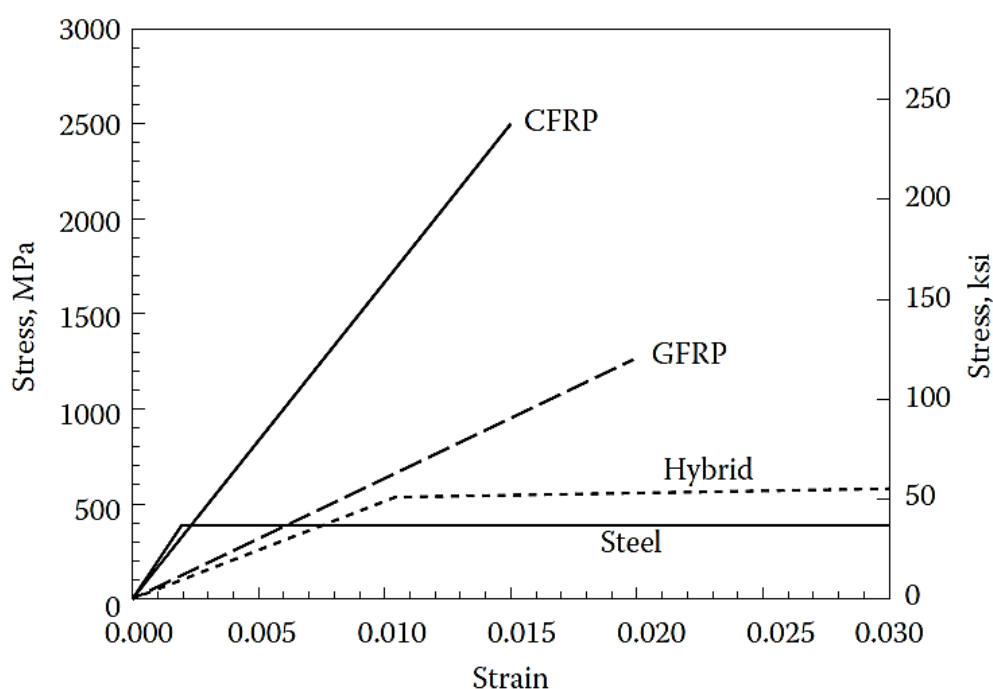


Figure 2.8: Typical stress-strain curves of steel, CFRP, GFRP.
(ACI 440R-07, 2007)

Table 2.1 shows that unidirectional carbon fibres have been the dominant fibre type that have been used, since their efficiency has been verified. Further, Ameli et al. (2007) reported that Glass Fibre Reinforced Polymer (GFRP) wraps were less effective than CFRP in increasing torsional strength. Ghobarah et al. (2002) found that torsional configurations with CFRP and

GFRP similar enhancement levels. Other researchers (Patel et al., 2016; Jariwala et al., 2013) indicated that wrapped sections with GFRP schemes can achieve a 117% increase in their ultimate torsional strength.

Epoxy resins (thermosetting polymers) were used by researches to impregnate and adhere the fibre fabrics or laminates to a member's surface. In contrast, Al-Bayati et al. (2018) used a cementitious based mortar to embed the CFRP laminates into surface grooves made in the surface of the beam. However, epoxy resins were more effective in enhancing torsional capacity than the proposed cementitious mortar (Al-Bayati et al., 2018).

2.3.2 Torsional Fibre Schemes

A summary of the available studies that have experimentally investigated the externally bonded FRP systems for beams is presented in Table 2.1. These studies showed that a different level of torsional capacity can be obtained with different arrangements of fibre wraps. Based on the fibres' orientation, section wrapping, and beam configurations, these schemes can be categorised into five main types, which include continuous vertically oriented wraps along the beam member, U-wrap, strip wrap (hoops), 45° oriented fibres, and horizontally oriented fibres. These are shown in Figure 2.9.

The beam tests that have been conducted show that the vertically and 45° oriented fibre wrap arrangements attained the maximum carrying capacities (Ghobarah et al., 2002; Panchacharam and Belarbi, 2002; Chalioris, 2008; Deifalla et al., 2013; Salom et al., 2004). The highest increment in ultimate strength in comparison to the unstrengthened control beam is reported to be between 70% and 149% in continuous fully wrapped beams with 90° oriented fibres-Figure 2.9a (Ameli et al., 2007; Chalioris, 2008; Ghobarah et al., 2002; Zhang et al., 2001; Panchacharam and Belarbi, 2002). However, under pure torsional loading, Ghobarah et al. (2002) found that the 45° inclined strips wrapped around a beam length (Figure 2.9d) provided the maximum strength, with a 72% increment when compared with vertical strips. Likewise, Salom et al. (2004) reported an increment in the torsional strength of 77% for T-flanged RC beams when strengthened with the 45° scheme.

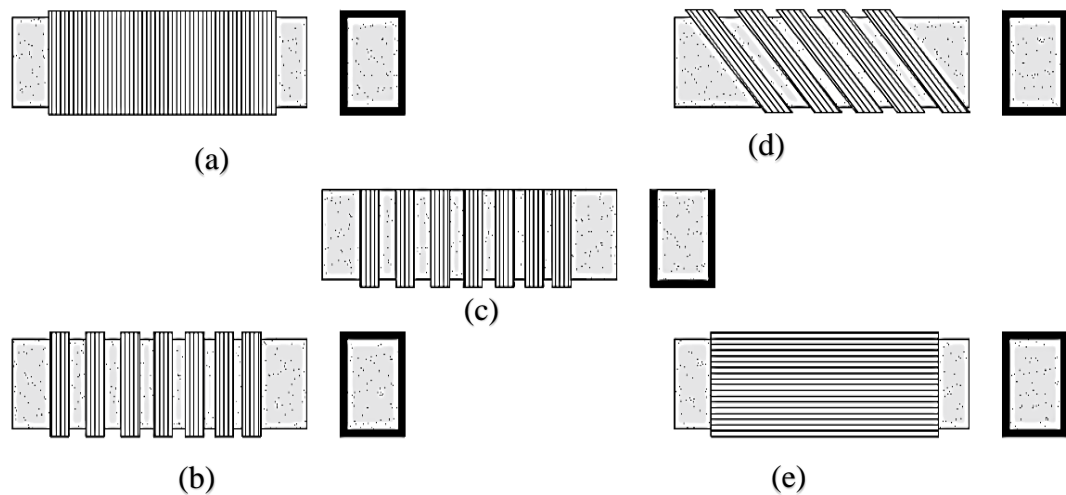


Figure 2.9: Beams strengthening schemes (a) Full-continuous wrapping (b) FRP hoops (c) U-wrap (d) 45° inclined Strips (e) Horizontally oriented warp

In contrast, the longitudinal arrangements (horizontally oriented fibres-Figure 2.9e) did little to enhance performance due to the de-bonding of the wraps from the members' surfaces caused by the twisting action (Patel et al., 2016; Zhang et al., 2001; Panchacharam and Belarbi, 2002). Also, when transverse strips are used, it was observed that the crack inclination angle increased and that the cracks become narrower in relation to the control and horizontally strengthened specimens. Panchacharam and Belarbi (2002) reported that the largest increase in the torsional crack capacity was obtained in members reinforced with longitudinal wraps (horizontal schemes), where these warps induce passive pre-stress effects.

The results of the previous studies indicate that the partially wrapped arrangement (U-wrap-Figure 2.9c) is less effective than the fully wrapped schemes. Zhang et al. (2001) found that the strength of the beams corresponded with an increase in the number of plies and a reduction in spacing. The influence of the fibre wrap ratio was also identified by Ghobarah et al. (2002) who showed that complete wrapping was considerably more efficient in comparison with the strip configurations; the maximum increase in member strength was 77% and 27% for complete and strip wraps,

respectively. In addition, the member failed in the un-strengthened zones between the FRP strips. Furthermore, even with the same fibre ratios, Chalioris (2008) found that beams with completely wrapped sections attained larger torsional loads (1.6 times) that of partially (strip) strengthened sections.

A three-sided U-wrap is a more practical configuration for strengthening a beam that is monolithically cast with a slab or a flanged beam. However, 'un-anchored' U-wraps have been found to be less effective than the full and partial wrapping (FRP hoops), as they suffer from premature de-bonding (Deifalla et al., 2013). Ma et al. (2018) employed U-wraps to strengthen RC solid beams with single and double carbon plies, where longitudinal strips were fixed at the ends of U strips in order to increase the bonding areas. However, only increments of 16-20% in ultimate loads were obtained.

Several authors (Chalioris, 2008; Salom et al., 2004; Panchacharam and Belarbi, 2002) have used anchors to prevent the premature debonding that initiates at the discontinuous ends of U-wraps. Although these anchorage systems increased the member's capacities, the effectiveness of U-wraps was still less than the full sectional jacking schemes. Deifalla and Ghobarah (2010b) did manage to increase the capacity of flanged beams by 69% using steel angles attached to the beam's corners and fixed to the flanges by anchor bolts. They found that a three-sided U-wrap with a proper anchorage system would be more efficient with flanged beams, since flanges provide additional torsional stiffness for the un-strengthened side.

As discussed earlier, a recent attempt was made by Al-Bayati et al. (2018) to strengthening RC beams using the Near Surface Mounted (NSM) technique. This technique do require extensive surface preparations which consist of pre-cut grooves inside the beam's concrete cover, grooves filling, and surface levelling after embedding the FRP strips (laminates or ropes) into the grooves using epoxy or cementitious based materials. Further, full externally wrapped section (CFRP fabric) was notably more robust than the embedded CFRP laminates or ropes (NSM). Since, the observed increments in ultimate torque using NSM technique were ranged between 10% to 23%.

Table 2.1: A summary of the torsional configurations of beams and details of the fibres that have been experimentally tested.

Author	Beam Section		Fibre Type		Configuration				Fibres Orientation ¹			Number of Plies	
	Rectangle	Flanged	CFRP	GFRP	Full	Hoops	U	Strips	0°	90°	45°	1	2
Zhang et al. 2001	✓	-	✓	-	-	✓	-	✓	✓	✓	-	✓	✓ ⁷
Ghobarah et al. 2002	✓	-	✓	✓	✓	✓	-	✓	-	✓	✓	✓	
Panchacharam and Belarbi 2002	✓	-	-	-	✓	✓	✓	✓	✓	✓	-	✓	✓
Salom et al. 2004	-	✓	✓ ^{5,9}	-	-	-	✓	-	✓	✓	✓	-	✓
Hii and Al-Mahiadi 2004	✓	-	✓	-	-	✓	-	-	-	-	-	✓	-
Deifalla and Ghobarah 2005	-	✓	✓ ⁵	-	-	-	✓	-	-	-	✓ ⁵	✓	-
Al-Mahaidi and Hii 2007	✓ ²	-	✓	-	-	✓	-	-	-	✓	-	✓	✓
Ameli et al. 2007	✓	-	✓ ³	✓	✓	✓	✓	-	-	✓	-	✓	✓
Chalioris 2008	✓	✓	✓	-	✓	✓	✓	-	-	✓	-	✓	✓
Mohammadzadeh and Fadaeel 2010	✓	-	✓	-	✓	✓	✓	-	-	✓	-	✓	✓
(Deifalla and Ghobarah, 2010b)		✓	✓ ⁵		✓		✓				✓ ⁵	✓	-
Jariwala et al. 2013	✓	-	-	✓	✓	✓	✓	✓	✓	✓	✓	✓	-
Deifalla et al. 2013	✓	✓	✓	-	✓	✓	✓	-	-	-	✓ ⁵	✓	-
Atta and Shafiey 2014	✓ ⁴	-	✓	-	✓	-	✓	✓	✓ ⁸	✓	-	✓	-
Allawi et al. 2015	✓ ⁶	-	✓	-	-	✓	-	-	-	✓	-	✓	-
Patal et al. 2016	✓	-	-	✓	-	✓	✓	✓	✓	✓	✓	✓	-
Al-Bayati et al. (2018)	✓		✓			✓		✓		✓		- ⁸	-
Ma et al. (2018)		✓	✓				✓	✓	✓	✓		✓	✓

1. Inclined from the member longitudinal axis.

2. Rectangular solid sections and box sections were tested.

3. One ply only uses for CFRP strengthened specimens.

4. Dapped-end beams were tested.

5. $\pm 45^\circ$ bi-directional inclined fibres sheets were used.

6. Box sections were tested.

7. Various numbers of plies (1,2 and 3) were used for hoops only.

8. CFRP laminates

9. [0, 90] bi-directional fibres sheets were used.

2.3.2.1 Loads Combinations

In most cases it appears that the torsional strengthening tests for RC beams have been tested under pure torsional loading which has been monotonically applied. Nevertheless, Salom et al. (2004) verified the effectiveness of CFRP jackets under a cyclic torsional load (half-cycle). Deifalla and Ghobarah (2010b) tested flanged beams under torsional (T) and shear (V) loads with T to V ratios of 1 and 0.5. The results showed that the increase in T/V reduced the member's strength and promoted a higher rate of crack development.

In other studies (Patel et al., 2016; Jariwala et al., 2013) the influence of torsion (T) and flexural (M) forces with various wrapping methods (Table 2.1) were investigated (the T/M ratio was 1.56). In contrast with the specimens under pure torque, an improvement in cracking load was obtained. This improvement confirms the effect of bending compression stresses, as described earlier in Section 2.2.1. Atta and El-Shafiey (2014) investigated three different strengthening configurations with dapped-end beams subjected to combined loads, including torsion, bending and shear. The test results indicated the viability of FRP composites towards enhancing torsional carrying capacities.

2.3.3 Analytical Methods and Design Details for FRP Schemes

The truss analogy has commonly been utilised by researchers to analyse and predict the behaviour of torsionally strengthened RC members. The contribution of FRP schemes is to increase the capacities of sections and this has been calculated in accordance with the composite's properties and fibre orientations. Vertical fibres (90°) restrain the diagonal shear cracks in a similar manner to transverse steel reinforcement. The superposition (Eq.2.4) of steel and FRP has been adopted in the literature to compute the ultimate torsional moment that can be resisted by externally strengthened RC sections (e.g. Ma et al., 2018; Al-Bayati et al., 2018; Hii and Al-Mahaidi, 2007; Salom et al., 2004; Panchacharam and Belarbi, 2002; Ghobarah et al., 2002). Where a good agreement has been obtained with the predicted and experimentally observed capacities for the tested beams.

Ma et al. (2018); Panchacharam and Belarbi (2002) evaluated the FRP contribution according to the fib Bulletin 14 (2001) formula for strengthening to resist torsion; a good agreement was observed with the test data. This

formula (Eq.2.5) was derived according to the space truss mechanism and shear flow distribution (Berd't's theory), where it is applicable for fully wrapped sections with vertically oriented fibres. Also, the fibre's effective strain (ε_{fe}) is based on Triantafillou and Antonopoulos (2000) work and the calibration of the published experimental data, as provided in Figure 2.10 and Eq. 2.6 to 2.8, which correlates ε_{fe} with the concrete tensile strength of concrete (assumed to be equivalent to $f_c^{2/3}$). It must be noted that due to the limited data obtained from the tests with GFRP and Aramid fibre reinforced polymers (AFRP), Triantafillou and Antonopoulos (2000) recommend using the debonding formula with caution. The effective strain of FRP composites is less than the fibre's fracture strain, since the concrete members failed when the applied principal strains exceeded their capacities (Triantafillou, 1998). Another investigation by Priestley and Seible (1995) identified that at larger strain magnitudes, openings of the inclined cracks can adversely affect the shear transfer mechanism due to a loss of aggregate interlock

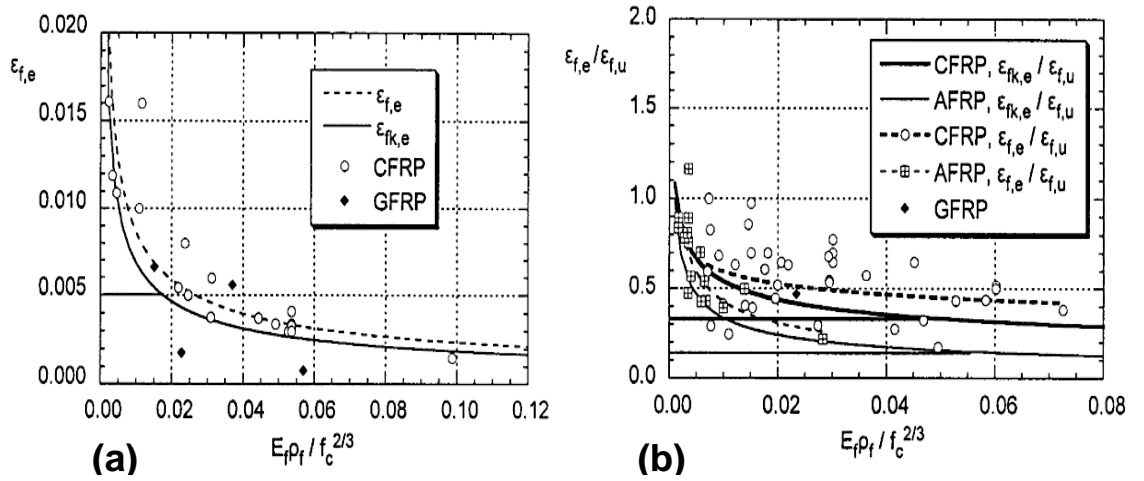


Figure 2.10: Effective strain of FRP composites in terms of $E_f \rho_f / f_c^{2/3}$ (a) concrete shear failure with FRP de-bonding (b) concrete shear failure with (or followed by) the fracture of FRP

(Triantafillou and Antonopoulos, 2000)

$$T_u = T_{u_{steel}} + T_{u_{frp}} \quad \text{Eq. 2.4}$$

$$T_{u_{frp}} = 2\varepsilon_{fd,e} E_f t_f b_f S_f^{-1} b h \cot \alpha \quad \text{Eq. 2.5}$$

$$\varepsilon_{fk,e} = K \varepsilon_{f,e} < \varepsilon_{max} \quad \text{Eq. 2.6}$$

$$\varepsilon_{fd,e} = \frac{\varepsilon_{fk,e}}{\gamma} \quad \text{Eq. 2.7}$$

$$\text{CFRP (full wraps): } \varepsilon_{f,e} = 0.17 \left[\frac{f_c^{\frac{2}{3}}}{E_f \rho_f} \right]^{0.3} \varepsilon_{fu} \quad \text{Eq. 2.8a}$$

$$\text{CFRP (debonding failure (U or side wraps)): } \varepsilon_{f,e} = 0.65 \left[\frac{f_c^{\frac{2}{3}}}{E_f \rho_f} \right]^{0.3} \times 10^{-3} \quad \text{Eq. 2.8b}$$

$$\text{AFRP (full wraps): } \varepsilon_{f,e} = 0.048 \left[\frac{f_c^{\frac{2}{3}}}{E_f \rho_f} \right]^{0.47} \varepsilon_{fu} \quad \text{Eq. 2.8c}$$

$$\rho_f = 2t_f \sin \alpha_f b_w^{-1} \text{ and } \frac{2t_f b_f}{b_w S_f} \text{ for continuous and strips wraps, respectively} \quad \text{Eq. 2.8d}$$

Where;

T_u = ultimate torsional moment carried by a section

Tu_{frp} = contribution of FRP

Tu_{steel} = contribution of steel

$\varepsilon_{fd,e}$ = design value of effective fibre strain

$\varepsilon_{fk,e}$ = characteristic effective strain

$\varepsilon_{f,e}$ = effective strain

ε_{fu} = FRP ultimate tensile strain

ε_{max} = 5000 microstrain

K = reduction factor ($K = 0.8$)

γ = partial safety factor

ρ_f = fibre reinforcement ratio

t_f = FRP thickness in mm

b_f = FRP width in mm

b_w = minimum width of a cross section in mm

S_f = spacing of FRP strips (centre to centre) in mm

E_f = FRP modulus of elasticity in GPa

α = inclined cracks angle with respect to the member axis (assumed = 45°)

α_f = angle of fibres from the member longitudinal axis in degrees

f'_c = concrete compressive stress in MPa

In order to consider the various fibre orientations with either full, U, or side wraps, Hii and Al-Mahaidi (2007) modified the fib Bulletin 14 (2001) formula (Eq. 2.9) which has been proposed by the fib Bulletin to be used with strengthened members under direct shear actions. Again, a modification of the shear stress distribution has been performed by considering the shear flow distribution in order to comply with Bredt's formula (double the shear flow area), where the shear flow area is proposed to match with A_o , which can be in line with design codes provisions, as detailed in Appendix A. Further, the evaluation of ρ_f is related to the thickness of the section's walls (Eq. 2.10), while α is permitted to be taken to be 45° or a value between 30° to 45° . Al-Bayati et al. (2018) used this modified fib formula to evaluate the contributions of the near surface mounted CFRP laminates and ropes. In both studies, the ultimate predicted torsional capacities were closely correlated with the experimental data; this was found to be more significant for schemes with epoxy resins. However, this approach has not been verified with members under combined loadings and hence the effect of these loads on the strut's angles (α) has not been considered.

$$Tu_{frp} = 2 \varepsilon_{fd,e} E_f \frac{t_f b_f}{s_f} A_o (\cot(\alpha) + \cot(\alpha_f)) \sin(\alpha_f) \quad \text{Eq.2.9}$$

$$\rho_f = \frac{t_f}{t_c} \text{ or } \frac{t_f b_f}{t_c s_f} \text{ for full and strip wraps respectively} \quad \text{Eq.2.10}$$

$$t_c = \frac{3A_c}{4P_c} \quad \text{Eq.2.10a}$$

Where;

t_c = thickness of a section walls in mm

A_c = gross sectional area ($b h$) in mm^2

P_c = outer perimeter of a section in mm

Salom et al. (2004) adjusted the ACI Committee 440.2R-08 (2008) recommendations to evaluate the strain levels of torsionally strengthened RC beams by considering the shear flow analogy, as described in an earlier investigation (Hii and Al-Mahaidi, 2007). It was suggested that these recommendations should only be used for designing members with shear strengthening schemes. Like the fib Bulletin 14 (2001) approach, the

contribution of fibres is based on the truss analogy and an α equivalent to 45° ($\cot\alpha = 1$), as given in Eq. 2.11. While, the effective strain (ε_{fe}) value is based on bond reduction factors (k_v) that correspond to the effective bonding length (L_e), f'_c , and wrap types. A re-statement of Eq.2.11, as given in Eq.2.12, has been carried out by (Salom et al., 2004) with a view to compare fibre strain readings with analytical results. In addition, the area of shear flow (A_o) was assumed to be equivalent to the total wrapped area (A_c). The comparisons revealed that most of the analytically obtained values agreed with the lower-bound measured strain values.

$$T_{ufrp} = \frac{2A_o A_f E_f \varepsilon_{fe}}{s} (\cos\alpha_f + \sin\alpha_f) \quad \text{Eq.2.11}$$

$$\varepsilon_{fe} = \frac{T_{ufrp} S_f}{2A_o A_f E_f (\cos\alpha_f + \sin\alpha_f)} \quad \text{Eq.2.12}$$

Where;

$A_f =$ area of FRP sheets in mm^2

$\varepsilon_{fe} =$ effective fibres strain ≤ 4000 microstrain (ACI-Committee 440.2R-08, 2008)

2.3.3.1 Softened Truss Method with FRP

Chalioris (2007) employed the Softened Truss Method (STM) to predict full beam responses under pure torsional loadings, where the applied longitudinal (σ_l) and transverse (σ_t) stresses are equivalent to zero. The analytical model that has been developed is based on Hsu (1993) work, which takes into consideration equilibrium, compatibility and material constitutive conditions. Chalioris superimposed the contribution of the fibres sheets into the equilibrium equations in two orthogonal directions (longitudinal and transverse), as shown in Figure 2.11; these stress equations comply with the rotating angle theory, where cracks coincide with principal concrete stresses (σ_d and σ_r). However, this model does not consider other fibre orientations and also neglects the tensile stress of concrete ($\sigma_r = 0$) in the principal direction (r). Consequently, the crack's inclination angle (α) can be related to the normal stresses in the steel and fibres, as given in Eq.2.13, and can also be related to the geometry conditions, as provided in Eq.A.5 - Appendix A, where $\varepsilon_2 = \varepsilon_d$. The thickness of the shear flow zones (t_d) corresponds with the principal strains and (α) (see Eq. 2.14), since the derivation details have been provided by Hsu (1990). In order to consider CFRP constitutive laws, Triantafillou and Antonopoulos (2000) formulae (Eq.2.8a to d) have been

employed. For concrete strut strength, Belarbi and Hsu (1995;1996) model was incorporated, given previously in Eq. 2.3a - c.

Allawi et al. (2015) utilised the Chalioris (2007) model to evaluate the behaviour of multi-cellular box girders wrapped by vertically oriented CFRP hoops. An iterative algorithm was proposed to satisfy the member's conditions at each increment of the principal strains. Comparisons between both experimental and STM model outcomes were conducted in both studies (Allawi et al., 2015; Chalioris, 2007); good correlations were observed.

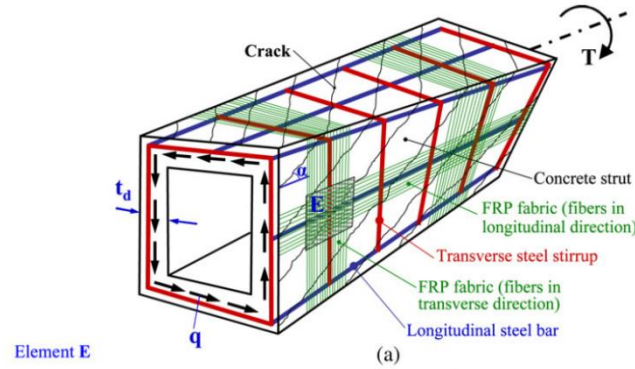


Figure 2.11: Space truss mechanism of strengthened RC beam with externally bonded FRP schemes.
(Chalioris, 2007)

$$\tan(\alpha) = \sqrt{\frac{\rho_{st} f_{st} + \rho_{ft} f_{ft}}{\rho_{sl} f_{sl} + \rho_{fl} f_{fl}}} \quad \text{Eq.2.13}$$

$$t_d = \frac{A_o}{p_o \sin^2 \alpha \cos^2 \alpha} \left(\frac{\varepsilon_d}{\varepsilon_d - \varepsilon_r} \right) \quad \text{Eq.2.14}$$

Where;

$\rho_{st} f_{st}$ = steel ratio and stress (MPa) in transverse direction respectively

$\rho_{ft} f_{ft}$ = fibre ratio and stress (MPa) in transverse direction, respectively

$\rho_{sl} f_{sl}$ = steel ratio and stress (MPa) in longitudinal direction, respectively

$\rho_{fl} f_{fl}$ = fibre ratio and stress (MPa) in longitudinal direction, respectively

t_d = thickness of shear flow zone in mm

A_o = area of the shear flow zone in mm² (Table A.1 - Appendix A, Hsu (1990))

P_o = perimeter of the shear flow zone in mm (Table A.1, Hsu (1990))

Note: Eq. 2.3c (softening coefficient (ξ)) should be used with A_o and P_o computation formulae

2.4 Beam-Column Joints

A large number of studies have investigated the behaviour of RC beam-column joints and parameters that can affect their capacities. Comprehensive literature reviews have been presented by Helal (2012), Kim et al. (2009), Sasmal (2009), Hamil (2000) and Parker (1997). Generally speaking, these studies showed that the majority of the tested members were subjected to cyclic loads. This loading had been used to help ensure that the yielding occurred in the beam rebars and that the robustness of the joint zones was sustained under seismic excitations rather than to investigate the joint shear strength. However, a number of studies (Hamil, 2000b; Vollum and Newman, 1999b; Parker, 1997; Sarsam and Phipps, 1985) have considered RC beam-column joints that are subjected to beam concentric monotonic (gravity) loads in order to quantify parameters that influence the joint shear mechanism. These parameters are discussed later in this thesis (Section 2.4.1). However, much less attention has been paid to examining the effect of torsional forces on joint behaviour. Most of the available published work have identified the influence of the eccentricity of the beam axis on the column axis, as well as the effect of transverse beams and slabs. A review of these works is provided in Section 2.4.2.

2.4.1 Joint Forces and Transfer Mechanism

The role of beam-column joints is to provide an efficient load path to transfer the beam forces into the column region, without damaging the column. The action of forces in an exterior beam-column joint is shown in Figure 2.12. The imposed horizontal joint shear forces, or “joint demand”, can be evaluated by Eq. 2.15.

$$V_{jh} = T_B - V_c \quad \text{Eq. 2.15}$$

Where T_B and V_c are the beam tensile forces at the column face and the column shear forces, which are given in Eq.2.16 and Eq.2.17, respectively.

$$T_B = \frac{M_b}{j_d} = \frac{P L_b}{j_d} \quad \text{Eq. 2.16}$$

$$V_c = \frac{P(L_b + 0.5h_c)}{L_c} \quad \text{Eq. 2.17}$$

Where P is the beam load, M_b is the beam bending moment, j_d is the flexural arm, and h_c is the column depth.

The vertical shear forces (V_{jv}) can be evaluated according to Eq. 2.18 (Paulay and Priestley, 1992), while the joint shear stress (v_j) and the column axial stress (σ_c) can be determined by Eq. 2.19 and Eq. 2.20, respectively. However, for a beam under a combined load (flexural, shear and torsion), the beam tensile forces (T_B) need to be adjusted to consider the interaction between these loads; none of the available studies have addressed this interaction in their evaluation of joint demands.

$$V_{jv} = \frac{V_{jh}}{h_c} h_b \quad \text{Eq. 2.18}$$

$$v_j = \frac{V_{jh}}{h_c b_e} \quad \text{Eq. 2.19}$$

$$\sigma_c = \frac{N}{h_c b_e} \quad \text{Eq. 2.20}$$

Where b_e is the effective joint width that can be determined according to (ACI-ASCE 352R-02 Committee, 2002)

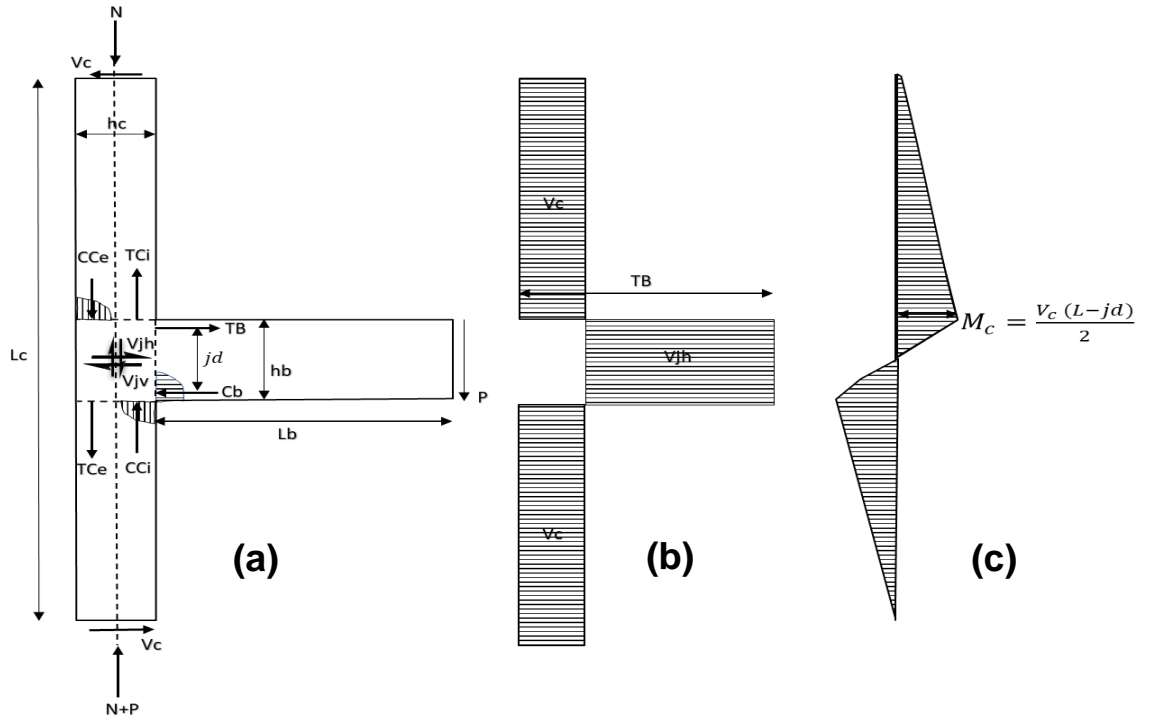


Figure 2.12: a) Acting forces on the beam and column b) joint shear forces c) column and joint bending moment

The joint shear strength and the force transfer mechanism are mainly affected by the concrete compressive strength, the joint transverse reinforcement, bond and anchorage stresses, joint aspect ratio, and the column axial loads. Regarding these influencing parameters, two resisting actions, including the

diagonal strut and truss mechanisms, can transmit the joint forces (Figure 2.14). Several analytical models that are based on the diagonal strut mechanism (Vollum and Parker, 2008; Hwang and Lee, 1999; Parker, 1997; Kassem, 2016) have been presented, wherein the strut capacity corresponds with the concrete compressive strength and strut geometry. However, the dimensions of a compression strut is proportional to the depth of the beam compression zone and column compression node at the joint boundaries (Figure 2.13), where it is straightforward to evaluate the depth of flexural zone for concentrically loaded beams that are essentially under bending forces. Whereas, for members under combined actions, the situation is more complex, especially in the presence of torsional forces as discussed in Chapter 6.

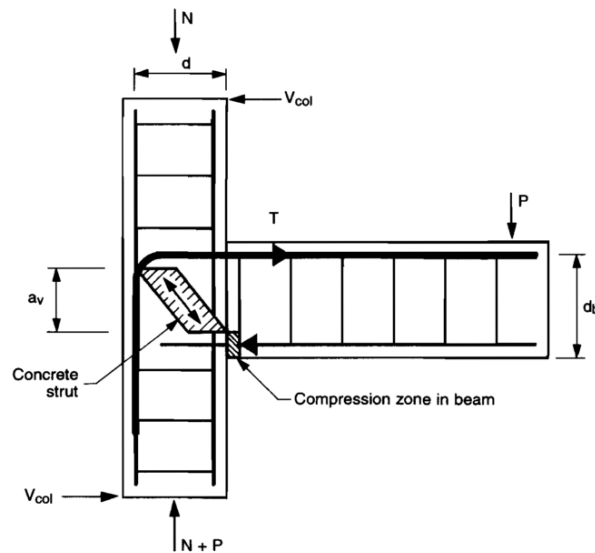


Figure 2.13: Joint forces transfer mechanism according to the strut-tie method

(Parker, 1997)

The joint truss mechanism was first introduced by Paulay et al. (1978) and was subsequently adopted by NZS 3101 (2006) for the design and analysis of RC beam-column joints. The truss based models satisfy the equilibrium of forces, compatibility of strain and the material's constitutive law, (Pantazopoulou and Bonacci, 1992; Attaalla, 2004), or may just satisfy the compatibility of stresses in accordance with Mohr's circle (Tsonos, 2008; Tsonos, 1996; Paulay et al., 1978), as shall be discussed in Chapter 6. The contribution of the truss mechanism is related to the ratio of transverse reinforcement and the bonding stresses between the rebars and concrete. Further details about the most influential joint parameters and their effects on the joint mechanisms and shear strength are given in the following sections.

2.4.1.1 Concrete Compressive Strength

Based on a review of previous research, Wong (2005) reported that joint shear strength is proportional to concrete compressive strength (f'_c). In addition, Hamil (2000b) and Vollum and Newman (1999a) state that the joint shear strength is related to the square root of ($\sqrt{f'_c}$) of the joint zones without steel ties. Likewise, Sasmal (2009) has correlated the experimentally obtained strengths of six tested RC joints with their $\sqrt{f'_c}$. By comparing deep beam resisting mechanisms, Parker (1997) and Sarsam and Phipps (1985) showed that the joint capacity is related to the concrete strut strength.

Paulay and Priestley (1992) describe how a main diagonal concrete strut efficiently transfers the compressive stress that is introduced at the joint's boundaries between two opposite corners in the lack of joints ties, as shown in Figure 2.14. Vollum and Parker (2008) derived a joint model without joint links, based on the main diagonal concrete strut (D) that was developed between the compression nodes (Figure 2.14). As mentioned previously, the capacity of the diagonal strut is related to the concrete compressive strength, while the concrete strength is affected by the concrete softening level.

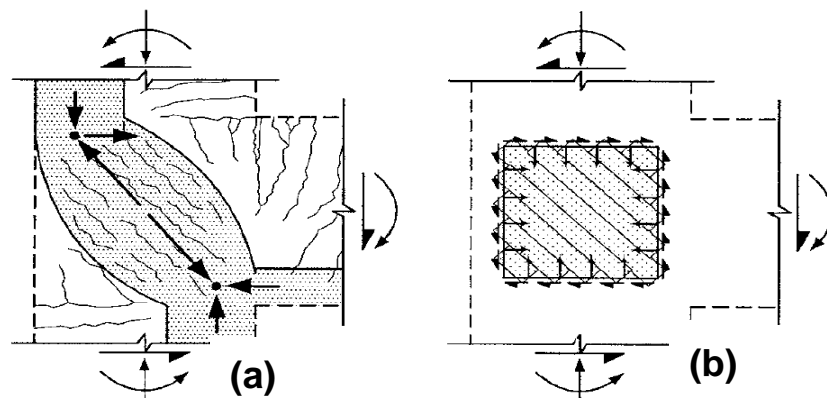


Figure 2.14 : a) Joint diagonal strut mechanism b) Joint truss mechanism
(Hwang and Lee, 1999)

2.4.1.2 Transverse Reinforcements

The contribution of the joint transverse reinforcement to the joint capacity has been confirmed in several studies (Hamil, 2000b; Vollum and Newman, 1999a; Parker, 1997; Sarsam and Phipps, 1985; Paulay and Priestley, 1992). However, Hamil (2000b) , and Vollum and Newman (1999a) have identified

that joint strength can be effectively enhanced by positioning the joint ties in the top half of the joint zone, below the flexural beam tension bars. The role of the joint ties in improving the joints is defined by two mechanisms – (i) by confining the joint cores and (ii) by acting as the horizontal truss elements that balance the compressive strut field and vertical tension ties, as shown in Figure 2.14 (Hamil, 2000b; Bonacci and Pantazoupoulou, 1993).

The NZS 3101 (2006) code provisions for joint design are based on the actions of a single direct strut (D) and the truss mechanism; this requires horizontal joint ties, vertical bars and diagonal struts, given that both actions are capable of transferring shear forces through the joint boundaries. The ACI Committee 318 (2014) recommends that transverse reinforcement is required in an unrestrained direction (unconfined by a member), such as in case of the exterior joints, in order to avoid joint degradation due to shear cracks.

2.4.1.3 Bond and Anchorage

The bond stresses between the steel rebars (the ties and the tension bars) and the surrounding concrete are significant to the joint truss mechanism as a significant proportion of the beam stresses are introduced into the joint via bond forces. By providing adequate bond and anchorage conditions, Paulay and Priestley (1992) have demonstrated that compression strut fields are induced by means of bonding along the lengths of the beam bars into the joint region.

Figure 2.15 shows the variation of stresses over the main bars of the beam and column within the joint boundaries, where the resisting compression struts are in equilibrium with the longitudinal and transverse tensile forces in the joint rebars and ties. Bonacci and Pantazoupoulou (1993) reported that bond failure prevents the joints from mobilising their full strength. A direct strut mechanism can dominate when bond deterioration occurs due to insufficient bond length or plastic strain with large splitting cracks (Paulay et al., 1978). However, after joint cracking, Scott (1992) found that the influence of loss in bond stresses over the flexural bars could be compensated for by using both U and bent down bars.

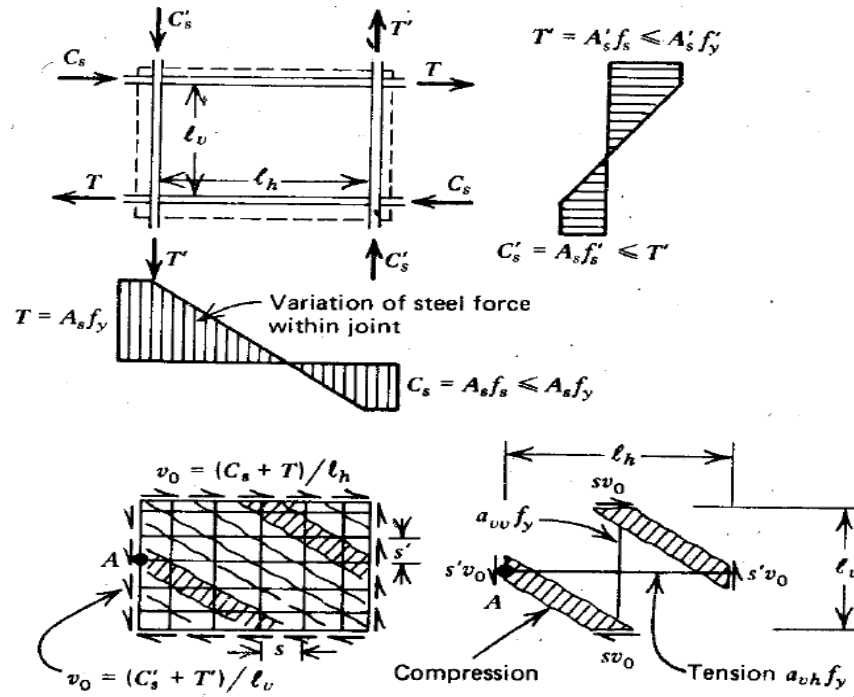


Figure 2.15: Bond stresses and the joint truss mechanism

(Paulay et al., 1978)

2.4.1.4 Joint Aspect Ratio.

Vollum and Parker (2008) indicated that the behaviour of the RC joints is affected by the beam depth to column depth ratio (joint aspect ratio). Chun and Shin (2014) tested 14 exterior RC beam-column joints with different aspect ratios (0.67, 1, 1.5, 2, and 2.5). They found that the joint's deformations were proportionate to an increase in the aspect ratio. Hamil (2000b) experimentally confirmed the effect of the aspect ratio on joint strength. He noticed a reduction in joint strength by about 25% when the joint aspect ratio altered from 1.4 to 2. Similarly, Vollum and Newman (1999a) reported that the joint's shear strength decreased linearly by around 35% when the aspect ratio increased from 1 to 2. These degradations in joint strength are explained by the fact that a steeper concrete strut is formed by the larger aspect ratio, which adversely affects the shear transfer mechanism and resistance capacity (Park and Mosalam, 2012). Based on the outcome of the above reviewed research, a joint with an aspect ratio of less than 1 is likely to experience only minor joint damage at the point that the beam fails in flexure.

2.4.1.5 Column Axial Load

The influence of the column's axial load on the ultimate joint strength is still being debated in the extant literature. Meanwhile, Shannag and Alhassan (2005), Pantelides et al. (2002a) and Parker (1997) found that an increase in the column load was beneficial for improving joint strength. However, this improvement was obtained for the tested joints that subjected to low and medium axial load ratio ranging from 0.1 to 0.3 of the column load capacity (Shannag and Alhassan, 2005; Parvin et al., 2010). Antonopoulos and Triantafillou (2003) observed a rise in the joint shear strength for externally wrapped beam-column joints by increasing the column axial load to $0.1 A_g f_c'$. Moreover, based on finite element analysis results, Hamil (2000b) found that the ultimate joint shear strength was increased by the column's axial load; while he reported these results were not validated with the test results. In contrast, a high level of axial load could induce buckling of column's rebars or promoting sudden joint's failures (Shigeru Hakuto and Hitoshi, 2000).

Interestingly, to evaluate the nominal shear capacity of RC concrete members, ACI Committee 318 (2014), Eurocode 2 (2004), and NZS 3101 (2006) incorporated the axial load in their guidance. Moreover, axial loads have been considered in several analytical models that were formulated according to the strut mechanism or panel action (truss mechanism) (Tsonos, 2008; Pantazopoulou and Bonacci, 1992; Parker, 1997; Wong, 2005; Paulay and Priestley, 1992). The role of the column load in improving the initial cracking capacity of the joints has also been confirmed (Hamil, 2000b).

2.4.2 Previous Research (beam-column joint with eccentric load and torsional moment)

As discussed in the previous sections, torsional forces affect the member's behaviour and their failure modes. In particular, the presence of torsion is likely to increase the level of diagonal shear cracks and reduce the load carrying capacities. Previous studies have concentrated on the influence of the eccentricity of the beam axis from the column axis, as well as the effect of transverse beams and slabs.

Raffaella et al. (1992) experimentally investigated the influence of different beam to column width ratios, which were cast with transverse beams framed into columns. Four specimens of beam to column width ratios of 2.43 and 2.14 were tested. The test results indicated that the wide beam failed due to

anchorage loss of the flexural reinforcement, which resulted in torsional distress within the transverse beams. The authors suggested that the torsional forces produced by wide beam reinforcement should not exceed the cracking torque capacity of the transverse beams. An additional four eccentric RC beam-column assemblages were tested, wherein the beam's eccentricity was measured with respect to the column's centreline. A reduction in joint strength was observed and related to the beam eccentricity, and this reduction correlated with the level of torsional cracks developing on the column's sides.

In another study, Vollum and Newman (1999b) tested ten specimens that consisted of a square column that was monolithically framed with a concentric (c) beam and a transverse eccentric (e) beam, where the eccentric beam did not intersect with the column (adjacent to the column's face) in eight specimens. The test results revealed that failure can occur in the concrete before yielding of the beam reinforcement due to the combined loads from both the concentric and large eccentric beam loads. It was found that the torque effect on the concentric beam decreased in specimens where the eccentric beam intersected with the column, while the extent of joint cracking could be related to the level of load from the eccentric beam. In addition, the above authors presented an interaction curve (Figure 2.16) illustrating the influence of biaxial loading (c and e directions) and torsion (T) in reducing the uniaxial joint strength (V_{j0}).

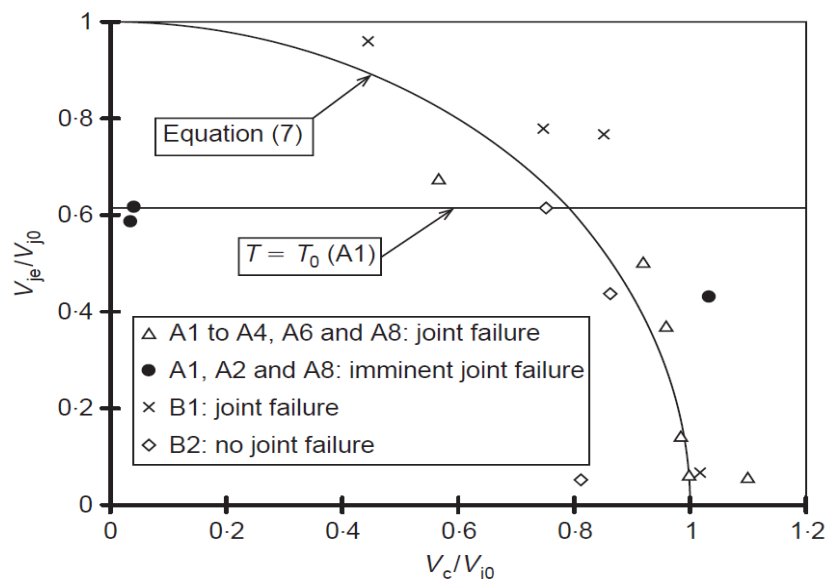


Figure 2.16: Influence of biaxial loading on the joint strength
(Vollum and Newman, 1999b)

Shimizu et al. (2000) studied the shear strength of eccentric RC beam-column joints under earthquake actions. They analysed the damage caused by the earthquake loading that was associated with the torsional effects of the eccentric beams. Their analysis results agreed with the previous research by (Vollum and Newman, 1999b; Raffaele et al., 1992) with respect to the relationship between the decline in the joint strength and the eccentricity of the beams. However, in order to consider this torsional effect, the authors proposed a formula to estimate the reduction of the column's capacity. This formula is empirically derived from experimental results that have been previously published; it takes into account torsional span ratio, reinforcement strength, and concrete compressive strength.

Further research was conducted by Kusahara et al. (2004) to investigate the beam eccentricity effects on interior RC beam-column joints. The tests considered beam eccentricity and its relationship with the joint link ratios. The specimens were tested under cyclic loading; severe cracking developed on the side of the joint that aligned with the eccentric beam due to the high joint demand caused by the beam's flexural reinforcement. The investigators also found that the joints with eccentric beams suffered from torsional cracks that developed on the joint. The authors found that the reduction in the shear capacity of the eccentric joints decreased when using additional shear reinforcement (hoops).

Hassan (2011) considered the presence of a slab on the joint's behaviour; he tested four full-scale corner beam-column joints with slabs under uniaxial loading. Twisting deformations were observed in the loaded beams - these resulted from the restraining effect of the slab - torsional cracks developed in the unloaded beam, combined with longitudinal cracks that formed in the slab, parallel to the unloaded beam. Engindeniz (2008) suggested a reason for the slab increasing the joint shear demand; "several paths consisting of diagonal compression struts in the slab, torsion, and weak-axis bending of the transverse beam". In the context of slab forces, the ACI-ASCE 352R-02 Committee (2002) recommends considering the participation of slab rebars on the joint shear stress input for type-2 connections (under seismic actions).

More recently, Elshafiey et al. (2016) investigated the effect of beam torsional moments on RC beam-column joints. The specimen's geometry, the section's dimensions and the loading details are shown in Figure 2.17. The beam widths varied from 200mm (SP1-6) to 350mm (Sp8), as provided in Table 2.2. A constant axial load of 400 kN was applied to all specimens, while the eccentric

(e) beam load was imposed at 200mm and 400mm from the beam's free end. The test results showed that failures can occur in the joint regions due to the lack of joint stirrups and the high beam stiffness and due to the interaction between bending, torsion, and shear forces (Table 2.2). This interaction altered the crack patterns on the beam's sides and the relationship with the level of shear forces, as inclined diagonal cracks were dominated at the beams sides where the torsional and shear forces were additive. The authors reported that the increase in torsional load moved the failure zones from the joints into the beam regions. However, they did not define how the mechanism of torque, along with the flexural and shear forces, increased the compression concrete struts and the rebar's tensile forces. In addition, the joint shear demands and their influence on the beam's longitudinal reinforcement ratios, the joint forces, and the strengths were not quantified.

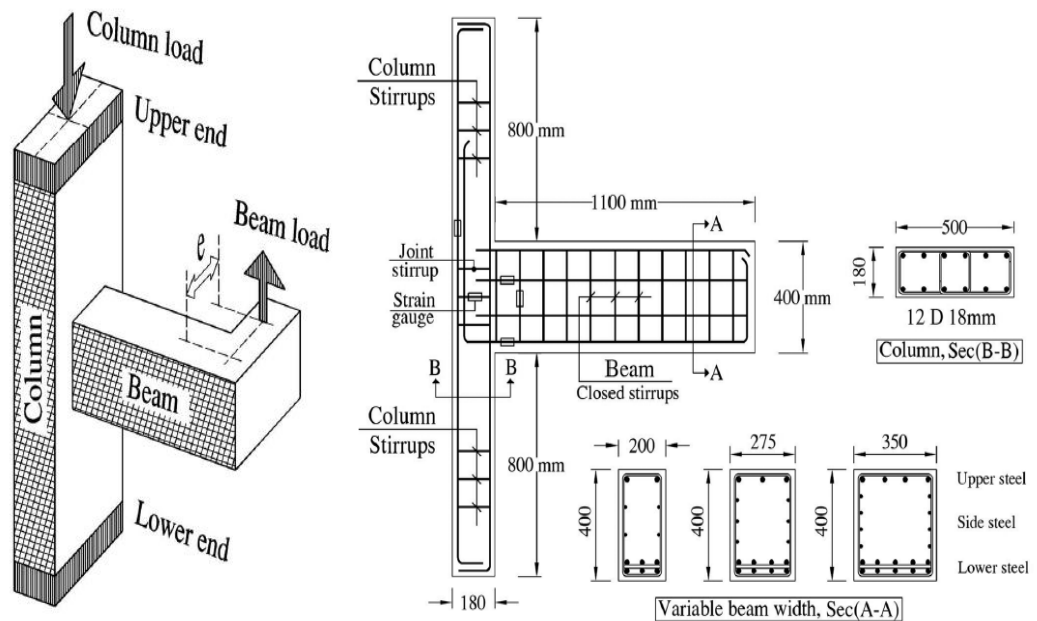


Figure 2.17: Test and specimen details (Elshafiey et al., 2016)

Table 2.2: Test results (Elshafiey et al., 2016)

Specimen	f'_c (MPa)	Beams Widths (mm)	Ultimate Load (P) (kN)	Ultimate Torque (kN.M)	Joint links	Failure mode
Sp1	25.3	200	90.9	18.18	-	Joint failure
Sp2	25.6	200	101.1	20.22	3Φ12	Beam failure
Sp3	26.0	200	105.5	21.1	-	Joint failure
Sp4	25.1	200	121.2	24.24	3Φ12	Joint -beam failure
Sp5	25.7	200	70.1	28.04	-	Beam failure
Sp6	24.4	200	66.4	26.56	3Φ12	Beam failure
Sp7	24.7	275	115.4	46.16	3Φ12	Joint -beam failure
Sp8	25.1	400	163.7	65.48	3Φ12	Joint failure

2.4.3 Codes Provisions

Within this section the following code provisions for the beam-column joint forces and concrete shear strength are described; these provisions can be applied for monolithic framed structures in non-seismic regions.

- BS8110 (1997)
- Eurocode 2 (2004)
- ACI-ASCE 352R-02 Committee (2002)
- NZS 3101 (2006)

2.4.3.1 BS8110 (1997)

There are no specific provisions that are presented in BS8110 (1997) for evaluating the beam-column joint forces and strengths. Nevertheless, in correlation with the joint's shear strength and axial compressive stresses, this section summarises the clauses corresponding to the design of members under shear stresses according to BS8110.

The shear resistance of the RC column is given in Eq. 2.21, in which the concrete (v'_c) contribution and transverse reinforcement (links) are combined.

$$V = v'_c b_v d + \frac{A_{sv} f_{yv}}{S_v} \quad \text{Eq. 2.21}$$

Where;

$$v'_c = v_c + 1.25 \frac{0.6 N}{A_c} \frac{V_h}{M} \quad \text{or} \quad \text{Eq. 2.21-i}$$

$$v'_c = v_c \sqrt{1 + \frac{N}{A_c v_c}} \quad \text{Eq. 2.21-ii}$$

$$v_c = \frac{0.79}{\gamma_m} \left[\frac{100 A_s}{d b_v} \right]^{\frac{1}{3}} \left[\frac{400}{d} \right]^{\frac{1}{4}} \quad \text{Eq. 2.21-iii}$$

$\frac{100 A_s}{d b_v}$ taken as not greater than 3

$\frac{400}{d}$ taken as not less than 1

A_{sv} = the area of the transverse reinforcement

f_{sv} = the yielding strength of the transverse reinforcement

S_v = centre to centre spacing of shear links

N = compression axial load

A_c = the gross section area

V = ultimate shear forces

h = the section depth

M = the ultimate bending moment

γ_m = the partial factor of safety (1.25)

d = the section effective depth

b_v = the section width

The code incorporates the compression axial load (Eq. 2.21-i and ii) in the evaluation of the nominal concrete shear strength, while it recommends using Eq. 2.21-ii “to avoid shear cracking prior to ultimate load”. Moreover, BS 8110 stipulates that the shear stress that is induced in a section ($v = V/b_v d$), should not exceed the value of $0.8 \sqrt{f_{cu}}$ or 5 MPa, where f_{cu} is the cube compressive strength of concrete.

2.4.3.2 Eurocode 2 (2004)

Like BS 8110, no joint provisions are given in (Eurocode 2, 2004). Eurocode 2 introduced the “variable strut inclination method” to evaluate the joint’s shear strength, which corresponds to the diagonal concrete strut capacity with no direct influence on shear resisting from the concrete.

- The member’s shear strength ($V_{Rd,c}$) without transverse reinforcement is given in Eq. 2.22.

$$V_{Rd,c} = \left[C_{Rd,c} K (100 \rho f_{ck})^{\frac{1}{3}} + 0.15 \sigma_{cp} \right] b d \quad \text{Eq. 2.22}$$

Where:

$$C_{Rd,c} = \frac{0.18}{\gamma_c}$$
$$K = 1 + \sqrt{\frac{200}{d}} \leq 2.0$$
$$\rho = \frac{A_{s1}}{b d}$$
$$\sigma_{cp} = \frac{N}{A_c}$$

Where; γ_c is a partial factor of safety, d is the effective section depth, b is the section width, f_{ck} is a characteristic compressive strength for concrete, A_{s1} is the area of the tensile rebars, A_c is the gross sectional area

- For members that do require shear links, Eurocode 2 (2004) permits the use of the “variable strut inclination method”, which conforms with the truss mechanism. The member shear strength that can be provided by vertical shear links (Eq. 2.23) is limited to the resisting capacity of the concrete strut ($V_{Rd, max}$), as given in Eq. 2.24, where the maximum applied shear forces (V_{Ed}) should not exceed $V_{Rd, max}$.

$$V_{Rd,s} = \frac{A_{sw}}{S} Z f_{ywd} \cot \theta \quad \text{Eq. 2.23}$$

$$V_{Rd,max} = \frac{b Z v_1 f_{cd}}{\cot \theta + \tan \theta} \quad \text{Eq. 2.24}$$

Where:

A_{sw} = the shear reinforcement area

S = the spacing between shear links

Z = the lever arm between the upper and lower chords

f_{ywd} = yield strength for shear links

$$v_1 = \left(0.6 - \frac{f_{ck}}{250}\right) \text{ [a reduction factor for cracked concrete]}$$

f_{cd} = the diagonal compressive forces in concrete

θ = the angle of concrete struts from the member longitudinal axis;

Eurocode 2 (2004) recommends that θ can be selected within the range of 22° to 45°

2.4.3.3 ACI-ASCE 352R-02 Committee (2002)

The ACI-ASCE 352R-02 Committee code presents provisions for designing two types of RC beam-column joints in relation to both the loading conditions and the deformation levels. These two types include Type-1 and Type-2, where Type-2 connections are relevant to members subjected to deformation reversals that are induced by seismic actions, and Type-1 connections are designed on the basis of strength without considerable inelastic deformation. This section reviews the Type-1 provisions, where the ductility requirements are not applied.

- To evaluate the design joint shear demand (forces), (ACI-ASCE 352R-02 Committee, 2002) provides a formula (Eq. 2.25) for joints type-1. This formula corresponds with the flexural strength of the connected beams, where the shear forces are based on the yielding of the beam's rebars in the flexural tension zone. However, the code does not consider the strain hardening and the large plastic deformation that can arise from combined forces (e.g. bending, shear, and torsion), given that these influence the joint forces and the distortion level.

$$V_{jh} = A_s f_y - V_c \quad 2.25$$

Where;

V_{jh} = the joint shear forces

A_s = area of flexural reinforcements

F_y = the yielding strength of the flexural reinforcement

V_c = the column shear forces

- According ACI-ASCE 352R-02 Committee (2002), the joint resisting strength (V_n) is given in Eq. 2.26, since the function of $\sqrt{f'_c}$ in correlation to the confinement factor (γ) depends on the number of the joint faces that are framed with other members (beams and column) regardless of the joint link's contribution and bond condition in the joint region.

$$V_n = 0.083 \gamma \sqrt{f'_c} b_j h_c \quad 2.26$$

Where;

$\sqrt{f'_c}$ = concrete compressive strength in MPa.

γ = The confinement factor for the Type-1 joint is taken as:

15 and 12 for continuous and discontinuous corner joints, respectively.

20 and 15 for continuous and discontinuous exterior joints, respectively.

20 and 24 for continuous and discontinuous interior joints, respectively.

h_c = the column depth

b_j = the effective width of the exterior joint shall be taken as the least of the following,

- $(b_b + b_c)/2$
- $b_b + b_c/2$
- b_c

Note: the b_b and b_c are the beam and column width respectively.

ACI-ASCE 352R-02 Committee stipulates that the joint transverse reinforcement should be provided by unconfined sides. Whereas, the later version of ACI Committee 318 (2014) states that joint links are required to avoid buckling of the column's main reinforcement. Moreover, to satisfy bond conditions, member rebars should be developed into the joint region in accordance with the code's provisions. However, the code model cannot be utilised as a rational method to identify the shear transfer through the joint region by considering the influential parameters, such as joint links, truss action and the column's axial load.

2.4.3.4 NZS 3101 (2006)

The New Zealand code provides design recommendations for beam-column joints that consider the type of loads and the ductility demand. The code assumes that the single diagonal strut action and joint truss mechanism can both carry the joint shear forces. For the joints under non-seismic loading, the

computing of shear forces (V_{jh}^*) is the same as suggested in Eq. 2.25, while the code restricts the joint's demand on the concrete crushing capacity of the compressive struts that are given in Eq. 2.27.

$$V_{jh}^* \leq 0.2 f'_c b_j h_c \text{ or } 10 b_j h_c \quad \text{Eq. 2.27}$$

- The shear resisting capacity (V_{jh}) of the joint is presented in Eq. 2.28, where the contributions of the diagonal strut (V_{ch}) and truss mechanisms (V_{sh}) are superimposed. The provided areas of horizontal (A_{jh}) and vertical (A_{jv}) joint shear reinforcements shall correspond to Eq. 2.28-ii and 2.28-iii, respectively.

$$V_{jh} = V_{ch} + V_{sh} = V_{ch} + A_{jh} f_{yh} \quad \text{Eq. 2.28}$$

Where;

$$V_{ch} = V_{jh}^* \left[0.5 + \frac{C_j N}{A_g f'_c} \right] \quad \text{Eq. 2.28-i}$$

$$A_{jh} = \frac{V_{jh}^* - V_{ch}}{f_{yh}} \quad \text{Eq. 2.28-ii}$$

$$A_{jv} = \frac{V_{jh}^* \frac{h_b}{h_c} - V_{cv}}{f_{yv}} \quad \text{Eq. 2.28-iii}$$

$$V_{cv} = 0.6 V_{jh}^* \frac{h_b}{h_c} + C_j N \quad \text{Eq. 2.28-iv}$$

N = the column's axial load

V_{cv} = vertical shear forces that are carried by the diagonal concrete strut

f_{yh} = yield strength of the horizontal shear reinforcements

f_{yv} = yield strength of the vertical reinforcements

$$C_j = \frac{V_{jh}}{V_{jx} + V_{jz}} \quad [\text{for unidirectional joint loads, } C_j \text{ factor is taken as unity}]$$

A_g = the column gross sectional

The shear transfer capacity of the diagonal concrete strut according to the code provisions (Eq. 2.28-i) depends on the depth of the column's flexural compression zone at the joint boundaries and the amount of bond stress that develops over this depth. It is assumed that the dimension of the diagonal

strut between the column and the beam nodes is not affected by the beam's compression zone. However, this assumption is applicable to the flexural dominated beam failure under cyclic forces, where a large reduction in the beam's compression zone can occur due to severe cracks and spalling of concrete induced by the beam's plastic hinge.

2.5 Long-Term Behaviour of Reinforced Concrete Members under Sustained Torsional Loads

The long-term response of reinforced concrete members is affected by the time-dependent characteristics of concrete, i.e., creep and shrinkage. Creep and shrinkage increase deformation and influence the redistribution of stresses; excessive member deflections can be caused by creep and shrinkage. The phenomena of creep and shrinkage are affected by a number of factors, such as the environmental conditions, member details, and the properties of the concrete. A summary of the main known factors that affect creep and shrinkage in structural concrete is given in the (ACI 209.1R-05, 2005) report, which includes the following:

- Properties of concrete material (e.g. aggregate and binder).
- Concrete mixture proportions.
- Period and type of curing.
- Ambient conditions (e.g. temperature and relative humidity).
- Structural design details, size and shape of the members.
- Loading age.

Several models have been introduced to predict the creep and shrinkage of concrete - for example, ACI 209.R-92 (1992), Eurocode 2 (2004), and fib Model Code (2010a). Bazant and Baweja (2000) suggest that these models are considered the most influential factors in the codes expressions. However, these models are outside the scope of this study; the actual creep coefficients and shrinkage strains are experimentally quantified in this investigation. To account for the effects of time dependent deformations on the member's behaviour, there is a considerable amount of literature that has considered the beam's deflections and curvatures under sustained flexural loads. However, few studies have investigated the long-term influence of torsional load. Further, none of the conducted research works have addressed the sustained torsional forces on the strengthened RC members with FRP's warps. A review of these previous works that considered time-dependended torsional deformations is presented in Section 2.5.3.

2.5.1 Creep

Under sustained load, concrete strain develops with time – this is called creep. The creep strain can be several times larger than the instantaneous elastic strain. The rate of the strain development varies with time; it is rapid just after the application of the load and slows significantly with time (Figure 2.18). Gilbert (2002) reported that 50% of the total creep is induced in the first 2 to 3 months of loading and 90% of creep takes place within three years. In another study, Troxell (1958) identified that 70% of creep occurs within the first three months and about 83% of the final creep develops in the first year. Further details are given by Neville and Brooks (2010), who found that 25%, 50%, and 75% of ultimate creep takes place at about 14, 90, and 365 days, respectively. These studies indicate that at least half of the ultimate creep occurs in the first 90 days of loading.

Two types of creep components have been identified, basic and drying creep (ACI 209.2R-08, 2008; Neville et al., 1983). Basis creep develops with no movement of moisture in or out of the concrete samples, while drying creep arises as an additional component under drying conditions (Neville et al., 1983).

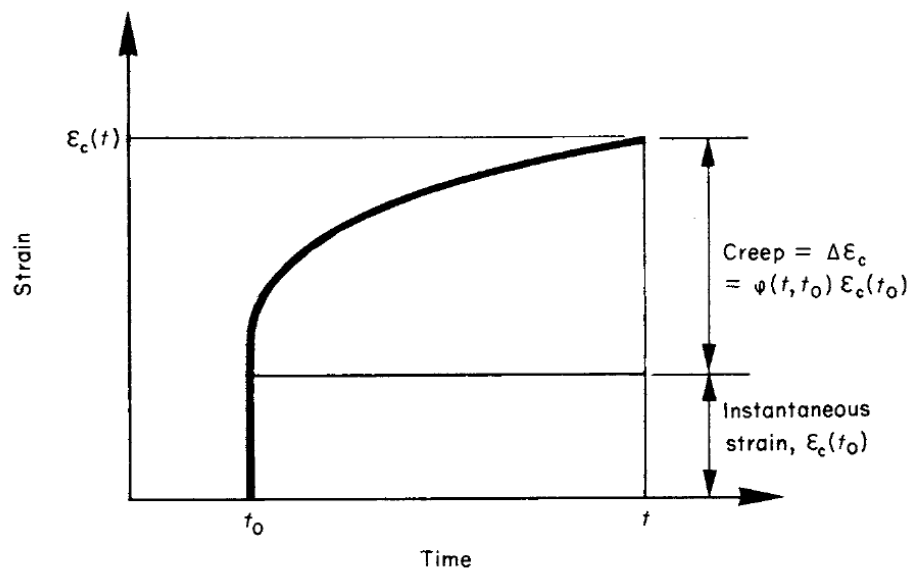


Figure 2.18: Creep strain under sustained load

(Ghali et al., 2002)

Aside from the interaction between drying creep and shrinkage, the total concrete strain of a member at any given time subjected to a constant load is often assumed to be the sum of the initial strain induced by the load stress and the time dependent deformations (creep and shrinkage), as shown in

Figure 2.19 (Neville, 2011). Hence, for practical applications, it is common that the evaluation of compressive creep is experimentally carried out by deducting the instantaneous strain and the shrinkage strain from the measured total strain, as given in Eq. 2.29a. However, the tensile creep induced strains could be obtained by adding the measured total strain to the shrinkage strain (since they act in opposite directions) and deducting the instantaneous strain as given in Eq. 2.29b.

$$\varepsilon_{cr(t)} = \varepsilon_{t(t)} - \varepsilon_{e(t_0)} - \varepsilon_{sh(t)} \quad \text{Eq. 2.29a}$$

$$\varepsilon_{cr(t)} = \varepsilon_{t(t)} - \varepsilon_{e(t_0)} + \varepsilon_{sh(t)} \quad \text{Eq. 2.29b}$$

Where;

$\varepsilon_{cr(t)}$ = the creep strain at time t

$\varepsilon_{t(t)}$ = the resulting total strain at time t

$\varepsilon_{e(t_0)}$ = the initial strain induced by the load at time of loading (t_0)

$\varepsilon_{sh(t)}$ = the free shrinkage strain for unloaded samples at time t

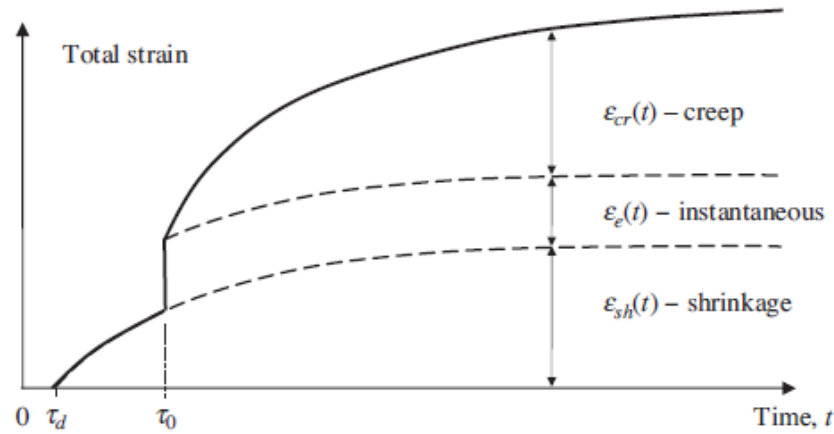


Figure 2.19: Components of concrete strain under constant load

(Gilbert and Ranzi, 2010)

Based on the assumption of a linear relationship between stress and strain for members under constant loads, an effective modulus of elasticity method is widely adopted to consider the effect of creep strain on concrete structures (Eq. 2.30) (Gilbert, 1988). However, this method neglects the ageing of concrete and stress variation throughout the loading stages. Therefore, with a

view to account for the ageing effects, the age-adjusted effective modulus was introduced by Trost (1967) and extended by Bazant (1972), where the ageing coefficient $\chi_{(t,t_0)}$ is simply incorporated to adjust the effective modulus, as presented in Eq. 2.31. Ghali et al. (2002) indicated that the ageing coefficient varies between about 0.6 and 0.9. For samples where the initial loading exceeds five days, Neville et al. (1983) suggested that the average value of the final ageing coefficient can be taken as equal to 0.8. The value of 0.8 has been used by Forth et al. (2003), along with Nie and Cai (2000), while Gilbert and Ranzi (2010) recommend lower values, e.g. 0.65 and 0.75 for members that were loaded during early ages and later ages (larger than 28 days), respectively.

Creep is a load dependent deformation that is either caused by compression or tension stresses; any increment or decrement in the member stresses ($\Delta\sigma$) affects the resulting strain levels. Ghali and Favre (1986) employed the principal of superimposition approach to account for stress variation ($\Delta\sigma_t$) due to the load, or any other factors, e.g. shrinkage and creep restraint or temperature deformation. This is because the total strain at time (t) is approximated to be equivalent to the sum of the instantaneous creep that is produced by the initial load (σ_0), in addition to the strain (elastic and creep) caused by the change of stress ($\Delta\sigma_t$), as given in Eq. 2.32. Similarly, the linear superposition of creep was considered by Mu et al. (2008) in order to evaluate the curvature of a beam due to shrinkage. Importantly, restrained members under constant strain exhibit a stress relief known as concrete relaxation. Neville et al. (1983) indicated that creep and concrete relaxation mechanisms are closely connected, and they are influenced by the same factors. Also, it has been identified by Altoubat and Lange (2001), Neville (2011), and Ranaivomanana et al. (2013), that concrete relaxation affects the cracking resistance of concrete by reducing the restrained shrinkage stresses.

$$E_{eff(t,t_0)} = \frac{E_{t_0}}{1 + \phi_{(t,t_0)}} \quad \text{Eq. 2.30}$$

$$E_{adj(t,t_0)} = \frac{E_{t_0}}{1 + \chi \phi_{(t,t_0)}} \quad \text{Eq. 2.31}$$

$$\begin{aligned} \varepsilon_{t(t)} &= \left[\frac{\sigma_{t_0}}{E_{t_0}} + \frac{\sigma_{t_0}}{E_{t_0}} \phi_{(t,t_0)} \right] + \left[\frac{\Delta\sigma_t}{E_{t_0}} + \frac{\Delta\sigma_t}{E_{t_0}} \chi \phi_{(t,t_0)} \right] + \varepsilon_{sh(t)} \\ &= \frac{\sigma_{t_0}}{E_{eff(t,t_0)}} + \frac{\Delta\sigma_t}{E_{adj(t,t_0)}} + \varepsilon_{sh(t)} \end{aligned} \quad \text{Eq. 2.32}$$

Where;

$E_{eff(t,t_0)}$ = the effective modulus of elasticity of concrete

E_{t_0} = the modulus of elasticity of concrete at time (t_0)

$\phi_{(t,t_0)} = \frac{\epsilon_{cr}}{\epsilon_e}$ [the creep coefficient at time (t)]

$E_{adj(t,t_0)}$ = the age adjusted modulus of the elasticity of concrete

t_0 = the initial time of loading

χ = the adjusted ageing coefficient

σ_{t_0} = the initial stress at time (t_0)

$\Delta\sigma_t$ = the stress variation at time (t)

2.5.2 Shrinkage

Shrinkage strains represent the volumetric changes in the concrete that are associated with the drying process (water loss) and chemical changes in the hydrating cement paste. As opposed to creep, shrinkage is independent of load, given that the majority of shrinkage deformations initiate when drying begins in the hardened concrete and develop gradually at a continuously decreasing rate, as shown in Figure 2.20. In the presence of reinforcement, the restrained shrinkage deformations can produce compression stresses in the steel bars and tensile stresses in the concrete. These stresses can affect the member's curvature in singly and unsymmetrically reinforced sections (Mu et al., 2008; Neville et al., 1983). Regarding internal reinforcement restraint, shrinkage can promote cracks in members that are externally restrained by adjoining members. For example, external end restraints are imposed when a member is cast between existing structures (Beeby and Forth, 2005; Shehzad et al., 2019).

Various types of shrinkage have been identified in the extant literature (Hasan, 2016; Neville, 2011; ACI 209.1R-05, 2005), including plastic shrinkage, autogenous shrinkage, carbonation shrinkage, and drying shrinkage. Carbonation shrinkage develops due to the chemical reaction between the cement paste in the hardened cement and carbon dioxide that ingresses from the surrounding atmosphere (Neville, 2011). However, ACI 224R-01 (2001) reported that the shrinkage caused by carbonation reactions is of minor importance in comparison to the total drying shrinkage, as the expected penetration of carbon dioxide does not exceed 12mm into the members that are made from concrete of low porosity. Another type of shrinkage is plastic shrinkage, which occurs in fresh concrete and results from the loss of moisture

by the rapid evaporation of moisture from the concrete surface. Cracks that are linked to plastic shrinkage can be avoided by reducing the surface loss of water.

Autogenous shrinkage is a chemical process that takes place in the hydrating cement matrix without moisture exchange with the surrounding atmosphere at an ambient temperature. ACI 209.1R-05 (2005) indicates that this type of shrinkage can be inconsiderable for many normal strength concrete. However, autogenous shrinkage tends to be more important in the drying concrete of low cement/water ratios or with high cement content, such as high performance concrete mixtures (Figure 2.20). This is because the available water is insufficient to maintain the hydration reactions which need and reduce the capillary pore water (Gribniak et al., 2008; Sakata and Shimomura, 2004). In general, the ratio of autogenous shrinkage to the overall long-term shrinkage strain ranges from between 10% to 20% for normal strength concrete, as shown in Figure 2.20 (Hasan, 2016).

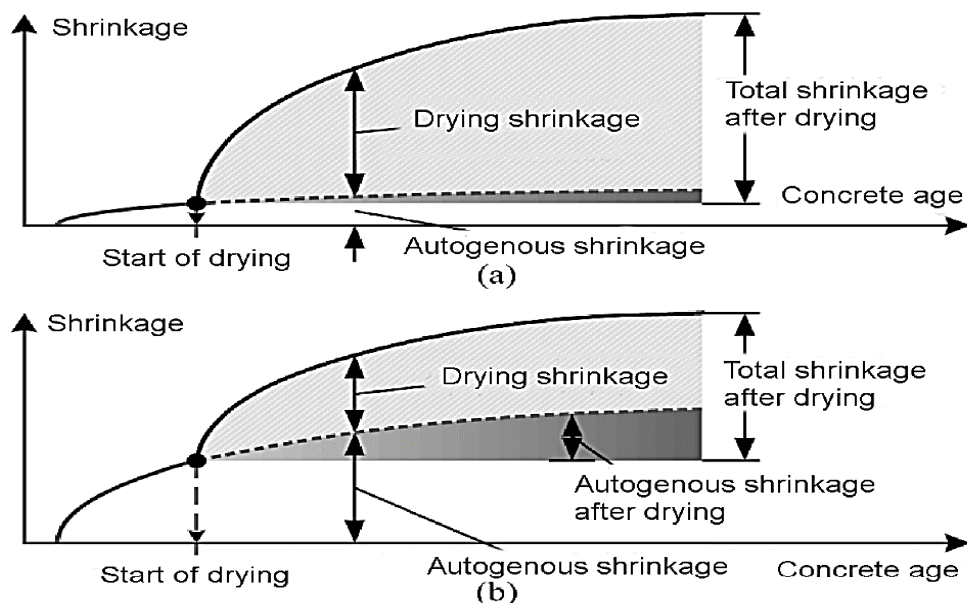


Figure 2.20: Components of shrinkage for (a) normal and (b) high strength concrete

(Gribniak et al., 2008)

The most significant long-term shrinkage for hardened concrete is drying shrinkage, this is significantly affected by the surrounding humidity,

temperature and member size and shape (exposed area). Drying shrinkage is also influenced by the mixture properties (e.g. binder quantity, water content, and type of aggregate) (Neville and Brooks (2010); Gilbert (2002); ACI 224R-01 (2001)). For normal strength concrete, with a disregard for autogenous shrinkage contribution, drying shrinkage is often considered the total long-term shrinkage deformations (ACI 209.1R-05, 2005). Nevertheless, in most cases, separating the shrinkage types is not required, since the total shrinkage ($\varepsilon_{sh(t)}$) can be taken as the sum of all the shrinkage components (Gilbert 2002).

2.5.3 Members under Sustained Torsional Load

As mentioned earlier, very few tests have been carried out under a sustained torsional load. A review of the available published works has therefore been produced, where it is found that no studies have investigated the time dependant behaviour of externally strengthened RC members with FRP wraps under constant loads, including torsional forces. However, these research outcomes have shown that there is a significant increase in member deformations in terms of twist angle over time, as this reflects the influence of concrete creep. A discussion of these studies is provided in this section.

For plain concrete samples under sustained torque, Neville et al. (1983) reported that the creep coefficients obtained from torsionally loaded samples were very close to the samples under compression loads. Also, they indicated that the strains in the principal directions (compression and tension) were equal, as there was no change in the axial strains for the loaded and unloaded samples. Ishai (1964) tested 78 rich cement mortar samples, which were torsionally loaded for periods of up to 24 weeks. The creep was identified by measuring the variations of the twist angle over time, as given in Figure 2.21. It can be noted that the resulting shape of the twist angle-time curves is similar to the development of the creep deformations.

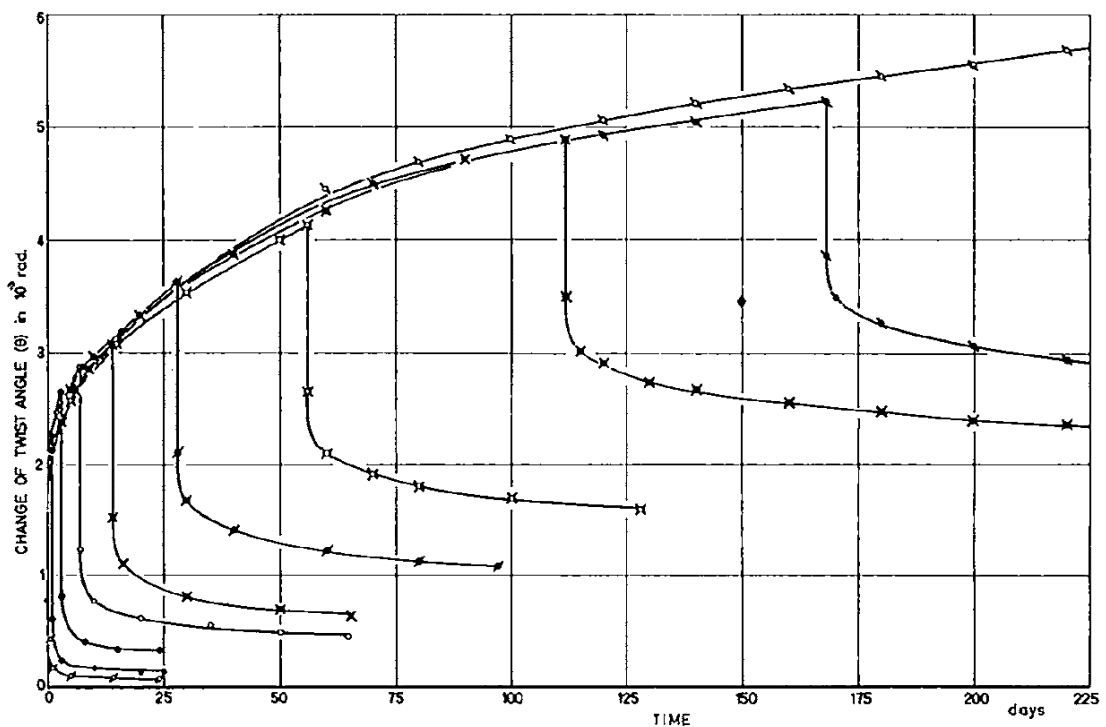


Figure 2.21: Torsional creep and creep recovery for samples stored in water

(Ishai, 1964)

Experimental and analytical investigations of RC beams under sustained pure torsion were carried out by Inge Karlsson and Anderson (1974). The aim was to identify the time-dependent post-cracking behaviour of the tested beams, by taking into account the creep of concrete. The full-scale beams were loaded for 400 days under the same ambient conditions (a temperature of 20C° and a relative humidity of 60%) as the supplementary concrete samples. An increase in the beam's deformations in terms of twisting angles over time was observed (Figure 2.22), as the authors indicate that the deformation variations correspond to the creep of concrete. The ratio of instantaneous angle of twist to the final measured twist of angle ranged between 2.5 to 3. The twisting of the beams was influenced by the creep rate, in which the deformations varied rapidly after the load's application and gradually slowed over time, as shown in Figure 2.22. Also, the authors introduced an analytical approach based on the truss model to evaluate the time-dependent twist deformation under pure torsion; this approach is discussed in details and presented in Appendix A.

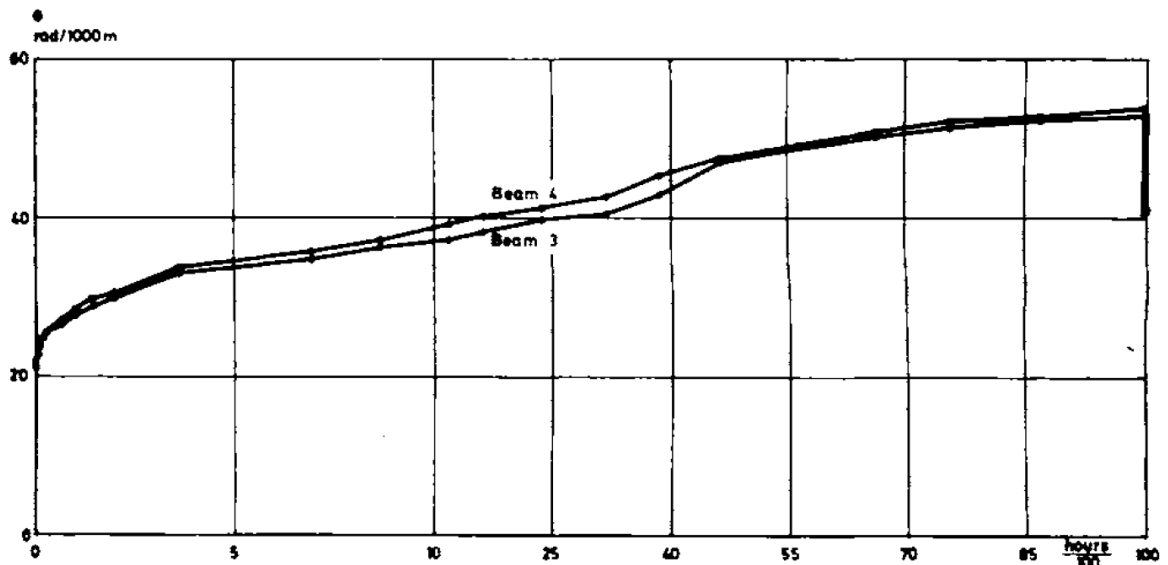


Figure 2.22: Twist angle over time for the RC beams
(Elfgren 1973)

Further experimental investigations into the role of sustained torsion on the behaviour of RC beams were carried by Goode (1975). The beams were loaded for a period of up to two years; the beams were unloaded and reloaded through the testing duration. The loads correspond to the beam's cracking level, which were predicated according Saint Venant theory. Two different cross-sectional dimensions and concrete compressive strengths were employed, where the member geometry and concrete strength controls the cracking stiffness of the members. The beams were tested as pairs, where each pair had the same geometry but different transverse reinforcement ratios, and where either the links spacings were doubled or halved.

Figure 2.23 shows the long-term rotational deformations for a group of the beams. A considerable increase in the beam's rotations can be noted, in which the average twist angle after one year was about five times the initial angle, as shown in Figure 2.24. Nevertheless, in comparing these results with the final rotational ratio obtained by Inge Karlsson and Anderson (1974) (which was approximately three), it is found that this increase was likely related to the level of the initial loads and the formation of new cracks. In the Inge Karlsson and Anderson (1974) tests, the beams were initially exposed to their upper limit (the yield threshold) and cracks mostly extended over the beams. The authors identified that elastic theory (Saint Venant) can predict the cracking load, as described in Section 2.2.

Goode (1975) found that in the beams loaded to 75% of their ultimate capacity, the maximum crack width increased from 0.3 mm (measured on first loading) to 0.7 mm at the end of the tests. The influence of the beam links in enhancing torsional stiffness was more obvious when the truss mechanism was mobilised after the beams reached their cracking loads.

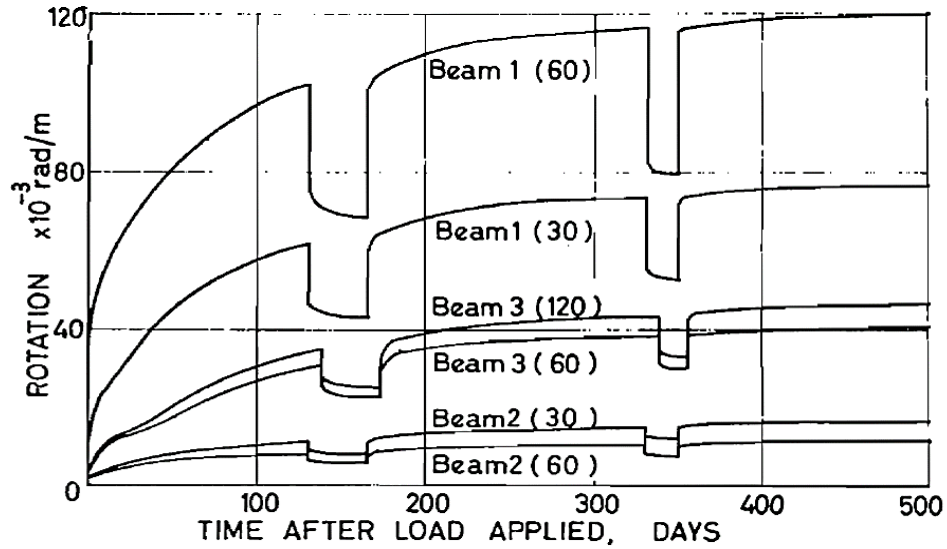


Figure 2.23: Beam rotations, unloading, reloading and recovery with time for the beam with different stirrups spacings (120, 60, and 30 mm)

(Goode, 1975)

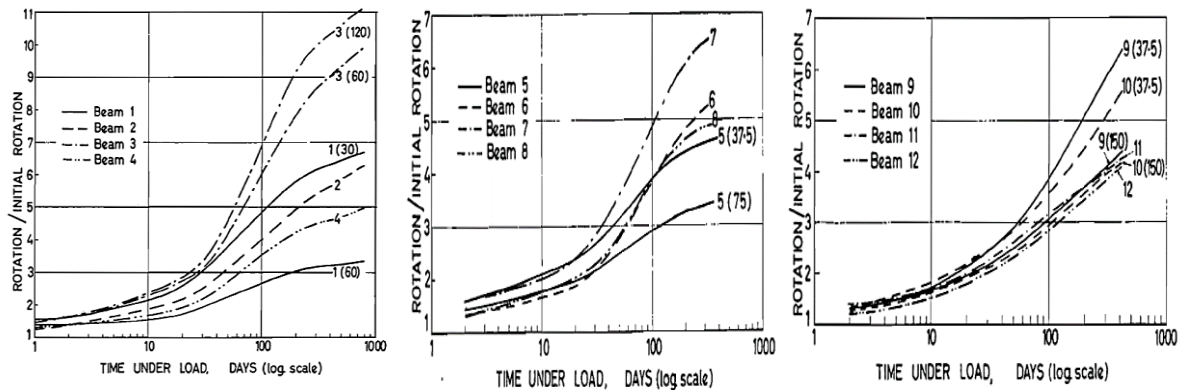


Figure 2.24: The ratio of the long-term rotation to the initial rotation for the tested beams

(Goode, 1975)

Anil and Pandit (1980) tested plain and reinforced concrete beams under constant torsion for about 500 days, while the amount of the sustained load was subsequently increased at the loading periods. The test outcomes

conform with the previous studies, where the influence of concrete creep on the increase of the beam rotations over time at a decreasing rate were identified (Figure 2.25 and 2.26).

The growth of the time dependent twist angles was 2.1 times the short-term twist angle for the plain concrete samples and 2.07 for the reinforced concrete beams. However, there was a drop in the final twist angles of about 25% for the pre-stressed beams. This decline can be attributed to the reduction in the tensile creep strains, which were counterbalanced by the pre-stressing actions in the direction of the tensile stresses produced by the torsion.

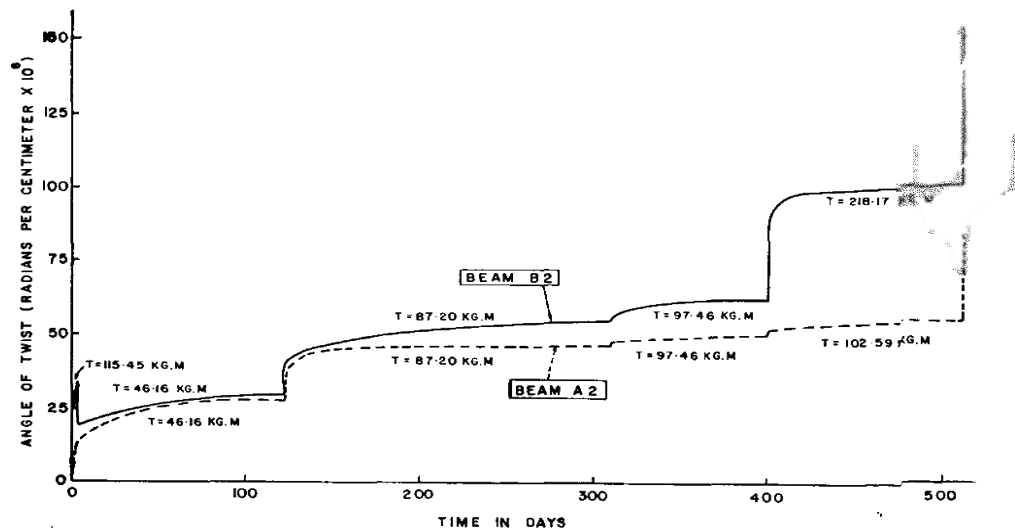


Figure 2.25: Twist angle-time curves for the plain concrete beams under different load values

(Anil and Pandit, 1980)

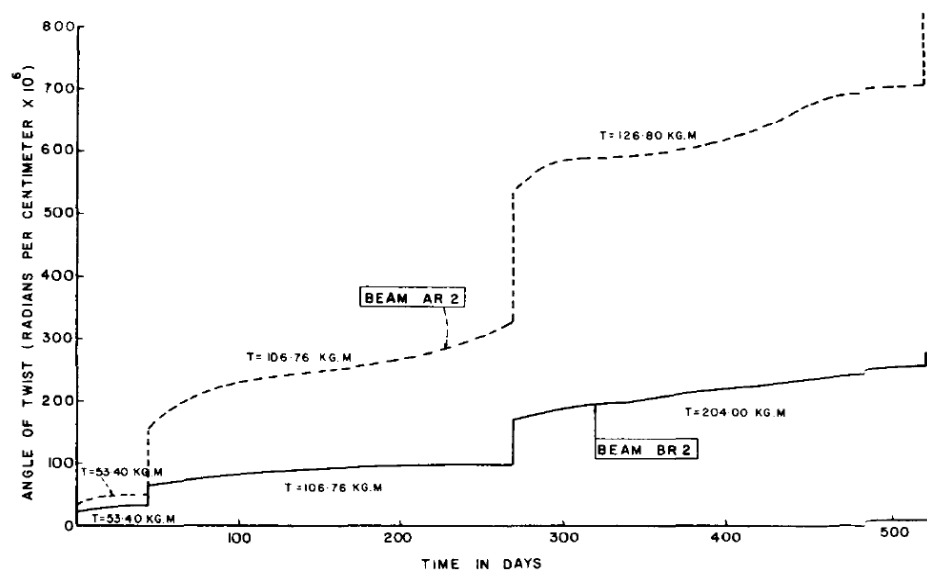


Figure 2.26: Twist angle-time curves for the reinforced concrete beams under different load values

(Anil and Pandit, 1980)

A more recent investigation of the long-term deformations that develop under torsional loads was conducted by Allos and Rashid (1989). Eight pre-stressed beams were tested for periods of up to 350 days, and the companion beams were loaded to failure in order to determine the torsional capacities. The time-dependent deformations in terms of the ratio of the final to the instantaneous rotations were graphically presented by using a hyperbolic expression (Figure 2.27); this expression was developed by Ross (1937) and Lorman 1941 (Neville et al., 1983).

A similar observation to that reported in previous studies (Anil and Pandit, 1980; Goode, 1975; Inge Karlsson and Anderson, 1974) can be deduced from the twist-time curves that presented by Allos and Rashid (1989); the rise in the beam's rotations with a progressively decreasing rate due to creep strains is illustrated in Figure 2.27. The amounts of the total time-dependent beam rotation ratios varied from 1.39 to 3.92, while it has been found that the long-term twist angle increased in relation to the magnitude of the applied torque when the member loads were less than 35% of the ultimate load. Otherwise, the applied torque at the levels of the yield threshold did not appreciably affect the long-term rotation values. Again, the author believes that regarding such a high torsion, the influence of developing new cracks and further propagations of the already formed cracks on the increase of the time-dependent beam's rotations should be minimised.

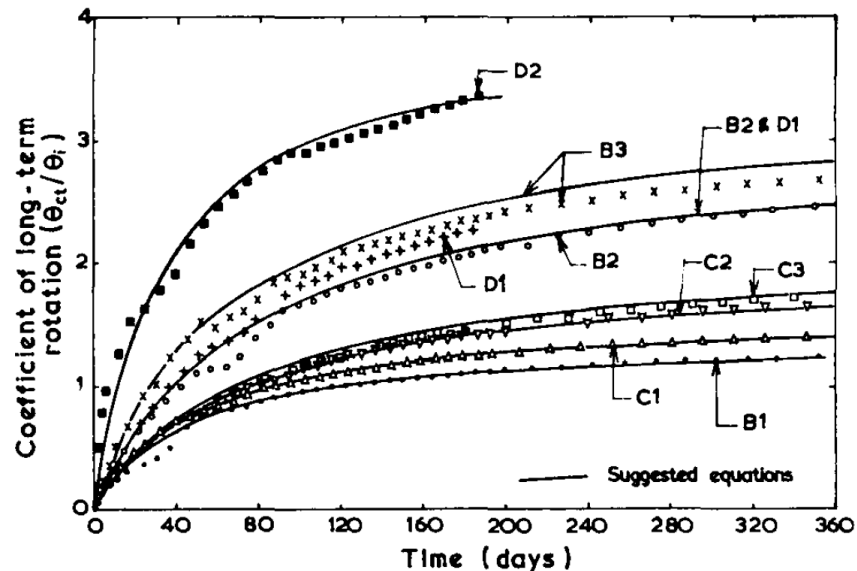


Figure 2.27: The rotations ratios (coefficient) for the beams under sustained torsion
(Allos and Rashid, 1989)

2.6 Numerical Modelling of RC Sections under Torsional Forces.

2.6.1 Introduction

A non-linear finite element analysis of reinforced concrete structures under torsional forces is reviewed in this section. For over 50 years, many researchers have utilised Finite Elements (F.E) techniques to analyse reinforced concrete structures under different loads conditions. In particular, Vecchio and Collins (1992) attempted to model reinforced sections subjected to torsional loads based on MCFT constitutive relationships. They utilised a plane stress material model and the subsequent derived concrete constitutive relationship that they deduced from testing reinforced concrete panels in order to simulate the nonlinear behaviour of reinforced concrete beams. However, limited works have been devoted to investigate the behaviour of reinforced concrete three-dimensional models under eccentric loads or direct torques combined with other forces (e.g. bending and flexural shear), as given in Section 2.6.4. In addition, there have been few research attempts for modelling a strengthened RC member with FRP wraps that consider the effect of out and in-of-plane stresses induced by torque actions, as discussed in this section. Moreover no efforts have been made in the extant literature to model beam-column joints under torsional forces as well as investigate the influence of sustained torsion on the time-dependent behaviours of RC structures. This demonstrates the need to employ a constitutive model for concrete that should realistically reflect its tri-axial behaviour, as torsion is a three-dimensional problem. Further, the developed F.E. model should be capable of simulating both short-term and long-term behaviours in complex geometries and loading conditions, like beam-column joints strengthened with CFRP warps.

2.6.2 Concrete Constitutive Models

Constitutive relationships are essential to formulate the material stiffness matrix and relate stresses and strains developed across the model's elements. The models of concrete behaviour that are commonly used in nonlinear F.E analysis can be broadly classified as (i) plasticity models, (ii) damage continuum models, (iii) coupled plasticity, and (iv) damage models. These models have been calibrated based on experimental data by incorporating a number of parameters (Cotsovos et al., 2009). These

parameters typically correspond to the post-cracking behaviour of concrete in both compression and tension, which also includes concrete softening, tension stiffening, and shear retention ability across cracks (i.e. aggregate interlock). However, the concrete constitutive models that are based on uniaxial or biaxial stress-strain behaviour can be considered unrealistic for multiaxial stress states. For example, for a concrete specimen under confining stresses (e.g. triaxial compression), the failure stresses are a function of the three principal directions (Robert and Manfred, 2015; Kurt H. Gerstle, 1978). Furthermore, concrete compressive strength is not only a function of the uniaxial compressive strain (ϵ_1), but also a function of the lateral strains governing the tensile damage in the lateral directions (2 and 3). Moreover, the damage mechanics can be employed to define the post-peak softening behaviour of concrete materials that cannot be characterised by the classical plasticity theory. Correspondingly, Selby and Vecchio (1997; 1993; 1991) refined the MCFT constitutive relationships in order to account for the confinement and lateral expansion effects for a member under multiaxial stresses. This refinement that has been incorporated into the total strain model, which allows us to simulate complex behaviour, such as confinement enhancement effects, concrete degradation-softening phenomenon in relation to cracking levels, loss of tension stiffening, and crack slip. The introduced constitutive relationships are based on an orthotropic nonlinear elastic model (see Figure 2.28) that accounts for the asymmetric response of concrete under multiaxial stress conditions, where the total strain model is the continuum damage model. The accuracy of the Selby and Vecchio model that is based on the total strain model has been verified through a finite element analyses of RC beams subjected to bending and torsion, along with RC shear walls under axial and lateral loads, as presented in Selby and Vecchio (1997; 1991).

Two commercially available finite element programs (Midas FEA and DIANA) have utilised for the total strain model based on MCFT theory and its three-dimensional refinement by Selby and Vecchio (1991; 1993) to simulate the nonlinear response of concrete. Hii and Al-Mahaidi (2006; 2005) employed the total strain model to simulate the concrete behaviour of RC beams under torsional forces using the DIANA program. The hardening and softening behaviours of concrete corresponded to the Thorenfeldt function (Thorenfeldt, 1987), while the lateral cracking and confinement effects were quantified based on the Selby and Vecchio (1993) model. The reduction in shear

stiffness for cracked concrete was adjusted by using the shear retention factor (which should be taken less than 1). A bilinear stress–strain relationship was employed for concrete behaviour in tension. Similarly, Prakash et al. (2010) utilised the total strain model to investigate the RC columns subjected to different torsion, bending, and shear ratios using the same compression function and models that were employed by Hii and Al-Mahaidi (2006; 2005). In terms of tension, the concrete behaviour was based on an exponential softening relationship that corresponded to the concrete fracture energy and bandwidth of a crack (smeared crack mode). Further details about these investigations are discussed in Section 2.6.4.

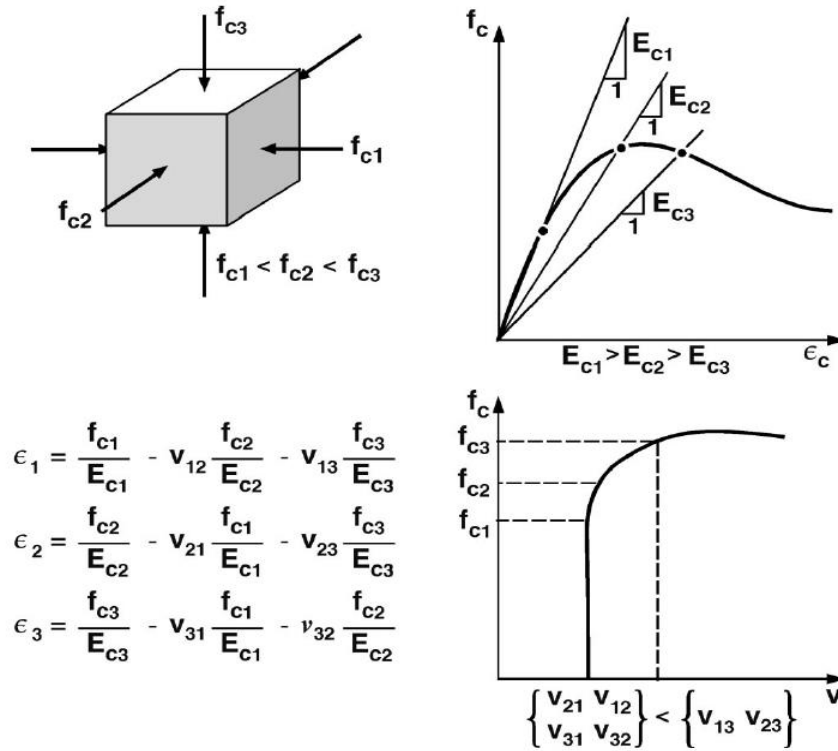


Figure 2.28: Symmetry conditions in the orthotropic model

(Selby and Vecchio, 1997)

The ANSYS package is utilised William and Warnke's (1974) failure criterion for determining the state of failure for both cracking and crushing failure modes conforming to the smeared crack mode. The incorporated concrete model has been formulated based on a regression analysis of experimentally obtained data that were involved in testing of concrete cylinders and cubes under uniaxial compression and tension loads (Cotsovos et al., 2009). The

formulated constitutive relationships in compression and tension are presented in Figure 2.29. The presented graphs (Figure 2.29) show the strain hardening (ascending branch) and strain softening (descending branch) behaviours for concrete before and beyond the peak strength values, while the failure is governed by the William-Warnke function as a failure surface. The failure surface can be defined in ANSYS by using only two parameters (the uniaxial tensile and compressive strengths) out of five. The other parameters include peak biaxial compressive strength and confined triaxial compressive strength (compressive meridian and tensile meridian). However, one of the drawbacks of ANSYS is the proposed model in tension; this model does not correspond with the concept of fracture energy that is commonly used to model the cracking of concrete. In this concept, concrete cracking is characterised by using only the tensile strength of concrete - i.e. a single material property (Ronagh and Baji, 2014). A number of researchers have used the ANSYS package for the analysis of RC beams under torsional forces, which are also described in Section 2.6.4.

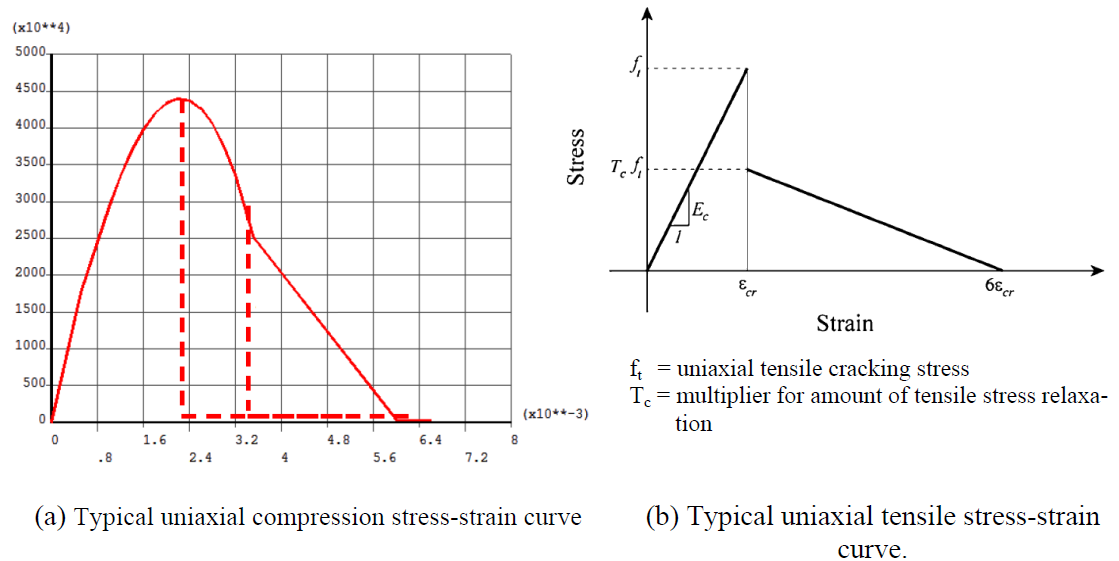


Figure 2.29: Concrete modelling in ANSYS

(Cotsovos et al., 2009)

A non-smeared approach is incorporated in the commercially available software ABAQUS, based on the concrete plasticity model (i.e. damage plasticity model-DPC). This plasticity model employs the yield function introduced by Lubliner et al. (1989), as amended by Lee and Fenves (1998), which in turn is a modification of the Drucker-Prager strength hypothesis. It assumes that there are two failure modes of concrete, tensile cracking and crushing in compression, using isotropic damaged elasticity in combination with isotropic tensile and compressive plasticity. This function is adopted to define the yield criterion, flow potential and viscosity parameters. The behaviour of concrete under uniaxial tension and compression that is utilised in ABAQUS is presented in Figure 2.30, which involves hardening and softening branches. It can be noted that for tensile loading, damage and plasticity are initiated when the equivalent applied stress reaches the peak uniaxial tensile strength (σ_{to}). While under compressive loading, concrete damage is initiated at a different stage than the plasticity limit (σ_{cu}), which corresponds to the damage level (d_c). Recently, Obaidat et al. (2020) and Ganganagoudar et al. (2016) utilised the DPC model (ABAQUS) to investigate the behaviour of RC beams subjected to torque actions.

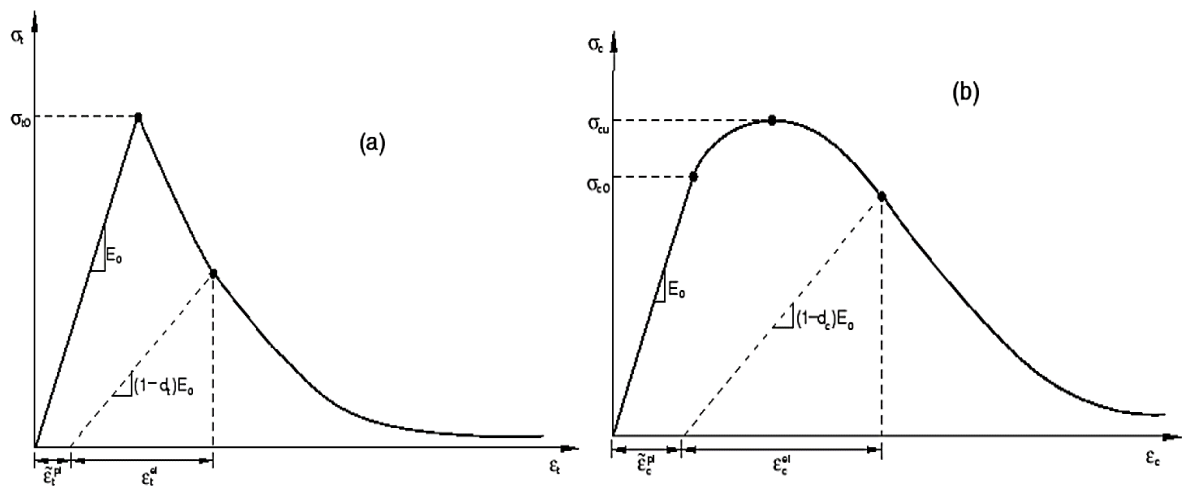


Figure 2.30: Concrete modelling in concrete damage plasticity (a) Tension (b) Compression

(ABAQUS, 2008)

2.6.3 Concrete Cracking

It is generally agreed that one of the most important factors that affects the nonlinear behaviour of RC structures is cracking of concrete. Due to a physical discontinuity caused by a formed crack, the earliest attempt (Ngo and Scordelis, 1967) to simulate the cracking of concrete was based on the discrete crack concept. This concept represents the development of a crack by discontinuous nodes along the boundaries of the elements. However, this concept cannot be considered feasible to model a complex three-dimensional problem; the model needs to be updated to mesh through the analysis process, which is very time consuming and cumbersome. Further, cracks are forced to develop at the element's boundaries, and hence, a mesh bias is produced (Borst et al., 2004; Rots, 1988). In addition, it can produce stability and convergence problems due to using interface elements that are required at the location of expected cracks.

Rashid (1968) introduced the smeared crack concept as a counterpart to the discrete crack concept, where the influence of cracking is smeared over a finite area. The smeared crack assumption of a locally formed crack is evenly scattered over a wide surface, in which numerical modelling is relatively simple (Midas, 2015). Thus, this concept considers the presence of cracks by modifying the coefficients in the material stiffness matrix. Also, using the smeared crack concept preserves the topology of the created mesh, which does not restrict the orientation of the crack's planes (Rots, 1988). Hence, the smeared concept dominates in modelling of reinforced concrete structures. This smeared concept can be categorised into fixed cracks and rotating cracks modes. Further details about the smeared crack concept and its modes are discussed in Chapter 7.

2.6.4 Previous Research Investigations Using Finite Elements Models

As previously discussed, limited attempts have been carried out using the finite element method to investigate the behaviour of RC sections under torsion actions. A summary of the available numerical models in the extant literature using finite elements method is presented in Table 2.3. Generally, most of these models were created based on the smeared crack concept, which have confirmed the feasibility of this concept significantly when they employed the total strain cracks model (Prakash et al., 2010; Hii and Al-

Mahaidi, 2006; Hii and Al-Mahaidi, 2005; Selby and Vecchio, 1991). However, recent research conducted by Obaidat et al. (2020) and Ganganagoudar et al. (2016) have utilised the damaged plasticity model to simulate the response of RC beams. The outcomes of the research of Obaidat et al. (2020) show significant deviations from experimental results for several specimens - i.e. overestimating and underestimating the torsional capacity and twist angles, receptively. The authors argued these deviations would be fewer if a suitable bond model was used between FRP's strips and concrete, rather than assuming perfect bond conditions. Moreover, there was still a deviation in the observed F.E. values from the test values (post cracking behaviour) for the unstrengthened beam (no strips used). Also, discrepancies were noted in the tests' peak torque, the corresponding twist angles and the numerically obtained values (reached to 20%) based on Ganganagoudar et al. (2016) model.

As mentioned in Section 2.6.1, the earliest attempt to utilise the total strain model-smeared crack concept to simulate torsional behaviour of RC beams was made by Selby and Vecchio (1991). A more recent development of the F.E. model based on the total strain crack model for modelling RC beams strengthened with CFRP wraps has been proposed by Hii and Al-Mahaidi (2005; 2006). This model has shown very good agreement with the experimental results in terms of torque-twist angles, strains, and crack developments. The proposed models accurately predicted the pre-cracking and post-cracking behaviours in all loading stages, significantly after the adjustment of the shear retention factor. Hii and Al-Mahaidi (2005) identified the optimal shear retention factor, which was 0.25. Further, they found that concrete tensile strength computed according to $0.3\sqrt{f'_c}$ was most relevant to the tests results. Hii and Al-Mahaidi (2006) also recommend increasing the value of the shear retention factor (up to 0.3) by using a greater number of CFRP wraps. The CFRP wraps were modelled as an orthotropic linear-elastic material using plane stress elements and the contribution of the transverse direction and shear stiffness of the CFRP warps was neglected. The interaction between CFRP wraps and concrete was assumed to be perfectly bonded. Other attempts have been made by Ameli et al. (2007) and Santhakumar et al. (2007), who investigated the behaviour of strengthened RC beams using the ANSYS package in accordance with William and Warnke's (1974) failure criterion. Ameli et al. (2007) modelled the FRPs laminates using elastic shell elements, where the fibres' modulus of elasticity

and strength were reduced based on the measured thickness ratio of the used laminates (laminate thickness/fibre thickness). This is because the resin- the laminate matrix strength and stiffness are very small compared to the fibres, which corresponds with the fib Bulletin 14 (2001) recommendations. When compared with the experimental results, the numerical solution produced deviations through the cracking stage in terms of torque-twist angle. Meanwhile, the observed torsional capacities were reasonably predicted. Santhakumar et al. (2007) used a layered solid element to simulate the CFRP laminate, although the authors did not provide further details about the parameters that should be employed to adjust the layered solid element. Further, the produced load-deflection curves were not validated using experimental obtained values. In addition, there were significant deviations between the experimental and the F.E. moment-strain curves before cracking stage and peak load. All the aforementioned models assumed perfect bond conditions between steel rebars and concrete and did not introduce any model (FRP's-concrete bond model) that can be used to consider the interaction between wraps and concrete surface.

Prakash et al. (2010) utilised the total strain crack model to investigate the influence of combined torsion, bending and shear forces on RC columns. The ratio of torsion to bending (T/M) was found to be 0.4 and the examined columns have different height-to-diameter ratios. A rotated smeared crack concept was utilised to represent the concrete cracking and the confinement of concrete was considered according to Selby and Vecchio's (1993) model, which was incorporated into the total strain crack model in DIANA software. Perfect bond conditions were assumed between embedded bars and concrete. The overall behaviour of the modelled columns was reasonably well predicted in comparison with the test results. However, the numerical results were somewhat stiffer than the experimental values for columns under 0.4 T/M loads ratio. Good agreement was obtained in the elastic portion between the numerical and experimental results for columns under bending and shear loads before stopping the analysis due to a convergence problem. For columns under pure torsion loads, the created model was underestimated in the elastic region, while they agreed well with the test results at the post-cracking stage. On the other hand, this investigation confirmed the viability of the total strain crack model to simulate the cracking of concrete and the developed strain levels.

Mostofinejad and Talaeitaba (2011) introduced the F.E. model to simulate the nonlinear behaviour of different RC beam sections (i.e. rectangular, box, and T-beam's sections) under torsion. The model was based on the smeared crack concept with using William and Warnke's (1974) concrete failure criterion (see Table 2.3). A comparison between the numerically obtained torque-twist curves and experimental observations reveal that the proposed model cannot adequately present the post-cracking behaviours for the modelled beams. Meanwhile, the model reasonably predicted cracking and ultimate torque with agreement with the test values, which ranged between 78% to 89%. Deifalla et al. (2020) attempted to model lightweight concrete T-flanged beams subjected to different ratios of combined shear, torsion, and bending using the smeared crack concept (ANSYS package). The stress-strain relationships for the lightweight concrete were based on experimentally obtained data. The produced load-deflection curves, using the proposed numerical model, showed consistent deviations from the test results in both pre and post-cracking stages. However, the predicted ultimate loads showed good agreement with the tests results -i.e. the coefficient of variation was only 0.033.

Table 2.3: Summary of FE studies on RC sections under torsional forces

Author	Numerical approach	Concrete Model	F.E. Software	Load details ¹	Member's details
Selby and Vecchio (1991)	3D F.E., Smeared crack concept, Rotated angle crack mode	Total strain crack model	SPARCS	The torque was applied as nodal forces at the beam's end	RC beams
Hii and Al-Mahaidi (2005)	3D F.E., Smeared crack concept, Fixed angle crack mode	Total strain crack model	DIANA	Load applied via loading arm to produce torsion	RC beams and strengthened RC beams with FRP's wraps
Hii and Al-Mahaidi (2006)					
Ameli et al. (2007)	3D F.E., Smeared crack concept	William and Warnke model	ANSYS	The torque was applied at the beam's free end	RC beams and strengthened RC beams with FRP's wraps
Santhakumar et al. (2007)	3D F.E., Smeared crack concept	William and Warnke model	ANSYS	The loads were applied on two opposite moments arms joint to the beams	RC beams and strengthened RC beams with FRP's wraps
Prakash et al. (2010)	3D F.E., Smeared crack concept, Rotated angle crack mode	Total strain crack model	DIANA	The torque was applied at the column's free end using a rigid block	RC columns
Mostofinejad and Talaeitaba (2011)	3D F.E., Smeared crack concept	William and Warnke model	ANSYS	The load was applied on the free end of the beams in the form of two forces equal in magnitude and with opposite directions (couple).	RC beams
Ganganagoudar et al. (2016)	3D F.E., Damage Plasticity Model	Lubliner et al, Lee and Fenves model	ABAQUS	The torque was applied at the beams free end	Strengthened RC beams with FRP's wraps
Deifalla et al. (2020)	3D F.E., Smeared crack concept	Experimentally measured stress-strain relationships were used	ANSYS	The load was applied at a single line of nodes on the upper plate of the free beam end	RC T-Flanged beams
Obaidat et al. (2020)	3D F.E., Damage Plasticity Model	Lubliner et al. and Lee and Fenves model	ABAQUS	The torque was applied at the beams free end	Strengthened RC beams with NSM ² FRP's strips.

¹ All models loaded up to failure (short-term loads)

² Near Surface Mounted FRP strips

2.7 Conclusions

After the review it is clear that no one has clarified the behaviour and the level of the joint's forces for a beam-column joint subjected to multiple actions including torsion with considering different beam wraps. The review is attempted to obtain as much help from related research investigations as possible. Accordingly, the current considerations of torsion in RC members and proposed torsion mechanisms, theories, and analytical models present in the literature has been presented with a view to identify the beam torque effects on the pre and post cracking capacities of RC members. The previous research on the behaviour of the strengthened reinforced concrete beams with different FRP schemes under torsional forces has also been reviewed, wherein the level of enhancement in the beams' torsional strengths have been quantified in accordance with the fibre configurations, fibre orientations, and the types of fibres used. Joint force transfer mechanisms and factors affecting the joint shear strengths have been discussed by taking into account the actions of the diagonal strut and truss mechanism analogies. Further, an attempt has been made to identify the influences of eccentric forces on the joint's deformations and strengths. The design guidelines according to the codes of practice for RC beam-column joints have been critically reviewed by recognising the influential factors that are incorporated in the recommendation's expressions. The time-dependent effects of torsional forces have been assessed in relation to creep and shrinkage deformations. The numerical models and the conducted investigations using finite elements method have been reviewed and discussed. Based on the extant literature, the following main conclusions can be made:

- In comparison to concentrically loaded joints, much less research has investigated the effect of beam torsion on joint behaviour. The extant research has concentrated on the influence of the eccentricity of the beam axis from the column axis, as well as the effect of transverse beams and slabs, in which it has been observed that the joint's strength is reduced due to the eccentricity of the beams. However, none of the published works have addressed the influence of combined forces including torsion on the joint's demands and distortion levels.
- The absence of a rational analytical model to predict the behaviour of beam-column joints strengthened with torsional FRP schemes that are subjected to beam torsion is confirmed.

- The literature has identified that torque combined with flexural and direct shear forces can reduce the capacity of RC beams and affect their behaviour in terms of decreasing the member's ductility and altering rebar strains, the flexural compression zone, section curvatures, plastic hinge location, and cracking levels.
- Several analytical models based on MCFT and STM methods have been proposed to predict the member's behaviour under actions of pure torsion or combined loads. The derived expressions correspond with the smeared stresses and strain distributions over the section's sides, where the force variations in the bottom and upper chords cannot be identified. Empirical constitutive formulas for cracked concrete have been introduced within the MCFT and STM methods to account for the softening of concrete, which complies with the level of tensile stresses.
- The effectiveness of externally bonded CFRP wraps and strips for enhancing torsional strength and the behaviour of RC beams has been confirmed. Five distinctive schemes have been specified, which include continuous vertically oriented wraps along the beam member, U-wrap, strips wrap (hoops), 45° oriented fibres and horizontally oriented fibres.
- The truss model has been employed to predict the strengthened member capacities by superimposing both wraps and rebar contributions. However, the variation of the strut inclination angle through the member sides due to interactions between the torsion, flexure, and shear was not considered.
- There is no research that has investigated the effects of FRP beam strengthening schemes on the beam-column joint behaviour where the joints are subjected to the action of beam torsion, and none has quantified the influence of fibre orientations and ratios on the joint behaviour, failure mode and plastic hinge position.
- The main factors that can affect the joint's shear strength and force transfer mechanism has been identified from the literature. These include concrete strength, transverse reinforcement (joint ties), bond and anchorage, column axial load, and the joint's aspect ratio. Corresponding to these factors, the literature has shown that two resisting actions, including the diagonal strut and truss mechanisms, can transmit the joint's forces.
- The code provisions (e.g. BS8110, Eurocode2, ACI-ASCE 352R-02, and NZS 3101) for joint design strengths are based on different approaches. These include the truss mechanism, variable strut

inclination method, diagonal strut capacity, and the function of concrete strength.

- The code provisions for RC joints do not provide guidelines to evaluate joint shear demand under combined actions. Further, in non-seismic regions, the design provisions do not consider strain hardening and the large plastic deformation in the beam's main rebars; these plastic strains can arise due to the interaction between the combined loads and can be transmitted to the joint zone.
- Only a few studies have investigated the influences of sustained torsional loads on RC beam deformations, while no attempt has been made to address these time-dependent deformations on beam-column joints strengthened by FRP wraps. Also, there is a lack of quantifying strain variations in concrete and reinforcement (e.g. top and bottom) over the member's sides that are associated with torsional time-dependent deformations.
- The experimental results showed changes in the beam's twisting deformations influenced by creep and the rate of creep, wherein the beam's rotations varied rapidly after load application and gradually slowed over time.
- The literature indicates that there are considerable rises in the RC beam's time-dependent rotations; these were on average between 1.39 and 5 times larger than the short-term twist angles.
- Limited attempts were carried out using finite element method to simulate the behaviour of RC sections subjected to torque actions. While, no efforts have been paid to predict the short and long-term torsional behaviour of RC beam-column joints considering a beam torque.
- The total strain crack model and smeared crack concept have been successfully utilised in the previous research investigations to model the RC sections and strengthened RC beams with FRPs warps under torsional forces.

Based on the literature and the lack of direct relevant research, this investigation intends to provide a better understanding into the behaviour of reinforced concrete beam-column joints under combined loads with considering the following aspects.

- I. The failure mechanism, ductility and deformation levels of the beam-column joints subjected to multiple actions including torsion.
- II. Quantifying the increase in the beams forces, developed strains, and plastic hinge location that correspond to the type of beam warps and level of torsional moment.
- III. Identifying the effects of wrapping degree (full or partial) and wraps fibres orientations on damage of concrete, struts angles, and joints distortion levels.
- IV. Developing a rational approach based on the truss analogy to evaluate the joints forces (demands) which accounts the interaction between the combined forces.
- V. Proposed an analytical model to predict the joints strengths under combined loading with considering the influential parameters that affect the RC joints which were addressed in the literature.
- VI. Investigating the effects of sustained torsional forces that combined with flexural and direct shear on the beam-column joint behaviours with presence of a beam wraps.
- VII. The variation in the developed strains in the rebars and the concrete surfaces due to sustained torsion.
- VIII. Investigating the behaviours of the beam-column joint subjected to different torsion to bending-shear ratios by using the total strain crack model-smeared crack concept (MIDAS FEA); in addition, quantifying the rise of the rebars strains induced by various loading ratios, together with two different concrete strengths and multiple CFRP layers.

Chapter 3 Experimental programme

3.1 Introduction

The experimental programme that was conducted within the laboratories of the School of Civil Engineering (University of Leeds) is described in this chapter. The design details of the test specimens, geometries, and the procedure that was utilised for testing the specimens are all presented. The experimental work consisted primarily of testing eight equivalent exterior RC beam-column joints, which were constructed using concrete and deformed steel bars. In addition, in order to comply with the torsional strengthening systems that have been proposed in the literature, three different CFRP wrapping systems were employed to strengthen the beam region of the beam-column joints. Supplementary tests for determining the mechanical properties of the materials used to construct the specimens are detailed, together with the required instrumentations, loading rigs, and number of samples.

3.2 Aim of Experimental Programme

The aim of this program is to investigate the short and long-term behaviour of RC beam-column joints subjected to torsion and with effective CFRP strengthening systems applied only to the beam. The short-term testing programme was set to identify the failure modes, crack pattern, joint deformations, ductility, and carrying capacity of the beam-column joints under torsion combined with flexural and direct shear forces. Further, quantifying the strain escalations in the beam's main rebars due to the interaction between the applied loads and measure the rebar strains at different locations was performed in order to determine strain developments and possible plastic hinge locations. This short-term investigation was also intended to analyse the effect of three effective strengthening configurations (e.g. full wrapping, strips, and 45° strips) on the behaviour of beam-column joints.

The main objective of the long-term testing programme is to evaluate the influence of a sustained torsional force on the beam-column joint in terms of time-dependent rotation, deflection, crack propagations and widths. In addition, the strain variations on the beam's surfaces and rebars due to the long-term torsional forces are considered. This programme involves the investigating the time-dependent behaviour and the strain developments in the beam-column joint subjected to consecutive loading stages, where the 1st

stage was under sustained bending moment and after a couple of months, torsional forces were applied to supplement the initial bending forces.

3.3 Beam-Column Joint Details

As identified earlier in Chapter 2, the beams wrapping schemes can enhance beams stiffness and carrying capacities; this can be very significant when the induced stresses increase the level of inelastic deformations in the flexural plastic zone (near the column's face) where a damage can be developed in the column of the joint. Hence, it is important to recognise the effects of the wrapping schemes and any changes to the combined forces resulting from a change in building use or a structural change to the frame. On the other hand, the perimeter beams in monolithic framed structures are under significant torque in corresponding to the level of bending moment from the slab (Pham et al., 2019). Further, the influence of the slab loads on the torsional distress of the perimeter beams become more critical in the case of column removal or loss; ultimately ensuring that the damage is kept away from the joint and is located in the beam itself.

The tested beam-column joint is hypothetically located at the 4th floor of a six storey ordinary moment resisting frame (i.e. typical frame components that are often designed to attain limited torsional loads in corresponding to codes provisions). The frame detail is shown in Figure 3.1, which was analysed with SAP 2000 software to quantify the member forces. The members were designed according to the ACI Committee 318 (2014) recommendations, while the joint panel details correspond with the ACI-ASCE 352R-02 Committee (2002) recommendations - connection Type-1. Hooked end bars (90°) were used without any splice to provide a sufficient bonding length and prevent anchorage failure of the joint's horizontal bars. The joint's aspect ratio is 1.05; a number of studies have noted a decrease in joint shear capacity with an aspect ratio larger than 1.4 (Chun and Shin, 2014; Hamil, 2000b). The beam and column lengths of the exterior joint have been extended beyond the contra-flexure points as determined from the SAP modelling. A non-symmetrical distribution of live loads (see Appendix B) has been considered between the floors and spans, such that the maximum induced beam torque is 2.24 kN.m this is close to the calculated threshold value (3.04 kN.m), where the threshold limit is defined as 25% of the torsional cracking moment (ACI Committee 318, 2014). Hence, the design is 'standard' and no additional torsional reinforcement was needed in accordance with the ACI 318-14

recommendations. More details about the frame dimensions, loads arrangements, loads combinations, modelling details, torsion reinforcements check, and the joint design details are presented in Appendix B.

The beam-column joints were scaled down to $\frac{3}{4}$ of their nominal size in order to be compatible with the laboratory testing apparatus. Similar reinforcement ratios for columns and beams were used in the scaled model, while beam and column sizes were reduced to 300 x 210 mm and 285 x 210 mm, respectively (It should be noted that even at this size, the specimen is still equivalent to some full-scale in-situ RC elements). A typical section detail and the layout of the exterior beam-column joint specimens are shown in Figure 3.2. While the specimens were re-orientated (180° about the beam's main axis) in order to apply the loads from the beam's bottom side rather than from the beam's top side due to the limitation in the testing infrastructure.

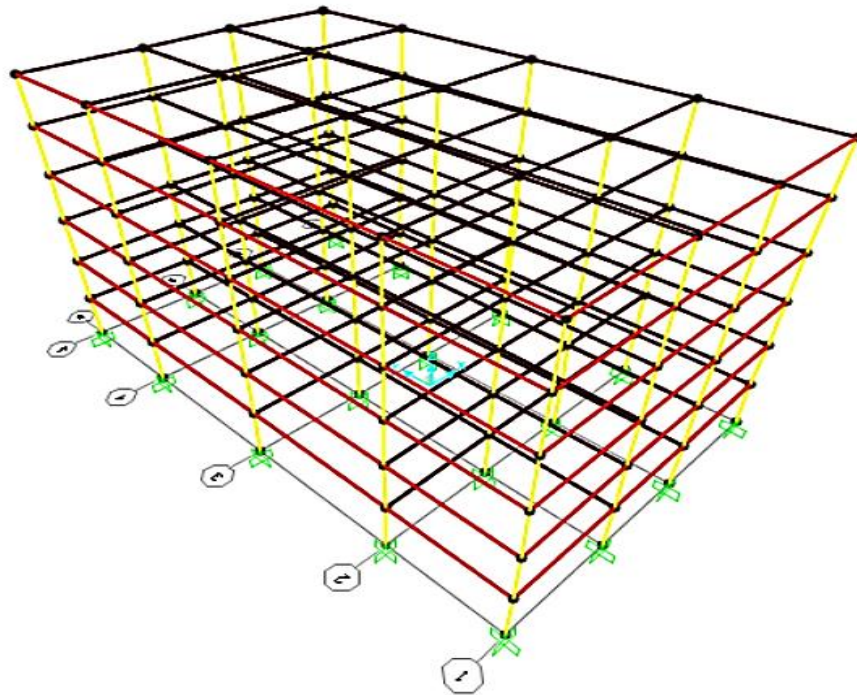


Figure 3.1: Frame Model

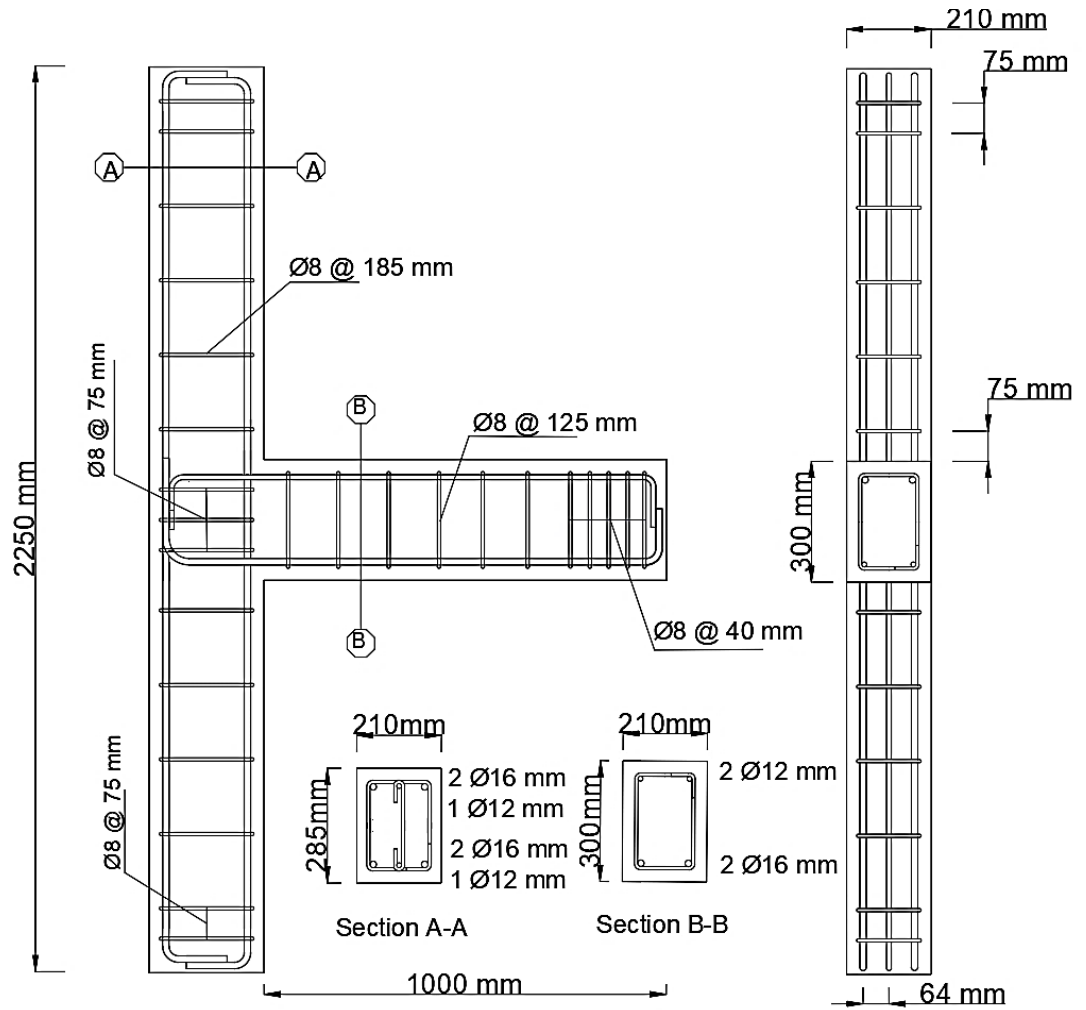


Figure 3.2: Reinforcement and section details for the scaled specimen

3.4 Experimental Plan

The experimental plan is categorised into two main testing series, as shown in Figure 3.3; the short-term series and the long-term series. The beam-column joints in the short-term series were tested under a monotonic load; the load was applied either at the beam tip (flexural test -see Appendix C) or at the end of a rigid steel cantilever arm (see Figure 3.22), so as to induce a torque combined with the flexural and shear forces. These specimens were tested up to failure. Meanwhile, the long-term specimens were subjected to sustained loads, which lasted for a period of no less than 90 days; since the previous studies showed that at least half of the concrete creep develops in the first 90 days of loading (Neville and Brooks, 2010; Gilbert, 2002; Troxell, 1958). The control (unstrengthened) specimens were tested and considered

as a baseline in order to help investigate the effect of the torsional moment on the beam-column joint's behaviour. Further details about testing setups and procedures are presented in Section 3.9.

In addition to the beam-column joint specimens, supplementary tests were carried out to identify the mechanical characteristics of the concrete mix, the creep coefficients, and the shrinkage.

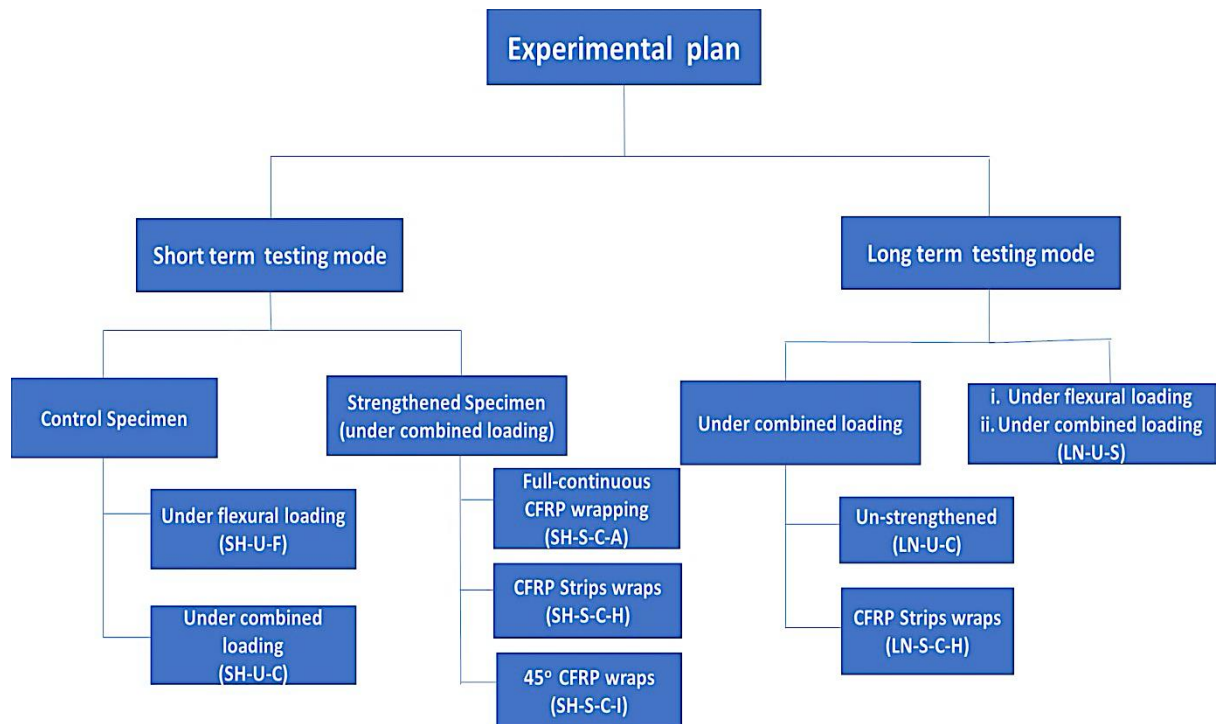


Figure 3.3: Experimental programme plan

The specimens were identified as X-I-F-R, according to the type of testing, beam loading, and strengthening scheme. Here, X refers to the test series, I refers to the control (unstrengthened, or strengthened) specimen, F is the loading type, which includes flexural, combined with torque or sequential loading (flexural and direct shear followed by torsion), and R refers to the strengthening configuration by the externally bonded CFRP sheets (the sheets were bonded using epoxy resins).

The short-term test group (SH) and a long-term test group (LN) were divided to strengthened or unstrengthened members and then according to their loading type- i.e. F, C, and S refer for flexural, combined, and sequential loading, respectively. The strengthened members were further subdivided into three categories based on the wrapping configurations (A for full-continuous beam wrapping, H for strip (hoops) beam wraps, and I for 45° inclined strip wrapping).

The first group (short-term) consisted of five specimens, SH-U-F, SH-U-C, SH-S-C-A, SH-S-C-H, and SH-S-C-I, while the second group (long-term) included the following specimens: LN-U-C, LN-S-C-H, and LN-U-S. The groups and specimen details are given in Table 3.1.

Table 3.1: Beam-column joint details

Group	Loading type	Member detail	Specimen	Scheme Type
SH (short-term testing mode)	Flexure and Shear	Control (unstrengthened)	SH-U-F	N.A.
	Combined with Torsion		SH-U-C	N.A.
	Combined with Torsion	Strengthened	SH-S-C-A	Full-continuous
	Combined with Torsion		SH-S-C-H	Strips
	Combined with Torsion		SH-S-C-I	45° strips
LN (Long-term testing Mode)	Combined with Torsion	Unstrengthened	LN-U-C	N.A.
	Sequential		LN-U-S	N.A.
	Combined with Torsion	Strengthened	LN-S-C-H	Strips

3.5 Strengthening Schemes with CFRP

This study considered full and partial strengthening systems, with a view to explore the influence of two different levels of strength and confinement of the beam area on the joint behaviour. Hence, three different externally bonded CFRP schemes were employed to strengthen the beam regions, as shown in Figure 3.4. These schemes consisted of either continuous full-wrapping or partial wrapping, with vertically oriented CFRP hoops and 45° inclined strips.

fib Bulletin 14 (2001) recommendations were adopted to predict the enhancement level in the torsional capacity for each specimen at ULS (ultimate limit state). As mentioned in Chapter 2, these recommendations are based on the space truss mechanism, which can be used to evaluate the FRP capacity. The designed FRP strain (ε_{ef}) and fibre ratio (Table 3.2) were modified according to the effective fibre strain (Triantafillou and Antonopoulos, 2000), as given in Eq. 2.8a, and the effective fibre ratio (ρ_f) according to Hii and Al-Mahaidi (2007) (Eq.2.9 to 2.10). The employed wrapping schemes were formed from a single layer (ply) of CFRP strips-wraps, in order to compare the contributions of different schemes with using identical plies number. Further, the majority of proposed schemes in the extant literature were introduced by using one ply as presented in Table 2.1; while the effectiveness of using multiple FRP's layers is limited by the failure of concrete substrate in corresponding to concrete strength as discussed in Section 2.3.3.

The overall member's torsional capacities were determined by the superposition of both rebar and CFRP contributions (Eq.2.4). The ACI Committee 318 (2014) recommendations were employed to evaluate the torsional member's strength, which represents the steel rebars' contribution (T_{Usteel} is the lesser of Eq.3.1 and 3.2).

$$T_{Usteel} = \frac{2 A_o A_t f_{yt}}{s} c o t a \quad \text{Eq.3.1}$$

$$T_{Usteel} = \frac{2 A_o A_l f_y}{P_h} c o t a \quad \text{Eq.3.2}$$

Where;

T_{Usteel} = ultimate torque produced by steel rebars in N.mm

A_t = the area of one stirrup leg in mm²

f_{yt} = the yield strength of stirrup in MPa

S = Spacing between stirrups centre to centre in mm

p_h = Perimeter that is enclosed by stirrup in mm

A_o =

Area of shear flow equal to 0.85 of the area enclosed by stirrups in mm

Table 3.2: CFRP schemes details

Specimen	Scheme Type	Fibre Ratio (ρ_f) Eq. 2.8d & Eq. 2.10	Effective Fibre strain (ϵ_{ef}) (Micor-strain)- Eq. 2.8a	Fibre orientation angle	CFRP width (mm)	CFRP Strip spacing c/c	Number of plies
SH-S-C-A	Full	0.47%	4200	90°	210	-	1
SH-S-C-H	Hoops	0.23%	5000	90°	100	200	1
SH-S-C-I	Inclined strips	0.23%	5000	45°	100	200	1
LN-S-C-H	Hoops	0.23%	5000	90°	100	200	1

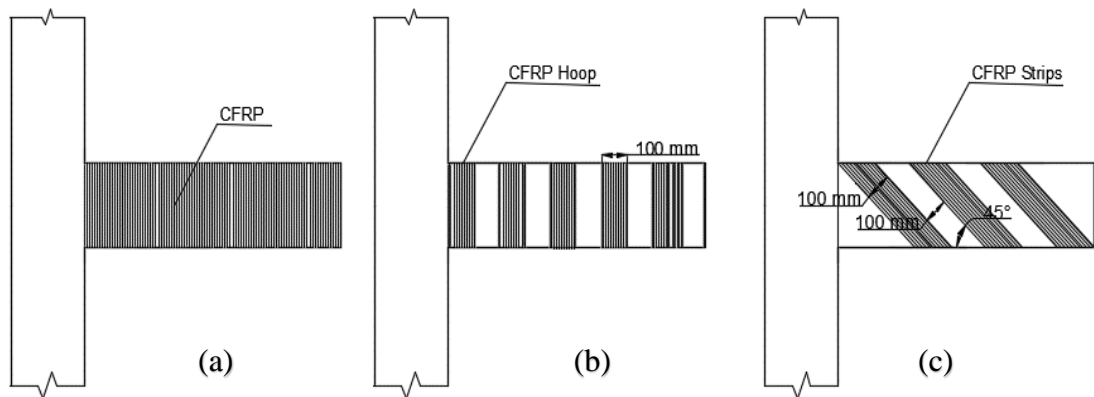


Figure 3.4: Strengthening schemes, (a) Full wrapping, (b) Strip wrapping-hoops, (c) 45° inclined wrapping

3.6 Casting Specimens

Each beam-column joint was cast using two batches of concrete, where a mechanically driven drum mixer of 200-liter capacity was used for mixing the concrete. A slump test was carried out to verify the workability, in accordance with BS EN 12350-2 (2000). Several samples were also taken (Figure 3.5) from each batch; these included, three cubes, six cylinders, three prisms (100*100*500 mm), and two bobbins for the short test specimens, while eight additional prisms (200*75*75mm) and two additional bobbins were used for the long-term test specimens. Table 3.3 shows the concrete samples and test details.

Table 3.3: Concrete samples details

No	Test description	Specimen	Dimension
1	Concrete compressive strength ($f_{ck, \text{cube}}$)	Cubes	100*100*100 mm
2	Concrete compressive strength (f_{ck}), splitting tensile test ($f_{t,sp}$) and modulus of elasticity (E_c)	Cylinders	300*150 mm
3	Compressive creep and shrinkage	Prisms	200*75*75 mm
4	Flexural strength ($f_{t,fl}$)	Prisms	100*100*500 mm
4	Tensile creep, shrinkage and direct tensile test	Bobbins	365*75 mm

A T-shape steel mould was built according to the beam-column joint size, where the concrete mix was poured into the mould and was compacted using a hand-held vibrator (see Figure 3.6). The specimens and sample surfaces were adequately levelled with a trowel after completion of the casting and subsequently covered with polyethylene sheets. All the plain concrete samples were demoulded after 24 hours and kept in the controlled fog room for 28 days under 99% relative humidity conditions (Figure 3.7). While the beam-column joint specimens were cured by using the wet hessian cloth and were covered with the polyethylene sheets (Figure 3.7) prior to the tests to prevent moisture loss to the atmosphere.



Figure 3.5: Casting of samples



Figure 3.6: Casting using the hand-held vibrator



Figure 3.7: Curing of the samples

3.7 Material Properties

3.7.1 Concrete Properties

The constituent materials that were used to produce concrete are high strength cement, normal-weight fine aggregate, normal-weight coarse aggregate, and water. The required (characteristics) compressive strength (f'_c) for the concrete is 35MPa (equivalent to a C35/45), which is based on ACI Committee 214R (2011). Several trial mixes were cast to verify the batch quantities and its characteristics. Table 3.4 shows the details of the materials and the mixing proportions for concrete (1 m³), which were adopted for casting the specimens. The compressive strength, tensile strength, and the modulus of elasticity of each batch of concrete were identified in the laboratory. The concrete samples were cured inside a curing room (99% relative humidity) and tested according to the relevant testing standard as presented in Sections 3.7.1.5 and 3.7.1.6. In addition, concrete creep induced deformations were determined by subjecting the concrete samples to sustained loads during the testing periods (Section 3.7.1.7 and 3.7.1.9); while shrinkage induced strains were recorded when the concrete sample were exposed to drying after 28 days curing (Section 3.7.1.8).

Table 3.4 Concrete mix proportions.

Cement Kg/m3	Fine Aggregate Kg/m3	Coarse Aggregate Kg/m3	Mixing Water Kg/m3	f'_c (Cylinders) MPa
320	920	960	165	35

3.7.1.1 Coarse Aggregate

Ten mm uncrushed natural coarse aggregate from north Nottinghamshire (Tarmac Roadstone) was used in all tests. Table 3.5 shows the grading details of the coarse aggregate; the grading curve complied with BS 882 (1992) limits, as shown in Figure 3.8. The drying of the coarse aggregate was carried out using the drying parker plant in the Casting Shop at the University of Leeds.

Table 3.5: Particle size distribution of coarse aggregate

Sieve Size (mm)	Weight Retained (g)	% Retained	Cumulative % Retained	% Passing
14	0	0	0	100
10	145.5	14.55	14.55	85.45
8	439.5	43.95	58.5	41.5
5	398	39.8	98.3	1.7
2.36	13.5	1.35	99.65	0.35
1.18	3.5	0.35	100	0
pan	0	0	100	0
Total	1000			

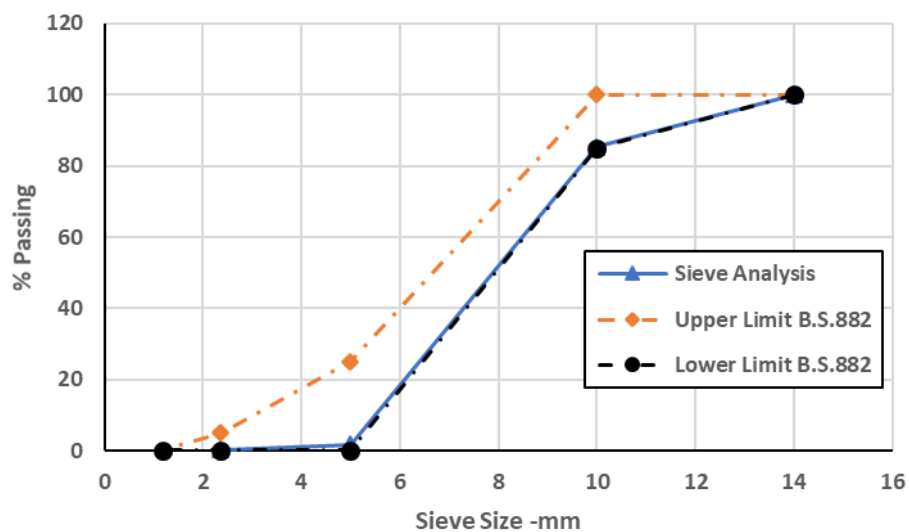


Figure 3.8: Grading of coarse aggregate and BS 882 limits

3.7.1.2 Cement

The cement used in the concrete mixes for all specimens was Portland cement (CEM 52.5 N), which complies with the requirements of BS EN 197-1 (2011). The cement was supplied in airtight bags of 25 kg; storage conditions maintained their dryness and protected them from atmospheric and humidity

effects. The chemical composition and physical properties of the cement that provided by the manufacturer are shown in Table 3.6.

Table 3.6: Chemical and physical properties of cement

Property	value	Unit	Requirements of standard
Initial setting time	110	min	≥ 45
Soundness (expansion)	1.1	mm	≤ 10
Compressive strength 2 days	27	MPa	≥ 20
Compressive Strength 28 days	58	MPa	≥ 52.5
C ₃ S	51.33	%	-
C ₂ S	21.14	%	-
C ₃ A	7.49	%	-
C ₄ AF	8.86	%	-

3.7.1.3 Fine Aggregate

River clean washed sand with a 5 mm maximum fine aggregate size was used in the casting of the specimens of this experimental work. Sieve analyses were performed to determine the grading of the fine aggregate, as given in Table 3.7. As can be seen in Figure 3.9, the grading curve conforms with the stipulated limits presented in BS 882 (1992).

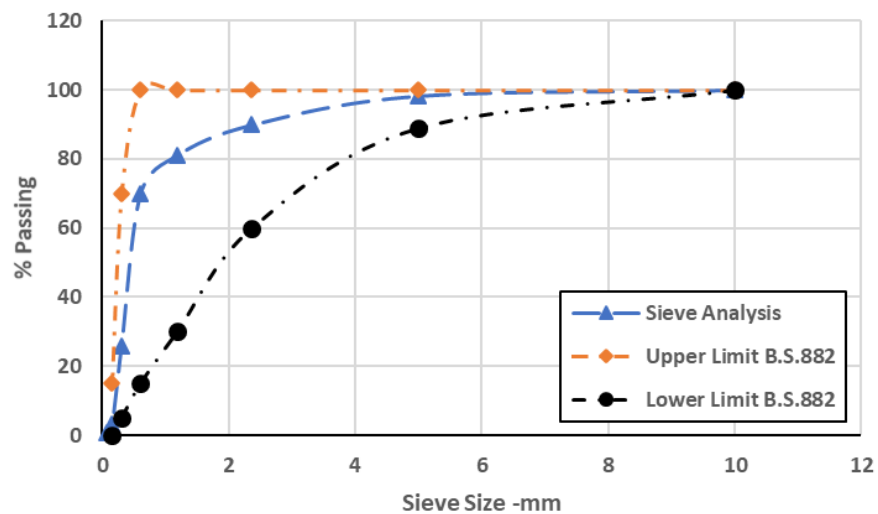


Figure 3.9: Grading of fine aggregates and BS 882 limits

Table 3.7: Particle size distribution of fine aggregates

Sieve Size (mm)	Weight Retained (g)	% Retained	Cumulative % Retained	% Passing
10	0	0	0	100
5	8.5	1.7	1.7	98.3
2.36	42	8.4	10.1	89.9
1.18	44	8.8	18.9	81.1
600 µm	56	11.2	30.1	69.9
300 µm	219.5	43.9	74	26
150 µm	114.5	22.9	96.9	3.1
75 µm	11.5	2.3	99.2	0.8
Pan	4	0.8	100	0
Total	500			

3.7.1.4 Mixing Water

Clean tap water was used for mixing and curing, in accordance with the EN BS 1008 (2002) standard.

3.7.1.5 Compressive and Tensile Strength Tests

The compressive strengths of the concrete mixes were determined according to the BS EN 12390-3 (2009) standard, where six concrete cubes of 100x100x100 mm and six cylinders of 150x300 mm were tested at 28 days for each concrete mix. The average compressive results for both cubes and cylinder samples are given in Table 3.8.

Table 3.8: Experimental results of concrete compressive strength

Mix Identification	f'_c (cylinder) MPa	STD MPa	f_{cu} (cube) MPa	STD MPa
SH-U-F	34	1.2	43.5	2.8
SH-U-C	35.5	1.8	45.3	3.5
SH-S-C-A	30	2.5	38.6	3.7
SH-S-C-H	33.8	2.7	43.2	3.4
SH-S-C-I	36.6	2.3	46.1	4.5
LN-U-C	33.7	2	42.7	4.1
LN-U-S	34.2	3	44.3	3.2
LN-S-C-H	33.4	2.8	44.2	4.3

The indirect tensile tests were performed to determine the tensile strength of the concrete samples. The indirect tensile strengths were obtained via the split cylinder test and the flexural test. As shown in Table 3.3, the concrete prisms and cylinders were tested according to EN 12390-5 (2009) and EN 12390-6 (2009) to determine the flexural and tensile splitting strengths, respectively. Two bobbins were also employed to obtain the direct tensile strength. Figure 3.10 shows the test machines that were used for the compressive and tensile tests. Table 3.9 presents the results for the direct and indirect tests, as well as the predicted tensile strengths according to ACI Committee 318 (2014) and Eurocode2 (2004). ACI Committee 318 (2014) suggested that the tensile strength (f_t) should be equal to $0.33\sqrt{f'_c}$, which represents the level of the principal tensile stresses that produce shear cracking. It can be deduced from Table 3.9 that the direct tensile results are close to the ACI code's limit. While Eurocode 2 (2004) suggest that direct tensile could be approximately determined from the splitting tensile strength multiplied by a reduction factor equivalent to 0.9. Further, Raphael (1984) found that the tensile strength values of the tested samples under direct axial loads were less than those obtained from the flexural and splitting tensile tests.

Table 3.9: Experimental results of concrete tensile strength (f_t)

Mix Identification	f_t (split) MPa	f_t (direct) MPa	f_t (flex.) MPa	ACI -318 MPa	EC2 ¹ MPa
SH-U-F	3.10	1.86	4.20	1.92	3.15
SH-U-C	3.24	2.10	4.40	1.97	3.24
SH-S-C-A	2.71	1.89	3.80	1.81	2.90
SH-S-C-H	2.90	2.01	3.90	1.92	3.14
SH-S-C-I	3.42	2.11	4.52	2.00	3.31
LN-U-C	3.04	1.73	4.40	1.92	3.13
LN-U-S	3.15	2.33	4.10	1.93	3.16
LN-S-C-H	3.07	1.92	4.00	1.91	3.11

¹ Eurocode 2 (2004) proposed a formula to calculate “the mean axial tensile strength” ($f_{ctm} = 0.3 \left(f_c^{\frac{2}{3}} \right)$)



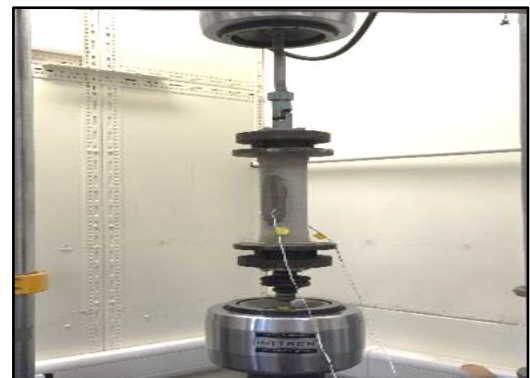
(a)



(b)



(c)



(d)

Figure 3.10: Testing Machines a) Compressive strength test b) Splitting tensile strength test c) Flexural test d) Direct tensile test

3.7.1.6 Concrete Modulus of Elasticity

The static modulus of elasticity (E_c) of the concrete was determined according to the BS 12390-13 (2013) method. Three cylinders of concrete (as described in Table 3.3) were tested for each mix, where two electrical resistance strain gauges were symmetrically fixed on the vertical sides of each cylinder, as shown in Figure 3.11. Strain readings and stresses were captured using data acquisition software, and these outcomes were used to evaluate the modulus of elasticity, based on equation 3.3. The test results are summarised in Table 3.10.

$$E_c = \frac{\Delta\sigma}{\Delta\varepsilon} = \frac{\sigma_a - \sigma_b}{\varepsilon_a - \varepsilon_b} \quad \text{Eq. 3.3}$$

Where, σ_a is the upper stress that corresponded to $\frac{f'_c}{3}$, σ_b is the lower stress that corresponded to $0.1f'_c$, ε_a is the corresponded strain reading at upper stress (loading cycle 3), and ε_b is the corresponded strain reading at lower stress (loading cycle 2).



Figure 3.11: Test of modulus of elasticity

Table 3.10: Concrete modulus of elasticity results

Mix Identification	Modulus of Elasticity at age 28 days
SH-U-F	31.6
SH-U-C	32.1
SH-S-C-A	29.8
SH-S-C-H	31.5
SH-S-C-I	32.2
LN-U-C	31.7
LN-U-S	32
LN-S-C-H	31.3

3.7.1.7 Compressive Creep Test

To identify the creep coefficients of the specimens under sustained loads, compressive creep tests were conducted. Each testing rig consisted of two concrete prisms (Table 3.3) subjected to a sustained compressive load controlled by a pre-calibrated steel tube dynamometer, as illustrated in Figure 3.12. The magnitudes of the applied loads corresponded with 20% of the samples' compressive strength at 28 days. Further, for strengthened specimen (LN-S-C-H), wrapped prisms with CFRP sheets with the same fibre ratio that was used for the specimen were tested to determine the creep coefficients.

The concrete surface strains were taken from two (opposite) sides of each prism, using a 150mm DEMEC dial gauge. The strain readings were taken before and after the application of the load to evaluate the elastic strain. The load level ($\pm 5\%$) was maintained over the tests durations by adjusting the nuts of the loading rig, while the strains were regularly measured throughout the testing period. The creep coefficient of each mix was calculated after subtracting the elastic strain and free shrinkage (measured on a duplicate control prism) from the measured total strain obtained from the loaded samples, according to Eq.3.4.

$$\varphi_c = \frac{(\varepsilon_t - \varepsilon_i) - \varepsilon_{sh_t}}{\varepsilon_i} \quad \text{Eq. 3.4}$$

Where, φ_c is the creep coefficient, ε_t is the measured total strain at time t, ε_i is the initial measured strain, and ε_{sh_t} is the free shrinkage strain at time t.



Figure 3.12: Compressive creep test

3.7.1.8 Shrinkage Specimens

For each mix, four concrete control prisms (Table 3.3) were used to obtain the shrinkage data. The prisms were exposed to drying after 28 days curing at which point drying shrinkage was recorded. Note: Two of the prisms were wrapped with CFRP sheets with the same fibre ratio that was used for the LN-S-C-H specimen; this was done on the 28th day when the curing was complete and ensured that the prisms and the joint specimen had the same drying path.

As with the loaded prism samples, DEMEC points were attached to two opposite sides of each prism using epoxy adhesive (see Figure 3.13). After curing, all prisms were stored in the control room at a temperature of 20°C (± 5) and an average R.H. of 50% ($\pm 10\%$). The ambient conditions (Temp. and R.H.) for the control room were close to the average environmental conditions of the laboratory where the tests of the beam-column joints were carried out. A hand-held dial gauge of 150 mm (Figure 3.14) was used to measure shrinkage over the test period. The ε_{sh_t} corresponded with the

average strain readings of the four prisms. There was no potential effect of the fluctuation in the ambient condition was observed; the obtained reading showed that all fluctuations in the shrinkage induced strains within the acceptable range of 5% for this test.

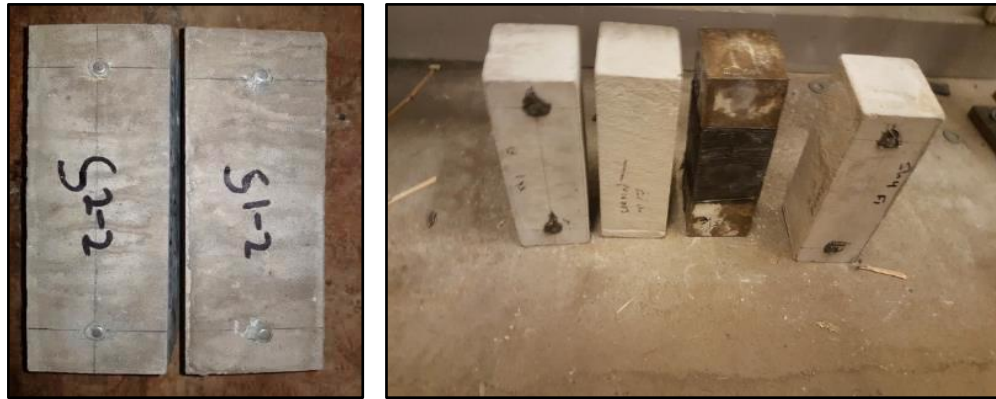


Figure 3.13: Shrinkage samples



Figure 3.14: 150 mm DEMEC gauge with calibration bars

3.7.1.9 Tensile Creep Test

The tensile creep of the concrete mixes used for the long-term tests was measured using concrete bobbins (see Figure 3.15), the details of which have been previously given in Table 3.3. Electrical Resistance Strain (ERS) gauges were glued to the specimens and a tensile stress of 1 MPa was applied at 28 days and was maintained throughout the test duration. Calibrated load cells were used to apply the load and were connected to data logger to monitor the load level. In addition, unloaded concrete bobbins were used to measure drying shrinkage. The specimens (bobbins) were cured in the fog room and thereafter were tested in the control room along with the shrinkage specimens

where the average relative humidity (R.H.) was 50% ($\pm 10\%$) and the temperature was 20°C (± 5).

A similar procedure to that used to calculate the compressive creep strains and creep coefficients was adopted to evaluate the tensile creep strains. As before, the elastic strain and free shrinkage readings were deducted from the measured total tensile strain obtained from the loaded bobbins.



Figure 3.15: Tensile creep test

3.7.1.10 Time-dependent Tests Results

The time dependent deformations of the concrete are presented in this section, as determined from the tests on the creep and shrinkage prism samples. Sample concrete prisms (eight prisms) were taken from each batch of concrete used for casting the beam-column joint specimens under sustained (constant) loads (LN-U-C, LN-S-C-H and LN-U-S) to determine creep coefficients and shrinkage data. The measured creep coefficients and shrinkage strains will be used to predict the curvature of the beams and surface strains (Chapter 5) according to Eurocode 2 (2004); these predictions were then compared with the experimental results given in Chapter 5.

Figure 3.16 shows the average compressive creep strains with time for the LN-U-C, LN-S-C-H, and LN-U-S specimens. The corresponding creep coefficients are presented in Figure 3.17. These coefficients were calculated from the experimentally measured compressive strains according to Eq. 3.4. A stress of 20% of the concrete compressive strength (f'_c) (as given in Table 3.8) was applied; this is less than the stress to strength ratio lower of 0.3,

which is the likely micro-cracking threshold (Neville et al., 1983) and should, therefore, maintain the development of creep at a decreasing rate. Similarly, Figure 3.19 shows the tensile creep strains; the tensile creep samples were subjected to a tensile stress equal to 1 MPa. This value corresponds to average stresses in concrete that can develop between cracks in the tension zone (Forth, 2015). The results obtained from the free shrinkage control samples are presented in Figure 3.18. The time-dependent Figures (3.16 to 3.19) are presented as smoothed curves in order to address any influence of the fluctuations in ambient conditions.

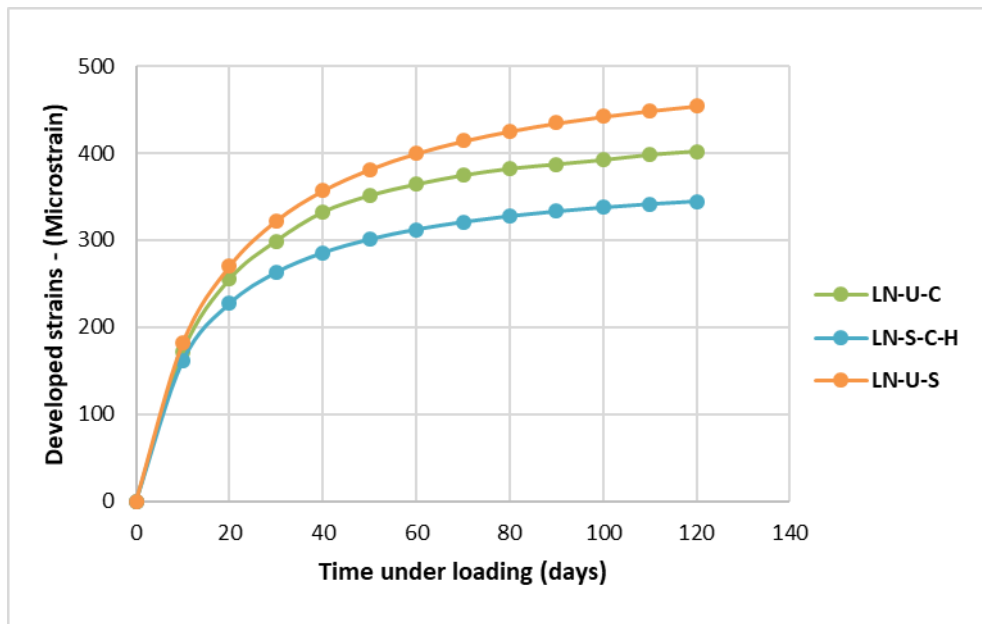


Figure 3.16: Compressive creep strains developments with time

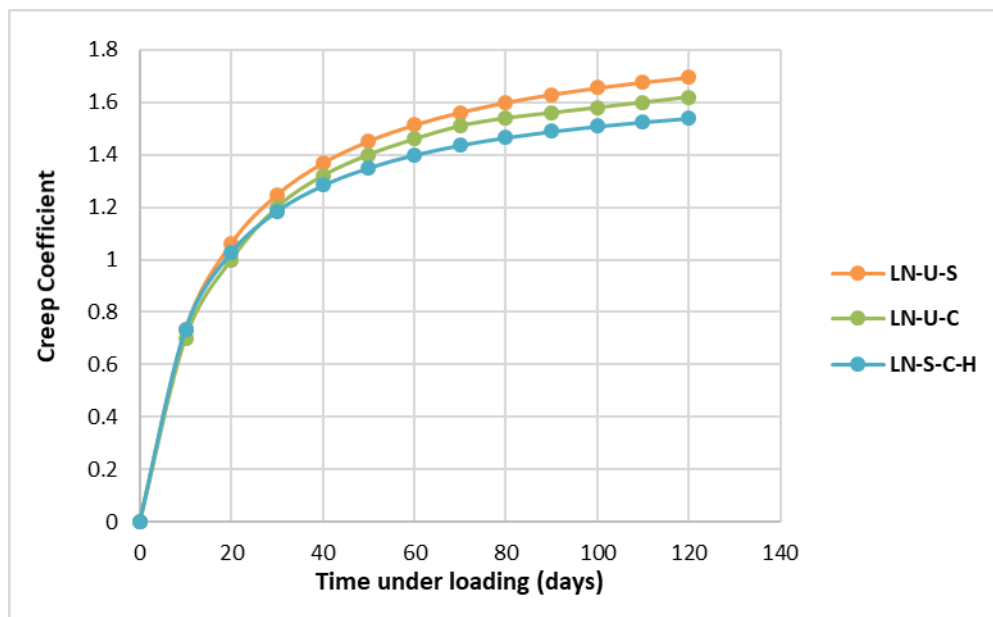


Figure 3.17: Compressive creep coefficients results

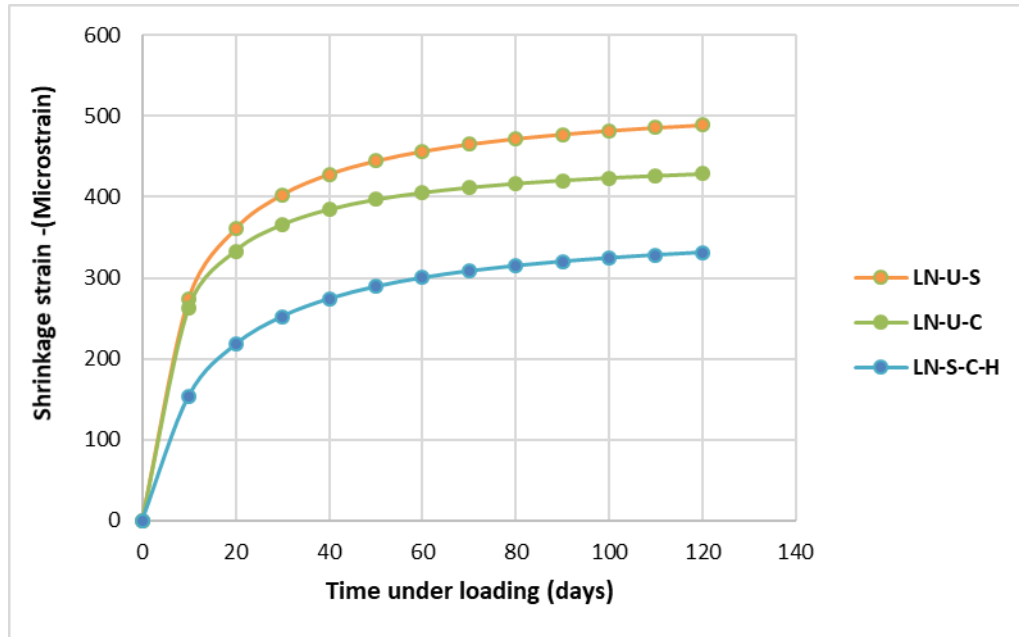


Figure 3.18: Developed shrinkage strains with time

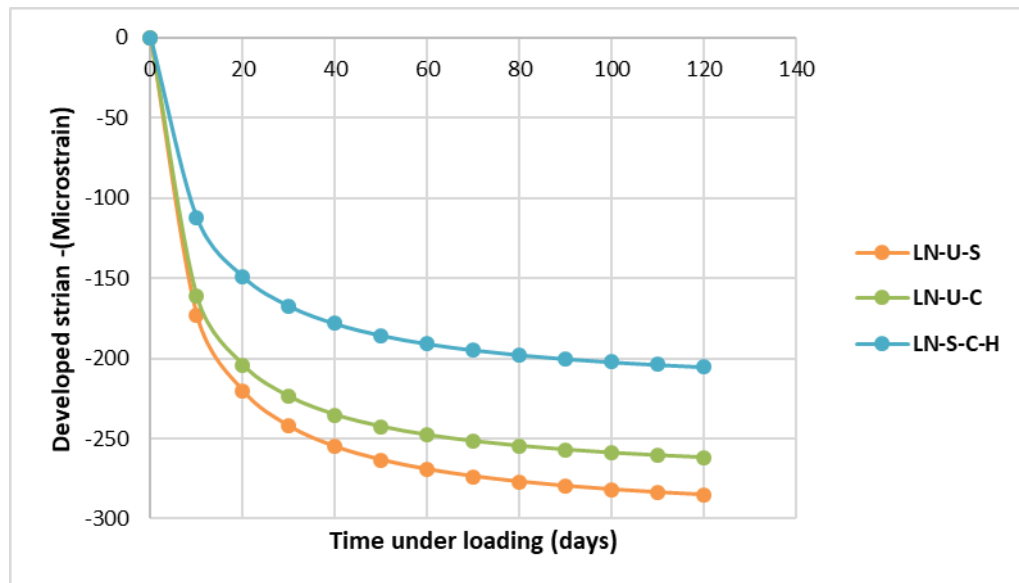


Figure 3.19: Tensile creep strains developments with time

Figure 3.16 represents the compressive creep for 3 mixes of the same concrete. After 120 days the LN-S-C-H specimen exhibited the lowest creep, being 76% of the highest creep obtained from the LN-U-S prism sample, of the factors that can affect creep (as presented in Chapter 2), mix proportion, loading age, properties of concrete materials, size and shape of members could all be considered constant. There was some variation in the

experimental ambient conditions, which could have affected the rate of moisture loss. However, a more significant effect on the latter is that prisms taken from the mixes used to cast the CFRP wrapped specimens (i.e. beams regions) were partially sealed in order to represent the larger the volume/surface (v/s) ratio of the CFRP wrapped sections and hence the slower 'evaporation' of moisture or longer drying path length in these beam-column joint specimens. Realistically, there was much less of a difference (about 12%) between the unstrengthened prism samples for both measured shrinkage and creep – this is well within the 20% error recommended by Brooks.

In terms of specific creep, tensile creep was much higher than compressive creep. The final specific tensile creep was between 3 to 4 times larger than the specific compressive creep after 120 days. This is in-line with the findings of Forth (2015). The analysis of the joint used in this investigation uses the truss mechanism where the inclined concrete strut is predominately under compressive stresses (arising from torsional shear-flow actions) during the pre-cracking stage. Hence, the compressive creep coefficients were used to evaluate the effective concrete modulus $E_{eff(t,t_0)}$ in accordance with the code model (Eurocode, 2004).

3.7.2 Steel Bars

Deformed high strength steel bars were used to reinforce the beam-column joint specimens, as shown in Figure 3.20. Sixteen-millimetre diameter ($\Phi 16$ mm) and $\Phi 12$ mm bars were used for the main reinforcement in all specimens, while $\Phi 8$ mm bars were used as the transverse reinforcement (beam stirrups and column links). Uniaxial tensile strength tests were performed on a number of steel samples – i.e. an average of three samples or more used for each rebar size, in accordance with the EN BS 10002-1 (2001) standard, with a view to identify the rebars' physical properties. The test properties of the steel rebar are given in Table 3.11.



Figure 3.20: Reinforcements detailing the beam-column joints

Table 3.11: Mechanical properties for steel bars

Bar diameter (mm)	Tensile strength (MPa)	Yield Strain	Max. Strain
16	563	0.0028	0.0053
12	565	0.0026	0.0071
8	571	0.0029	0.0079

3.7.3 CFRP Fabric and Epoxy Resin

Unidirectional carbon fibre reinforced fabrics (CFRP) of 0.22 mm thickness were employed to strengthen the beam areas using three different configurations, as described in Section 3.5. The specifications (as provided by the manufacturer) of the unimpregnated fabrics are shown in Table 3.12. A medium viscosity epoxy resin (EL2) from Easy Composites was used to attach and impregnate the CFRP fabrics. The mechanical properties of the cured EL2 epoxy resin (according to the manufacturer datasheet) are as follows: the tensile strength is 70-80 MPa, the elongation at break is 6-8%, and the modulus is 3.5-4.6 GPa.

Table 3.12: Mechanical properties of the carbon fibre sheets

Material	Property	Unit	Value
Fibre properties (unimpregnated)	Tensile strength	MPa	2530
	Tensile Modulus	GPa	230
	Strain	-	1.5%
	Density	g/cm ³	1.76

3.8 Application of CFRP Jackets.

Surface preparations and corners rounding (the radius about 15 mm) of the cured members (SH-S-C-A, SH-S-C-H, SH-S-C-I, and LN-S-C-H) were performed in order to try and avoid any stress concentrations and gaps between the CFRP laminate and the concrete (see Figure 3.21). These procedures were achieved using sand paper and a grinding machine, followed by surface cleaning, i.e., brushing, air blowing, and vacuuming to remove any dust and loose particles before the application of the CFRP sheets on the concrete substrate.

A dry layup technique was employed to reinforce the members, i.e., a priming coat with EL2 epoxy resin was applied by brush to the surface of the members; the sections were then wrapped with unimpregnated CFRP fabrics using the priming layer to adhere the wrapping. A 210 mm overlapping length of wrap was applied in the beam's transverse direction at the beam top side to prevent wrap debonding. Finally, the CFRP fabrics were adequately 'wet' with epoxy using an impregnation roller (Figure 3.21), whilst ensuring that any air bubbles or excessive resin between and through the fabrics were firmly expelled.

The dry layup method was utilised because is widely used to retrofit structures for number of reasons, (1) easy to use, (2) no need to expensive equipment such as that requires to vacuum and impregnating the fibres sheets in the case of using the wet layup method, and (3) this method can be use with different types of fibres and resins. However, any remain air voids can potentially induce cracks in the laminates; in addition, the resin proportion, impregnation, and final laminates quality are affected by the laborers skills.



Figure 3.21: Preparation and application of the CFRP sheets

3.9 Test Procedure and Instrumentation

3.9.1 Short-Term Testing Procedure

As described in the experimental plan (Section 3.4), five beam-column joints were tested under monotonic load up to failure. The load was applied to the tip of the beam for the flexural loaded specimen (SH-U-F) in order to induce bending and vertical shear forces (see Appendix C - concentric loading test setup). It was also applied at the end of a rigid steel cantilever arm for the SH-U-C, SH-S-C-A, SH-S-C-H, and SH-S-C-I specimens to produce a torque (T) in combination with flexural (M) and direct shear (S) forces, where the T/M - S ratio was equal to 1.57 to verify the efficiency of the torsional strengthening schemes under predominantly torsional loads - i.e. the applied torque was about 1.5 times larger than the combined bending moment. This was done to address the strain variations around the member sides, rebar yielding, and joint deformations due to torsional failure mode.

The length of the loading arm was 157 cm, measured from the vertical beam centreline (see Figure 3.22). A constant compressive axial load of a pre-specified magnitude ($0.1 A_g f_c'$) was applied to the column ends during the tests which represents a typical load from the upper floors of a structure, complied with the design codes (ACI Committee 318, 2014; Eurocode 1, 2002), where A_g is the column's gross area and f_c' is the compressive strength for the concrete. As discussed in the Chapter 2, this level of column load can potentially enhance the joint shear strength (Antonopoulos and Triantafillou,

2003); while buckling of the column's rebars and sudden joint's failure can be promoted under large axial loads (Shigeru Hakuto and Hitoshi, 2000). Hydraulic jacks were used to apply the loads, which were monitored through all the loading regimes via data acquisition software. For the beam's load, an average loading rate of 0.5 mm/min was employed (the load was applied under displacement control using LVDT 7) to capture the crack initiation and strain developments.

Technical instruments were used to evaluate the specimen's behaviour by measuring strains, deformations and loads. Several linear variable differential transformers (LVDT's) were employed to measure the deflection, twist angle, and the joint's deformations. Further, a number of electric resistance strain (ERS) gauges were fixed on the steel bars and CFRP sheets to capture the strain development through all loading stages. The instrumentation details are also given in this section. Figure 3.22 schematically illustrates the setup of the tests and the load application.

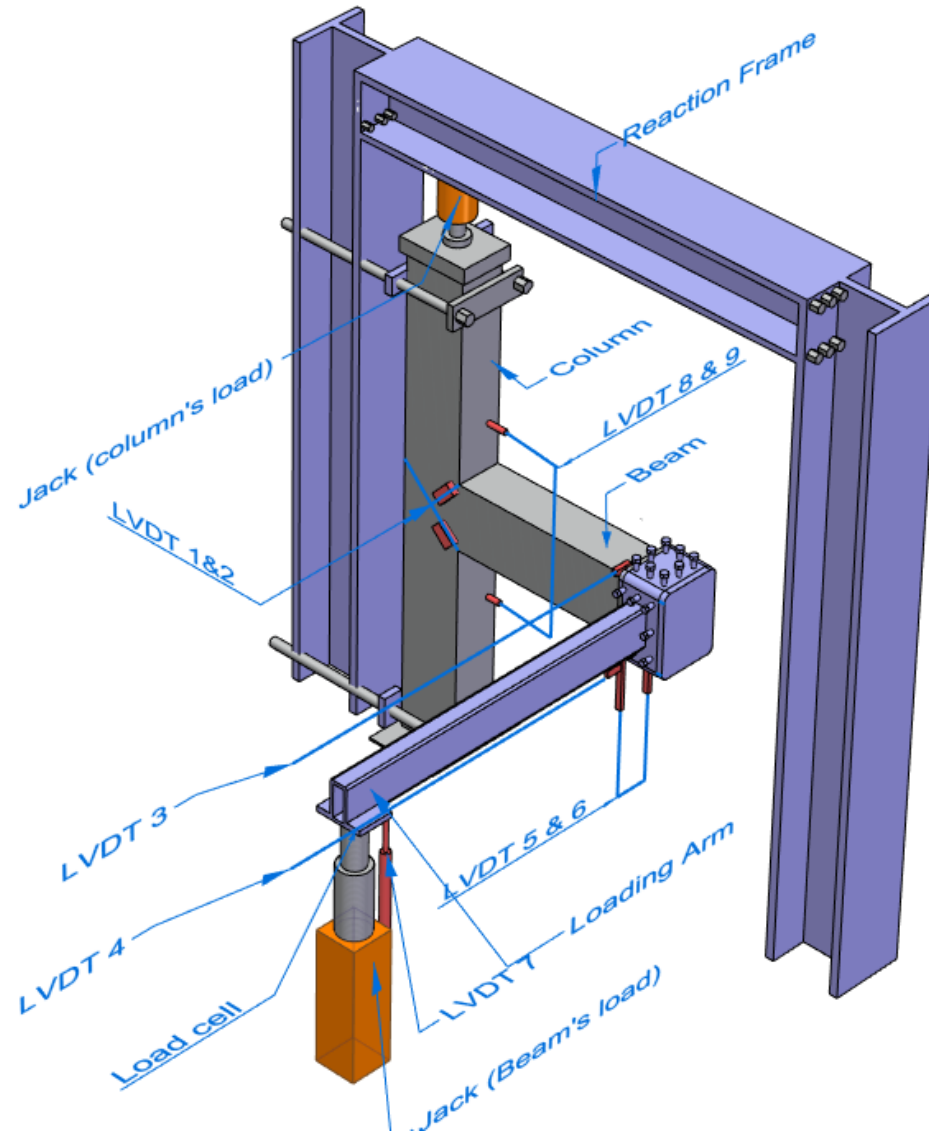
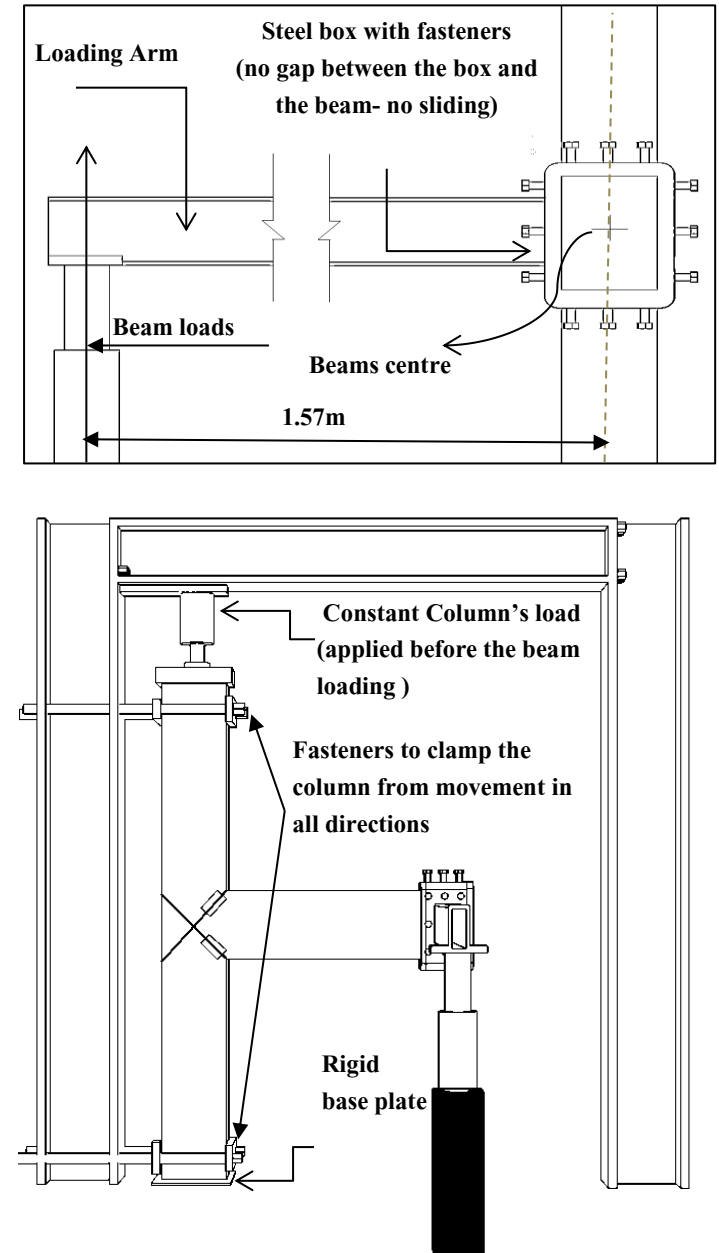


Figure 3.22: Testing schematic diagrams



3.9.2 Long-Term Testing Procedure

Three beam-column joints (LN-U-C, LN-U-S, and LN-S-C-H) were tested under a constant load for periods of no less than 90 days. The loads were applied at the end of the rigid steel cantilever arm to induce torsional, flexural, and shear forces in the LN-U-C and LN-S-C-H specimens (single loading stage- i.e. there was no change in the load value throughout the testing durations. The value of the applied loads for the specimens was about 90% of the torsional cracking load, which was predicted according to Eq. 3.5 (Hsu, 1968a). Since the predicted cracking load (T_{cr}) for specimen SH-U-C was closely matched with the experimentally observed load; where the actual (test result) and predicted T_{cr} were 11.4 and 11.47 kN.m, respectively.

$$T_{cr} = (1 + 0.04\rho_t)T_{Uc} \quad \text{Eq. 3.5}$$

Where,

T_{cr} = cracking torque (kN.M)

ρ_t = the total volume percentage of the main and transverse reinforcements

T_{Uc} = the torsional capacity of plain concrete sections according to Eq. 3.5.1 (kN.M), which corresponded to St. Venant theory

$$T_{Uc} = [6(b^2 + 10)h \sqrt[3]{f'_c}] \times (112.98 \times 10^{-6}) \quad \text{Eq. 3.5.1}$$

b = the width of the beam (in)

h = the total depth of the beam (in)

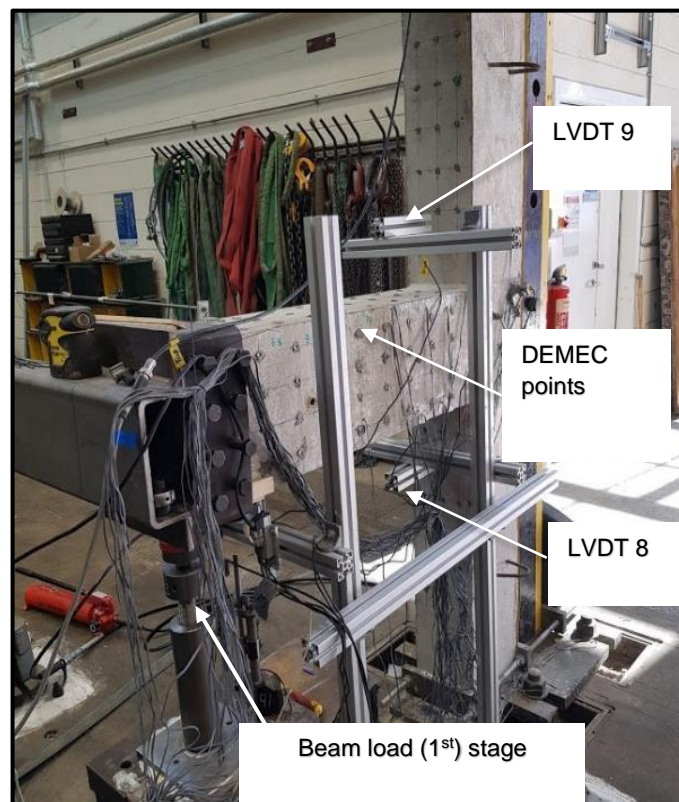
f'_c = the cylinder's compressive strength of concrete (psi)

Two consecutive loading stages were considered for the LN-U-S specimen; the first stage applied a constant load to the end of the beam (see Figure 3.23) which was 30% of the beam's bending capacity- about two times of cracking bending moment. This load was set to investigate the long-term flexural behaviour of the joint members in terms of the pattern of the cracks, the crack widths, and the strain variations due to creep and shrinkage. The steel cantilever loading arm was supported from the end of these specimens and kept horizontal to avoid any torsional loads resulting from the arm's self-weight. This was achieved using two LVDT's which were placed at the ends of the arm to ensure the loading arm was constantly level during the 1st stage.

The second stage began after 65 days of concentric loading (bending and direct shear imposed at the beam's tip) when, at this stage a torsional force was applied to the end of the beam via the steel cantilever loading arm. The 2nd stage took 100 days and examined the influences of torsional creep on the

strain and cracking developments. All loads were manually applied using jacks.

In a similar manner to the short-term testing procedure, a number of ERS gauges and LVDT's were used. While DEMEC points were also placed on the surface of the beam in order to measure the strain levels on the concrete surface. Initial readings of the surface strains were obtained during the pre-load stage before applying the sustained loads at age 28 days. After applying the sustained loads, the cracks observations, surface strain readings were recorded daily for the initial two weeks, and in the next two weeks, the strain readings and widths of existing cracks were taken twice in a week, and after that, once a week throughout the testing durations. However, the monitoring of the specimen's surfaces was performed every day to detect of new visible cracks. Accordingly, the cracks were measured using a crack width microscope along each crack and the largest crack width was quantified. The all specimens were tested in the laboratory which the average ambient conditions for the laboratory were close to for the control room (an average temperature of 20°C and an average R.H. of 50%) where the creep and shrinkage samples were tested (see Figure 3.24).



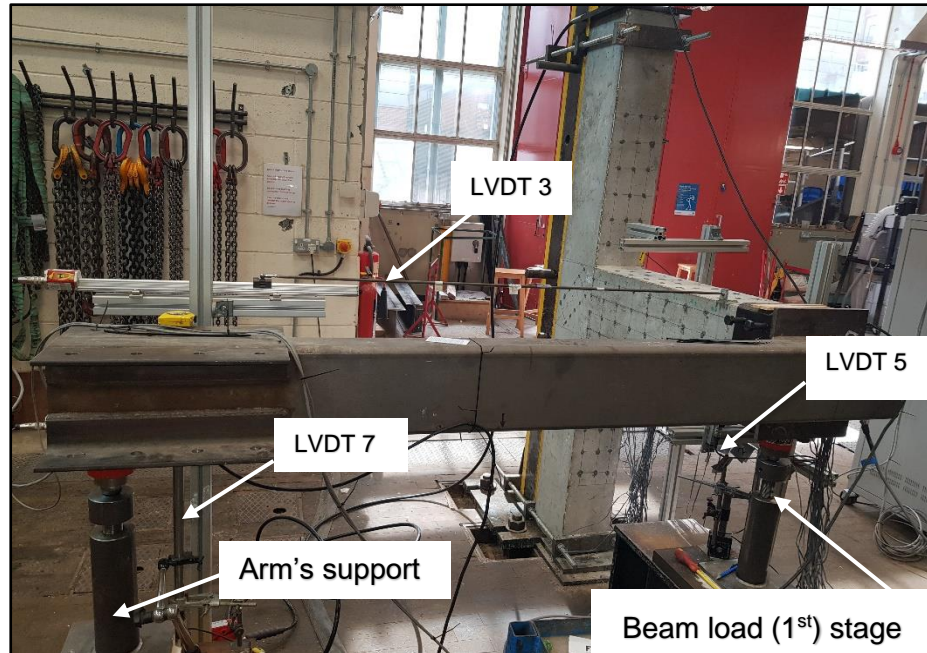
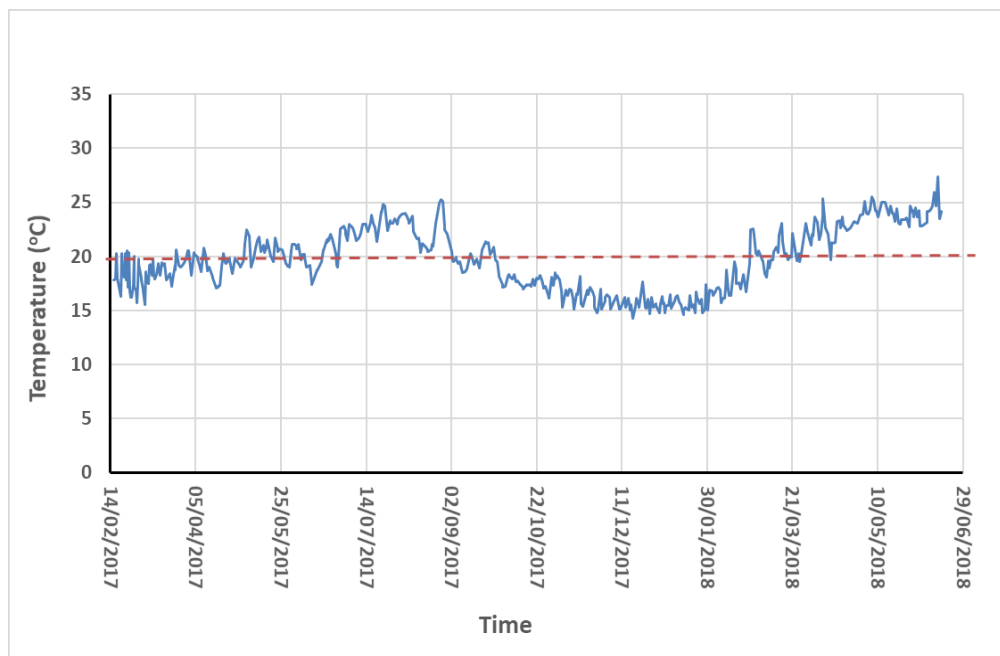


Figure 3.23: Test setup for two consecutive loading stages



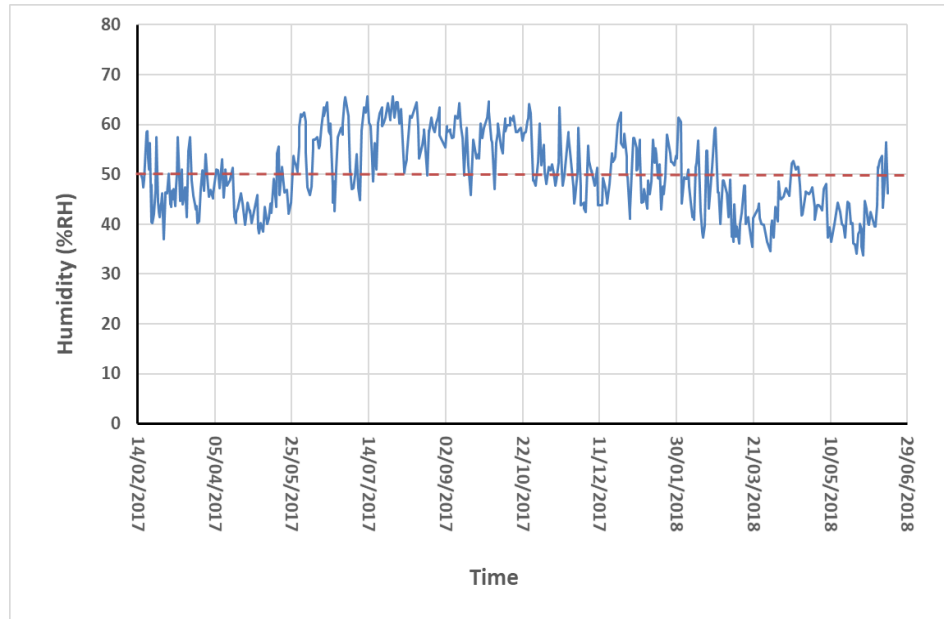


Figure 3.24: Environmental conditions of the laboratory

3.9.3 Electrical Resistance Strain (ERS) Gauges

Different sizes of metallic foil strain gauges (2, 5, 30 mm) were used to measure the strain at the surface of the CFRP wrap, the steel bars, and the concrete surfaces of the joint specimens. Before attaching the gauges, the surface of the steel rebar had to be prepared. This involved smoothing the steel rebars using sand paper, then cleaning the surface with a chemical substance (acetone). For the concrete mounted ERS gauges, a thin layer of epoxy adhesive was applied to the concrete prior to surface finishing with sand paper. The gauges were then bonded in their intended positions using a glue (CN cyanoacrylate) and connected to the data logger with special wires. Also, the ERS gauges were attached to CFRP wraps along the fibres direction by using a thin layer of epoxy adhesive with fast hardener (EL2).

Electrical resistance strain gauges were placed on the beam's main bars at 100 from the column face, while they were placed on the beam stirrups a distance of 200 and 450 mm away from the column face. Further strain gauges were fixed to the top main beam bars at the mid of the column and at the mid-height of the links in the joint regions. They were also located on the

column bars, 100 mm above and below the joint boundaries, as shown in Figure 3.25.

Further ESR gauges were attached on the beams rebars to capture strain developments induced by sustained load (long-term testing mode). Figure 3.26 shows the locations of these embedded ESR gauges in the beam's regions, where they are placed at different zones that range from a zone under high flexural stress (near the column face) to a zone under low flexural stress close to the beam's end. Also, within each zone, the gauges were mounted on the main rebars to capture strain variation around the beam's face due to the torque actions combined with flexural and direct shear forces.

For each strengthened specimen, three 2 mm ESR gauges were placed on the pre-cured CFRP sheets at 250, 450 and 650 mm from the column face (see Figure 3.27), where a thin layer of epoxy was applied on the laminate's surface. Before the bonding of ESR, final surface cleaning preparation is performed with a liquid conditioner and followed by applying a neutralizing liquid. The conditioner was used as a mild etchant and to accelerate the cleaning process. The neutralizing liquid was used to neutralizes any chemical reaction produced by the conditioner in which provides an optimal surface condition for ESR gauge to be glued on the CFRP's surfaces. The bonded ESR gauges were aligned to the fibres directions (e.g. ESR's were orientated at 90 and 45 degrees from the beam's longitudinal axis and glued to the vertical and 45° inclined strips, respectively).



Figure 3.25: Position of steel strain gauges

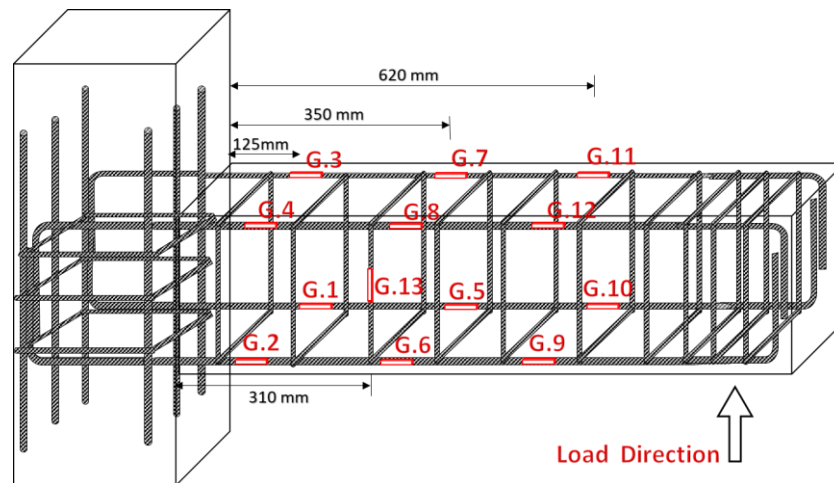


Figure 3.26: Strain gauge positions for long-term specimens

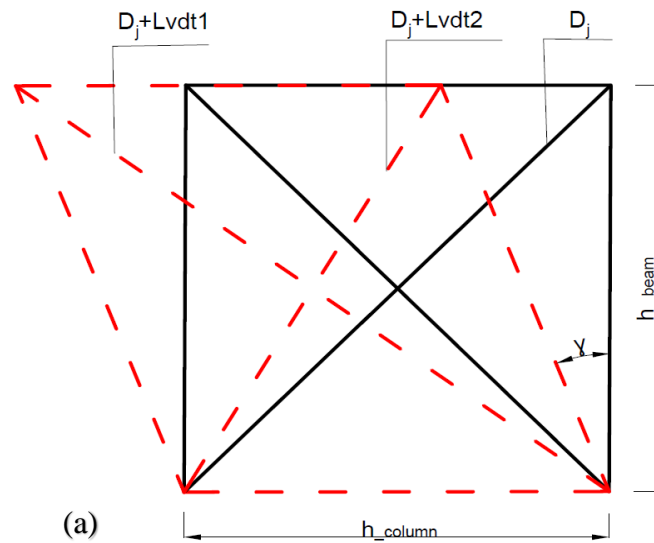


Figure 3.27: CFRP strain gauges

3.9.4 LVDT's

Several Linear Variable Displacement Transducers (LVDT's) were employed to measure the displacements and the twist angles of the beam-column joint specimens. LVDT's 1 and 2 were placed at the mid height of the column (joint distortion angle), LVDT 7 with the load cells (monitor the loads) and LVDTs 3 to 6 at end of the beams (deflection and twisting angle), LVDTs 8 and 9 on the columns (above and below the joint panels and near supports) to check the column's rotation, as shown in Figure 3.22. The LVDT's were calibrated before each test.

Two diagonal LVDT's (1 and 2) were fixed with aluminium brackets glued to the joint surface, as shown in Figure 3.28b. These measured the joint's average shear distortion angle (γ) by adopting a similar procedure that was used by Almusallam and Al-Salloum (2007); Sasmal (2009). A schematic diagram below (Figure 3.28a) illustrates the deformed shape of the joint, where the shear distortion angle (γ) was derived according to Pythagoras's theorem, as given in Equations 3.6 to 3.8.



(a)



(b)

Figure 3.28: a) Schematic diagram of the joint deformation b) Diagonal LVDT's

$$(D_j + LVDT_1)^2 - (h_{column} + \delta_h)^2 = (D_j + LVDT_2)^2 - (h_{column} - \delta_h)^2 \quad \text{Eq.3.6}$$

$$\delta_h = \frac{(2D_j + LVDT_2 + LVDT_1)(LVDT_1 - LVDT_2)}{4 h_{column}} \quad \text{Eq.3.7}$$

$$\gamma = \frac{\delta_h}{h_{beam}} \quad \text{Eq.3.8}$$

Where, D_j is the length of the joint diagonal, $LVDT_1$ and $LVDT_2$ are the change in length of the diagonals in mm, h_{column} and h_{beam} are the depth of the column and the beam in mm, respectively, δ_h is the deformation of the joint in mm, γ is the shear distortion angle in radians.

3.9.5 DEMEC Points

DEMEC studs were used to measure the surface strain of the concrete. The DEMEC points were glued along the length of the beam (long-term series), equally spaced at 100 mm and starting 5 mm from the face of the column of each row. Four rows of DEMEC points were fixed to the beam's sides at levels of 42, 114, 186 and 258mm, measured from the top of the beam (see Figure 3.29). A further three rows of points were glued to the top and bottom faces of the beam at levels of 42, 105, and 168 mm measured from the beam's side (see Figure 3.30). This allowed the strain due to torsion to be measured around the beam.



Figure 3.29: DEMEC points on the beam's sides



Figure 3.30: DEMEC points on the beam's bottom and top

3.10 Summary

This chapter has presented the methodology that was adopted during the experimental programme. This program aims to investigate the short and long-term behaviours of RC beam-column joints under combined loads which set out to quantify the interaction between torsion, flexure, and direct shear on the members' deformation, cracking history, failure and ductility levels. By incorporating three effective wrapping schemes using CFRP sheets, the testing program has considered changes to the joint demands, from the changes to the beam rebar strains at the column face and the joint's distortion levels. The time-dependent deformations and strain variation in the specimens was also monitored. The beam-column joints' details, geometries, materials used, jacketing and testing procedures have been described. The supplementary samples, casting, curing, test types along with the instrumentation used have also been presented. Following on from this chapter, the results of the short and long term experimental tests are described and discussed in Chapters 4 and 5, respectively.

Chapter 4 Short-Term Tests: Results and Discussion

4.1 Introduction

The results of the short-term tests for beam-column joints specimens that were subjected to monotonically increasing loads are discussed in this chapter. This series of tests involved five beam-column joints utilising two different loading conditions (either flexural and shear or combined with torsion) and three wrapping schemes (as all of which were described in Chapter 3). For each test subjected to flexure and shear only, the beam end deflection was monitored throughout all loading stages, and the maximum loads were recorded. For the beam-column joints subjected to combined forces including torsion, twist angles were also measured using LVDTs positioned at the beam tip. The rebar strain at critical regions of the beams and columns are also presented and discussed. In addition, (i) the CFRP strain levels for each strengthening scheme are provided and discussed; (ii) the propagation and crack patterns are discussed in relation to the level of load and strengthening type; and (iii) the ductility levels, joint distortions angles, and plastic hinge locations are presented. The failure modes and the parameters that affected the members' deformations and capacities are subsequently identified and comparisons are made with the interaction formulas presented in Chapter 2.

4.2 End Beam Deflection and Twist angle

In this section, the end beam deflections and twist angle variations of the control (SH-U-F and SH-U-C) and strengthened beam-column joints (SH-S-C-A, SH-S-C-H, and SH-S-C-I) are presented; the effects of the torsional forces and their interaction with the flexural and shear loads are investigated.

As deduced from the literature survey (Sections 2.2.1 and 2.2.2), the torsional forces produce tensile stresses in the beam's chords (top and bottom rebars). Hence, the yielding of rebars can occur either in the section's bottom (Mode-1), top (Mode-2), one side, or all sides (Mode-3) at different regions along the beam's length, depending on the ratio and direction of torsion, bending, and direct shear. Correspondingly, to determine the mode of failure at a region near to column's face (affect joint's demand and level of damage), a set of interaction formulas (Hsu, 1993; Thurlimann, 1979; Elfgren, 1972) have been utilised in this study to predict the member capacities under combined forces (Section 2.2.2). The ultimate carrying capacity that was experimentally

obtained for each beam-column joint is compared with the predicted peak load, as calculated according to Eq.2.2a (Mode-1) and Eq.2.2b (Mode-2).

Near to the column faces, the tests results is expected to correspond to Mode-1, due to the high strain levels caused by the superposition of the flexural and torsional tensile forces. In the top rebars (Mode-2), flexural compression forces counteracted the torsional tensile forces, hence minimising the strain in the beam's compression rebar (considerably at the column's face). While these compression forces were insignificant near to the beam's tip -away from the flexural plastic hinge region. Mode-3 (Eq. 2.2c) predominates in members subjected to substantial shear stresses; this mode did not apply in this experimental plan. All rebar strains will be discussed later.

In order to apply Eq.2.2a and Eq.2.2b, the nominal member strengths under pure torsion (T_{uo}), bending (M_{uo}), and shear (V_{uo}) all need to be evaluated using Eq.4.1 to 4.3 and which have previously been shown in Chapter 2 (Section 2.2.2). The torsion and shear formulas are based on the truss mechanism and they are applicable for sections that the yielding of the rebars occur before any failure in the concrete struts. For the strengthened beams, the nominal torsional strength was modified in this study in order to incorporate the fibre contributions (T_{uFRP}), which were computed according to Eq.2.4 using superposition.

$$M_{uo} = A_s f_{yl(bot \text{ or } top)} d_v \quad \text{Eq.4.1}$$

$$T_{uo} = 2A_o \sqrt{\frac{2A_{l \text{ top}} f_{yl \text{ top}} A_t f_{yt}}{P_h S}} + T_{uFRP} \quad \text{Eq.4.2}$$

$$V_{uo} = 2d_v \sqrt{\frac{2A_{l \text{ top}} f_{yl \text{ top}} A_t f_{yt}}{dv S}} \quad \text{Eq.4.3}$$

Where;

A_s = area of longitudinal reinforcement either in the bottom (Mode-1) or the top (Mode-2) of the beam

$A_{l \text{ top}}$ = area of longitudinal reinforcement in the top of the beams

$f_{yl \text{ top}}, f_{yl \text{ bot}}$ = tensile strength for top and bottom rebars, respectively

A_o , P_h = area and perimeter of shear flow zone calculated according ACI 318 code (Table A.1- Appendix A)

A_t = area of transverse reinforcement (stirrups)

f_{yt} = tensile strength of the beam stirrups

d_v = lever arm length between top and bottom rebars

S = spacing between stirrups centre to centre

4.2.1 Influence of Torsion

Figures 4.1a and 4.1b show the beam-end deflection curves for the unstrengthened specimens, SH-U-F and SH-U-C, respectively. The deflection curve for the SH-U-F sample, which was concentrically loaded to produce only flexural and shear forces, reveals that the rate of displacement increased after the yield of the beam bottom rebars at a load of approximately between 50 to 55 kN (more details about rebars strains are given in Section 4.5). The specimen showed a nonlinear response beyond the cracking load (about 22 kN). Tension failure mechanisms were identified, in which large plastic deformations in the rebar caused severe flexural cracks (Figure 4.2a) in the beam tension zone. Where significant increases of the beam's cracks widths were observed in a region near to the column's face (the plastic hinge region) beyond 50 kN. Prior to failure, a crushing of concrete was observed in the beam's top adjacent the column's face (the flexural compression zone-see Figure 4.2a), followed by ruptures of the beam's bottom rebars- i.e. the flexural plastic hinge region. The ultimate carrying capacity is very closely predicted (see Figure 4.1a) based on the flexural sectional analysis presented in the ACI 318 code using the measured tensile strength of the rebars (Table 3.11).

In contrast, Figure 4.1b shows a severe decline in load capacity (83%) for the SH-U-C sample when compared with the SH-U-F sample. The reduction in load capacity of the SH-U-C specimen is not surprising due to the presence of the applied torsional force which has clearly dominated here. Inclined cracks propagated around the beam after the cracking load of 7.6 kN and near the failure load, significant damage was observed in the form of very large cracks and spalling of concrete, which extended through the beam region at around 300 mm away from the column face, as well as near the loading arm at the end of the beam. These cracks and concrete damage (Figure 4.2b) were formed in the regions of significant plastic deformations induced in the rebars (transverse and main rebars). Since a beams with adequate ductile failure induced a torsional plastic hinge at a zone with a large concentration of torsional rotation- a beam twisting (Lopes and Bernardo, 2009), as shown in Figure 4.2b . This agrees with similar observations reported by Peng and Wong (2011) and Tirasit and Kawashima (2007) (as described in chapter 2), and illustrated how torsion can alter the plastic hinge location.

The beam twist angle (ψ) for the SH-U-C sample is plotted against applied torque in Figure 4.3. It can be observed that the beam rotation behaviour exhibited three different stages during loading: a linear elastic stage, a non-

linear post cracking stage (ascending) and a non-linear failure stage (descending). The linear elastic stage represents the concrete behaviour up to the cracking torque (11.4 kN.m), with a relatively high twisting rigidity that agrees with St. Venant's theory. After cracking, a non-linear increase in the beam's rotation with a lower twisting rigidity can be observed up to the peak load. The mechanism during this stage can be quantified according to the space truss analogy, as described in Appendix-A. After the peak load, the third stage involves a progressive decline in the member's stiffness and strength due to softening of the concrete struts and large plastic deformations in the beam rebars.

As mentioned earlier, the beam bottom rebar near the column face, which represents the flexural plastic zone, exhibited higher strains than those found in the top reinforcement (obtained strain data are presented in Section 4.5). This was due to the combination of torsion and bending moments that corresponds to a Mode-1 failure - yielding in the beam's bottom rebars (Figure 4.2b). From Figure 4.1b, it can be seen that the predicted ultimate load, according to Eq.2.2a, agrees well with the maximum value obtained from the SH-U-C test. This reveals that the capacity of the truss elements (e.g. steel rebars as equivalent ties and the concrete as an equivalent strut) was fully mobilised up to the peak load. After the peak load, severe degradation (softening) took place in the concrete strut as its strength reduced and the transverse reinforcement yielded corresponded with the levels of the principal compressive and tensile stresses that acted on the diagonal struts. These principal stresses related to the magnitude of the applied torsion and shear. However, Figure 4.1b showed an over-estimation of the peak load, according to Mode-2 (Eq.2.2b). This over-estimation indicates that the level of the applied torque did not cause yielding in the top rebars at the peak flexural compression zone which this agrees with minimal strain reading observation (Section 4.5).

The shift of the plastic deformation in the beam's rebars and concrete damage away from the column face and into the beam region as shown in Figure 4.2b (i.e., away from the flexural dominated zone which is often close to the column face) can possibly happen due to two effects. First, the variation of flexural stresses along the beam's length (e.g. maximum at column face) can promote yielding of the main reinforcement in the weaker chords (top rebars) that accompanied with severe cracks corresponding to level of plastic deformations in the steel rebars, where torsional forces dominate (e.g., low

bending to torsion ratio) such as the beam zones furthest from the face of the column. Secondly, at the column face, a considerable amount of beam shear is transferred into the column by the inclined concrete struts, which reduces the stress and strain levels in the stirrups located close to the column. In fact from the test it can be seen that larger shear deformations were observed in other beam's regions further away from the beam end, where the beam sides were severely damaged (Figure 4.2b).

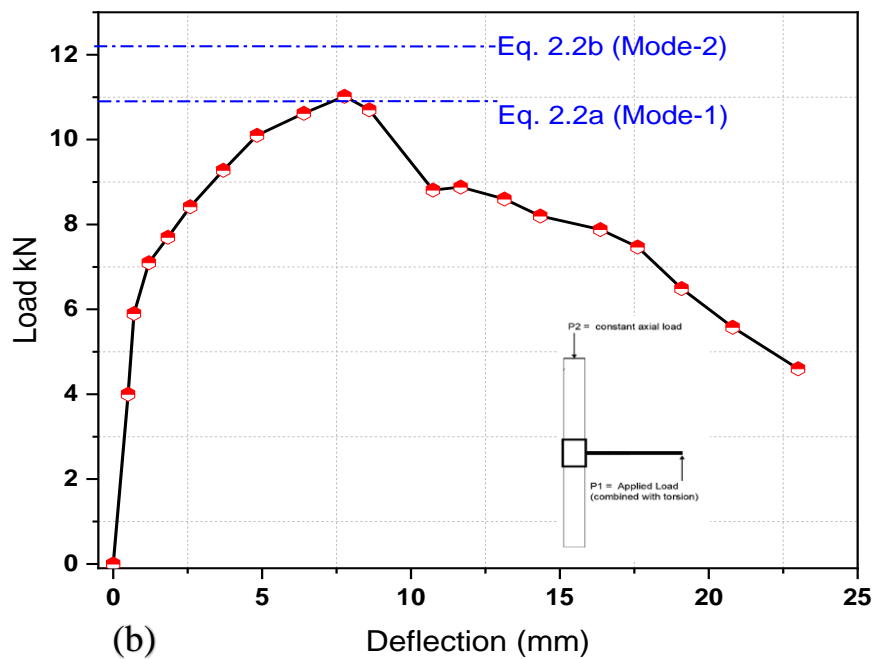
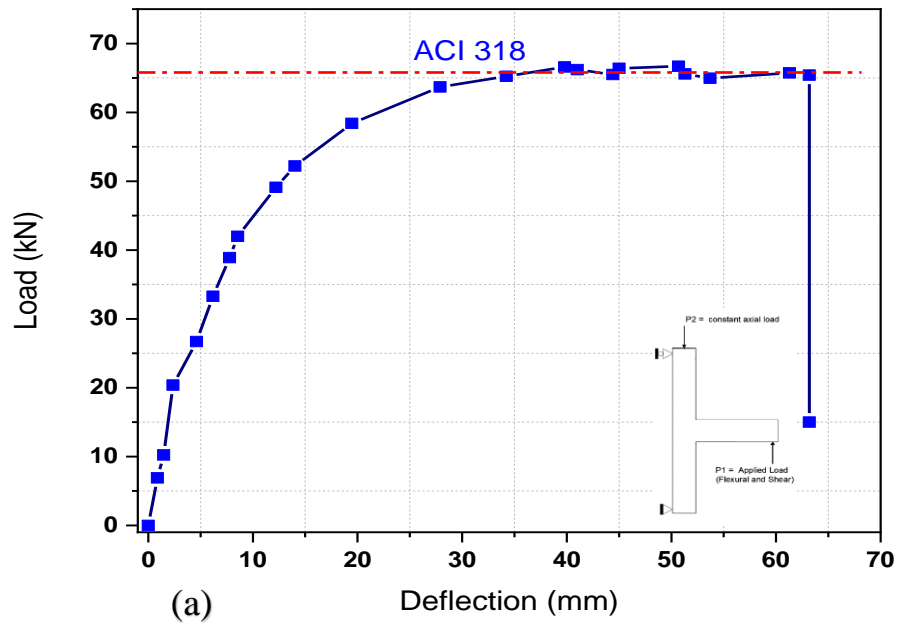
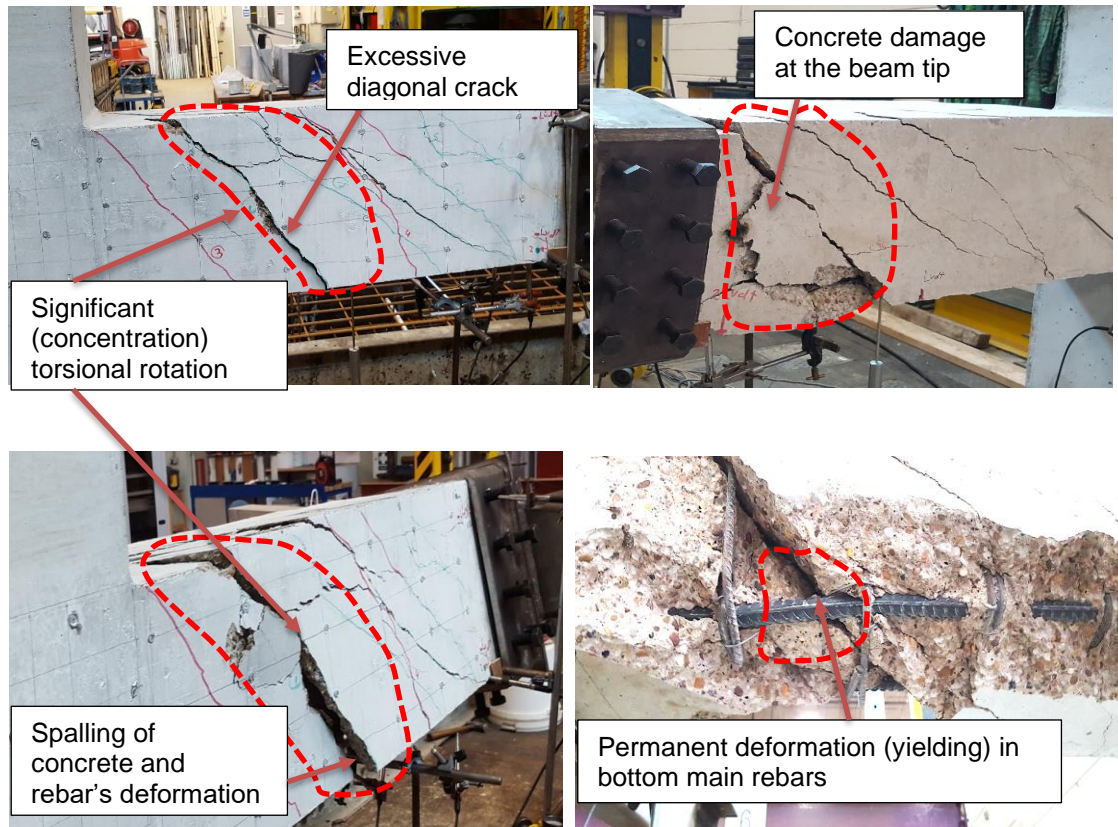
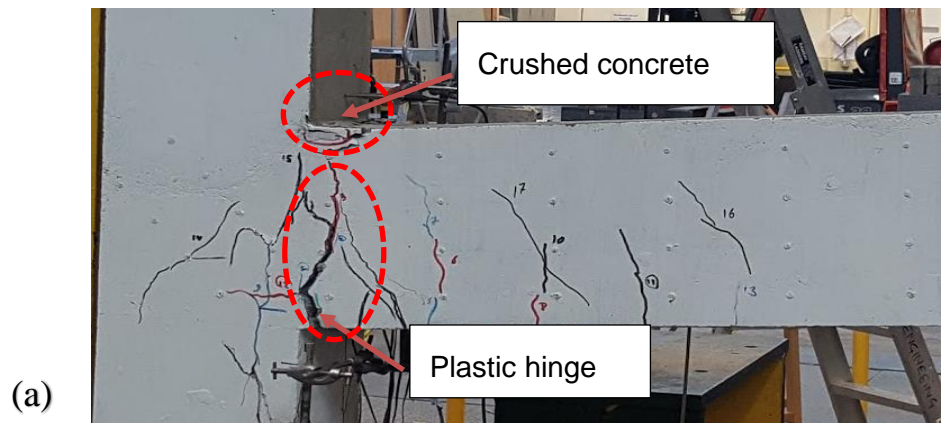


Figure 4.1: Load - end beam deflection (a) for SH-U-F sample (b) for SH-U-C sample



(b)

**Figure 4.2: SH-U-F and SH-U-C specimen failures (a) under flexural actions
(b) under combined actions**

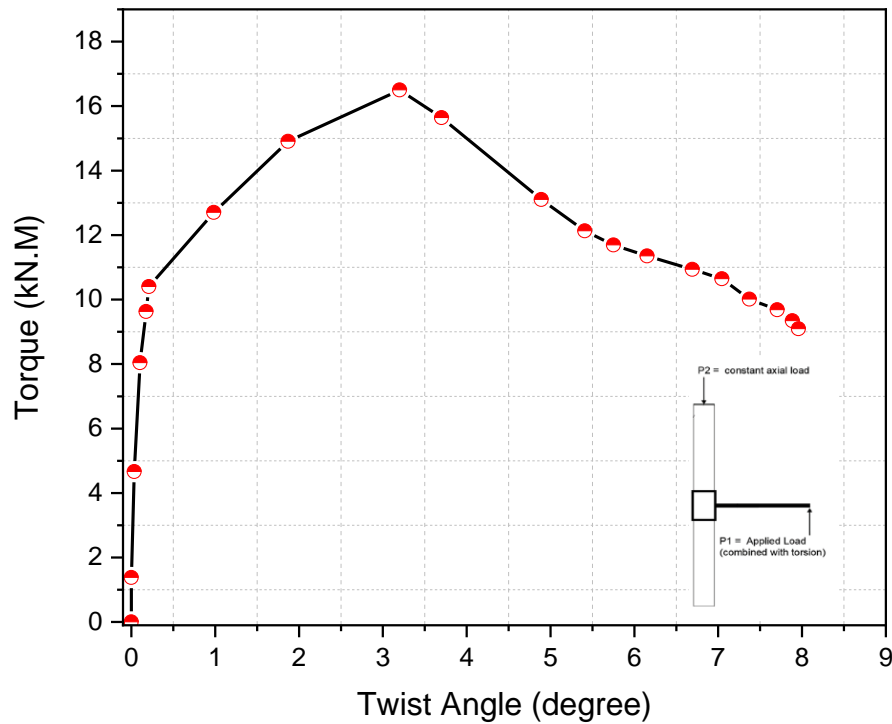


Figure 4.3: Torque-twist diagram for SH-U-C specimen

4.3 Effect of Torsional Strengthening Schemes

Figure 4.4 shows the effects of the different CFRP wrapping schemes on the strengthened specimens' behaviour. When compared with the SH-U-C, it is noticeable that the increase in load capacity is proportional to the increase in the wrapping-fibre ratio (ρ_f), as the fully wrapped specimen (SH-S-C-A) attained the maximum load levels (Figure 4.4 a, b, c, and d). Various enhancements to the cracking strengths (T_{cr}) were observed; these observations were more noticeable at the peak torques (T_u). The following section discusses in greater detail the behaviour of each strengthened member, fibre contributions, and the factors that affected the failure mode.

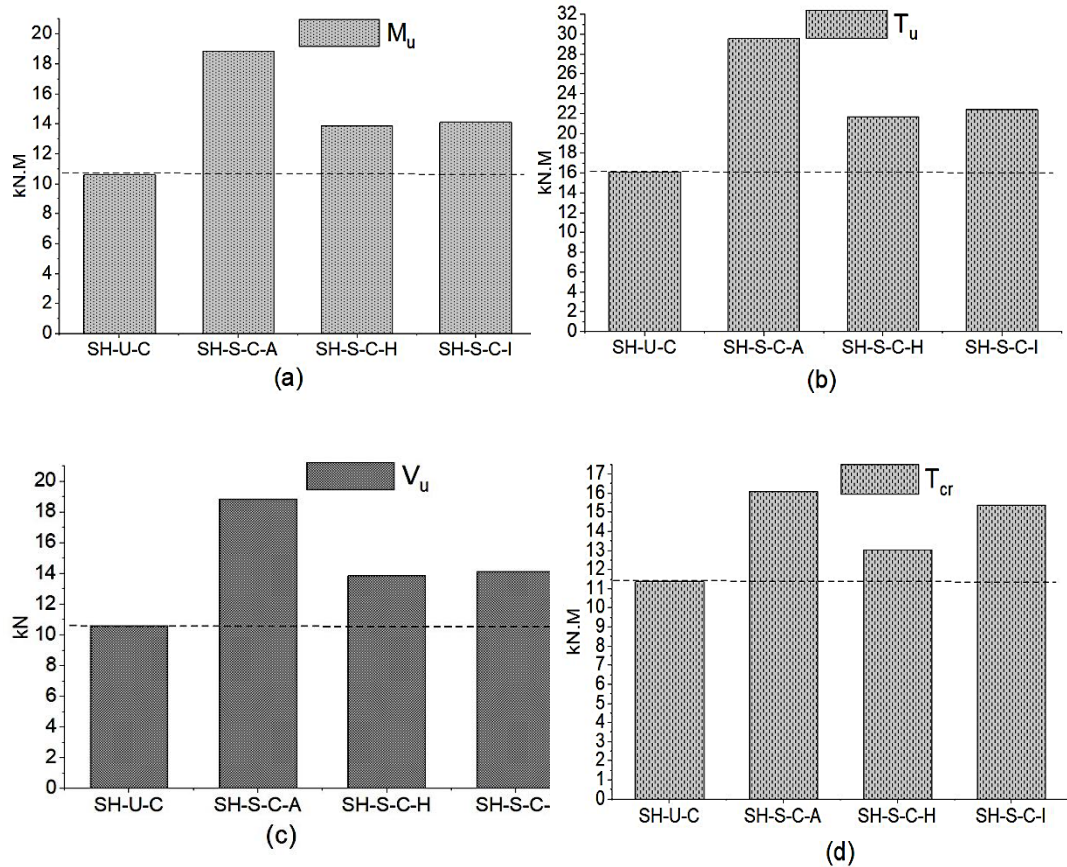


Figure 4.4: Peak capacities (a) Ultimate bending moment (b) Ultimate Torque (c) Ultimate vertical shear (d) Cracking Torque

4.3.1 Full Continuous Wrapping Scheme

Figure 4.5 shows the load and end beam deflection of the SH-S-C-A specimen compared with the SH-U-C specimen. A significant difference from the SH-U-C specimen can be noticed after the cracking load, as the SH-S-C-A specimen showed a linear increase in the load capacity up to the peak load, which corresponds to the elastic behaviour of the CFRP wraps and the confinement pressure that can be produced by full jacketing up to the rupture of the CFRP occurred. No damage was seen throughout the loading stages up to the peak load. These continuous transverse CFRP wrappings (90° oriented fibres) appreciably reduce the stresses and level of deformations induced in the beam stirrups. Also, enhance the strut's resistance by decreasing the softening of the concrete and confining the concrete. However, a sudden brittle failure was observed shortly after the peak load as the fibres ruptured and the concrete was crushed. Although crushing (spalling) of the concrete

was observed at failure, the concrete damage was concentrated to a region which extended from close to the column face to about 400 mm from the column face (Figure 4.6). This concrete damage was occurred in a region under relatively high bending moment, where the flexural compressive forces intensified the concrete strut forces that were already induced from both the torsion and shear actions. In compare with the un-strengthened specimen (Figure 4.2), the full wrapping promoted the beam damage to be extended to the column face. While no damage was noticed at the beam's tip near to the loading arm. In addition to an increase in the rebars strain levels at flexural plastic hinge zone near the column face (Section 4.5). In relation to this rise in strain levels, visible cracks were observed in the joint region (shortly before the peak load) along with increasing in the joint distortion angle as presented in Section 4.6

Due to the sudden failure and the complete loss of the beam's strength, it is important to assess the ductility of each specimen. Further details of this are provided in Section (4.4). According to Eq.2.2a, the predicted carrying capacity was slightly over (by 2%) the experimentally recorded peak load. While, according to Eq. 2.2b (yielding of the top rebars), the predicted torsional strength was significantly larger than those experimentally observed or obtained from Eq. 2.2a (Mode-1). As the ultimate measured strain in the bottom rebars (Figure 4.13b) was closer to the yield strain than those in the top rebars (Figure 4.13c). This difference reflects the influence of the rise in the bending moment load (Figure 4.4a) which was reduced the tensile forces in the beam top chords (flexural compression zone) and so it in no way approached a Mode-2 failure.

As shown in Figure 4.4, full wrapping (SH-S-C-A) produced the maximum torsional strength in comparison with other employed schemes (Sections 4.3.2 and 4.3.3), with an increase in post-cracking capacity of up to 83%. Also, an increase of 41% in the pre-cracking capacity was obtained. This significant rise in the loading capacity is in line with the previous research (Ameli et al., 2007; Chalioris, 2008; Ghobarah et al., 2002; Zhang et al., 2001; Panchacharam and Belarbi, 2002).

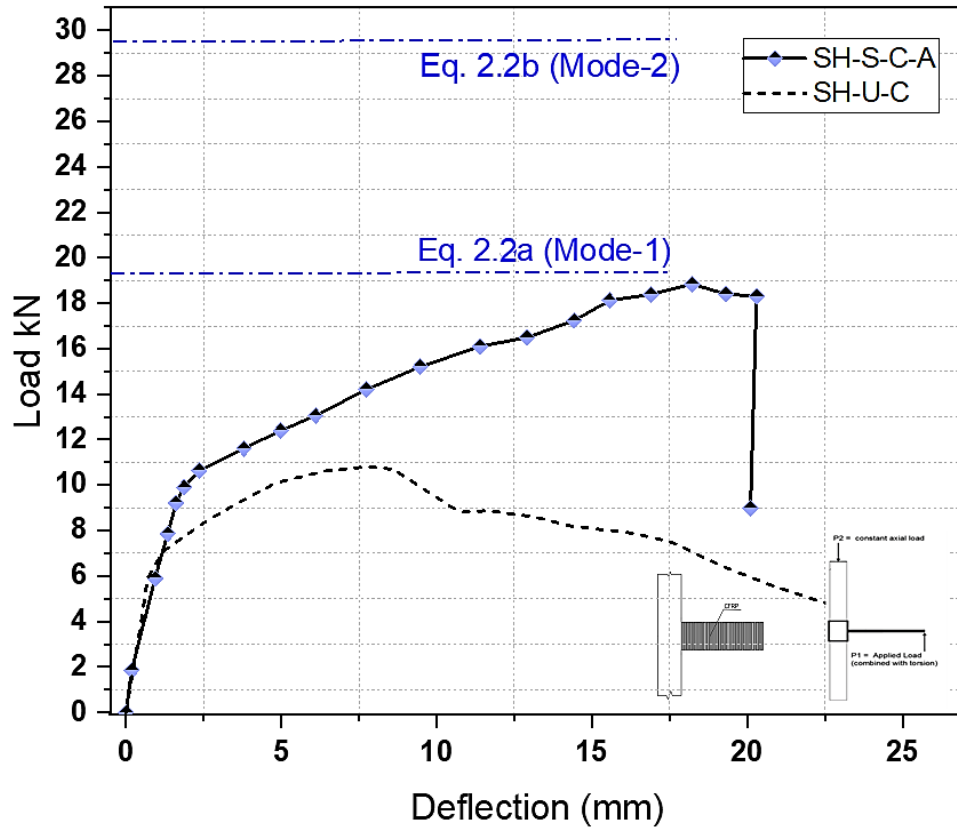


Figure 4.5: Load-end beam deflection for the SH-S-C-A sample

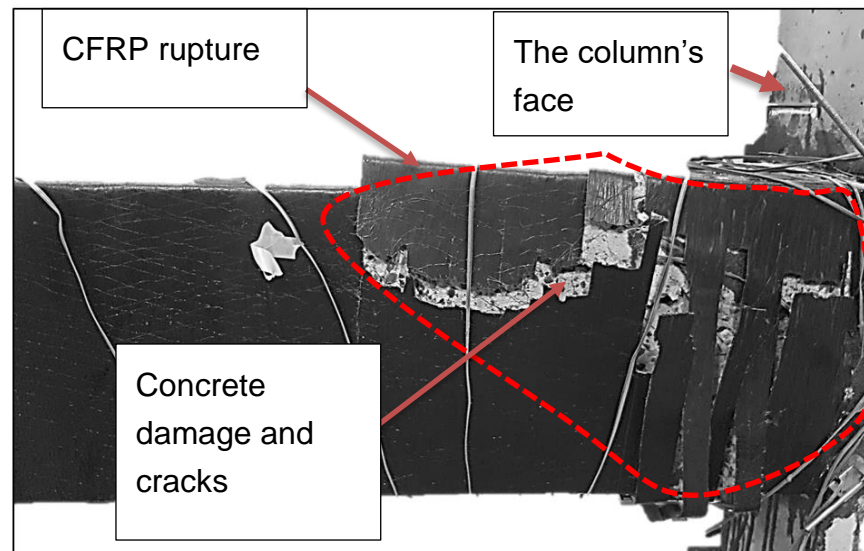


Figure 4.6: SH-S-C-A specimen failure under combined loads

4.3.2 CFRP Strips (Hoops)

The load-deflection curve (Figure 4.7) for the partially strengthened specimen with CFRP strips (SH-S-C-H) shows that the specimen exhibited three different stages as those observed from SH-U-C. These stages were linear elastic (pre-cracking) stage, a nonlinear post-cracking stage-up to peak load, and a nonlinear failure stage. When the SH-S-C-H specimen reached its cracking torque (14.8 kN.m), several inclined torsional cracks were observed, which spread along the beam's length. Progressive deterioration in the specimen's strength occurred after the peak load (Figure 4.7) and failure occurred when the CFRP sheets ruptured and there were widening of the developed cracks (Figure 4.8). Where the ruptures of CFRP strips and excessive diagonal cracks were concentrated in a region between the mid and the end tip of the beam. These excessive diagonal cracks propagated within this region as a result of increases in the tensile stresses that acted orthogonally on the diagonal concrete struts. The diagonal compressive stresses corresponds to levels of the shear stresses produced by torsion and direct shear loads. No damage was seen in the beam's flexural plastic hinge region near the column's face (Section 4.6). Also, it was observed that the CFRP hoops reduced the cracking levels when compared with the control specimen (SH-U-C), as shown in Figure 4.2b and Figure 4.8. On the other hand, the specimen attained a lower torsional capacity than the fully wrapped specimen (Figure 4.5). However, improvements of 30% and 35% were observed in their pre and post-cracking capacities, respectively, when compared with the unstrengthened specimen (SH-U-C).

Based on the damage to the beam, it is believed that significant deformations induced in the rebars (main rebars and stirrups) within the end third of the beam that reflected with an excessive crack formed across the beam's bottom and extended to the left side. This is because the ratio of torsion to bending loads and the influence of the strut action near the column region alters the location of the plastic hinge away from the column face – the flexural plastic hinge. Furthermore, the predicted carrying capacity for the SH-S-C-H specimen, according to the interaction formulas (Eq. 2.2a and Eq. 2.2b) was overestimated. Despite this over-estimation, the obtained peak load was closer to failure Mode-1 than Mode-2, as shown in Figure 4.7. That's obvious – if the interaction equations over predict then of course it will be closer to Mode-1 (bending and torsion are additive). According to Eq.4.2, the nominal

torsional capacity (T_{uo}) can be evaluated by assuming that both the main and transverse reinforcement reached their strength limit (yield point). However, this is not true when large plastic deformations occur in the beam stirrups, together with excessive degradation in the concrete struts such that the member's capacity starts to decline before the yielding of the main rebars. Hence, this study agrees with the design code provisions, such as ACI 318, whereby the member's design capacity should take the lesser of that computed according to the longitudinal or transverse reinforcement strengths, as described in Chapter 3 (Eq. 3.1 and 3.2).

The potential of the CFRP strip scheme to enhance the joint performance was affected by the cracks that developed in the unstrengthened regions and then extended to the wrapped zones; this appears to have increased the stress concentrations in the fibres over the cracks and restricted the shear transfer mechanism. Subsequently, the rupture of the fibres initiated along the crack lengths, as can be seen in Figure 4.8. This confirms that a reduction in the CFRP fracture limit can be correlated with the degree of concrete degradation, as identified by Triantafillou and Antonopoulos (2000), and Priestley and Seible (1995).

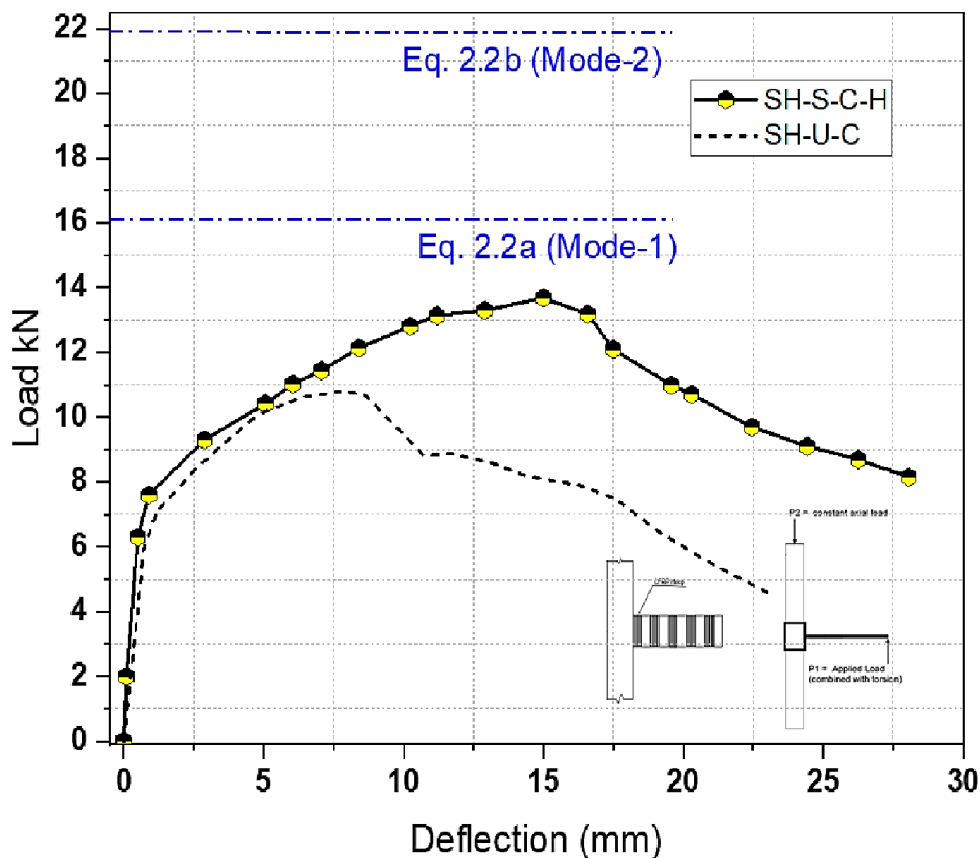


Figure 4.7: Load-end beam deflection for the SH-S-C-H sample

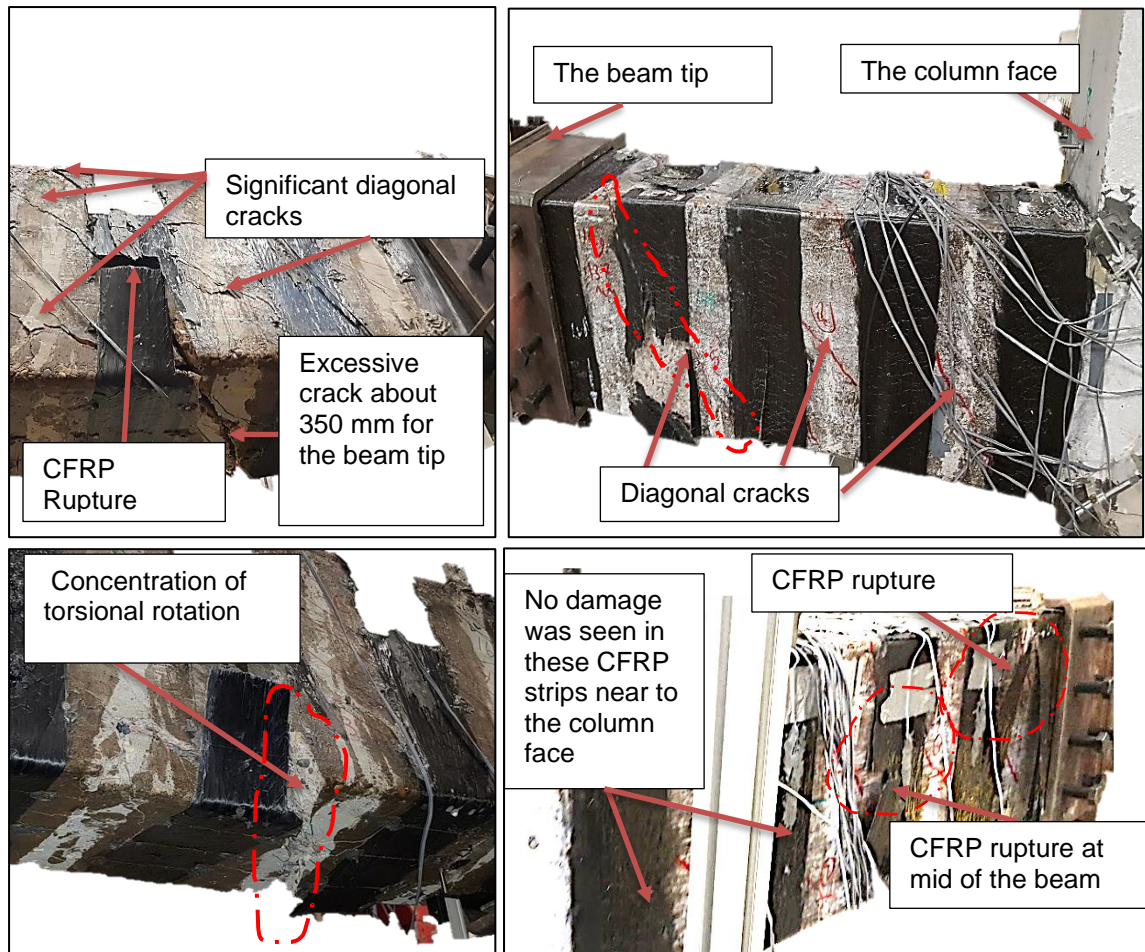


Figure 4.8: SH-S-C-H specimen failure under combined loads

4.3.3 45° CFRP Strips

Similar to the SH-S-C-H specimen, the partially strengthened specimen with 45° oriented CFRP strips (SH-S-C-I) shows three different load-deflection stages (i.e. pre-cracking stage, post cracking stage, and failure stage). Also, it demonstrated less torsional capacity when compared with the fully wrapped specimen (Figure 4.5). In comparison to the unstrengthened specimen (SH-U-C), larger pre- and post-cracking strengths were recorded (35% and 39%, respectively). It can be seen from Figure 4.9 that the behaviour of the SH-S-C-I specimen was close to SH-S-C-H specimen up to the peak load, with a marginal enhancement in its torsional capacity. At the post-cracking stage, the specimen load almost linearly increased up to the maximum recorded load

that corresponded with the elastic behaviour of CFRP strips. Also, the beam's regions experienced relatively lower cracking levels than in the SH-S-C-H specimen. This indicates the effectiveness of the 45° inclined strips in enhancing the shear cracking resistance of the concrete by restricting the development of the principal tensile strains that were induced in the perpendicular direction to that of the compressive concrete struts. However, there was a sharp decrease in the strength of specimen SH-S-C-I immediately once the peak load had been reached. This was thought to be due to the severe plastic deformations that occurred in the steel stirrups near the mid span of the beam. These stirrup deformations were obtained from the strain gauge readings on the stirrups (Figure 4.15b).

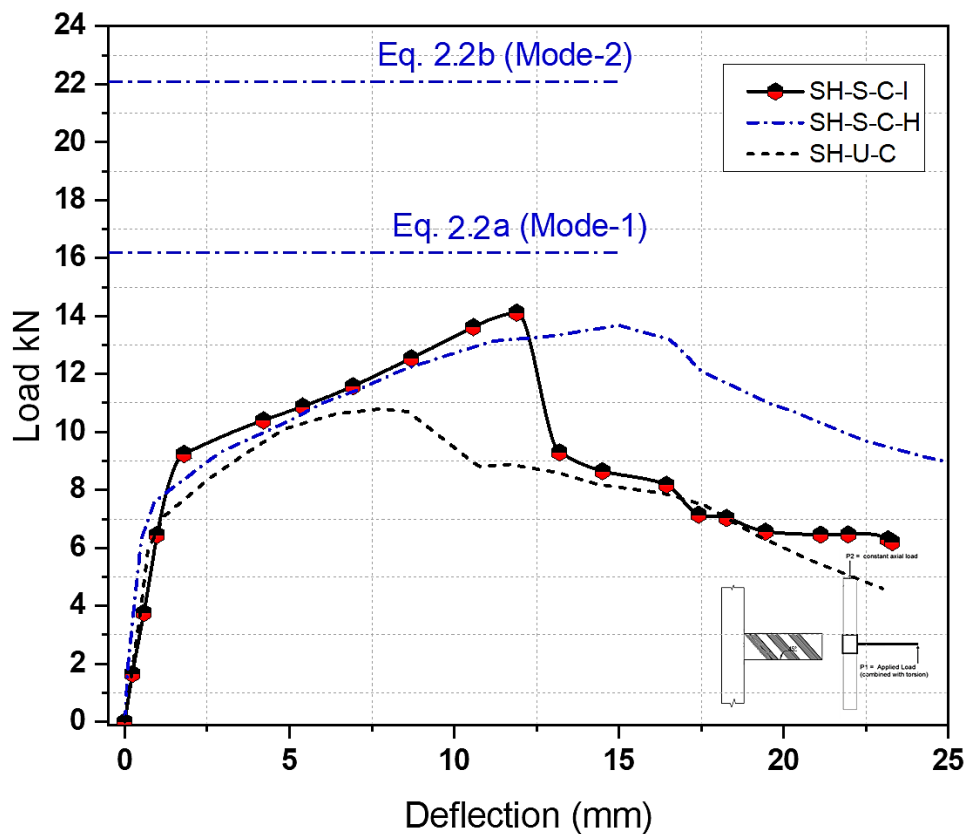


Figure 4.9: Load - end beam deflection for SH-S-C-I sample

As discussed in the previous section, it is important to verify the contribution of the transverse reinforcement based on the space truss model. At the point of yielding of the stirrups half way along the beam, severe concrete damage at this failure zone was also noticed (Figure 4.10), i.e., spalling of the concrete at the side and top of the beam's faces, followed by the rupturing of the CFRP strips on the section's sides. This indicated a significant progressive

degradation in the specimen's rigidity, which was reflected in the load-deflection (Figure 4.9) and twisting behaviour (Figure 4.11). Due to the deterioration in the transverse rebars and the stiffness of the concrete strut, the contribution of the main rebars appeared to decrease considerably. This reduced the peak measured load below that anticipated by the interaction formulas (Mode-1 and 2).

The fracture strength of the CFRP strips was affected by the formation of cracks in the concrete, similar to the rupture mechanism that was described for test SH-S-C-H. Also, the localised stresses at the rounded beam corners appeared to induce fractures in the CFRP strips, as shown in Figure 4.10. Finally, debonding (peeling off) of the CFRP strips was noticed and delamination of the concrete cover occurred within the damaged zones. This debonding failure was characterised by GangaRao et al. (2007), who stated that the FRP strips exhibited a high level of force that could not be transmitted to the concrete substrate.

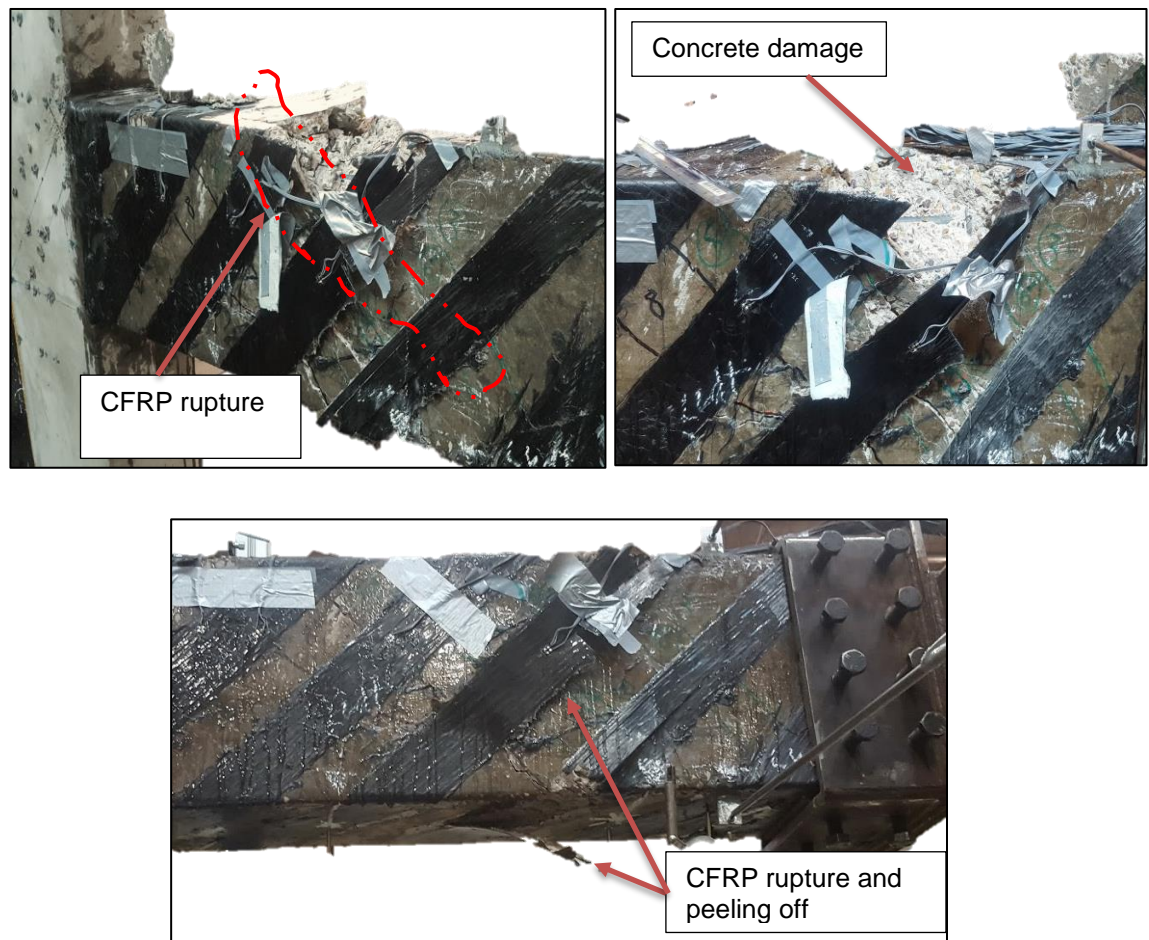


Figure 4.10: SH-S-C-I specimen failure under combined loads

4.3.4 Load -Twist Behaviour

The load-twist angle curves for all specimens that were subjected to torque actions are presented in Figure 4.11. At the beginning of loading, a similar trend for all tested specimens can be noticed; this trend of the linear elastic behaviour continued with high torque-twist ($T_{cr} - \psi_{cr}$) rigidity up to the cracking load. As mentioned earlier, the strengthened specimens showed different levels of enhancements to their cracking strength, although all exceeded the behaviour of the unstrengthened specimen (SH-U-C); these enhancements correspond to the confinement degree and the fact that the CFRP wraps arrest the cracks in the concrete by reducing the orthogonal tensile stresses. The strengthened specimens demonstrated a progressive increase in their loading capacities in the post cracking stage (ascending curves). Moreover, the strengthened specimens produced a larger torsional rigidity than the control specimen (SH-U-C), together with a linear response until the maximum load was reached. The SH-U-C-H specimen, on the other hand, exhibited a non-linear behaviour up to maximum load, since the propagation of the beam's concrete cracks started immediately after the cracking load in the regions between the CFRP hoops and there was yielding of the steel stirrups prior to the ultimate load.

The last stage (failure stage) was identified following the loss of the member's carrying capacity after the peak load was reached. At this stage, significant deterioration in the members torsional stiffness was observed due to severe concrete cracks, large plastic deformations in the steel stirrups and rupture of the CFRP strips. Despite the SH-U-C-H specimen with vertically oriented CFRP strips (hoops) showed higher stiffness levels during the declined failure stage than those observed from the SH-U-C-I specimen (45° inclined strips). An exception to the trend was specimen SH-S-C-A – the fully wrapped specimen. For this specimen the declined failure stage did not develop due to the brittle concrete failure, which was followed by the fracturing of the CFRP wraps shortly after the peak load.

Table 4.1 summarises the contributions of the CFRP systems as a percentage ratio of the improved cracking torque (ΔT_{cr}), ultimate torque (ΔT_u), torsional cracking rigidity (ΔK_{cr}), and post-cracking rigidity (ΔK_u), to the responses of the unstrengthened specimen (SH-U-C). The specimens torsional rigidities (K_{cr} and K_u) were evaluated as the measured torque with respect to the unit

angle of twist at the cracking and ultimate load, respectively. It can be concluded from Table 4.1 that the effectiveness of the CFRP wraps of increasing the member's torsional rigidities is significantly pronounced at post-cracking stage. These increases in the post-cracking rigidities (ΔK_u) ranged between 35% for CFRP strips scheme and 114% for full continuous wraps. In contrast, the influence of these external wrapping schemes before cracking (ΔK_{cr}) were insignificant.

Table 4.1: CFRP contribution for all specimens.

Specimen	T_{cr} Cracking Torque kN.m	T_u Ultimate Torque kN.m	ψ_{cr} Twist angle at T_{cr} ($\frac{^\circ}{m}$)	ψ_{max} Max. measure d angle ($\frac{^\circ}{m}$)	% Increase			
					ΔT_{cr}	ΔT_u	ΔK_{cr} Torsional cracking rigidity	ΔK_u Post - cracking rigidity
SH-U-C	11.4	16.11	0.35	8.4	-	-	-	-
SH-S-C-A	16.1	29.6	0.48	7.2	41	83	3.0	114
SH-S-C-H	14.8	21.7	0.44	8.41	30	35	3.3	35
SH-S-C-I	15.8	22.4	0.47	8.1	35	39	3.2	44

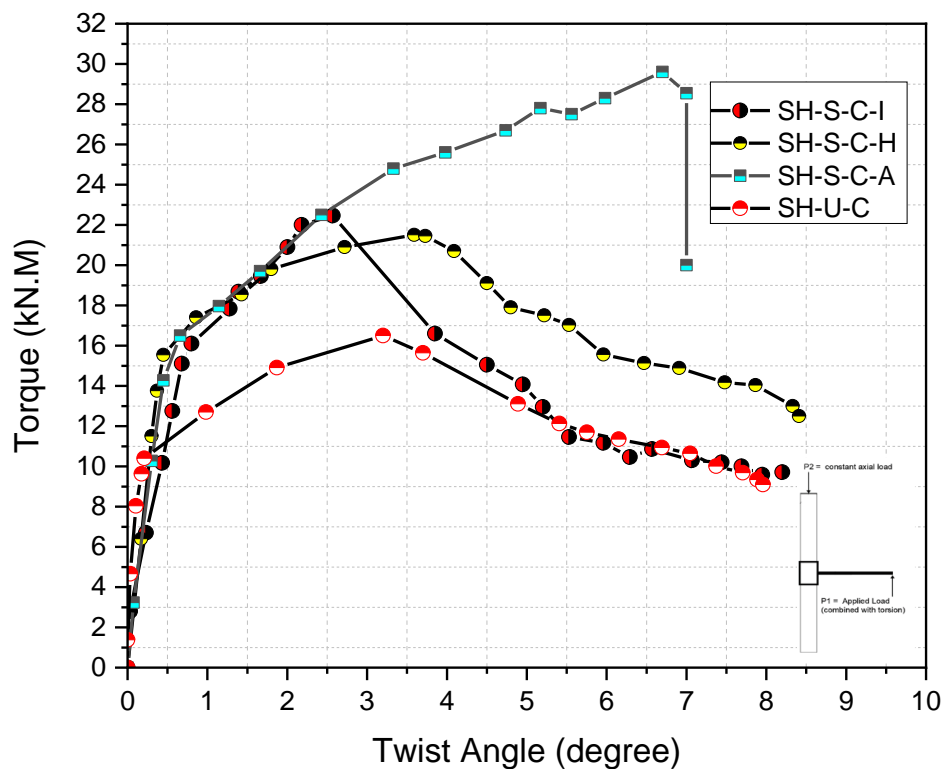


Figure 4.11: Torque-twist diagram for all specimens under torque actions

4.4 Ductility Index

The tested specimens behaved differently depending on the applied forces, strengthening schemes and materials properties. Hence, this section attempts to qualitatively assess the behaviour of each specimen according to the ductility index. The ductility index can be defined as the ratio of deflection (Δ_u) or rotation (ψ_u) at the peak load and it is measured at the yielding point, as schematically illustrated in Figure 4.12. Based on the torque-twist behaviours of tested RC beams, Teixeira and Bernardo (2018) and Bernardo and Lopes (2009) identified that the beams without sufficient torsional ductility were exhibited sharp drop in their carrying loads (as observed from SH-S-C-A and SH-S-C-I). Further, after the peak load, the adequate ductile behaviour of RC sections is maintained by gradual developing the softening effect- i.e. caused by diagonal cracking in the concrete struts. This produces a significant level of internal energy dissipation via a satisfactory level of deformation (Bernardo and Lopes, 2009); hence, a plastic behaviour can be developed. On the other hand, Lopes and Bernardo (2009) suggest that the location of the yielding point can be estimated in a region between the cracking and ultimate torque points from the torque-twist curve, due to fact that the yielding of transverse and the longitudinal rebars do not occur simultaneously in the failure region induced by torsion. Chiu et al. (2007) have also quantified the ductility of RC beams from the twist-torque curves in corresponding to the regions enclosed by 0.85 of the peak torque and the first observed yielding -either in the stirrups or the longitudinal rebars. While, several specimens showed a yielding only in the transverse rebars (stirrups). Accordingly, to identify the equivalent yielding point for the specimens that exhibited different levels of cracking and yielding (transverse and/or main rebars) through the loading stages, along with the yield displacement of the reduced stiffness, an equivalent elastic-plastic system was employed (Figure 4.12). This system was suggested by Park (1988) in which the secant stiffness of 0.75 of the peak load considers the decrease in sections stiffnesses. Elshafiey et al. (2016) have utilised this system to determine the ductility levels for beam-column joints under torsion and flexural loads.

Table 4.2 shows the ductility index for all beam-column joints, where it can be noticed that the member's ductility in terms of load-deflections ($P-\Delta$) reduced in accordance with the level of torsional forces attained. As a result of incorporating beam torsion, the failure of specimens mainly occurred in the

beam regions and was attributed to progressive degradation in the concrete's strength, such as that observed for SH-U-C and SH-S-C-H, or sudden crushing of the concrete struts with the complete rupture of the CFRP sheet, as observed in the failure of SH-S-C-A (see Figure 4.6), which significantly reduced the ductility level. For SH-S-F, adequate ductile behaviour up to the failure load was observed, where no damage was seen in the concrete at the compression zone prior to its failure; at the collapse load, the beam's top near to the column's face crushed. The torque-twist ($T-\psi$) ductility indices demonstrate that the specimens were considerably affected by the degree of wrapping, with the highest level of ductility being achieved when CFRP hoops were used. However, the brittle failure of the fully wrapped specimen illustrates the need for a balance between the enhancement level due to the wrapping schemes and the concrete strut's capacity. As discussed in the previous sections, the compressive strength of the diagonal struts is greatly influenced by the softening of the concrete (the post-cracking and failure stages), which took place due to the increase in the orthogonal tensile stresses. The CFRP hoops tend to reduce the cracking levels (e.g. at ascending and descending stages) and tend to improve the concrete response by way of two mechanisms: (1) increasing the confinement of concrete through lateral pressure provided by the CFRP hoops, and (2) resisting the diagonal tensile stresses. Although the SH-S-C-I specimen experienced relatively lower concrete deformations and fewer cracks than the SH-S-C-H specimen after the cracking load was reached, a sudden damage occurred in the concrete struts when the induced forces in the inclined compressive struts exceeded the softened concrete's compressive strength, which impaired the member's ductility.

Table 4.2: Ductility index

Index	SH-U-F	SH-U-C	SH-S-C-A	SH-S-C-H	SH-S-C-I
P-Δ¹	3.9	2.3	1.8	2.2	1.7
Tu-ψ²	-	3.43	1.86	5	2

¹ Load-Deflection index

² Torque-Twist index

The ductility levels for all specimens can be adversely affected if the specimens exhibit joint shear failures, anchorage failure or slippage of the beam tension rebars within the joint region. Therefore, the increase in the joint's demands due to both combined forces and wrapping schemes should be quantified, with a view to avoid brittle shear failures in the joint zones. The following section shows the strain development in the beam's main rebars near to the column faces, which correspond with the joint demands that were induced at different levels of torsion interacting with bending and shear forces.

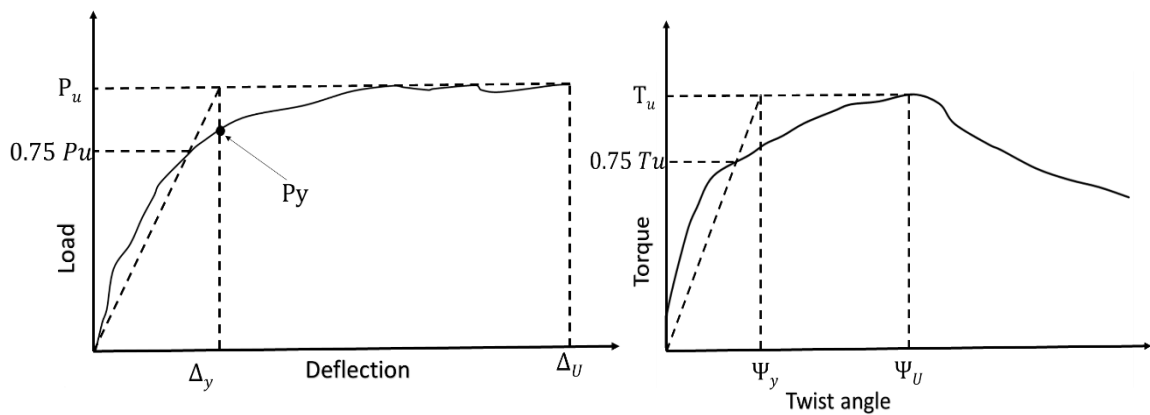


Figure 4.12: Ductility level, yield displacement of the reduced stiffness equivalent elasto-plastic system

4.5 Strain Development in Steel and CFRP Reinforcement

4.5.1 Strain Levels in the Main Steel Reinforcement

There is a lack of experimental data from previous research into the joint demand (forces) and deformations that arise from combined beam loading. The present study provides a discussion that involves the strain development in the specimen's steel rebars near the column face (joint region), as well as at other important regions. Figures 4.13a and 4.13b illustrate the strain readings from the beam's bottom main rebars at 100 mm from the column face, where these measurements represent the strain development in the beam's flexural tensile zones. A significant increase in the rebar's strain measurements occurred in the SH-U-C specimen under lower loads than the SH-U-F specimen, which was mainly due to the torsional tensile forces interacting with the flexural forces - see Figure 4.13a. Also, it is notable that the strain progressions increased considerably when the specimen reached

the cracking stage (beyond 7.3 kN), which conforms with the truss mechanism. Figure 4.13b shows different levels of strain developments for strengthened specimens, and compares them with the SH-U-C specimen. In other words, the applications of the vertically oriented CFRP wraps at 90° from the beam's longitudinal axis increased the transverse reinforcements ratios. Based on the truss mechanism, the increment in the transverse reinforcement increased the angle of the inclined struts such that they became steeper and reduced the amount of stress in the longitudinal main rebars. This is reflected in the behaviour of the SH-S-C-H and SH-S-C-A specimens, where, under the same load levels they produced lower strain values than the unstrengthened control specimen (SH-U-C). For sample SH-S-C-I, the inclined wraps reduced the concrete strut angle and produced larger longitudinal strains (plastic deformations), in which the highest obtained strain reading was 75% of the peak strain value of the SH-U-F sample; the SH-S-C-I sample only attained 22% of the maximum load of the SH-U-F specimen. On the other hand, when the peak load was reached and CFRP's strips were ruptured, an increase in the rebars strains was observed (see Figure 4.13b). These corresponded to a considerable rise in the twisting deformation (see Figure 4.11) and excessive diagonal cracks which significantly reduced the beam's strength and increased the loss of tension stiffness.

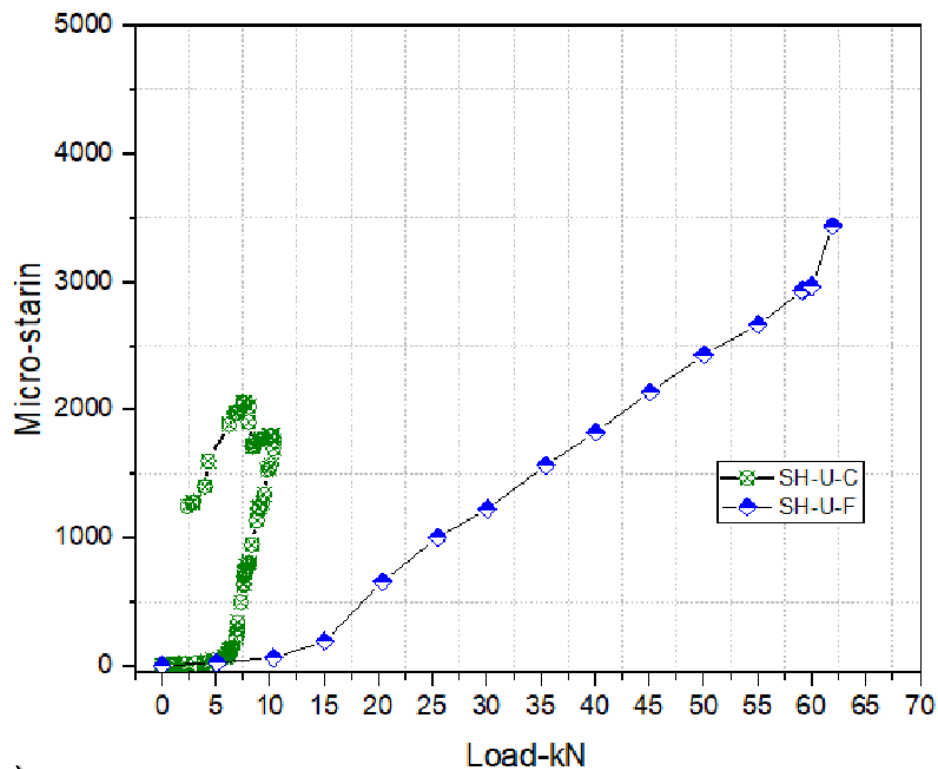
From Figure 4.13b it can also be seen that before the cracking loads (P_{cr}) were reached, where the specimen showed relatively higher stiffness than what was obtained at the pre-cracking stage the level of strain was low (less than 550 micro-strain). It is observed that the inclined strips increased the rate of longitudinal tensile strain before the cracking of the concrete, where it is believed that as soon as the load applied, the inclined principal tensile stresses produced from the torsional shear stresses are resisted by the 45° strips. The two orthogonal components of this resisting action increase the stresses in both the longitudinal and transverse directions at the section's sides, whilst decreasing the level of the principal tensile stresses on the concrete struts, thus improving the cracking behaviour of the SH-S-C-I up to the peak load.

Figure 4.13c shows the strain development in the top bars of the beams (flexural compression zone) for the specimens under combined actions. (SH-U-F was not presented here due to a technical issue in the strain gauge channel at the time of the test.) All specimens subjected to torsional forces

exhibited tensile strains that resulted from the torsion action; these were related to the ratio of the torsion to bending forces. The amounts of these strains were less than those induced in the bottom rebars, where torsional and bending forces were additive and hence associated with failure Mode-1.

Figure 4.14a and Figure 4.14b illustrate the strain in the exterior column bars (outer column bars) of all specimens at a position of 100 mm above and below the level of the top and bottom of the beam, respectively. These figures show that the strain varied from completely compression to being completely in tension above and below the beam, respectively. These transitions are similar to what is observed for members under flexural loading (SH-U-F specimen). At the middle of the column zone, the levels of developed strains in the beams bottom rebars had decreased due to the forces in the steel being transmitted by bond into the concrete within the joint zones (Figure 4.14c).

The level of strain corresponded with the magnitudes of the joint demands (V_{jh}), which can be quantified according to Eq.2.15. The beam forces (T_B) appeared to be affected by the levels of the combined forces and the strengthening configurations, since the beam forces would be significantly underestimated if they were based only on the flexural forces (Eq. 2.16), without considering the other forces (e.g. torsion and direct shear).



(a)

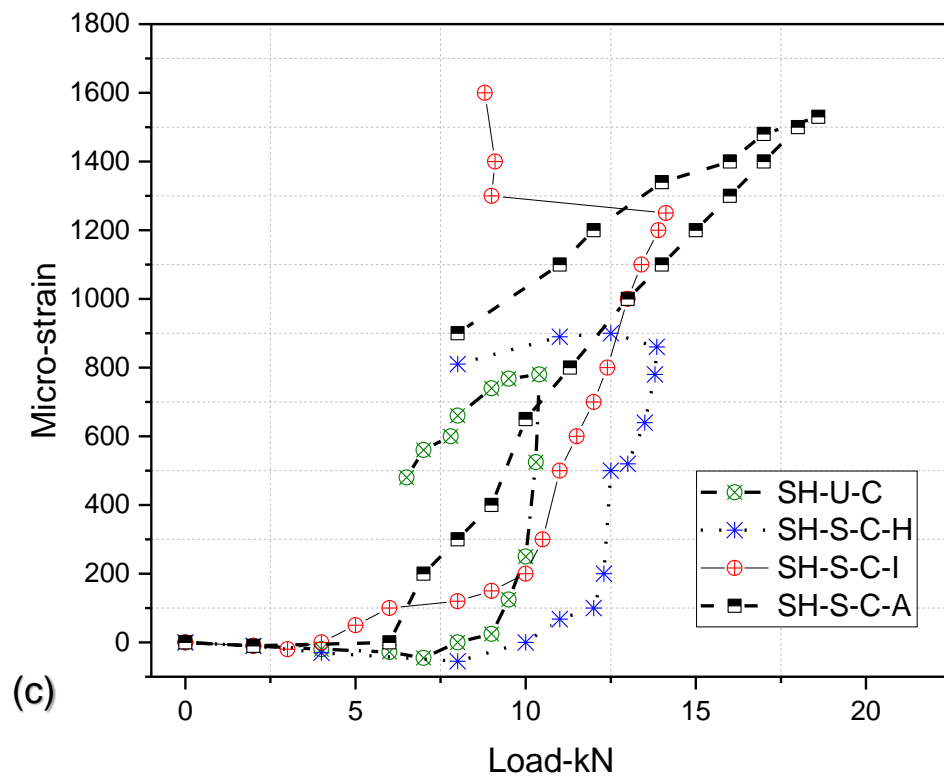
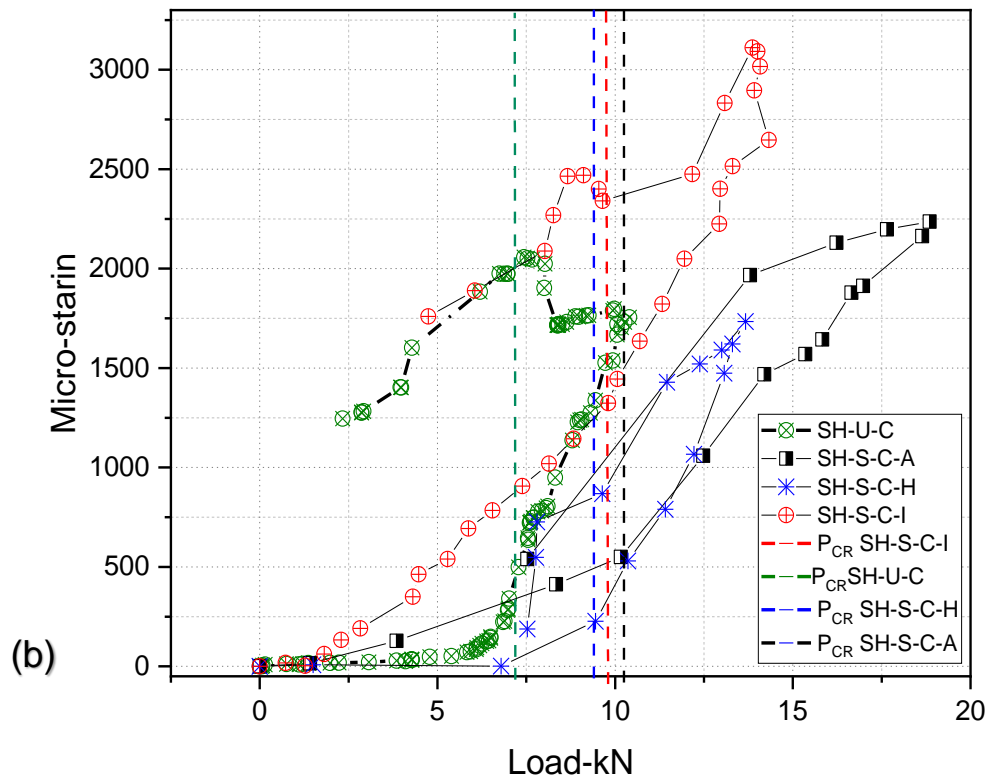
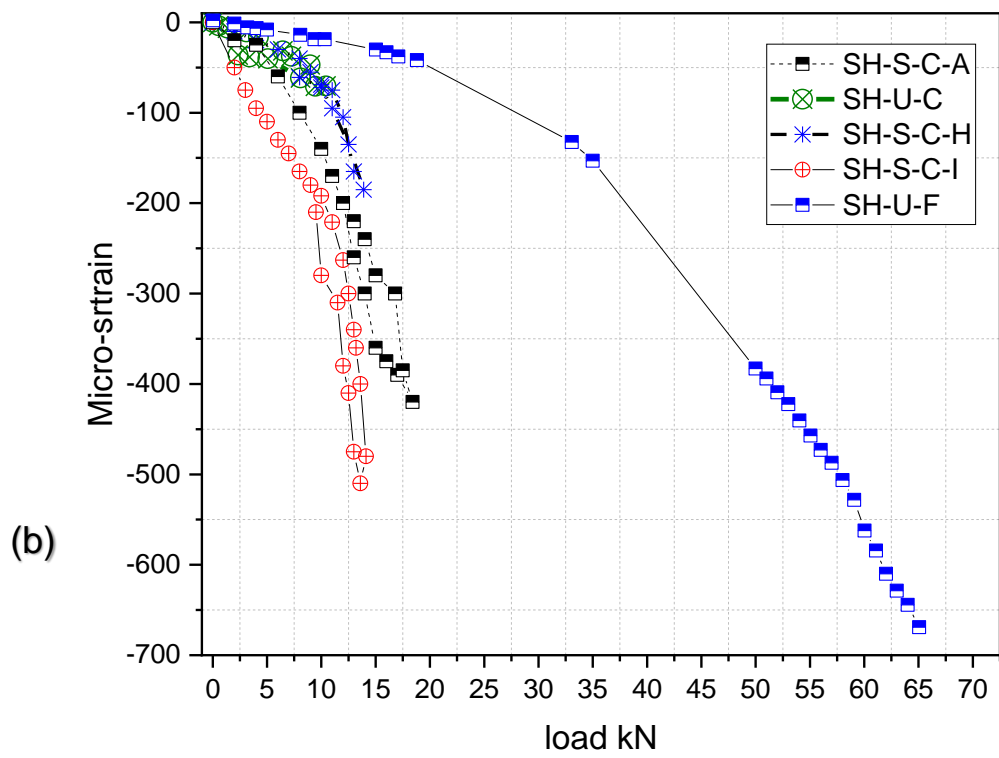
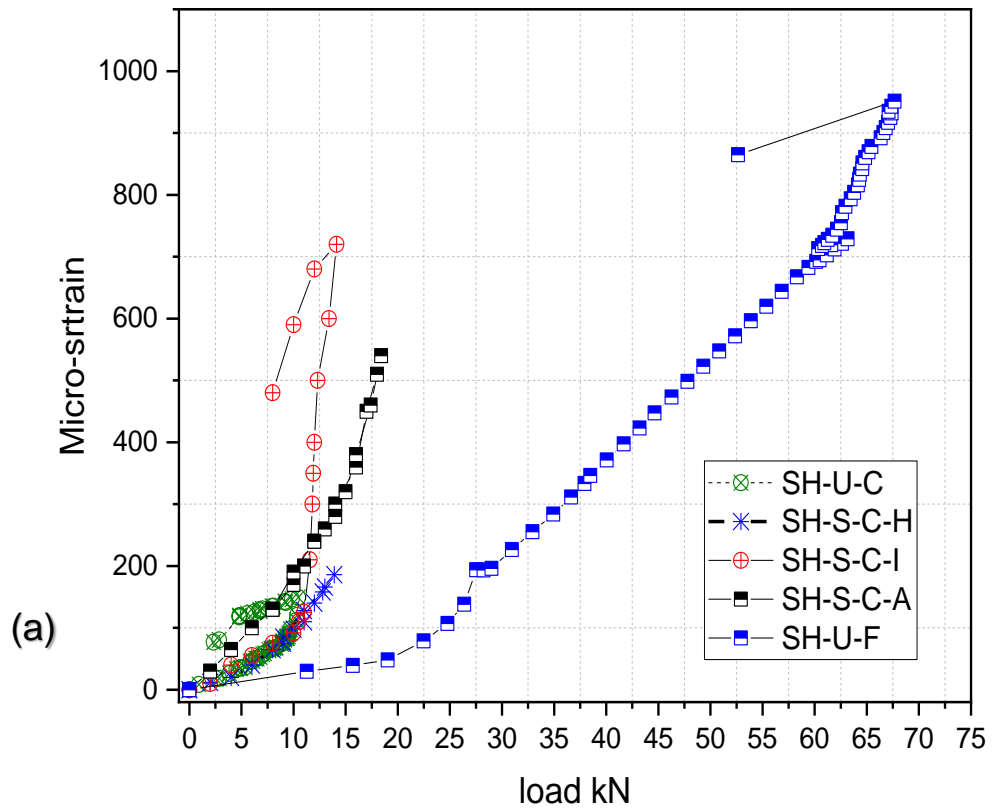


Figure 4.13: Strain development in the beam main rebars at 100 mm from the column face, (a) for control specimens (b) for strengthened specimens (c) in the beam top rebars



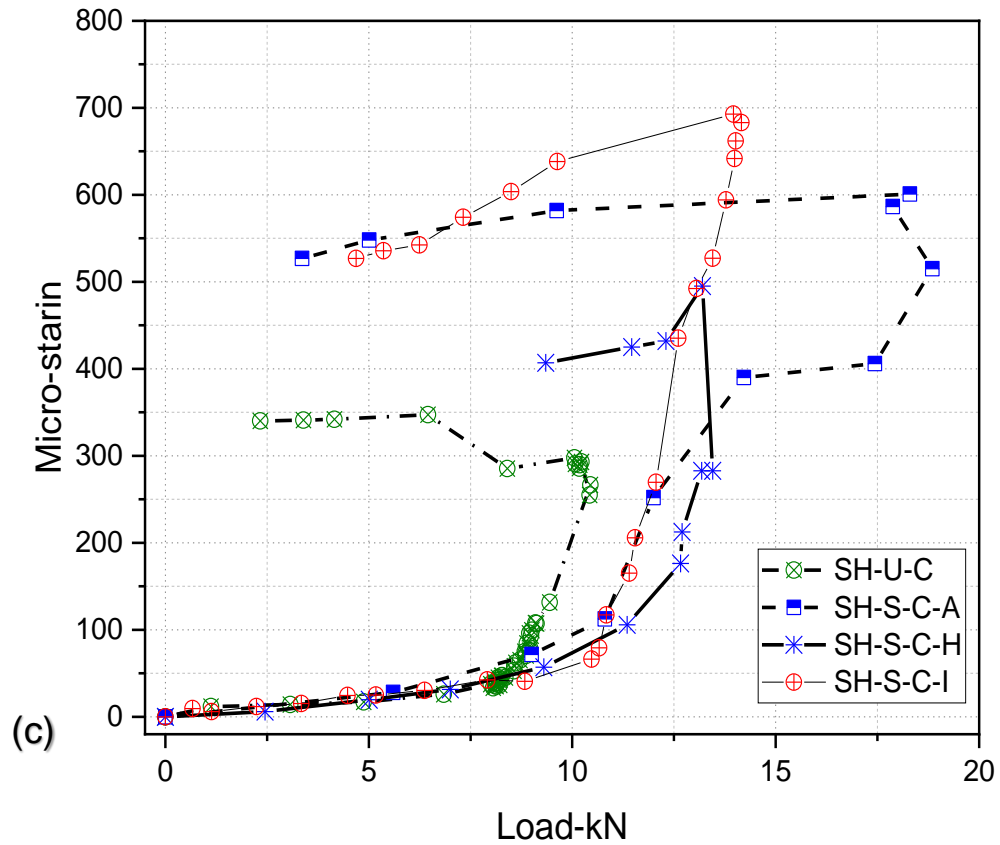
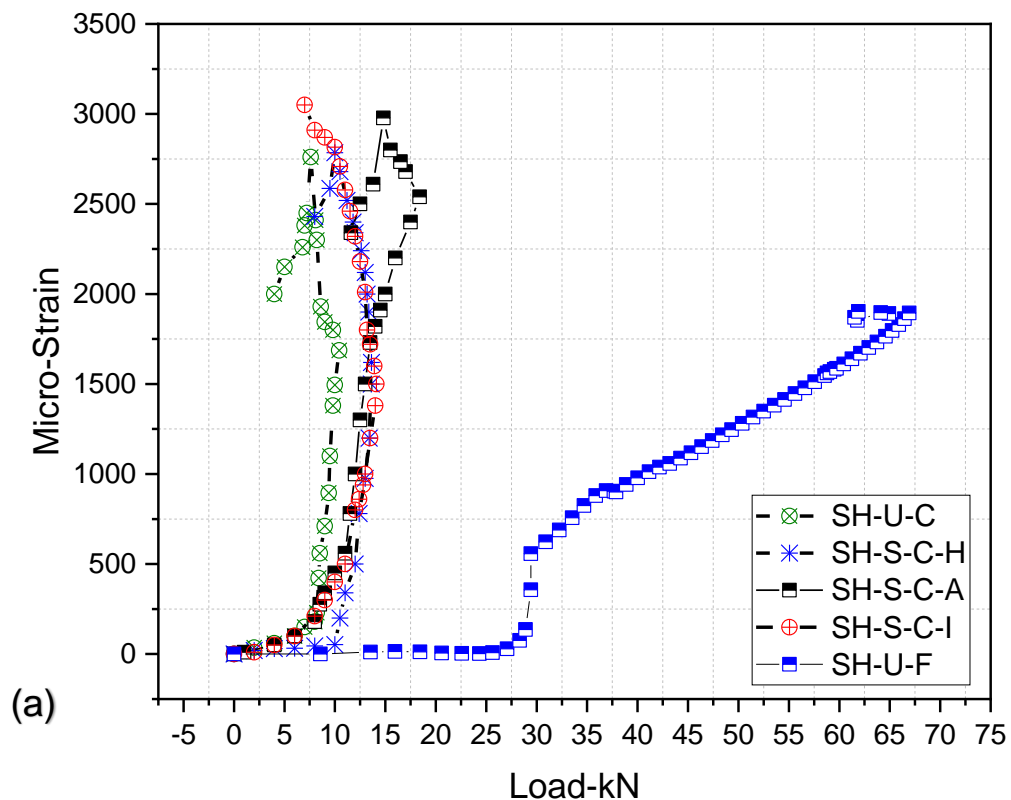


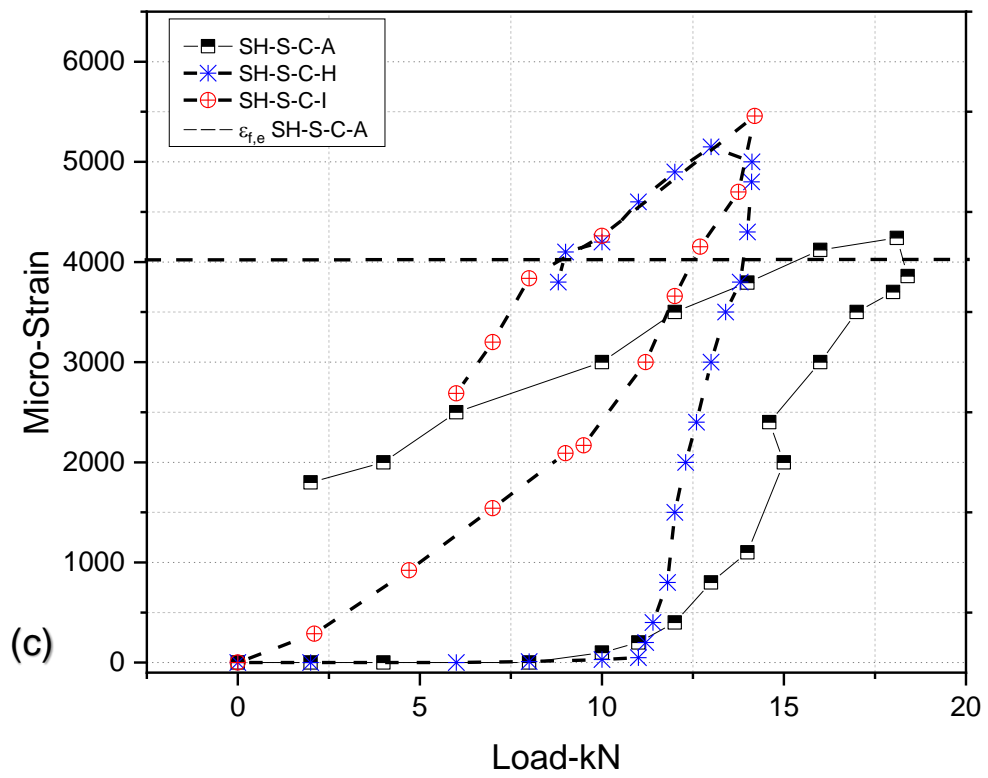
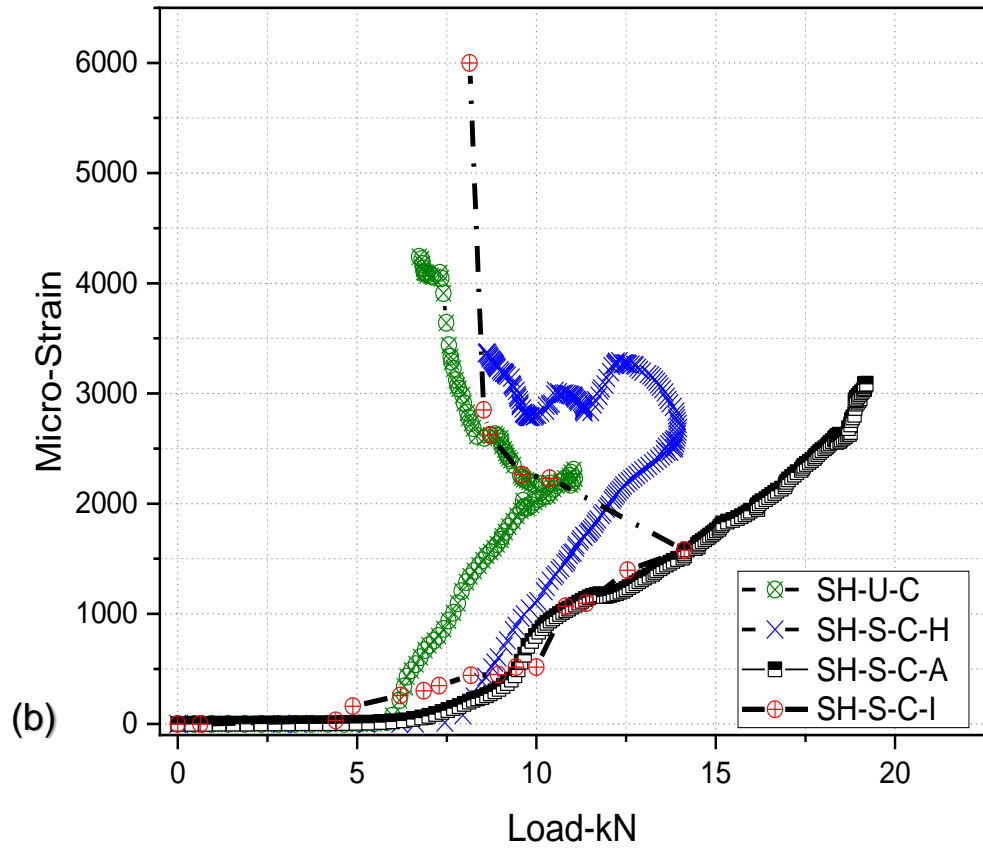
Figure 4.14: (a) Column exterior bar steel strain at the top of the joint (b) Column exterior bar steel strain at the bottom of the joint (c) in the middle of the joints (beam's bottom rebars)

4.5.2 Strain Level in Transverse Reinforcement

The strain measurements obtained from the beam's stirrups were consistent with the observed effects of the torsional forces and wrapping schemes. Figure 4.15a and Figure 4.15b illustrate that at 200 mm and 450 mm, respectively from the column face there is a considerable increase in the strain in the stirrups to well beyond the yielding strain of the steel in some cases. This is due to the large shear stresses induced by the torsion and the direct shear. Owing to the shear transfer mechanism into the columns through the inclined concrete struts in the beams, as mentioned earlier, the transverse strains in the regions that are close to the column face are reduced, as can be seen in Figure 4.15a. Figure 4.15b shows severe deformations in the SH-S-C-I and SH-S-C stirrups near the plastic failure zones (at around 300 mm away from the column face), where excessive cracks and concrete damage has occurred.

Figure 4.15c and Figure 4.15d illustrate the strain in the CFRP sheet at 250 mm and 450 mm away from the face of the column, respectively. These figures reveal that significant strains developed in the CFRP sheets due to the shear stresses. It is also apparent from the figures that the maximum effective fibre strains ($\varepsilon_{f,e}$) were well predicted by Eq. 2.8a and Eq. 2.10 (Triantafillou and Antonopoulos, 2000; Hii and Al-Mahaidi, 2007), which utilises the level of tensile strain in the concrete substrate in its prediction. The CFRP wraps were highly strained in the regions close to the failure zones, see the cases of the SH-S-C-I and SH-S-C-H specimens (Figure 4.15d) and the SH-S-C-A specimen (Figure 4.15c). The inclined CFRP configuration (SH-S-C-I) exhibited early strain development, which was consistent with the main rebar's deformations, as previously discussed. Interestingly, subsequent reductions in strain levels were noticed at, or shortly after, the peak load, which were followed progressive ruptures of the CFRP sheets and corresponding decrements in the specimen's carrying capacity. However, as can be seen from 4.15b, a significant increase in the strain levels induced in the beams stirrups beyond the peak loads due to ruptures of the CFRP wraps. This was accompanied with large twist deformations and severe cracking in the beams. The steel links of all the specimens located within the column / joint region exhibited lower strains (Figure 14.15e), as this region was away from the high shear forces experienced at failure (Hamil, 2000b).





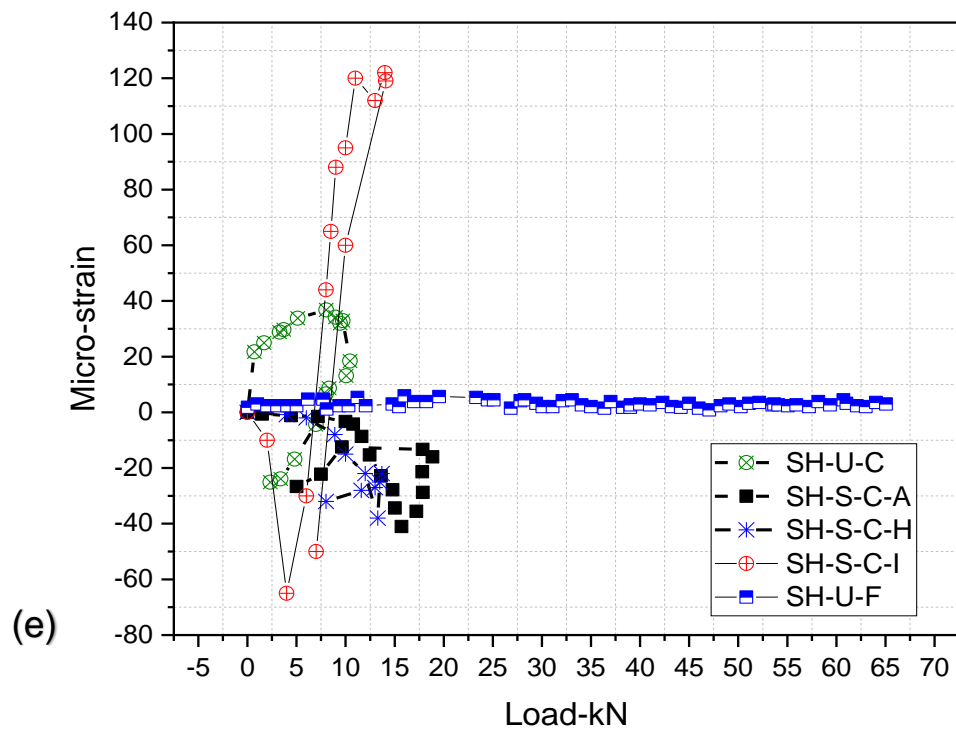
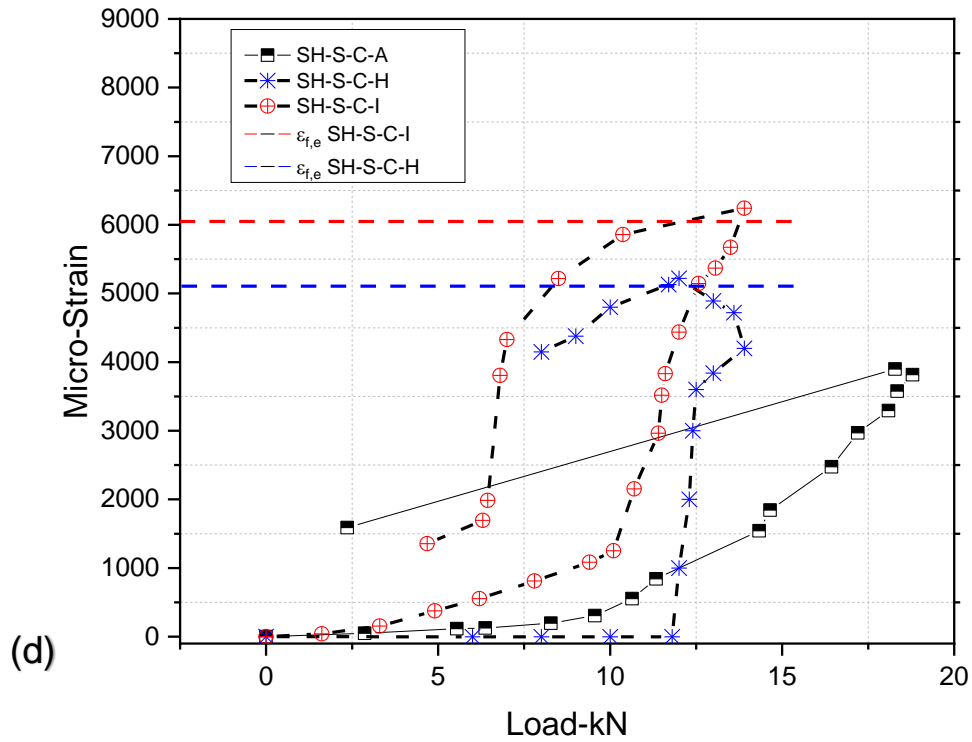


Figure 4.15: Strain development (a) in the beam stirrups at 200 mm from the column face (b) in the beam stirrups at 450 mm from the column face (c) in CFRP wraps at 250 mm from the column face (d) in CFRP wraps at 450 mm from the column face (e) in the column middle link at 145 mm from the column outer face.

4.6 Joint Distortion and Cracks

Figure 4.16 shows the relationship between the maximum shear distortion angle (γ) and joint shear forces (V_{jh}) for all the specimens. The joint shear forces (demands) were approximated based on the beam forces (T_B) in corresponding to Eq. 2.15. The beam forces were evaluated using the strain measurements (ε_{p_u}) at the maximum observed loads (P_u) (Figure 4.13a and 4.13b); where $T_B = \varepsilon_{p_u} E_s / A_s$ (E_s and A_s are the rebars modulus of elasticity and the area of the rebar (diameter of 16 mm), respectively). While it is inappropriate to use Eq. 2.16 to calculate the beam forces resulted from the combined loads as identified in the previous section. This is because it considers only the concentric loads (bending) in which underestimates the developed beam combined forces- i.e. neglects the interaction between bending, shear, and torsion. The evaluation method for the shear distortion angles is schematically illustrated in Figure 3.28. The joint distortions for all specimens (Figure 4.16) were directly influenced by the levels of the beam forces (joint demand). It was concluded in the previous sections that the corresponding joint demands were affected by the loads interactions and the fibre schemes.

As can be seen from Figure 4.16 the SH-S-C-I and SH-S-C-A specimens experienced joint shear distortions of 71% and 63% of those that were obtained from the SH-U-F specimen, respectively. Meanwhile, the peak loads that were reached were only 22% and 29% for the SH-S-C-I and SH-S-C-A specimens, respectively, when compared with the control specimen (SH-U-F). These significant increases in the joint demands reflect the need to adequately address the influence of the chosen wrapping configuration and the interaction between the imposed loads on the joint's behaviour. As identified by the review of the relevant research work and design provisions (Chapter 2), there is currently a lack of any available model that has proposed quantifying the joint demands and assessing joint behaviour under beam torsion combined with bending and shear. Further consideration must also be made of the influence of externally applied FRP configurations as proposed in chapter 6.

Several cracks propagated into the joint region of the SH-S-C-A and SH-S-C-I specimens due to increases in the shear demand resulting from the torsional forces, as shown in Figure 4.17b and 4.17c. This behaviour was similar to the SH-U-F specimen behaviour, where joint cracks developed due to flexural

loads (Figure 4.17a). While the cracks extended further in the control specimen (SH-U-F), they developed in the strengthened specimens in conjunction with the level of joint demand. However, aside from the joint demand value, the SH-S-C-A specimen exhibited a relatively greater number of cracks than SH-S-C-I; this is believed to be related to the lower concrete strength used for the SH-S-C-A specimen compared with SH-S-C-I specimen (see Section 3.7.1.5); in addition, the beam damage of the SH-S-C-A specimen was predominately occurred in a region close to the column (joint's region). Hence, the joint distortion was affected by the level of joint cracks. In contrast, as can be seen from Figure 4.17d and Figure 4.17e, no cracks were observed in the SH-U-C and SH-S-C-H specimens, since the damage completely shifted to the beam region.

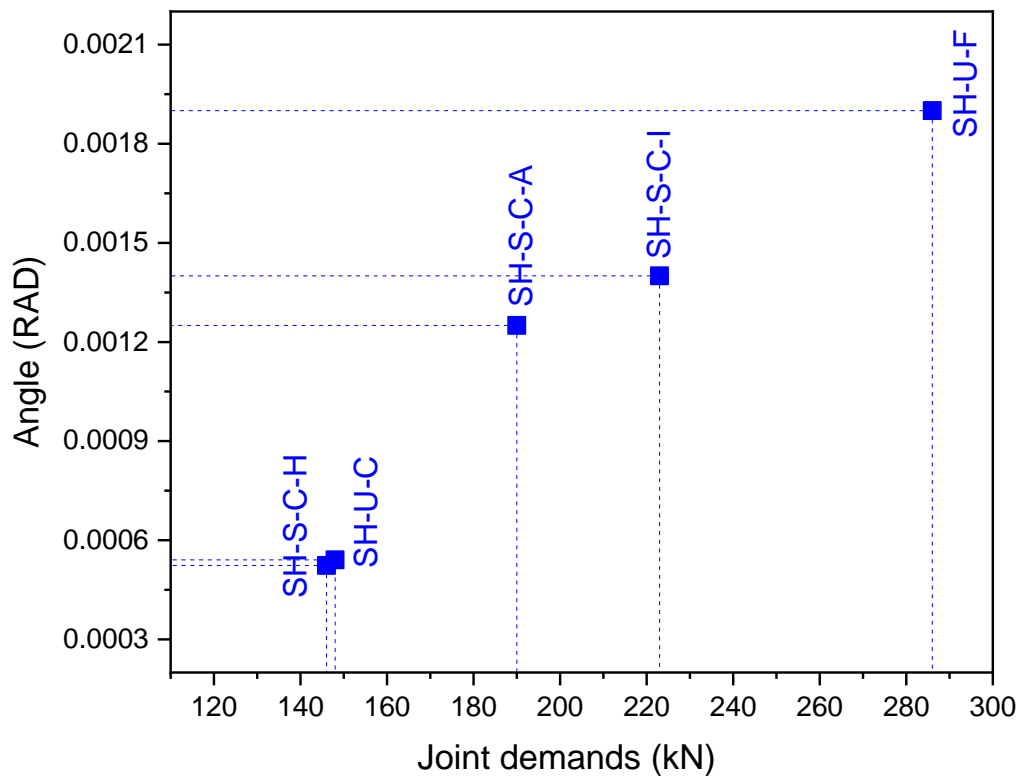
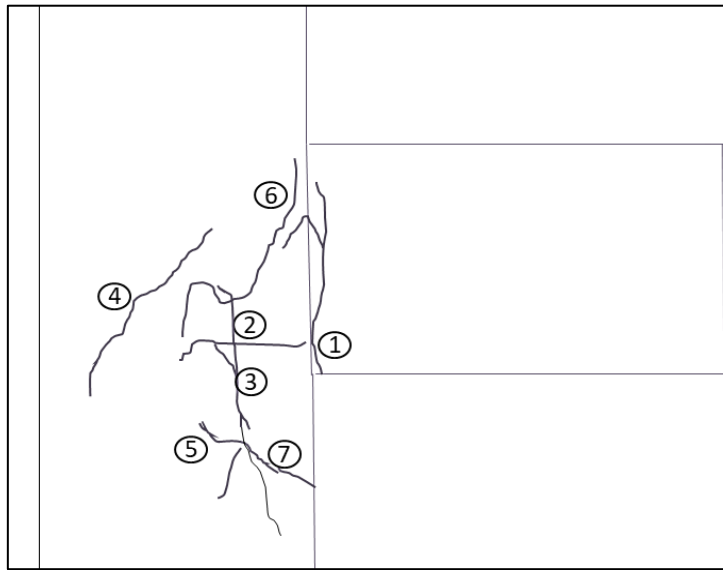
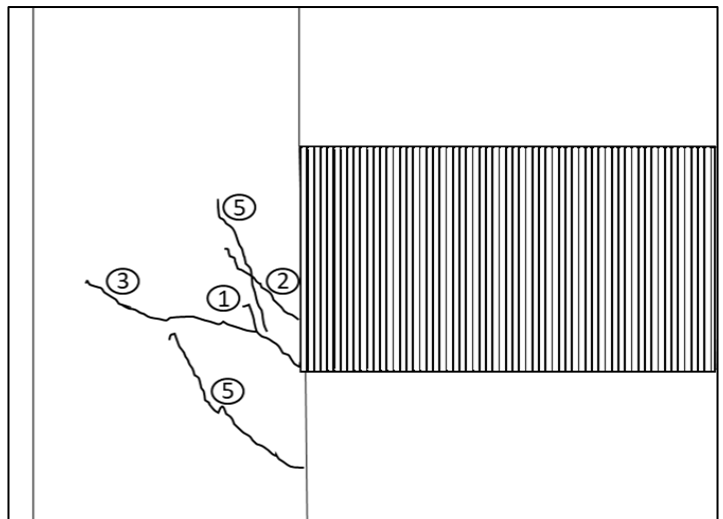


Figure 4.16: Joint distortion angles and joint demands

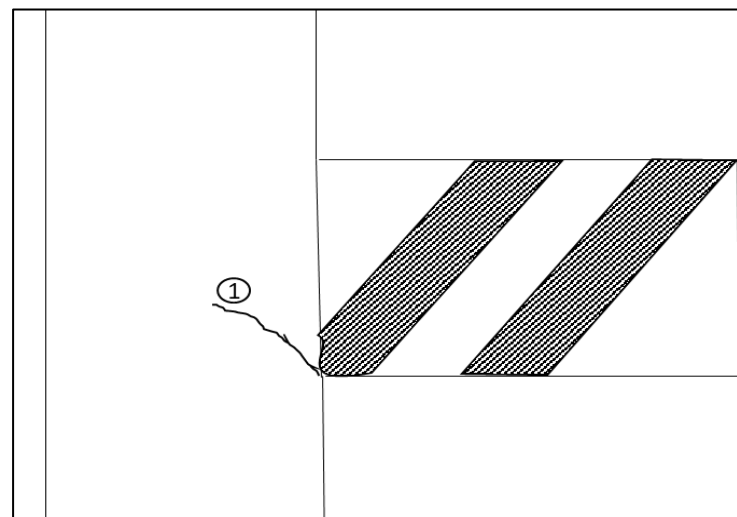
(a)



(b)



(c)



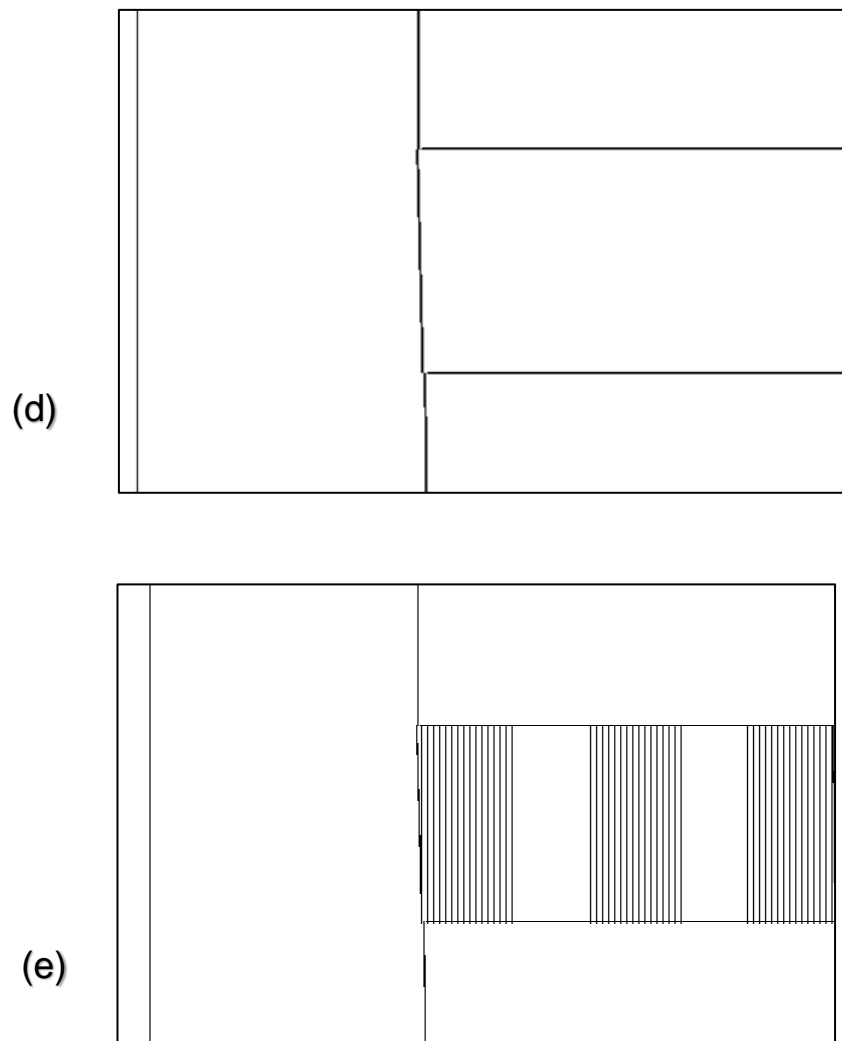


Figure 4.17: Joint cracks (a) for the SH-U-F specimen (b) for the SH-S-C-A specimen (c) for the SH-S-C-I specimen (d) for the SH-U-C- specimen (e) for the SH-S-C-H specimen

4.7 Summary

In this chapter, the behaviour of the five reinforced concrete exterior beam-column joints have been discussed and analysed according to the tests results. In general, the test outcomes demonstrated the influence of beam torque (with full and partial CFRP wrapping configurations) on the beams failure modes, the joint demands and damage levels . The following points are the main findings that can be deduced from the tests.

- 1- The test results confirmed that beam torque does reduce the beam's carrying capacity as it produces additional tensile stresses in the steel bars, which affects the joint's behaviour.
- 2- Beam torsion interacting with bending and direct shear forces alters the failure mode and the location of the beam's plastic hinge. The effect can be related to the loading level and the wrapping schemes. The fully wrapped specimen (SH-S-C-A) sustained larger bending, torsional, and shear loads than other specimens under combined loads which these loads were increased the stresses and strains levels at flexural plastic zone near to the column face. This had promoted the concrete damage to be extended from close to the column face.
- 3- The possible influential factors that affected the beams failure mechanisms have been identified and they are: level of shear stresses, softening level, and the angle of the inclined concrete struts, and longitudinal and transverse reinforcements (steel rebars and CFRP warps) ratios.
- 4- CFRP beam configurations have enhanced the member's pre-cracking and post-cracking capacities in different levels, which the maximum levels were obtained by using full wrapping scheme. This agrees with the extant literature (Deifalla et al., 2013; Chalioris, 2008; Ameli et al., 2007; Salom et al., 2004; Ghobarah et al., 2002; Panchacharam and Belarbi, 2002; Zhang et al., 2001). However, this study has shown that the CFRP arrangements and fibre ratios also influence the member's ductility, strain development, and joint cracks.
- 5- Based on the test results of the fully and 45° wrapped specimens (SH-S-C-A and SH-S-C-I), the additional forces that develop in the concrete compression struts where there is an imbalance in the reinforcement (over reinforced), lead to a sudden failure in the concrete (brittle-mode).
- 6- Deviations of 16% and 14% between the test results and predicted capacities (Mode-1) according to the interaction formulas for SH-S-C-I and SH-S-C-H have been observed due to concrete damage and the large stirrup deformations.
- 7- The increments in the strain of the beam's main steel rebars due to the combined loads were quantified. It was found that the strain amounts for the strengthened samples varied according to the fibre orientations and that the maximum measured strain developments were from the specimen with inclined CFRP strips (SH-S-C-I); as the highest

observed strain reading was 75% of the peak strain value of the SH-U-F specimen; the SH-S-C-I specimen only attained 22% of the maximum load of the SH-U-F specimen.

- 8- The developed strains in the compression flexural zone were affected by the level of the tensile stresses induced by torsion to flexural compressive forces.
- 9- The ductility of the members was reduced owing to the degree of concrete strut degradation which corresponded with the magnitude of shear stresses produced by the addition of torsion and shear forces and due to the degree of wrapping. Hence, the lowest ductility levels (less than 2) were obtained from SH-S-C-A and SH-S-C-I specimens.
- 10- The joint deformations and level of cracks were related to the joint demands that corresponded the beam forces that transferred into the joint region through the beam reinforcement. The test results showed that the joint demands were affected by the loads interactions and the fibre schemes. The SH-S-C-I and SH-S-C-A specimens experienced joint shear deformations of 71% and 63% of those that were observed from the SH-U-F specimen, respectively. While, their peak loads were only 22% and 29% for the SH-S-C-I and SH-S-C-A specimens, respectively, when compared with the SH-U-F specimen.
- 11- The vertically (90°) oriented CFRP wraps increased the angle of the inclined struts (became more steeply to the transverse direction) and reduced the amount of stress in the longitudinal main rebars. This is reflected in the behaviour of the specimens that strengthened with full-continuous and hoops wraps; where, under the same load conditions they exhibited lower strain levels than the SH-U-C specimen. Also, the full continuous transverse CFRP wrappings enhanced the strut's resistance by decreasing the softening of the concrete and confining the concrete up to the peak load.
- 12- The peak observed strains that developed in the CFRP wraps were very close to the predicted strains according to the effective fibre strains ($\varepsilon_{f,e}$) method. This method incorporates the level of tensile strain in the concrete substrate in its prediction
- 13- It was clear that the beam forces that transferred into the joint region would be underestimated if they were based only on the bending forces (concentric load) without any consideration of the torque and shear forces.

Chapter 5 Long-Term Tests: Results and Discussion

5.1 Introduction

This chapter comprises the results of the time-dependent behaviour of reinforced concrete beam-column joints under long-term loading. The time-dependent developed twist angles and deflection are presented and discussed. The long-term cracking behaviour of the tested specimens is discussed in corresponding to crack patterns, widths, and locations. In addition, this chapter presents strain developments in steel rebars and concrete surface in comparison with predicted time-dependent strains according to Eurocode 2 code (2004).

5.2 Time-Dependent Twisting and Deflection

5.2.1 Long-Term Twisting Behaviour

The long-term twisting of the joint beams under sustained torsional load for all specimens are presented in this section. The LN-U-S specimen was subjected to torsion after 65 days; this was following the stage-1 loading which subjected the specimen to moment loading. The variation in the beam twists due to the torsional loads applied in this stage-2 is discussed in this section. The magnitude of the applied torsional loads corresponded to 90% of the beam's nominal cracking torque based on Eq. 3.5. Hence, initially, no torsional (e.g. inclined) cracks were noticed on the member's surfaces when the torsional load was first applied; several visible cracks did appear over time, after loading. Further details of the crack development and patterns are discussed in Section 5.3. It can be seen in Figure 5.1 that the rate of development of the beam's twisting angle decreased with time in a similar way to that observed by (Allos and Rashid (1989); Anil and Pandit (1980); Goode (1975); Inge Karlsson and Anderson (1974)).

The LN-U-C exhibited the largest torsional rotations; whereas the LN-S-C-H appeared to be the stiffest specimen with lower time-dependent rotations than the unstrengthened specimens. Based on the truss mechanism, during the post-cracking stage, a reduction in the specimen's torsional stiffness can be attributed to the shortening of the inclined compressive strut due to creep and shrinkage in the concrete. However, to satisfy the geometric compatibility conditions of the shear deformation (γ) at each member's side, the transverse

rebars experienced tensile strains (Figure 5.22 in Section 5.5) that corresponded to the level of strut strains and the magnitude of the angle of inclinations (α). Hence, CFRP hoops appear to enhance the member's rigidity by reducing the level of strains in the stirrups and the softening of the concrete; this is related to the degree of confinement. The external wraps also reduced both the creep and shrinkage deformations. The decline in the time-dependent shear strains (γ) readily decreased the twisting deformations. For a member under pure torsion, the twist angle (ψ) can be correlated to the shear strain (γ), according to the thin tube analogy, where $\psi = \frac{P_o}{A_o} \gamma$ (P_o and A_o are the perimeter and area of the shear flow, respectively).

Figure 5.1 shows that the LN-U-S specimen twists less than the LN-U-C specimen; this can be attributed to the effect of the age of loading. After 65 days of loading (stage-1), a considerable amount of creep and shrinkage has taken place, as can be seen in Figure 3.16 and Figure 3.18. These could potentially reduce the specimen twisting levels that were observed in stage-2 after incorporating the torsional forces due to a decrease in the developed creep and shrinkage deformations in the concrete struts that resulted from stage-1 loading conditions. Further, the existing stresses possibly affected the levels of the introduced shear flow and the corresponding struts forces; according to the Mohr's circle relationships, the flexural compression stresses were decreased the amount of the normal tensile stresses produced from torsion in the beam top chords and the principal tensile stresses in the flexural compression zone. This reflected in a significant decrease in the numbers of inclined cracks in the LN-U-S specimen (Section 5.3) at the beam's top face and right side (top part) where the flexural and direct shear forces counteracted the torsional tensile forces.

The results indicate that the long-term twisting can be presented as a hyperbolic function (Eq. 5.1), which was proposed by Ross (1937) and Lorman (1941) and was further defined by Neville et al., 1983. By using a linear regression analysis, very strong relationships were obtained with R^2 values of no less 0.98, as shown in Figure 5.2. Based on the hyperbolic formula, time-dependent twisting deformations for a period of 365 days were predicted in order to identify the growth level of the beam's rotations compared with instantaneous twisting angles and the angles measured at 90 days loading age.

$$\psi_{(t, t_o)} = \frac{(t - t_o)}{A + B (t - t_o)} \quad \text{Eq. 5.1}$$

Where,

$\psi_{(t, t_o)}$ = twist angle at any time

$(t - t_o)$ = loading time

B= the slope of the straight line that is graphically computed from plotting $[(t - t_o) / \psi (t, t_o)]$ against $(t - t_o)$ of the tests results

A= the intercept on the ordinate of the plotted straight line

Figure 5.3 reveals that the long-term twist angles after 90 days under load were 2.24, 5.47, and 2.1 of the initial angles, when the torsional load was applied to LN-S-C-H, LN-U-C, and LN-U-S, respectively. It is also noted that the development rates of the beam rotations were higher during the first ten days of loading, when cracks started to appear. The development rate of LN-U-C increased more significantly than that of LN-S-C-H and LN-U-S, as it experienced much more severe cracking than the other specimens and these cracks took about 30 days to stabilise (no new cracks were seen after 30 days). Despite these rapid increments in the beam rotations during the early ages of loading, it was found that the rise of the predicted twist angles at an age of 365 days was only 6%, 18%, and 7% greater than that obtained at 90 days. These observations confirmed the influence of new cracks and the extent of the already formed cracks on the increase of the time-dependent rotations during the early stages. Interestingly, under the same loading conditions, the twist amounts of the CFRP wrapped specimen (LN-S-C-H) represents 41% and 37% of the LN-U-C specimen at ages of 90 and 365 days, respectively. Where, after a period of one year, using CFRP hoops substantially enhanced the member's rotational rigidity by 2.7 times that of the un-strengthened sections.

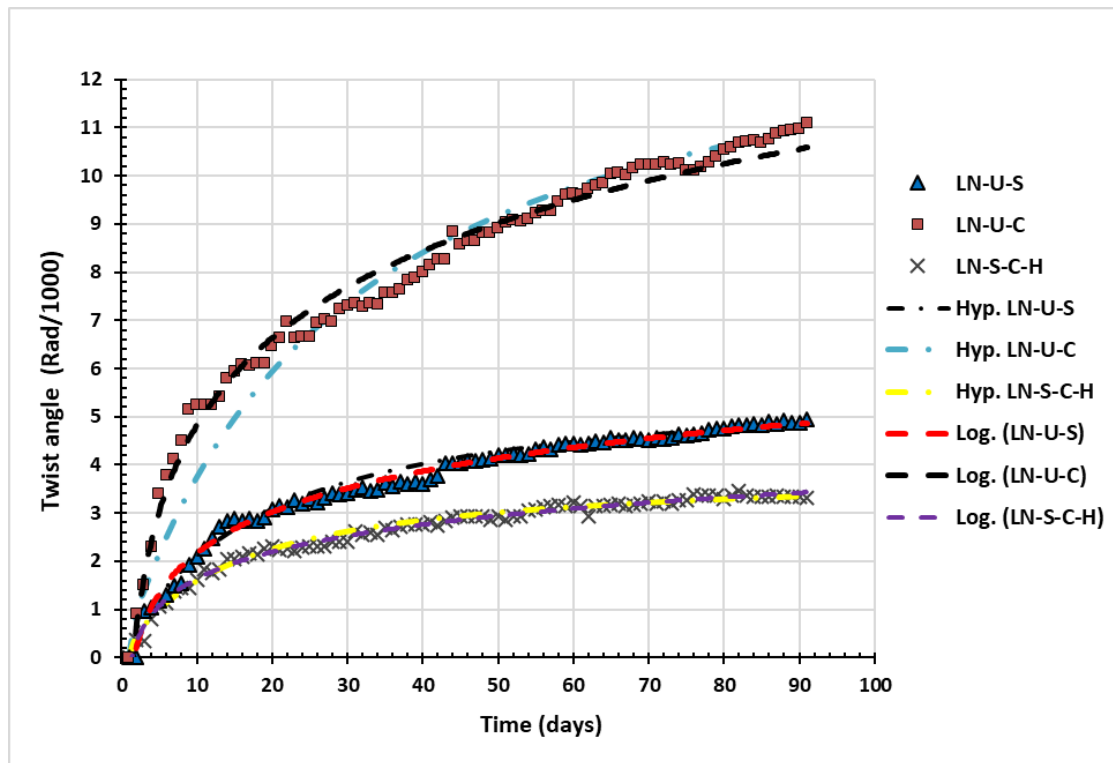


Figure 5.1: Developed end-beam twist angles with time for all specimens

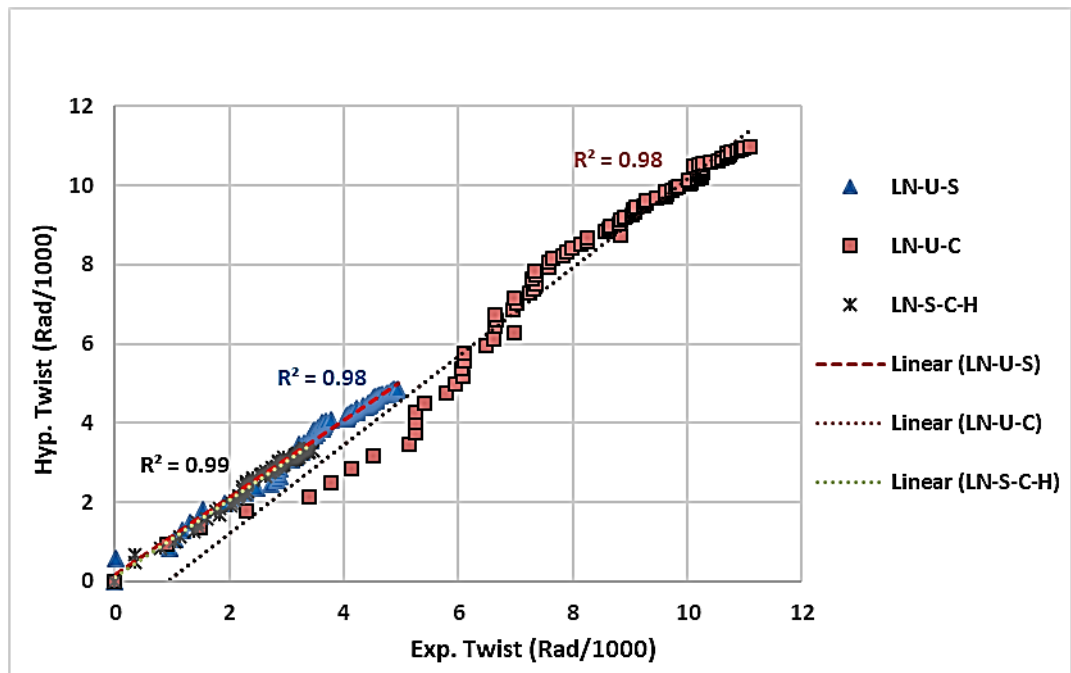


Figure 5.2: Correlation between experimentally measured and predicted twist angle using hyperbolic functions

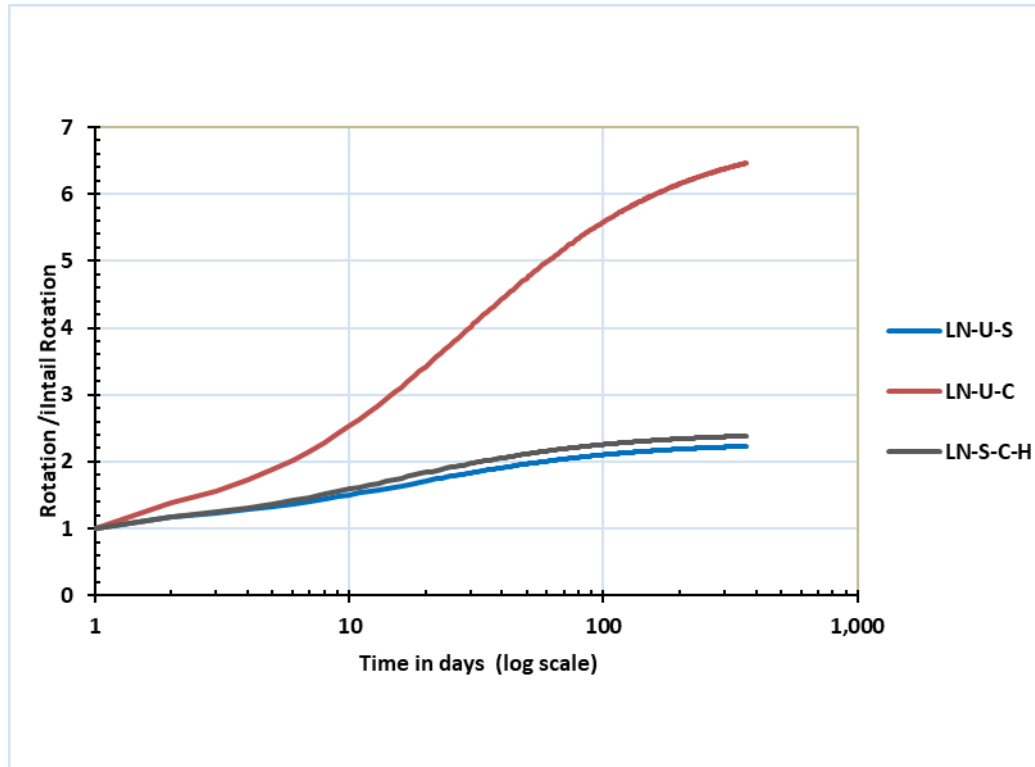


Figure 5.3: The increase in the long-term beam twist angles to instantaneous twisting with time

5.2.2 Long-Term Deflection

The LN-U-S specimen beam tip deflection is presented in Figure 5.4. Here, the specimen was initially under a sustained flexural load of about 30% of its ultimate bending capacity (stage-1). At the end of stage-1, it was subjected to torsional load, as described in Chapter 3. (Note: The LVDt results for the other specimens (LN-U-C and LN-S-C-H) were found to be inconsistent; this was likely due to the limited sensitivity of the LVDTs when measuring such small-scale time-dependent deflections observed due to the low bending loads. The aim of testing these two samples was to investigate the influence of beam torsion on the time- dependent rotations, strain development, crack formation, and strengthening wrap effects, which was achieved under predominately torsional loads.

The deflection of the LN-U-S specimen was compared with the predicted deflection according to the Eurocode 2 (2004) model, as shown in Figure 5.4. The Eurocode 2 (2004) model is based on computing beam curvatures under flexural forces, by considering compressive creep in the effective modulus of

elasticity, the tension stiffening effect and the shrinkage strains. Further details about the Eurocode 2 (2004) model are presented in Section 5.4. The Eurocode 2 model predicts the deflection through loading stage-1 (only flexural loads), and a mean value of 0.96 was found for the ratio of the test to the predicted deflections with a 5.6% coefficient of variation (COV). However, it is notable that the code model overestimated the deflection levels at the end of stage-1 by 9.3%. Eurocode 2 (2004) suggests to fix the coefficient taking into account the loading period (B) constant for member's under sustained load; this suggestion tends to increase the loss of tension stiffening that overestimates the predicted curvature (Forth et al., 2014).

During stage-2, it can be seen that the torsional forces considerably increase the deflection of the specimen. Also, when compared with the code model at the end of stage-2, the code under-predicts the total deflection by around 44%. This reveals that it is not appropriate to use the Eurocode 2 model to predict the deflection of flexural members that experience additional torsional forces. These increments in the beam deflection are mainly attributed to the growth of torsional and direct shear induced cracks (see Figure 5.5) that corresponded to the level of torque, in addition to the level of long-term concrete deformations (creep and shrinkage). As a result, the torsional cracks severely affected the member's stiffness.

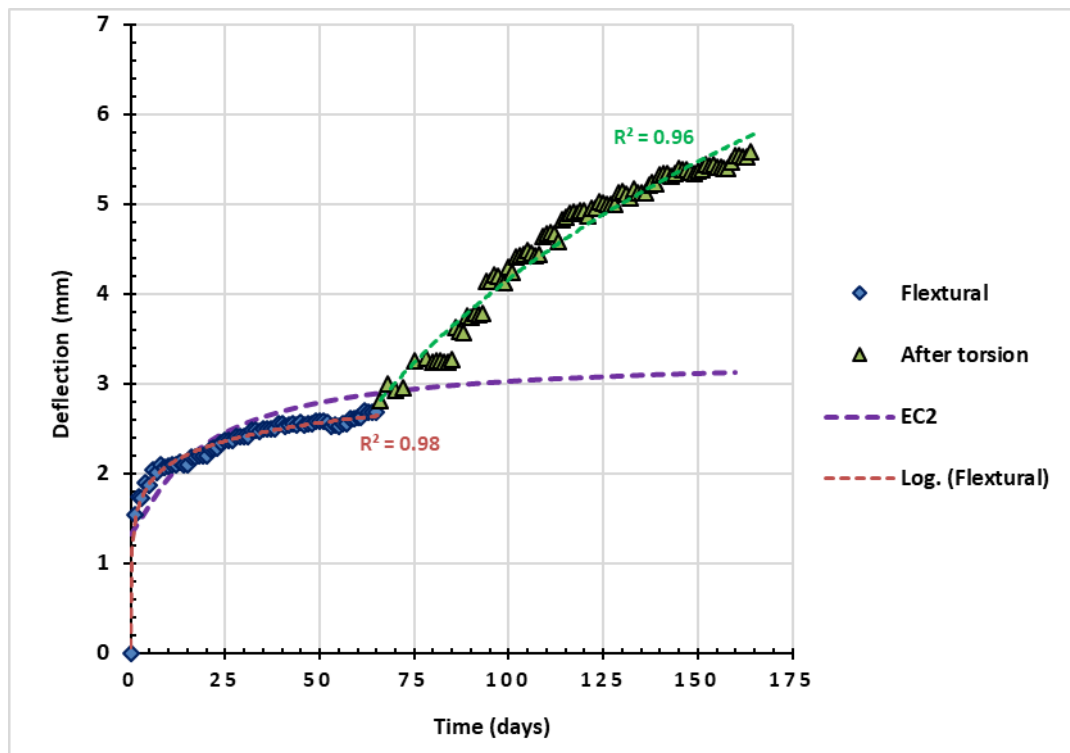


Figure 5.4: Developed end-beam deflection with time for LN-U-S specimen and Eurocode 2

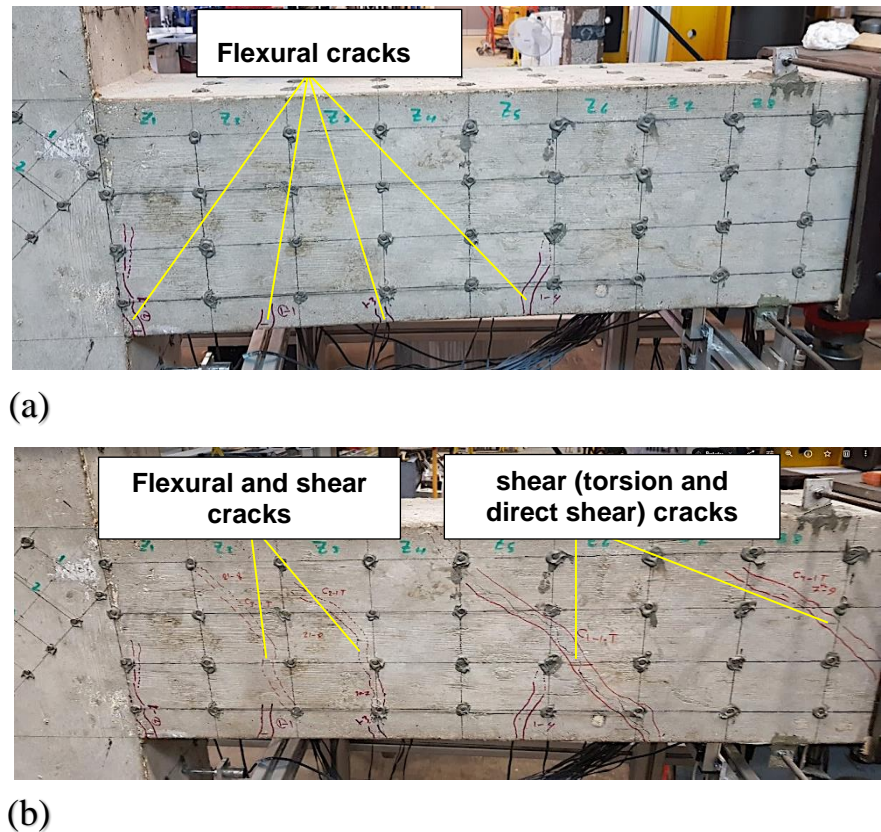


Figure 5.5: Developed cracks in LN-U-S specimen (a) at the end of stage-1 (b) at the end of stage-2

5.3 Observed Cracking

As discussed in the previous section, no inclined cracks were observed when the torsional loads were first imposed for all specimens. However, for LN-U-S specimen that subjected to 2 successive stages , a number of visible flexural cracks were initiated in the beam tension zone when the load applied at stage-1. This is because the imposed sustained load was about two times larger than the M_{cr} . After the appearance of any torsional or flexural cracks on the specimen's surfaces, the crack width development was regularly measured using a microscope, and the results were graphically presented against time as presented in Section 5.3.1.

Figure 5.6a, Figure 5.6b, and Figure 5.6c show the number of cracks, locations, and the patterns that formed in the beam area for the three specimens at the end of loading durations. Here, the beam length was divided into 8 equal zones (a 100 mm wide) in order to monitor the surface strain and crack development across the beam sides. It is noted that several inclined

cracks propagated in the LN-U-C and LN-U-S specimens due to the time dependent torsional and shear forces. For the LN-U-C specimen, the first visible cracks appeared after two days of loading, while most of cracks were observed in the first month of loading, as shown in Figure 5.7a. However, the cracking level in terms of crack widths and crack number was significantly higher during the first ten days. This was accompanied by substantial rates of creep and shrinkage during early stages of loading. For the strengthened specimen (LN-S-C-H), no new visible cracks were seen after a month of loading, while the first cracks were noticed on the fourth day after the load was applied (Figure 5.7b).

Figure 5.7c shows the crack development for the LN-U-S specimen during the two stages of loading. At stage-1, several flexural cracks occurred in the flexural tension zone (the beam's bottom) at the beam region that exhibited large bending stresses near the column's face. The growth of the time-dependent flexural cracks correlated with the increase in beam curvature that resulted from the creep and the shrinkage induced curvature for unsymmetrical reinforced sections. After the torsion was applied during stage-2, the first torsional inclined cracks were seen after two days and no further cracks were noticed after 20 days of the stage-2 loading period. A smaller number of shear cracks were observed in the LN-U-S specimen, which can be attributed to the age of loading and the interaction between the existing and introduced stresses at stage-2, as described in the previous section. Significantly, the most important part of the creep deformation had already developed in the beam zones closer to the column, which were subjected to high flexural stresses. However, these zones experienced some shear cracks (C_T1 , C_T2 , and C_T5), where flexural cracks increased the shear stresses above these crack regions. The shear cracks were further enhanced due to the effect of torsion increasing the shear stresses in the beam's sides. This is because the cracks initiate when the principle tensile stresses resulting from the combined action of bending, torsion, and shear exceed the concrete's tensile strength.

There was no crack noticed in the columns at the joint's region during the test's durations for all specimens. Since the columns were predominately under axial compressive load in which could enhance the cracking stiffens of the column (Hamil, 2000b). Further, the column axial loads can induce significant time-dependent compressive strains in the column's region correspond to level of concrete creep and shrinkage developments (Gilbert

and Ranzi, 2010). These compressive strains could reduce any tensile strain developed from torsional deformations.

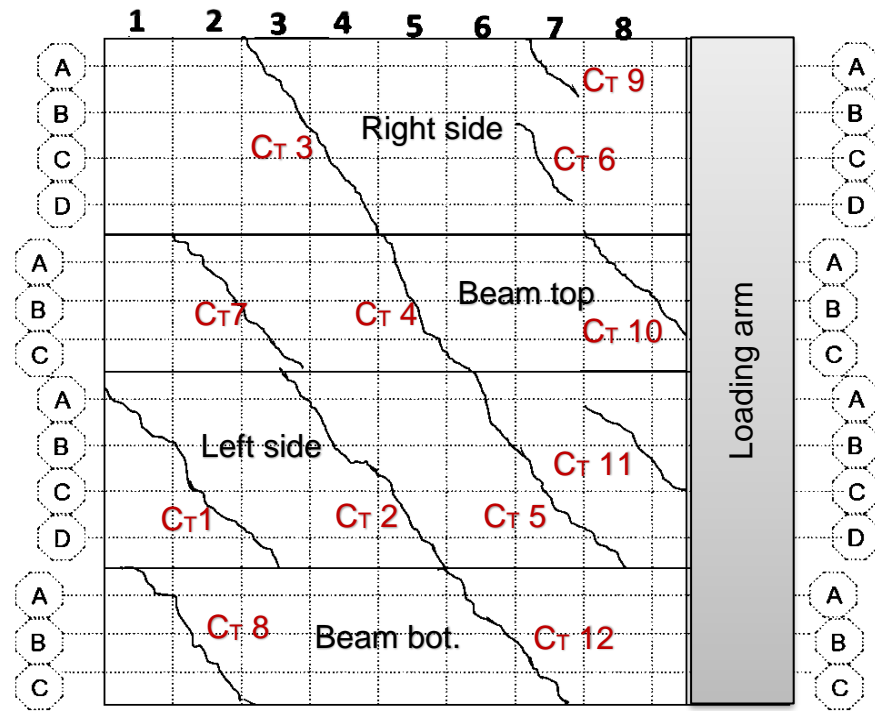
5.3.1 Crack Widths

The measured crack widths were compared with ACI 224R-01 (2001) and the Eurocode 2 (2004) recommendations. Reasonable crack width limits are suggested in accordance with durability and aesthetic requirements, where 0.3 mm was considered the maximum crack width (in moderate humidity exposure conditions). It can be seen in Figure 5.7a (LN-U-C specimen) that the widths of most of the cracks that appeared in the early stages of loading exceeded the code's limit. Furthermore, there was a significant widening of the torsional cracks over time. For example, when it first appeared, the maximum C_{T3} crack width was 0.15 mm, while at the end of the loading period it was 1 mm (about 7 times larger than the initial width). This time-dependent increase in the crack's widths corresponded with the shear deformation development and the reduction in the beam's rotational rigidity, which can be mainly attributed to the long-term deformations in the concrete struts induced by creep and shrinkage (as discussed earlier).

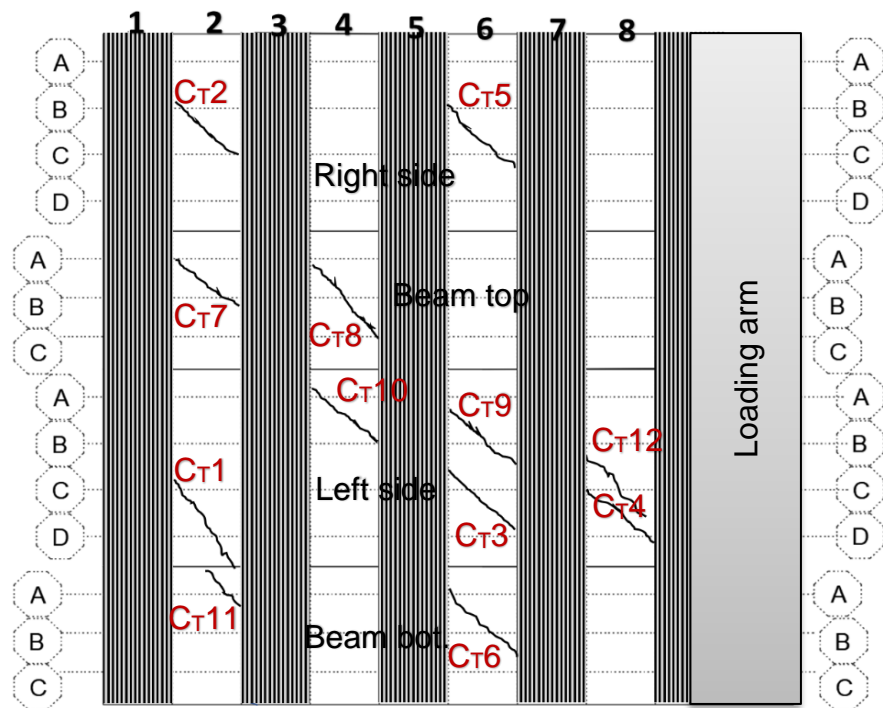
Figure 5.7b reveals that the width of the cracks that developed in the LN-S-C-H specimen were substantially lower compared to those of the unstrengthened specimen (SH-U-C). From this figure it can be seen that the maximum crack widths were consistent with the codes' recommendations. The CFRP hoops effectively enhanced the shear cracking resistance of the concrete by arresting crack propagations through resisting tensile forces and providing concrete confinement. Further, the CFRP wraps influenced the drying shrinkage and drying creep deformations by lengthening the drying path length. However, it was observed that the number of visible cracks were not reduced when using CFRP warps.

The width of the flexural cracks (C_F) corresponded to the level of bending stresses, given that the maximum observed crack widths (C_{F1} and C_{F6}) were at the position of the maximum bending region (zone 1), near the column, as shown in Figure 5.7c. During both loading stages, the flexural cracking level for the LN-U-S specimen was within the code's limit (0.3 mm). However, most of the torsional cracks (C_T) were less than the 0.3 mm width limit, although the widening of C_{T3} at the left side reached 0.48 mm by the end of the loading period. This was thought to be because the maximum induced shear stresses

occurred at the beam's left side, where both torsional and direct shear forces acted in the same direction. Also, as previously discussed, a greater cracking level would be expected when the torsional loads were applied during the earlier stage (large creep and shrinkage rates).



(a)



(b)

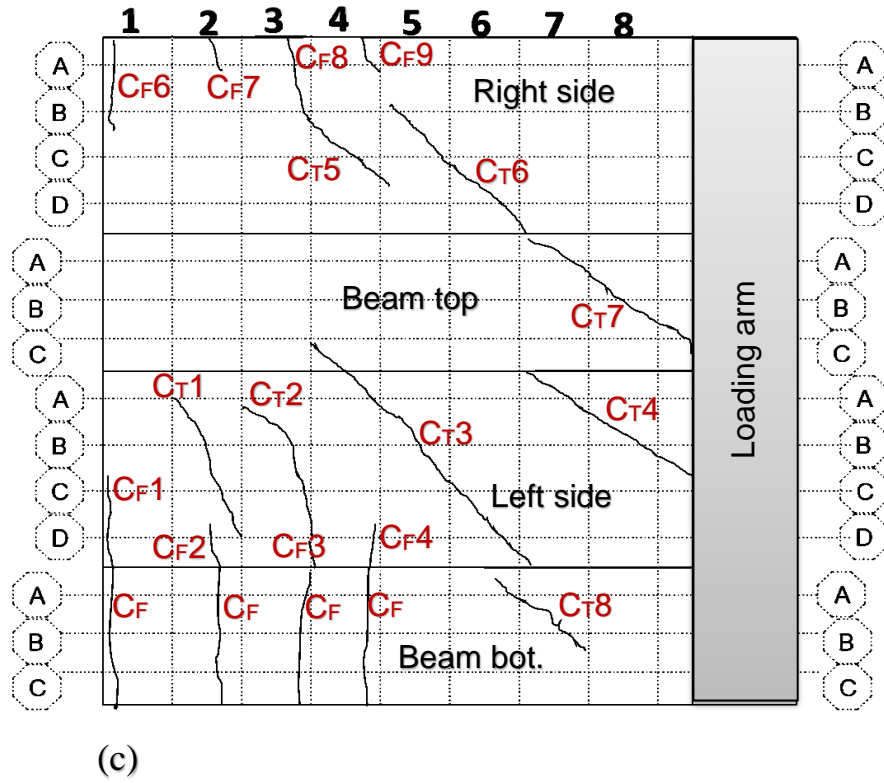
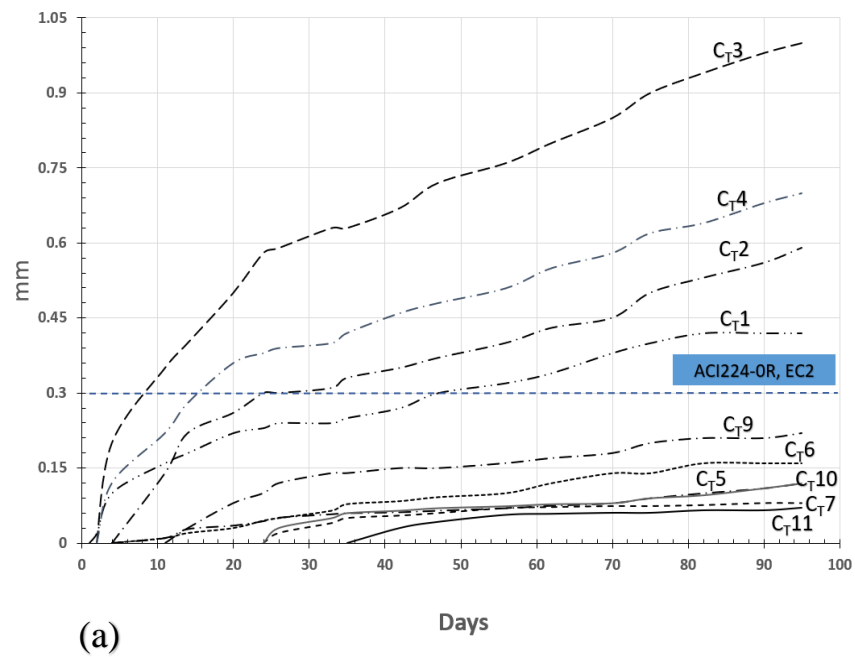


Figure 5.6: Observed cracks on the beam's sides at the end of loading durations (a) for LN-U-C specimen (b) for LN-S-C-H specimen (c) for LN-U-S specimen



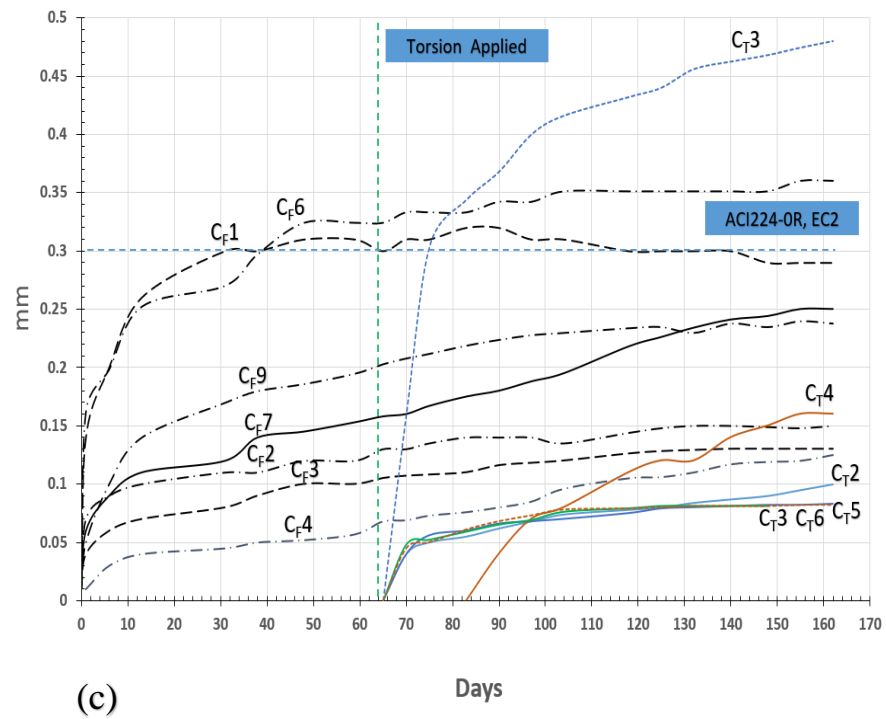
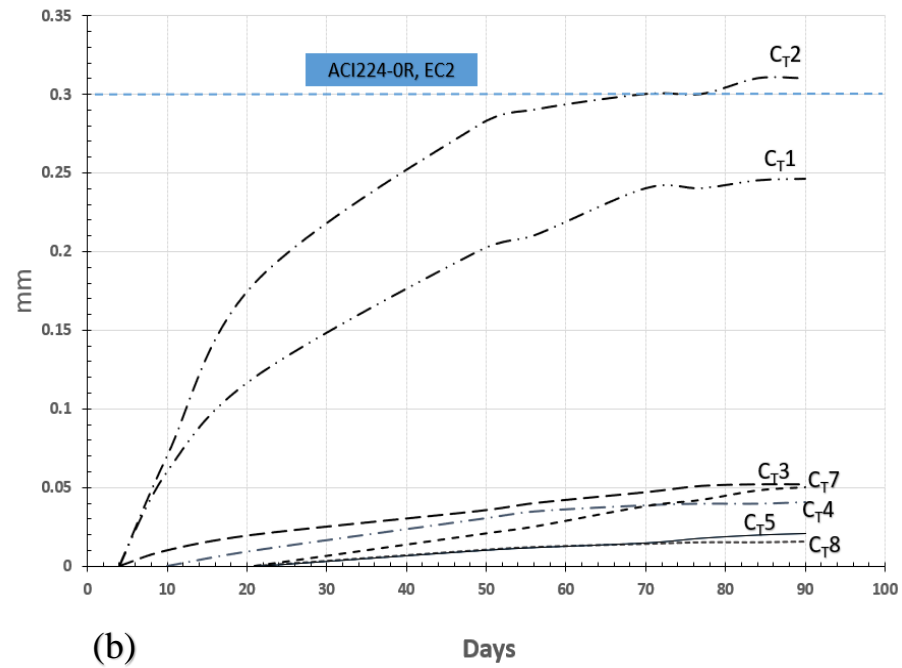


Figure 5.7: Developed crack widths over time (a) for LN-U-C specimen (b) for LN-S-C-H specimen (c) for LN-U-S specimen

5.4 Surface Strains Measurement

The surface strains in concrete were measured by using several DEMEC points that were installed at different levels (rows) on the four sides of the beam, along its length (left side, right side, top of the beam, and bottom of the beam) as presented in Figure 5.8. Each row was divided into 8 of 100mm zones in order to monitor the strain variations over the wrapped and unwrapped regions, as well as across the cracks, in greater detail. No research works have been found in the extant literature that demonstrated the effects of sustained torsional load on the variations of surface strains through the section's sides and depth. As such, this section presents detailed graphs of the development of strain on all sides of the beam as well as a comparison with the predicted surface deformations based on Eurocode 2 (2004).

	Z1	Z2	Z3	Z4	Z5	Z6	Z7	Z8	
SR									Top Side
Mid									
SL									
Top									Left Side
Mid1									
Mid2									
Bot.									
SL									Bot. Side
Mid									
RL									
Bot									Right Side
Mid2									
Mid1									
Top									

Figure 5.8: DEMEC points rows across the beam's depth and sides

5.4.1 Evaluation of Surface Strain from the Beam's Curvature Based on Eurocode 2 (2004)

The measured surface strains for specimens under combined loads were compared with the predicted strains in accordance with Eurocode 2 (2004), in order to quantify the influence of torsional loads on the longitudinal surface deformations. Eurocode 2 (2004) predicts the time-dependent beam curvatures (and hence strains) via the superposition of creep and shrinkage curvatures for members predominately under flexural loads. The calculations of the time-dependent curvatures due to the applied loads considers the creep effects by adopting the effective modulus of the elasticity method (Eq. 2.30).

A good agreement was obtained between the predicted deformations according to the code formulae and deformation measured during loading stage-1 (flexural loads) for the LN-U-S specimen, as presented in Sections 5.2.2 and 5.4.3. The following is a summary of the code equations that were used to compute the long-term beam curvatures:

I. The beams curvatures ($1/r$) due to long-term applied load

$$1/r = \varrho(1/r)_{cr} + (1 - \varrho)(1/r)_{uc} \quad \text{Eq.5.2}$$

Where;

$(1/r)_{cr}$, and $(1/r)_{uc}$ = the curvature for cracked and uncracked sections, respectively

as $(1/r)_{cr}$ and $(1/r)_{uc}$ are calculated from Eq. 5.2.1

$$\left. \begin{aligned} (1/r)_{cr} &= \left(M / E_{eff} I_{cr} \right) \\ (1/r)_{uc} &= \left(M / E_{eff} I_{uc} \right) \end{aligned} \right\} \quad \text{Eq. 5.2.1}$$

I_{cr} and I_{uc} = the second moment of area for cracked and uncracked sections, respectively

E_{eff} = the effective modulus of elasticity for concrete

ϱ = the coefficient allowing tension stiffening given by Eq. 5.2.2

$$\rho = 1 - B \left(\frac{M_{cr}}{M} \right)^2 \quad \text{Eq.5.2.2}$$

B = the coefficient taking into account the loading period (0.5 for sustained load and 1.0 for a single short term load)

M, M_{cr} = the applied and cracking bending moments, respectively

II. The beams curvatures ($1/r_{sh}$) due to shrinkage

$$1/r_{sh} = \varepsilon_{sh_t} \alpha_e \frac{S}{I} \quad \text{Eq.5.3}$$

Where;

ε_{sh_t} = the free shrinkage strain at time given (t)

α_e = the effective modular ratio given by $\alpha_e = \frac{E_s}{E_{eff}}$

E_s = the modulus of elasticity for steel rebars

S = the first moment of area for the reinforcing rebars about the section's centroid

I = the second moment of area for cracked and uncracked section

5.4.2 Surface Strains for Specimens under a Single Stage Loading

The time-dependent longitudinal surface strains in the concrete of the LN-U-C and LN-S-C-H specimens are presented in Figure 5.9 and Figure 5.10. These figures show the strain development at the beam's left and right side, where the four levels of DEMEC rows for each zone region are defined as Top, Mid1, Mid2, and Bot (Figure 5.8). Figure 5.11 illustrates the surface strain occurring in the beam's top and bottom face of the LN-U-C specimen, where at each face, three levels of DEMEC's were measured. The three levels were denoted; SL (left side of the face); Mid (mid of the face); and SR (right side of the face). The top and bottom surface strains for LN-S-C-H specimen were not measured due to space limitations on the surfaces.

The above-mentioned graphs reveal significant variations through the levels of each zone, between zones, and the beam's four sides, due to long-term torsional loads. It can be seen from Figure 5.9 that the surface strains for each zone were varied at the beam's right and left sides. For example, in zone 1

(Z1), the top and bottom levels of the beam exhibited time-dependent tensile and compressive strains at the left side of the beam (Figure 5.9a, Z1-L.side), respectively. Whereas, the strain measurements that were taken from the right side varied from increasing (extension) at the bottom and Mid 2 levels to decreasing (shortening) at the top and Mid1 levels. These variations in strain between the beam zones, sides, and levels also occurred in the LN-U-C beam's top and bottom sides, as shown in Figure 5.11. For the LN-U-C specimen, some zones at the right side and the top of the beam (e.g. Figure 5.9b, Z2-R.side; Figure 5.9e, Z5-R.side; Figure 5.9f, Z6-R.side; Figure 5.11c, Z4-top; Figure 5.11f, Z7-top) experienced compressive strains throughout the beam's depth. Similarly, compressive strain measurements were obtained at Z4-L.side, Z4-R.side, Z5-R.side, and Z6-R.side zones for the strengthened specimen (LN-S-C-H), as shown in Figure 5.10c, d, and e.

These observations correspond with the space truss mechanism, since it has been identified in the literature that after the initiation of cracks, the torsion is resisted by the inclined compressive stress in the concrete struts and that the concrete can be assumed to carry no tension. The longitudinal components of the diagonal compressive stress field are equilibrated by a tensile stress in the rebars. Furthermore, these inclined compressive stress field tends to push off the beam corners and those produced tensile stresses in the stirrups (Collins and Mitchell, 1980; Mitchell and Collins, 1974).

The induced long-term deformations (creep and shrinkage) potentially increased the compressive strains over time in the inclined concrete struts, which lead to an increase in the shear deformations and the beam's rotation levels. Meanwhile, after cracking, it is believed that the time-dependent concrete tensile strains, that were orthogonal to the compressive struts, developed over time to satisfy the compatibility conditions, since the level of principal tensile strains corresponds to the geometric relationships between the principal compressive strains, longitudinal, transverse, and shear strains. Hence, the surface strains varied along the beam zones, levels, and sides in correlation with the direction of the compressive stress field, the angle of inclination, the time-dependent deformations in the concrete struts, the longitudinal flexural strains and the crack propagations through the beam zones.

It is noticeable that the strains developed at a high rate in the early stages of loading and decreased at various decreasing rates over time (see Figures 5.9, 5.10, and 5.11); this corresponds to the creep and shrinkage developments

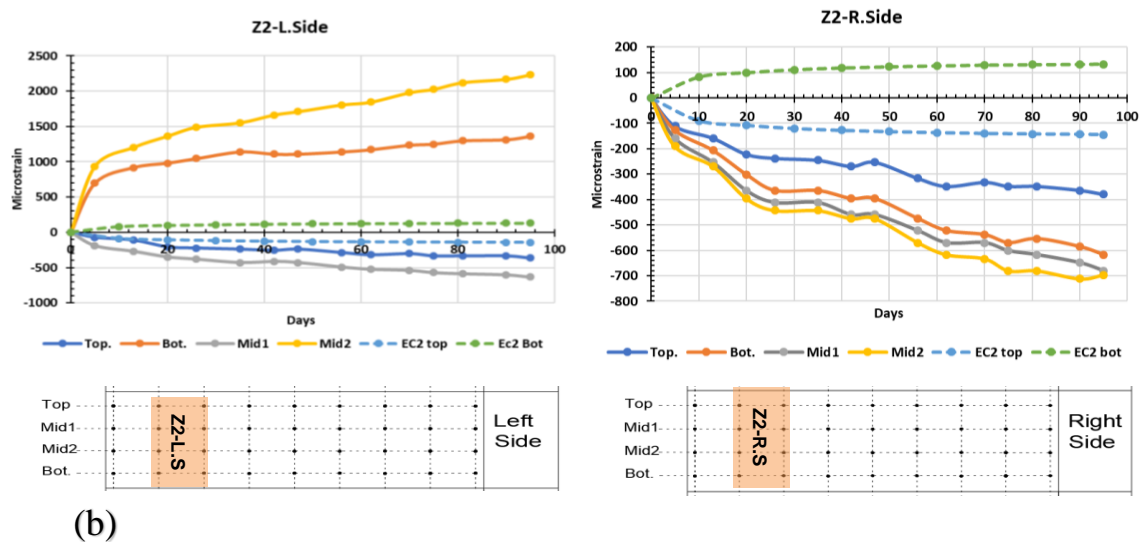
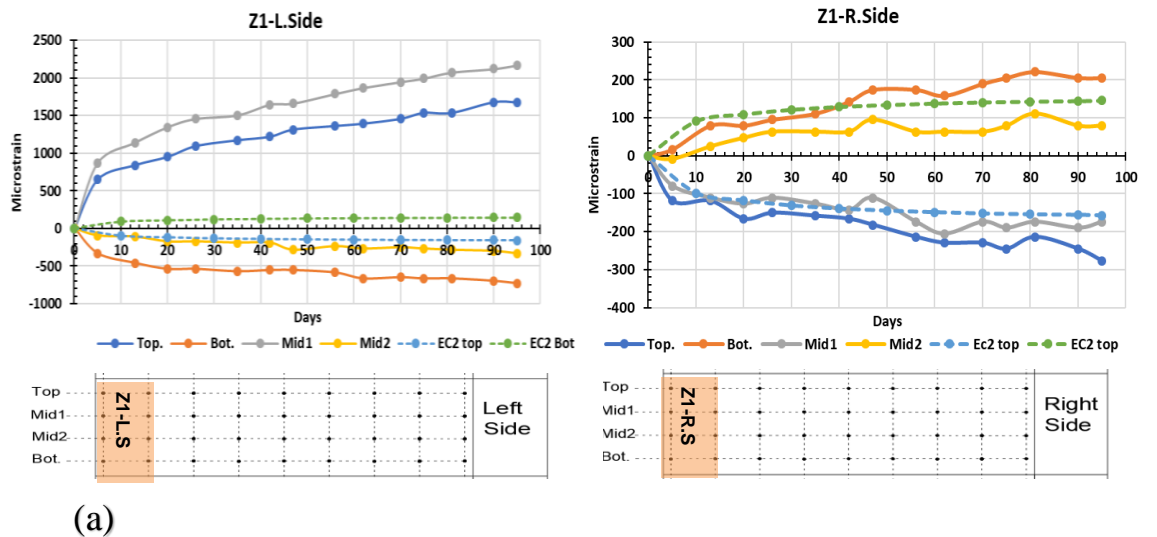
and stress to strength ratio. As the regions exhibited large tensile stresses, significant rates of time dependent strains occurred due to microcracking of the concrete (Forth, 2015). Hence, in comparison to the observed cracks (Figure 5.6), it can be seen from Figure 5.9 that the longitudinal tensile strains largely developed in the zone's levels and close to a torsional crack. For example, levels at Z1-L.side (Top and Mid1), Z2-L.side (Bot and Mid2), and Z3-L.side (Bot) were affected by a C_{T1} crack developed at the LN-U-C Left side. Likewise, the developed strains (about 5000 micro-strain) at level Z3-R.side (Bot and Mid2) and Z4-R.side (Mid1) which influenced by C_{T3} crack on the LN-U-C right side. Similar trend can be observed for other zone's levels (Figure 5.11) close to a formed crack such as Z2-Bot (SL and Mid) and Z3-Bot (SR) and developed C_{T8} crack. While for strengthened specimen (Figure 5.10), these increases were only noticed at Z2-L.side (Bot and Mid2), Z2-R.side (Mid1 and Mid2), and Z3-R.side (Top) which these zone's levels affected by C_{T1} , C_{T2} , and C_{T10} , respectively. However, the levels that were relatively far from the crack were under compression and corresponded to the concrete strut deformations.

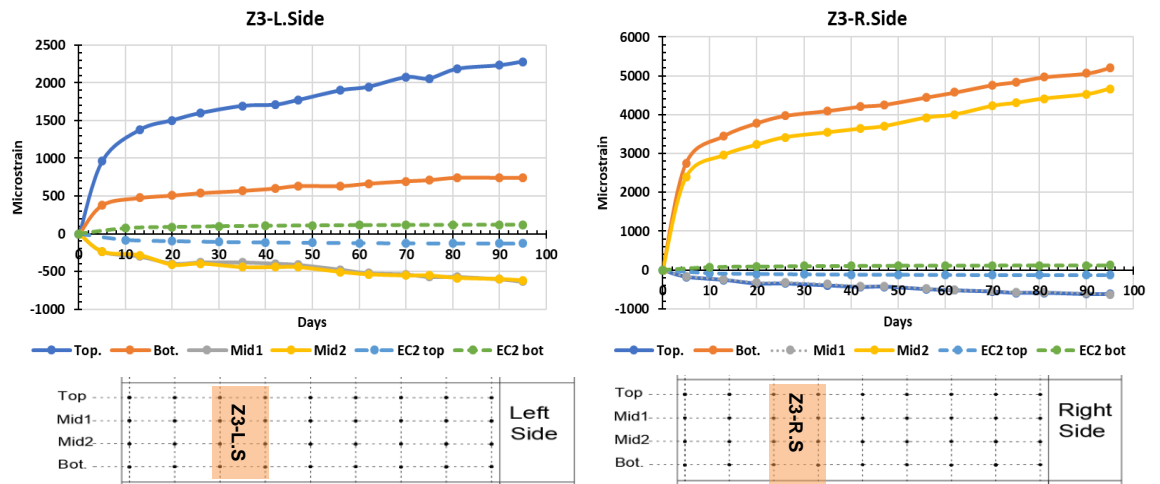
These measured results indicate that severe tensile strains can be promoted at any level of the beam zones due to sustained torsional loads. Nevertheless, the use of CFRP hoops reduced the level of tensile strains and crack propagation, as discussed earlier in the previous section. Hence, it was found that through the beam zones and sides, there were further levels (DEMEC rows) under compressive strains when compared with the unstrengthened specimen (LN-U-C).

In accordance with the predicted time-dependent surface strains based on Eurocode 2 (2004), Table 5.1 and Table 5.2 indicate how torsional forces can excessively alter the longitudinal strains through the beam's length, levels, and sides. Apart from the sharp increases in the tensile strains across the torsional diagonal cracks, it can be seen from Figure 5.9 significant increases in compression strains for unstrengthened specimen (e.g. Z1-L.side, Z2-L.side, Z2-R.side, Z3-L.side, Z4-L.side, Z5-R.side, Z6-L.side, Z7-L.side, and Z8) occurred in accordance with the diagonal principle compressive stresses and concrete time-dependent deformations.

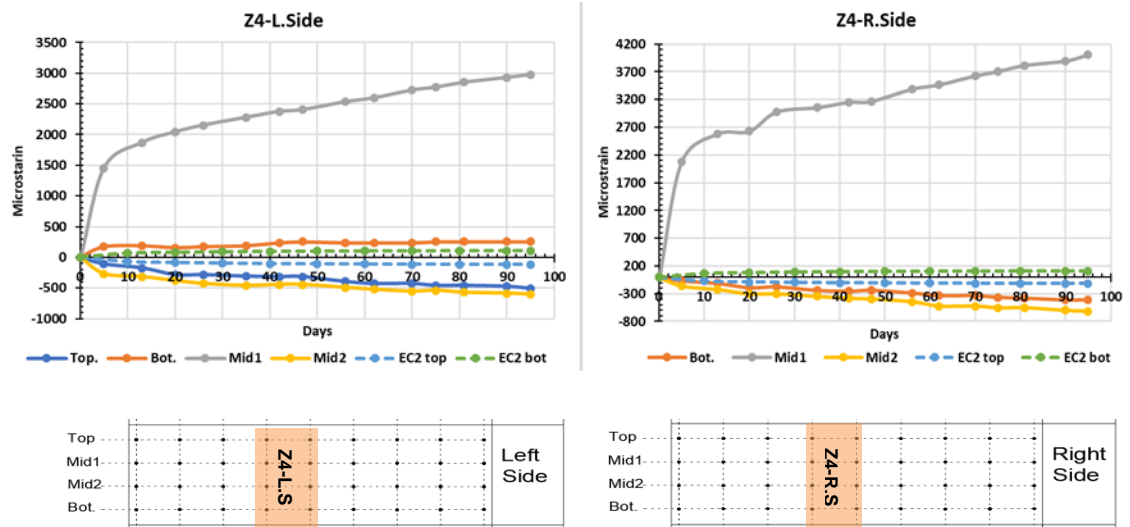
For the un-strengthened specimen (LN-U-C), Table 5.1 showed that the average increase in the time dependent strains induced by sustained torsional loads was up to 8.6 times than the predicted bending induced strains according Eurocode 2 (2004). While the average increase in the

instantaneous strains due to torsion was 1.8 times than the bending strains (Eurocode 2). Interestingly, the LN-S-C-H specimen (Table 5.2) with CFRP wraps demonstrated a lower disparity with the predicted strains (average of 2.4 times larger than the bending induced strains) when compared with the un-strengthened LN-U-C specimen. This observation was more obvious in the beam zones (e.g. Z3, Z5, Z7) that were externally wrapped, since vertically oriented CFRP hoops reduced the shear stresses in the concrete struts in the strengthened regions. Along the horizontal direction of the beam length, the influence of transverse CFRP wraps on longitudinal normal stresses was unappreciable and there was little difference between the measured horizontal strains and the calculated flexural strains. Despite this, the code prediction formulas do not consider the CFRP fibre's contributions on the member curvatures.

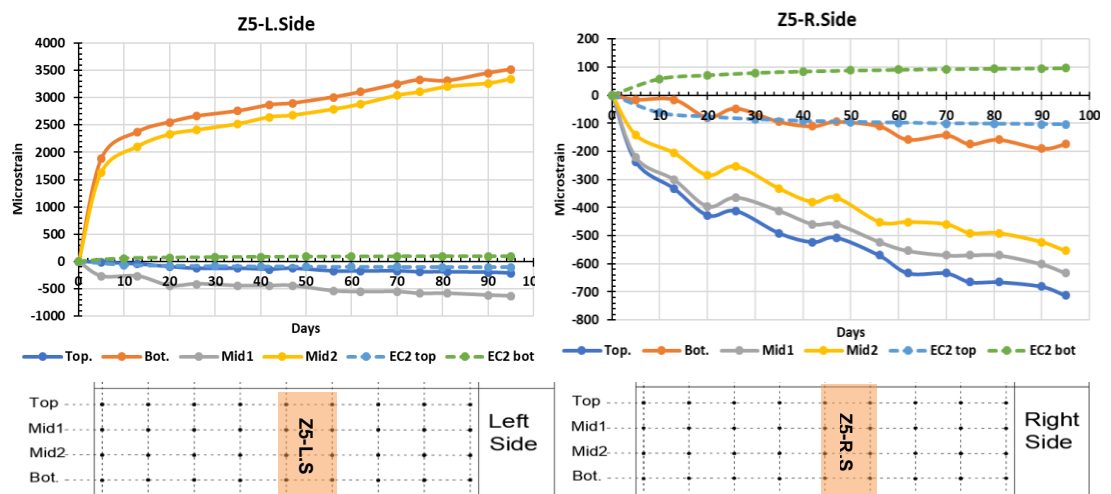




(c)



(d)



(e)

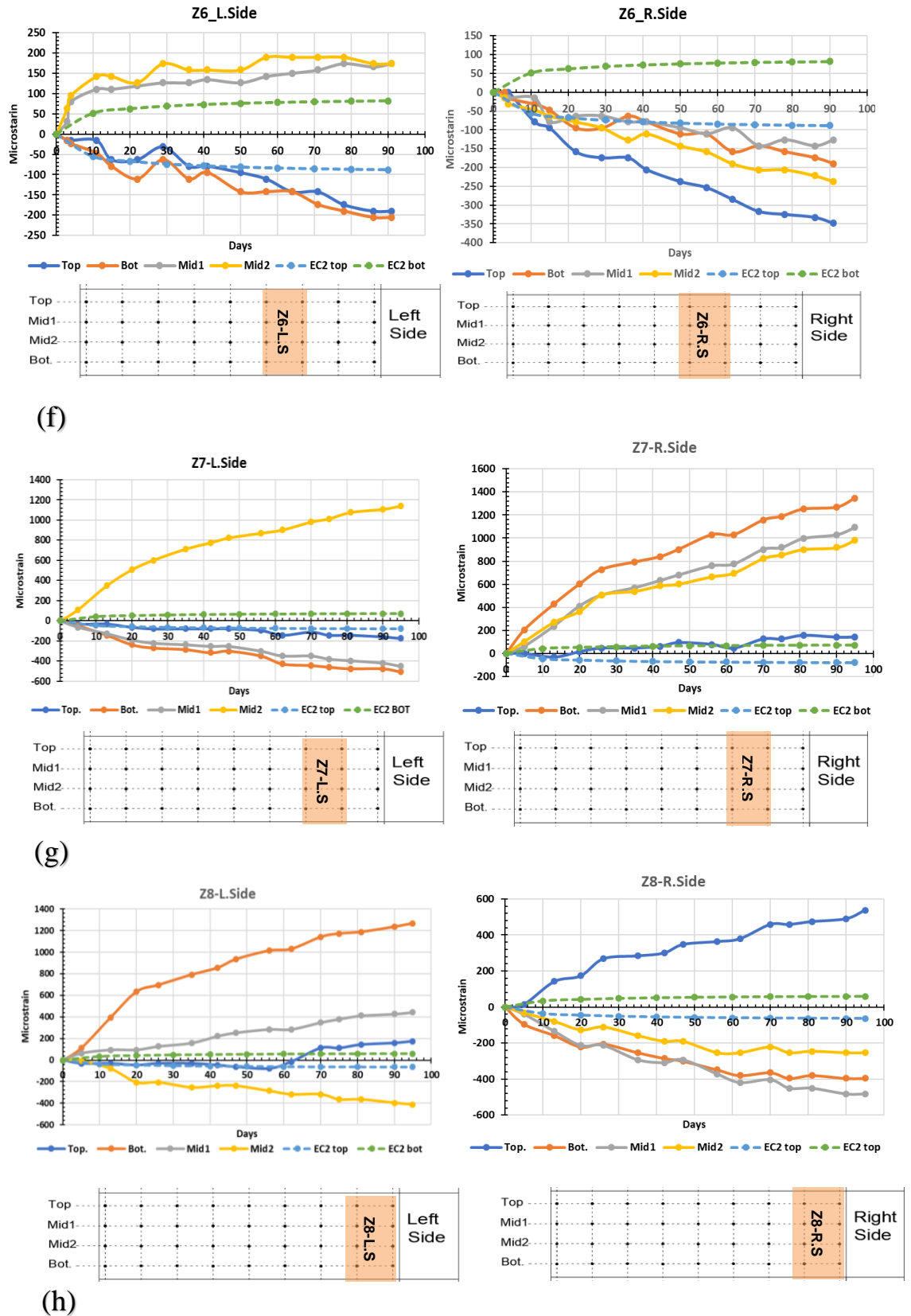
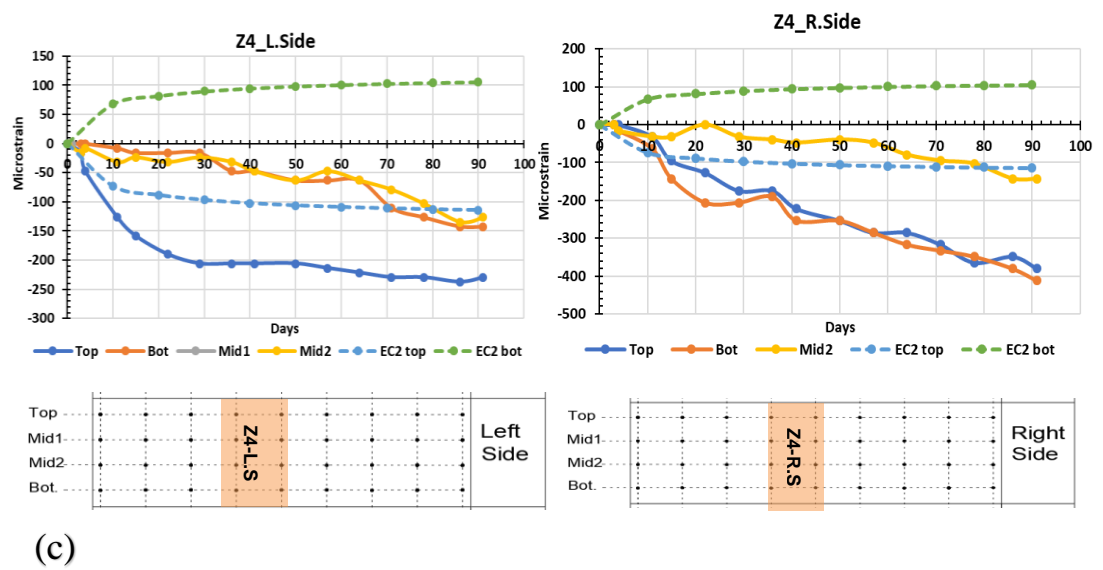
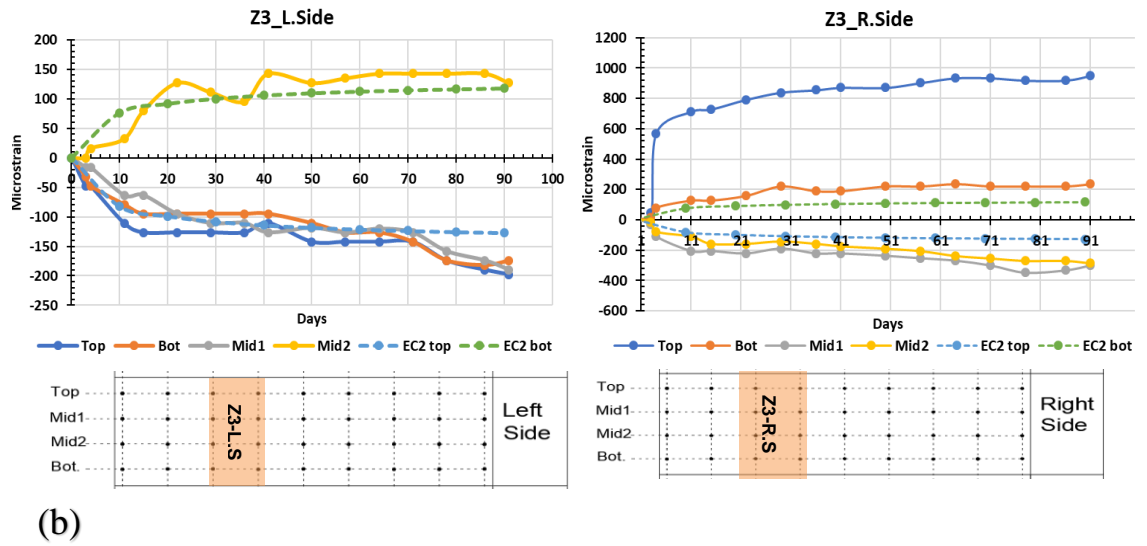
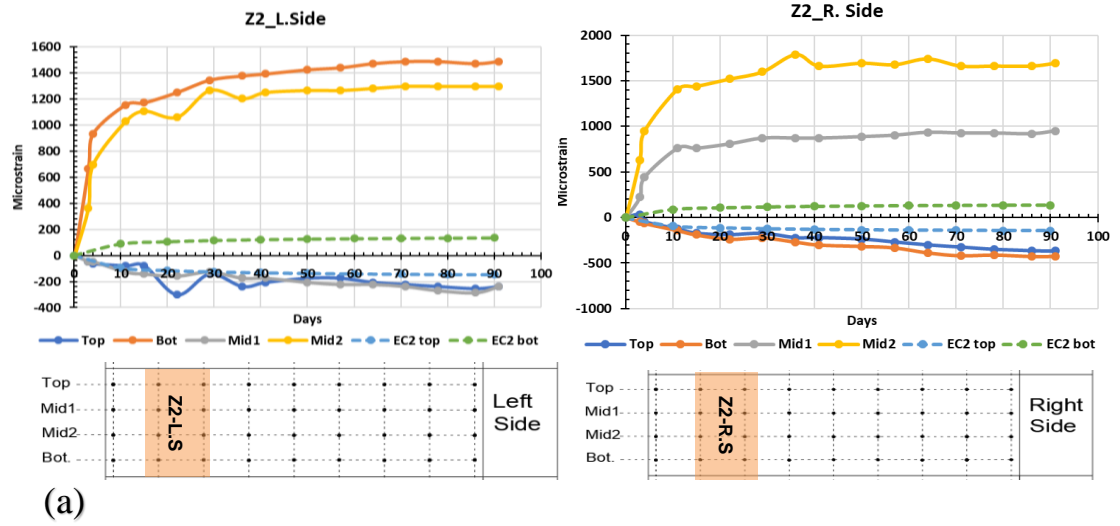
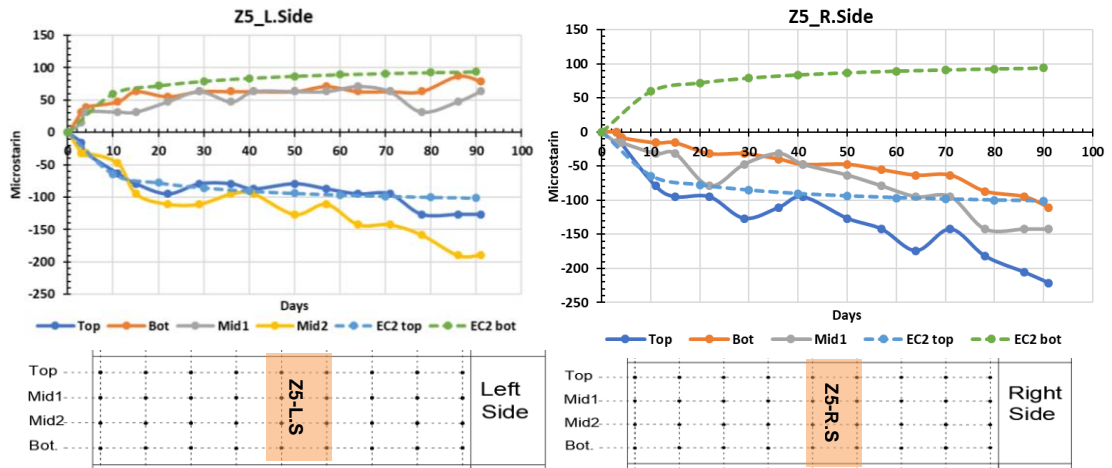
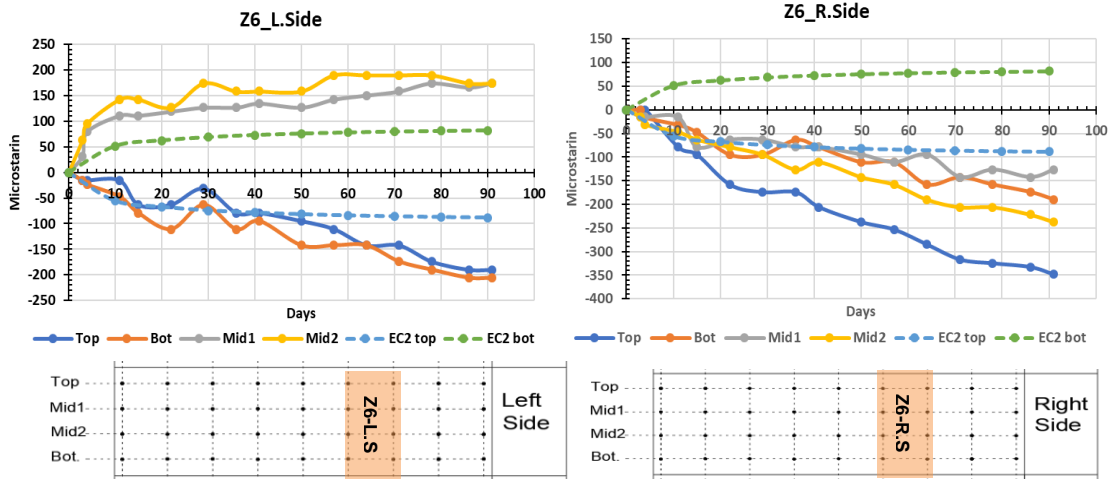


Figure 5.9: The developed surface strains at the beam's right and left sides for the LN-U-C specimen (a) Zone 1 (b) Zone 2 (c) Zone 3 (d) Zone 4 (e) Zone 5 (f) Zone 6 (g) Zone 7 (h) Zone 8

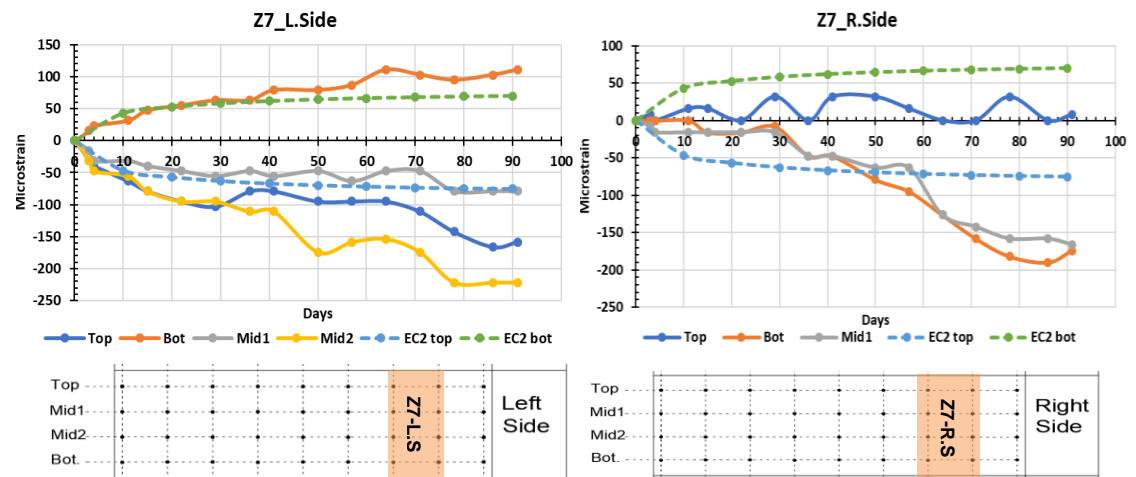




(d)



(e)



(f)

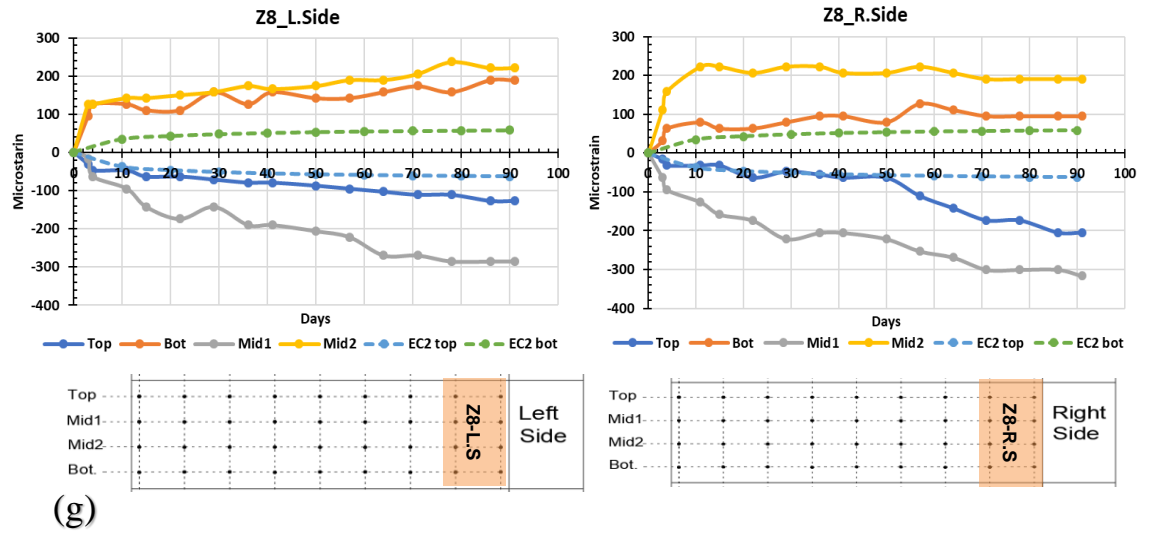
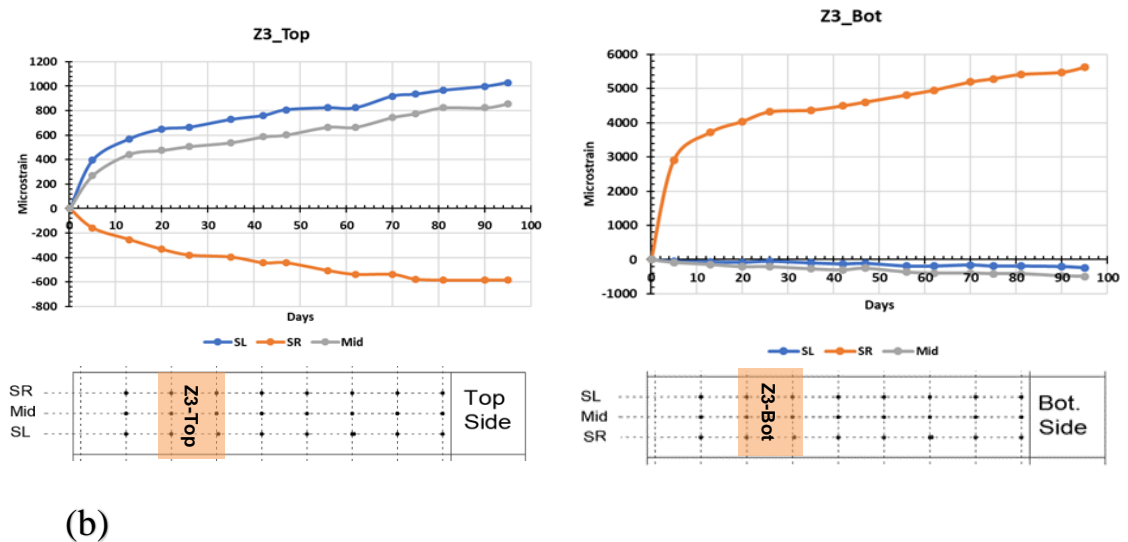
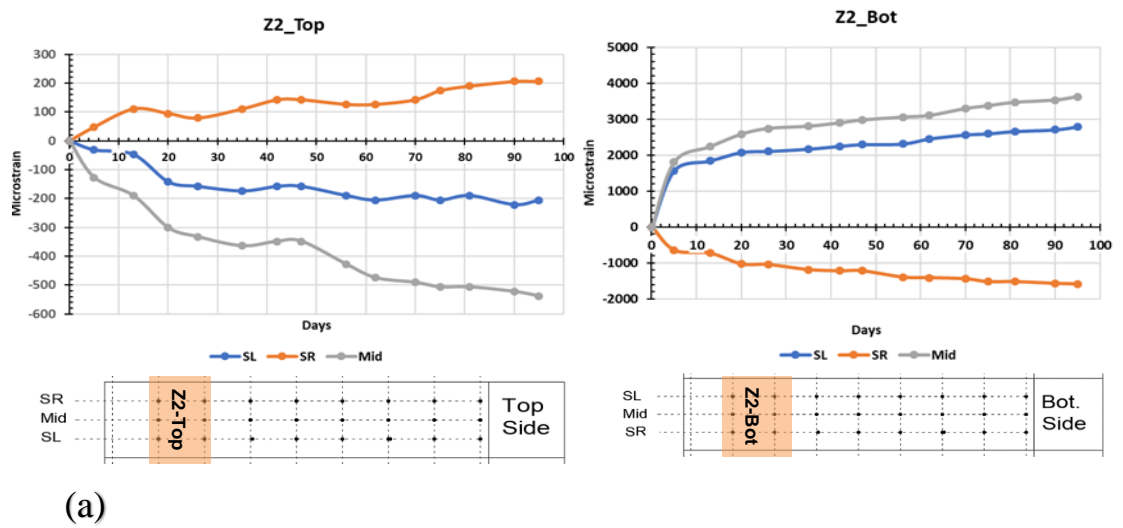
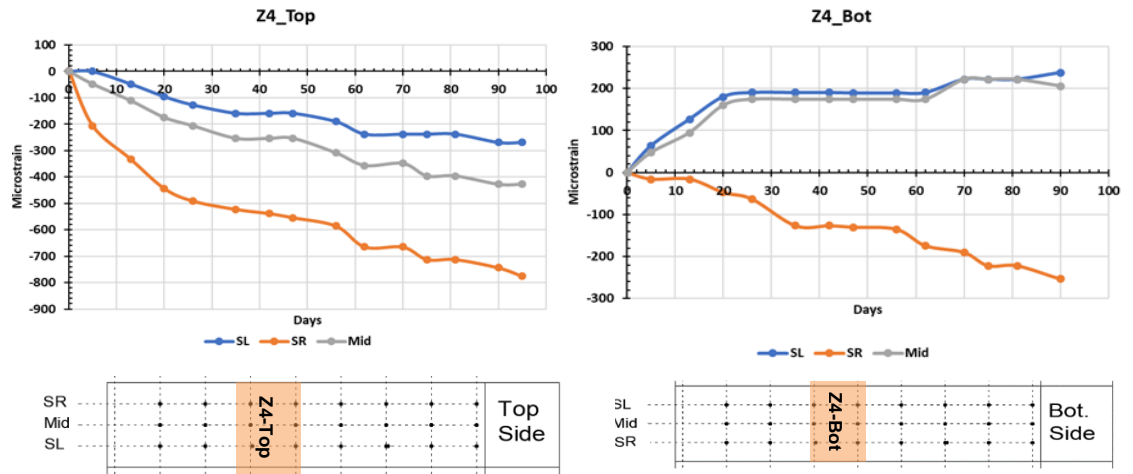
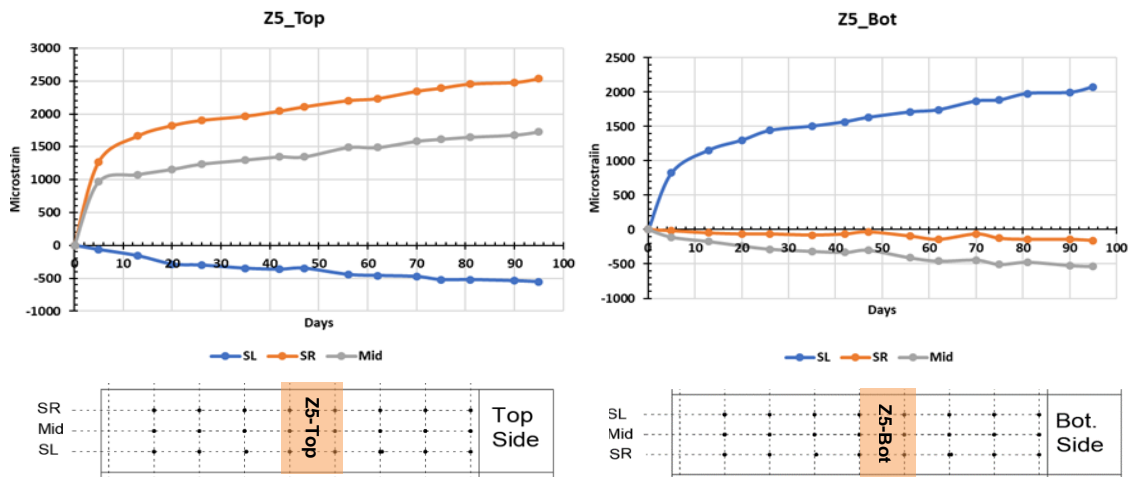


Figure 5.10: The developed surface strains at the beam's right and left sides for the LN-S-C-H specimen (a) Zone 2 (b) Zone 3 (c) Zone 4 (d) Zone 5 (e) Zone 6 (f) Zone 7 (g) Zone 8

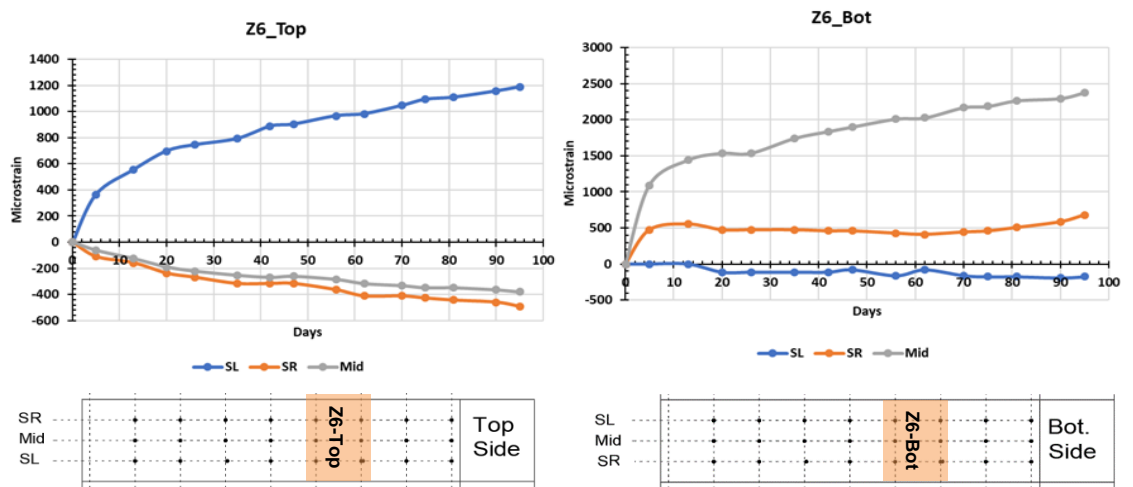




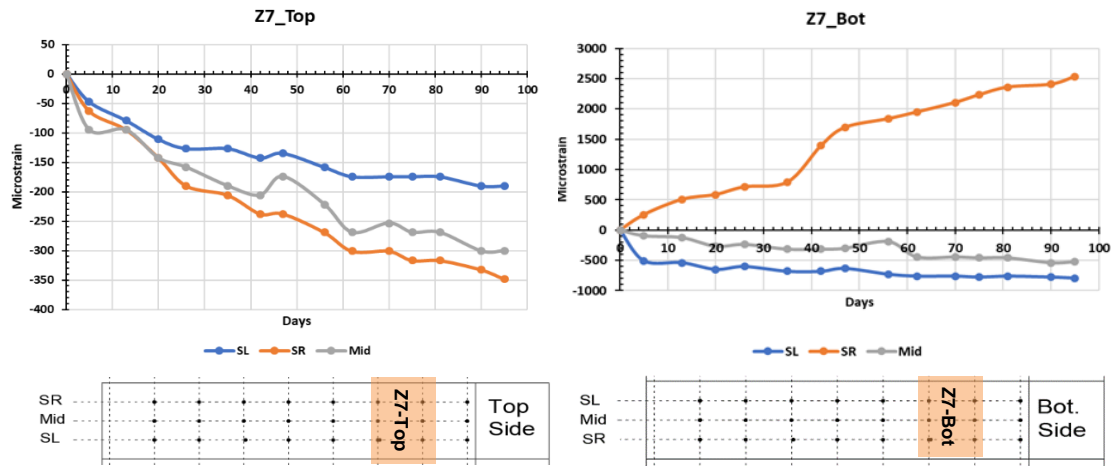
(c)



(d)



(e)



(f)

Figure 5.11: The developed surface strains at the beam's top and bottom sides for the LN-U-C specimen (a) Zone 2 (b) Zone 3 (c) Zone 4 (d) Zone 5 (e) Zone 6 (f) Zone 7

Table 5.1: The increases in the instantaneous and time-dependent surface strains for the LN-U-C specimen.

Zone	Level	Instantaneous strain		Time dependent strain at 90 days		Difference		Increase in strains due to torsion	
		Comb. μ_{strain}	Flex. (Ec2) μ_{strain}	Comb. μ_{strain}	Flex. (Ec2) μ_{strain}	Instant. (comb -flex) μ_{strain}	Time dep. (Comb-flex) μ_{strain}	(Inst. Dif.)/(Inst. Flex.)	(Time Dif.)/(Time Flex.)
Z1-L.Side	Top	126.64	-52.04	1551.34	-157.43	178.68	1708.77	3.43	10.85
	Bot	-277.03	48.11	-728.18	145.57	325.13	873.75	6.76	6.00
Z1-R.Side	Top	-71.24	-52.04	-277.03	-157.43	19.19	119.59	0.37	0.76
	Bot	84.94	48.11	205.79	145.57	36.83	60.22	0.77	0.41
Z2-L.Side	Top	-47.49	-46.84	-364.09	-144.12	0.65	219.97	0.01	1.53
	Bot	15.83	43.30	1361.38	133.27	27.47	1228.11	0.63	9.22
Z2-R.Side	Top	-189.96	-46.84	-379.92	-144.12	143.12	235.80	3.06	1.64
	Bot	-158.30	43.30	-617.37	133.27	201.60	750.64	4.66	5.63
Z3-L.Side	Top	63.32	-41.63	2279.52	-130.81	104.95	2410.33	2.52	18.43
	Bot	94.98	38.49	744.01	120.96	56.49	623.05	1.47	5.15
Z3-R.Side	Top	-47.49	-41.63	-617.37	-130.81	5.86	486.56	0.14	3.72
	Bot	61.54	38.49	5208.07	120.96	23.05	5087.11	0.60	42.06
Z4-L.Side	Top	-47.49	-36.43	-506.56	-117.51	11.06	389.05	0.30	3.31
	Bot	63.32	33.68	189.96	108.65	29.64	81.31	0.88	0.75
Z4-R.Side	Top	63.32	-36.43	4072.2	-117.5	99.75	4189.71	2.74	35.66
	Bot	-7.92	33.68	-411.58	108.65	41.59	520.23	1.24	4.79
Z5-L.Side	Top	-47.49	-31.23	-213.71	-104.20	16.26	109.51	0.52	1.05
	Bot	63.32	28.87	3514.26	96.35	34.45	3417.91	1.19	35.48
Z5-R.Side	Top	-31.66	-31.23	-712.35	-104.20	0.43	608.15	0.01	5.84
	Bot	-142.47	28.87	-174.13	96.35	171.34	270.48	5.94	2.81
Z6-L.Side	Top	39.58	-26.02	-194.30	-90.89	65.60	-103.41	2.52	1.14
	Bot	31.66	24.05	-205.40	84.04	7.61	-289.44	0.32	3.44
Z6-R.Side	Top	-31.66	-26.02	-344.00	-90.89	5.64	-253.11	0.22	2.78
	Bot	-7.91	24.05	192.30	84.04	31.97	108.26	1.33	1.29
Z7-L.Side	Top	-7.91	-20.82	-166.22	-77.58	12.90	88.64	0.62	1.14
	Bot	-15.83	19.24	-506.56	71.73	35.07	578.29	1.82	8.06
Z7-R.Side	Top	-47.49	-20.82	142.47	-77.58	26.67	220.05	1.28	2.84
	Bot	71.23	19.24	1345.55	71.73	51.99	1273.82	2.70	17.76
Z8-L.Side	Top	7.92	-15.61	182.05	-64.27	23.53	246.31	1.51	3.83
	Bot	79.15	14.43	1266.40	59.43	64.72	1206.97	4.48	20.31
Z8-R.Side	Top	7.91	-15.61	530.31	-64.27	23.53	594.57	1.51	9.25
	Bot	-15.83	14.43	-379.92	59.43	30.26	439.35	2.10	7.39
Average						59.60	899.8	1.80	8.6

Table 5.2: The increases in the instantaneous and time-dependent surface strains for the LN-U-C-H specimen.

Zone	Level	Instantaneous strain		Time dependent strain at 90 days		Difference		Increase in strains due to torsion	
		Comb. μ_{strain}	Flex. (Ec2) μ_{strain}	Comb. μ_{strain}	Flex. (Ec2) μ_{strain}	Instant. (comb -flex) μ_{strain}	Time dep. (Comb-flex) μ_{strain}	(Inst. Dif)/(Inst. Flex.)	(Time Dif.)/(Time Flex.)
Z2-L.Side	Top	-47.49	-47.40	-253.28	-146.24	0.09	107.04	0.00	0.73
	Bot	205.79	43.80	1519.68	135.22	161.99	1384.46	3.70	10.24
Z2-R.Side	Top	-7.92	-47.40	-403.67	-146.24	39.48	257.43	0.83	1.76
	Bot	-79.15	43.80	-427.41	135.22	122.95	562.63	2.81	4.16
Z3-L.Side	Top	-47.49	-42.13	-189.96	-126.97	5.36	62.99	0.13	0.50
	Bot	-31.66	38.93	-158.30	117.40	70.59	275.70	1.81	2.35
Z3-R.Side	Top	31.66	-42.13	933.97	-126.97	73.79	1060.94	1.75	8.36
	Bot	126.64	38.93	237.45	117.40	87.71	120.05	2.25	1.02
Z4-L.Side	Top	-126.6	-36.86	-229.54	-114.12	89.78	115.41	2.44	1.01
	Bot	-47.49	34.07	-142.47	105.52	81.56	247.99	2.39	2.35
Z4-R.Side	Top	-32.43	-36.86	-411.58	-114.12	4.43	297.46	0.12	2.61
	Bot	-80.81	34.07	-427.41	105.52	114.88	532.93	3.37	5.05
Z5-L.Side	Top	-15.83	-31.60	-126.64	-101.27	15.77	25.37	0.50	0.25
	Bot	15.83	29.20	94.98	93.64	13.37	1.34	0.46	0.01
Z5-R.Side	Top	-63.32	-31.60	-237.45	-101.27	31.72	136.18	1.00	1.34
	Bot	-63.32	29.20	-118.73	93.64	92.52	212.37	3.17	2.27
Z6-L.Side	Top	-31.66	-26.33	-221.62	-88.43	5.33	133.19	0.20	1.51
	Bot	-63.32	24.33	-189.96	81.76	87.65	271.72	3.60	3.32
Z6-R.Side	Top	-31.66	-26.33	-372.01	-88.43	5.33	283.58	0.20	3.21
	Bot	-26.64	24.33	-189.96	81.76	50.97	271.72	2.09	3.32
Z7-L.Side	Top	-63.32	-21.07	-153.40	-75.58	-42.25	-77.82	2.01	1.03
	Bot	15.83	19.47	110.81	69.88	3.64	40.93	0.19	0.59
Z7-R.Side	Top	15.83	-21.07	31.66	-75.58	36.90	107.24	1.75	1.42
	Bot	-63.32	19.47	-173.40	69.88	-82.79	-243.28	4.25	3.48
Z8-L.Side	Top	-31.66	-15.80	-134.55	-62.73	15.86	71.82	1.00	1.14
	Bot	79.81	14.60	174.13	58.01	65.21	116.12	4.47	2.00
Z8-R.Side	Top	-79.15	-15.80	-205.79	-62.73	63.35	143.06	4.01	2.28
	Bot	15.83	14.60	110.81	58.01	1.23	52.80	0.08	0.91
Average						52.37	250.5	1.81	2.4

5.4.3 Surface Strains for Specimen under Two Stages of Loading

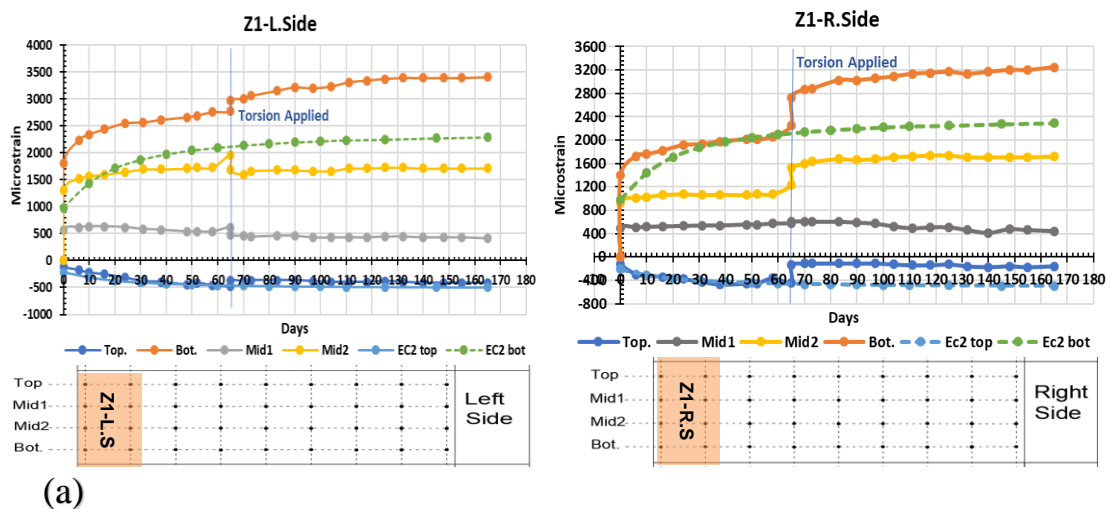
This section presents the developed surface strains for the LN-U-S specimen due to two different loading stages. Similar to the other specimens, the beam sides were divided into zones and levels of 100mm. Zone 8 was not accessible at the time of measuring due to the additional number of LVDT's, the loading cell, and the supporting base that was used to apply and monitor the imposed flexural load. Figure 5.12 shows the strain development around the beam's right and left sides along the seven zones, starting from the maximum flexural region near the column face. The strain measurements for the beam's top and bottom sides are presented in Figure 5.13 for six zones, where zone1 was obstructed by the column and as a result the measuring dial gauge could not be used. These figures illustrate both the instantaneous and time-dependent deformations to identify the influence of torsional load on the deformation levels once the stage-2 loads were applied during the test period.

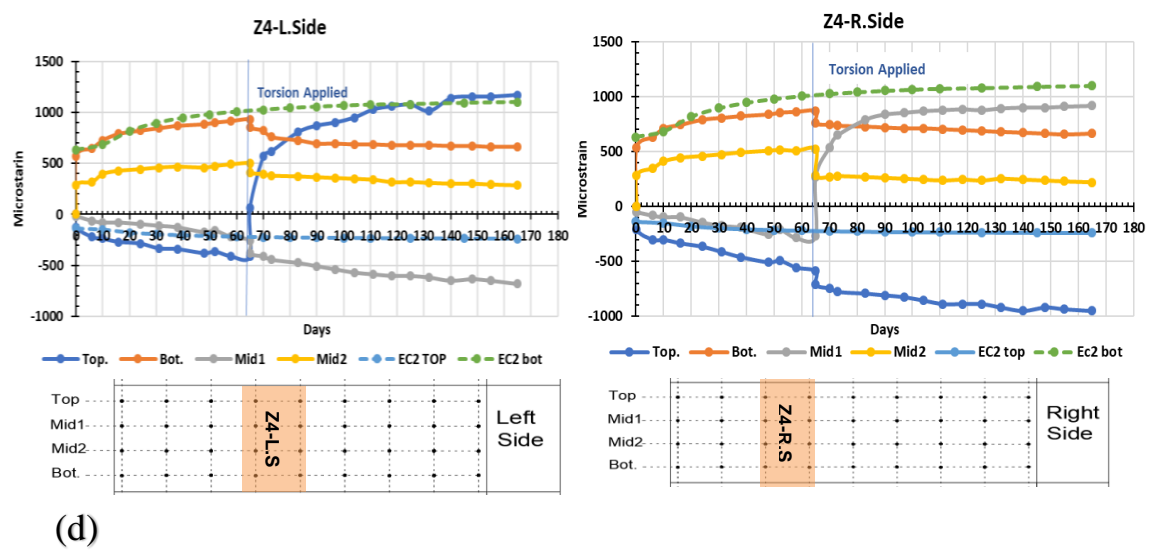
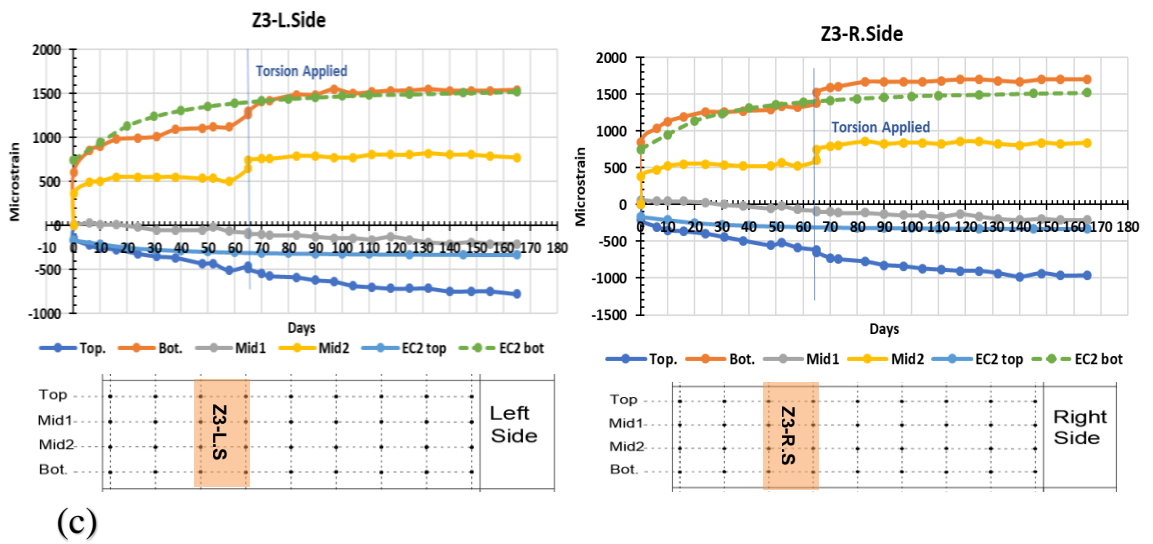
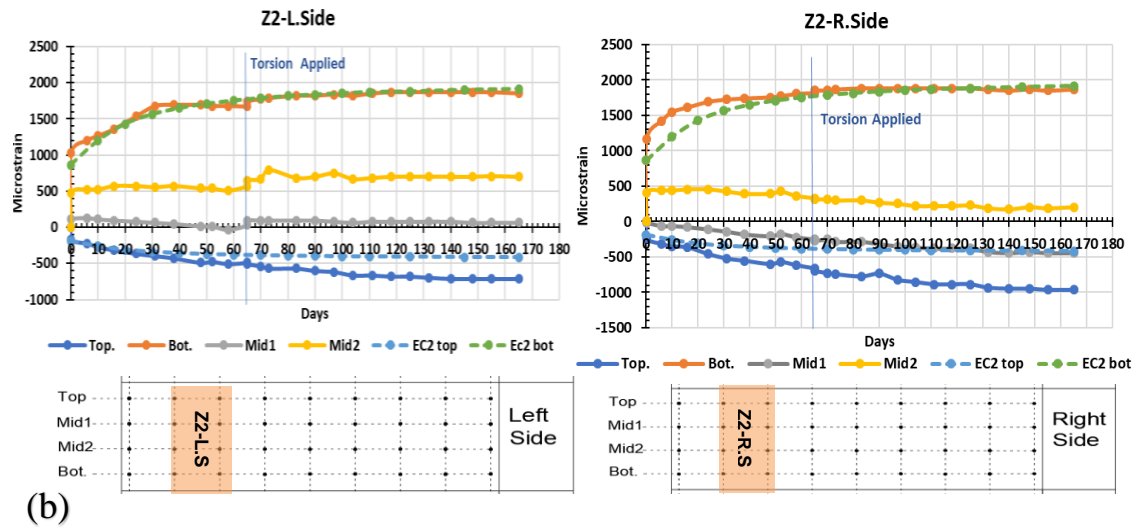
Under flexural load (stage-1), the induced strains typically varied in accordance with the load direction, as the maximum compression strains developed at the beam's top and the tensile strains developed at the bottom, while the strains reduced at the mid-levels closer to the neutral axis. In accordance with the flexural stresses, it can be seen in Figure 5.13 that the top and bottom sides of the beam were under compressive and tensile stresses, respectively, whereas at each side, the strains were almost identical to the zone's levels. Furthermore, Figure 5.12 indicates that the surface strains at the top and bottom levels of the right and left sides were reasonably predicted based on Eurocode 2 (2004) throughout the duration of stage-1. Also, it can be noted that the rate of time-dependent deformations significantly slowed during the end of stage-1.

When the torsional load was incorporated at stage-2, the level and the direction of the strains were altered, varying among the beam's sides, zones and levels. In general, an instant increase in the tensile stresses and strains were observed in several zones (Figure 5.12a; Figure 5.12c; Figure 5.12e, Z5-R.Side; Figure 5.13a, Z2-Bot; Figure 5.13b, Z3-Bot etc); this rise resulted from the torsion that interacted with the flexural and direct shear actions, as discussed in Chapter 4 and Chapter 2 (in accordance with the truss analogy). Also, the instantaneous torsional tensile stress reduced the developed compressive strains in the flexural compression region, in a number of the zones. However, some zones and levels experienced either an increase in compressive deformations or a decrease in tensile deformations within the

zones that exhibited inclined torsional cracks across one or more of the DEMEC levels. There was a considerable increase in the tensile strain orthogonal to a crack that occurred with the growth of compressive strains along a crack direction, corresponding to the principle compressive stresses. These reductions in the diagonal concrete struts affected the time-dependent flexural strains in the levels within these compression fields.

The average increase in total strains at once when the torsional load was applied at end of stage-1 was 47% as given in Table 5.3. While the average long-term strain at the end of stage-2 (165 days) that produced from torsional load was 4 times larger than the bending induced strains. According to figure 5.6c, sharp increases in the measured longitudinal tensile strains were obtained in the DEMEC's rows across the diagonal cracks (e.g. Figure 5.12d; Figure 5.12e, Z5-L.Side; Figure 5.12f; Figure 5.13f, Z7-Bot etc). Also, it was noted that the time-dependent deformations occurring during stage-2 were more pronounced in the zones subjected to low flexural stresses (far from the column face) as can be seen from Figure 5.12e; Figure 5.12f; Figure 5.12g; Figure 5.13c; Figure 5.13d, Z5-Bot; Figure 5.13e, Z6-Bot; and Figure 5.13f, Z7-Bot. Where lower amounts of creep deformation took place in these zones compared to during stage-1; in addition, as discussed in Section 5.2.1, the decrements in flexural compression stresses at those zones (i.e. far from the column face) could increase the level of the normal tensile stresses induced from torsion in the beam top chords and the principal tensile stresses in the flexural compression zone. This reflected in the increments of the instantaneous and time-dependent strains in these zones as presented in Table 5.3 (e.g. Z4 to Z7). Further, the development rates of the time-dependent deformations due to the torsional loads were significantly larger than those obtained during stage-1, as can be seen from Figure 5.12e, Z5-L.Side (Mid1); Figure 5.12e, Z5-R.Side (Bot.); Figure 5.13f, Z7-Bot (SR and Mid), etc.





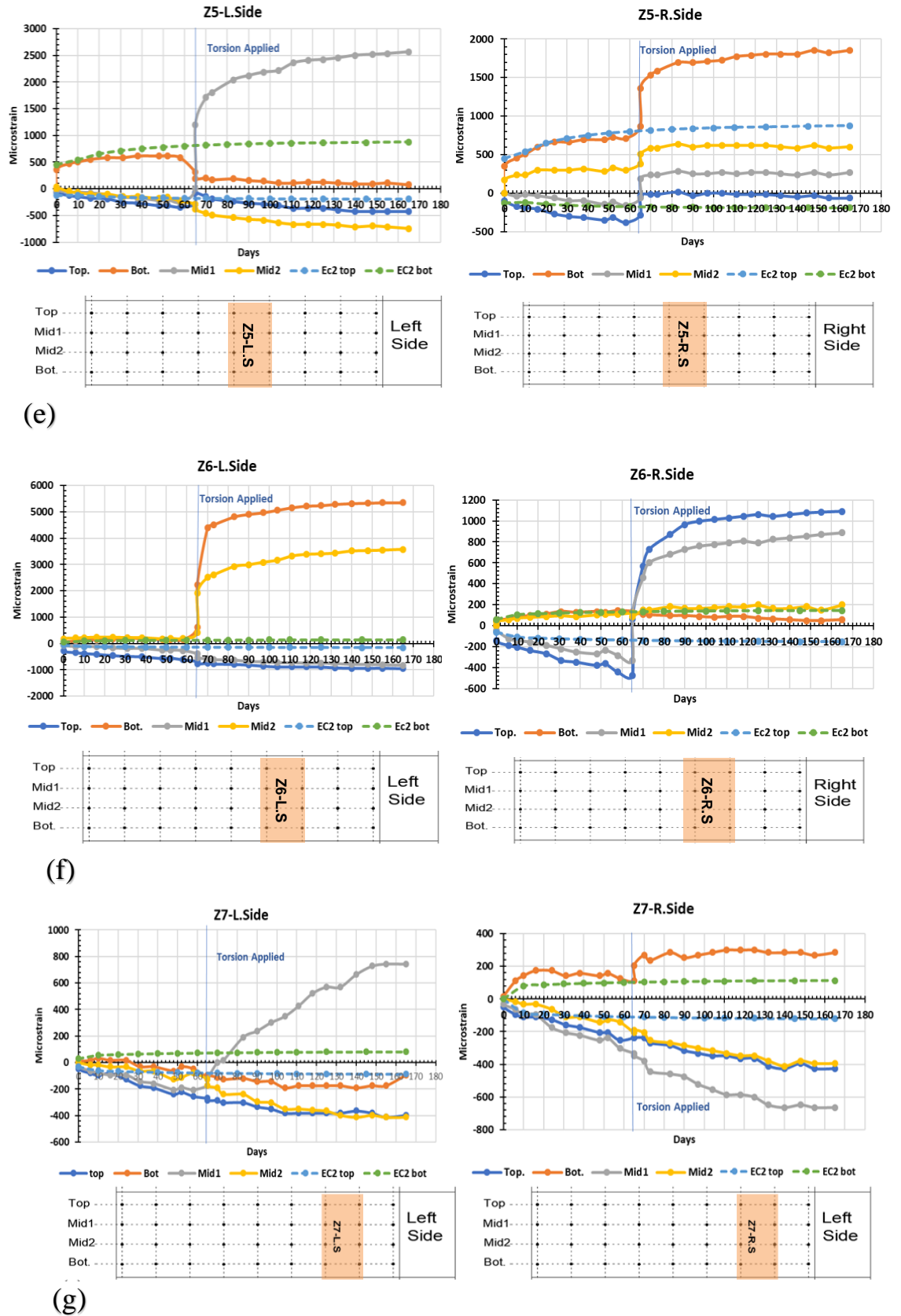
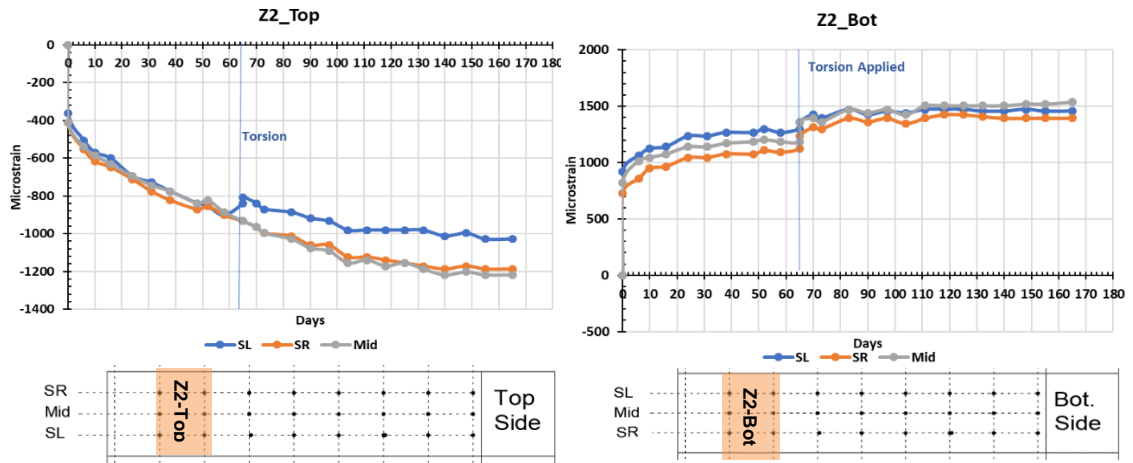
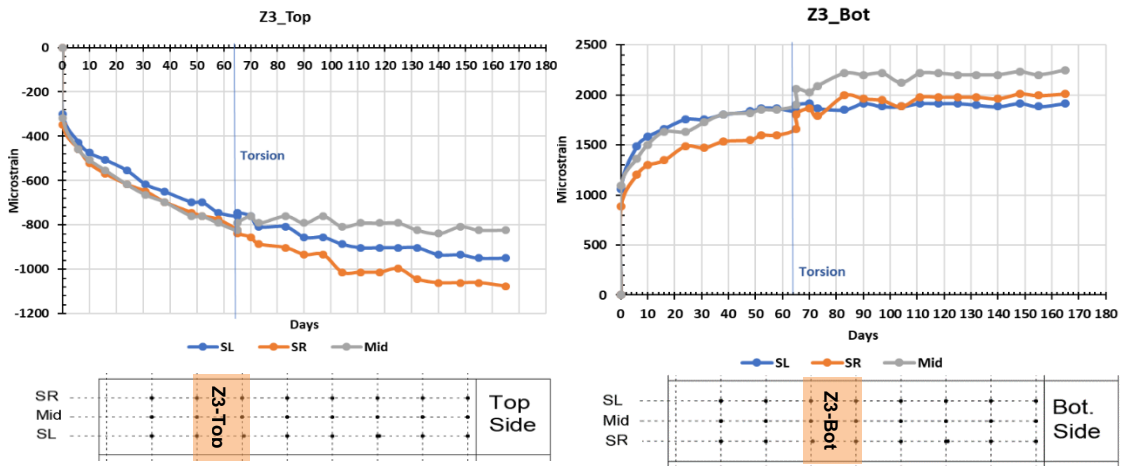


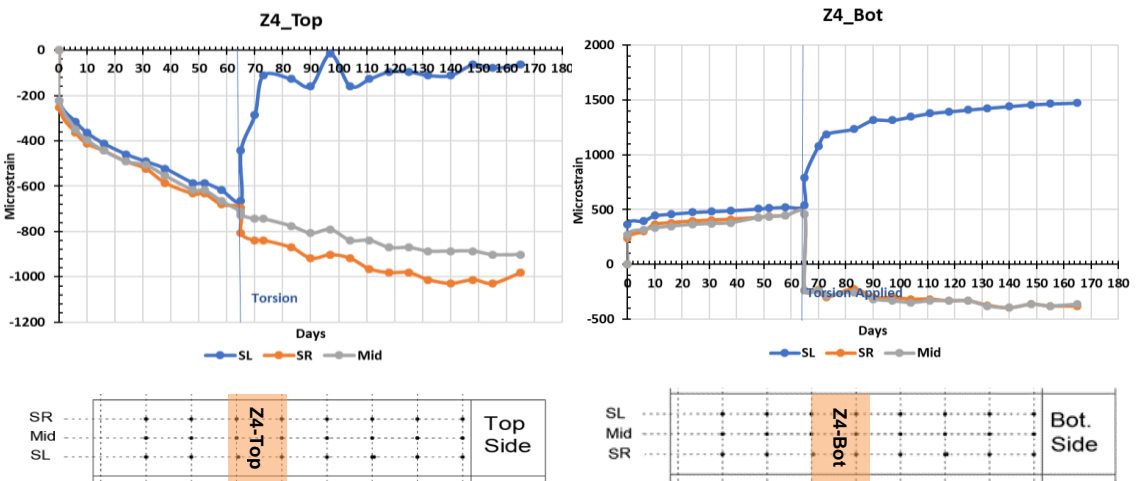
Figure 5.12: The developed surface strains at the beam's right and left sides for the LN-U-S specimen (a) Zone 1 (b) Zone 2 (c) Zone 3 (d) Zone 4 (e) Zone 5 (f) Zone 6 (g) Zone 7



(a)



(b)



(c)

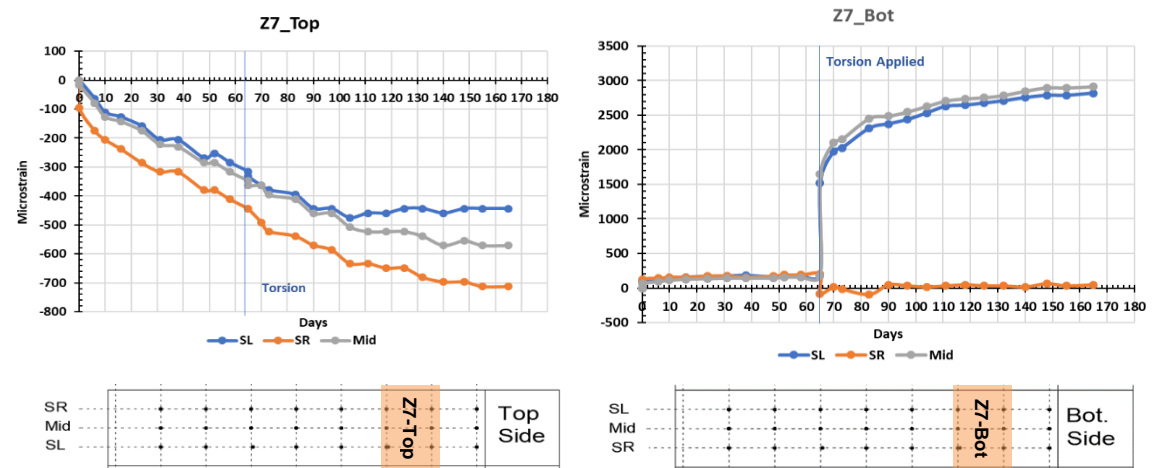
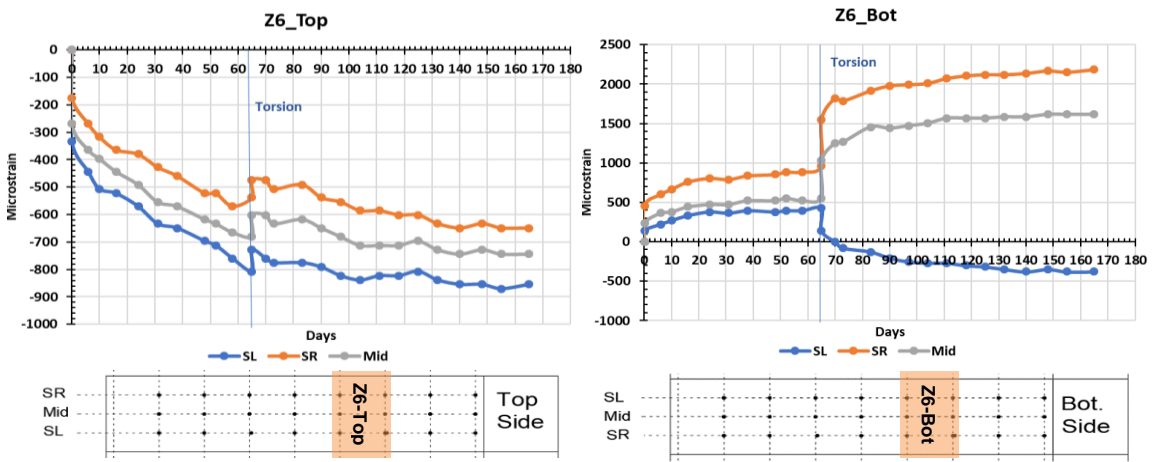
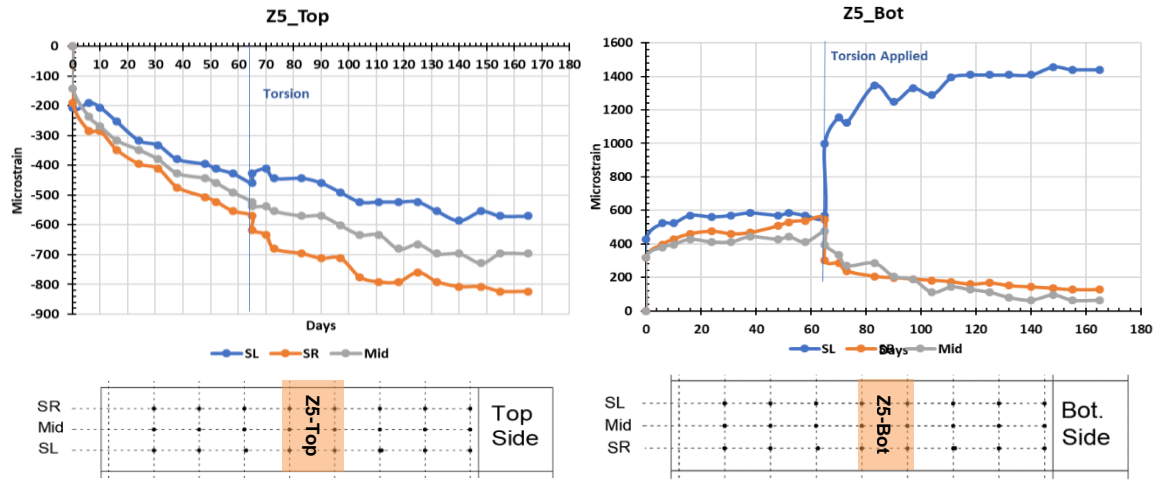


Figure 5.13: The developed surface strains at the beam's top and bottom sides for the LN-U-S specimen a) Zone 2 (b) Zone 3 (c) Zone 4 (d) Zone 5 (e) Zone 6 (f) Zone 7

Table 5.3: The increases in the time-dependent surface strains at end of stage-1 and stage-2 for the LN-U-S specimen.

Zone	Level	Strains at the end of stage 1 (after 65 days)			Strains at the end of stage 2 (165 days)		Difference at 65 and 165 days		Increase in strains	
		Flex. (Test) μ_{strain}	Flex. (Ec2) μ_{strain}	After torsion (stage 2) μ_{strain}	Total (at 165 days) μ_{strain}	Flex. (EC2 at 165 days) μ_{strain}	Inst. (after torsion - Flex 65)	Time-Dep. 165 (Total-Inst. - Flex 165) μ_{strain}	(Inst. Dif.)/ (Flex. 65)	(Dif. Time)/ (Flex. 165)
Z1- L.Side	Top	-459.1	-455.8	-474.9	-411.6	-497.5	15.8	70.1	0.03	0.14
	Bot	2654.4	2097.8	3245.2	3403.0	2289.7	590.7	522.6	0.22	0.23
Z1- R.Side	Top	-448.1	-455.8	-443.2	-158.3	-497.5	4.8	334.4	0.01	0.67
	Bot	2057.9	2097.8	2089.6	3086.9	2289.7	31.7	765.5	0.02	0.33
Z2- L.Side	Top	-506.6	-391.1	-490.7	-712.4	-416.1	15.8	312.1	0.03	0.75
	Bot	1708.0	1754.0	1718.0	1852.1	1915.0	10.0	72.8	0.01	0.04
Z2- R.Side	Top	-517.4	-391.1	-664.9	-965.6	-416.1	147.5	697.0	0.29	1.68
	Bot	1804.6	1754.0	1820.5	1867.9	1915.0	15.8	62.8	0.01	0.03
Z3- L.Side	Top	-506.6	-302.8	-459.1	-775.7	-330.7	47.5	492.4	0.09	1.49
	Bot	1123.9	1393.5	1266.4	1543.4	1522.1	142.5	121.2	0.13	0.08
Z3- R.Side	Top	-585.7	-302.8	-617.4	-965.6	-330.7	31.7	666.5	0.05	2.02
	Bot	1361.8	1393.5	1385.1	1701.7	1522.1	23.3	156.3	0.02	0.10
Z4- L.Side	Top	-395.6	-173.8	-284.9	1171.4	-190.1	110.6	1250.9	0.28	6.58
	Bot	918.1	799.9	316.6	664.9	875.1	601.5	811.8	0.66	0.93
Z4- R.Side	Top	-554.1	-173.8	-284.9	-949.8	-190.1	269.1	1028.8	0.49	5.41
	Bot	862.7	799.9	870.6	649.0	875.1	7.9	234.0	0.01	0.27
Z5- L.Side	Top	-348.3	-138.3	-680.7	-427.4	-153.4	332.4	606.4	0.95	3.95
	Bot	585.7	130.3	617.4	79.1	144.6	31.7	97.1	0.05	0.67
Z5- R.Side	Top	-379.9	-138.3	-474.9	-63.3	-153.4	95.0	4.9	0.25	0.03
	Bot	712.3	130.3	-142.5	1852.1	144.6	854.8	852.7	1.20	5.90
Z6- L.Side	Top	-517.4	-107.6	-680.7	-949.8	-120.2	-163	-666.3	0.32	5.55
	Bot	142.5	101.4	617.4	5350.5	113.2	474.9	4762.4	3.33	42.06
Z6- R.Side	Top	-443.2	-107.6	-427.4	1092.3	-120.2	15.8	1196.6	0.04	9.96
	Bot	142.5	101.4	-316.6	-506.6	113.2	-459	-160.7	3.22	1.42
Z7- L.Side	Top	-253.3	-77.0	-269.1	-411.6	-86.9	15.8	340.5	0.06	3.92
	Bot	-47.5	72.5	-110.8	-95.0	81.9	63.3	240.2	1.33	2.93
Z7- R.Side	Top	-253.3	-77.0	-237.4	-427.4	-86.9	15.8	356.4	0.06	4.10
	Bot	126.6	72.5	110.8	284.9	81.9	15.8	187.3	0.13	2.29
Average							164.4	646.5	0.47	4.0

5.5 Strain Development in the Steel Reinforcement

Based on the gauge measurements, the induced time-dependent strains in the steel rebars are presented here. The positions of ESR gauges were illustrated in Figure 3.26. It is believed that no attempt has been made in the literature to present the influence of torsion on the long-term deformation of the steel reinforcement strains.

Figures 5.14 to 5.22 show the developed strains in the beam's reinforcement for the LN-U-C, LN-S-H-C and LN-U-S specimens. From the Figures, it can be seen that there was often quite a lot of scatter in. It is believed that these discrepancies mainly relate to the cracking of the concrete, given that a crack formation can sharply increase the strain in the steel rebar at the crack's location (Scott and Beeby, 2005). Also, the redistribution of the stresses between the rebars and the concrete between cracks, in compliance with creep and shrinkage rates can potentially alter the strain levels. However, overall, a reasonable agreement, in which significant logarithmic correlation coefficients ($R^2 > 0.5$), were found over time, as can be seen in Figure 5.14, Figure 5.15, Figure 5.19, Figure 5.20, and Figure 5.22. These figures show that the strains in the rebars developed over time and varied throughout the beam's faces and along the beam's lengths, which correspond to the surface strain observations. For the specimens under single loading stage (LN-U-C and LN-S-C-H), maximum developed tensile strains were observed in the beam bottom left side (ERS G.2) as can be seen from Figures 5.14 and 5.15. These developed strains corresponded with the induced tensile stresses resulted from the interaction between torsion, bending, and direct shear loads. While the top beam's chords (i.e. ERS G4 and G3) exhibited compression strains related to level of bending stress and the compressive stress field from torsion shear-flow. Nevertheless, the trend of compressive strains were dominated in the LN-S-C-H (Figure 5.15). Further, by way of comparison between the strengthened specimen (LN-S-C-H) and the LN-U-C specimen, where both were under the same loading conditions, Figure 5.15 and Figure 5.21 confirm that the CFRP hoops can reduce the longitudinal strains and cracking levels. On the other hand, it was found in the both specimens that compressive strains could be obtained from gauges that are located in the regions did not exhibit cracks within the inclined compressive stress field (struts action). This was observed at the top or the bottom of the main rebars, regardless of flexural compression or tension zones. However, these localised readings reflect the strain levels at the point where the gauge was placed,

while the surface strain observations represent the average deformations over the measured zones after each 100 mm along the beam's length in which accounting the formed cracks.

Figure 5.17 showed the top chords exhibited scattered tensile strains where these influenced by developed inclined cracks (C_T2 and C_T3) that presented in Figure 5.6a. While it can be seen from Figure 5.20 that the measured strain from ERS-G.10 (bottom chords) was significantly higher than those observed from Figure 5.21 and ESR-G.9, where the developed strains (G.10) was affected by C_T9 crack (Figure 5.6a). For the LN-U-S specimen, most of the obtained readings became more scattered after the application of the torsional load and the formation of the torsional cracks, as shown in Figure 5.16 and Figure 5.19. These figures indicate that the rebar strains can be substantially altered in relation to the level of torsional forces and cracking of concrete. It is clear from the figures that during the 1st stage (flexural load), the bottom rebars experienced tensile strains and the top rebars were subjected to compressive deformations, while the fit lines were affected by the reading's discrepancies due to crack formations and stress redistributions.

For all specimens, Figure 5.22 illustrates the strain development in the beam's stirrups, 310 mm from the column. It can be observed that transverse rebars were under tensile strains for specimens under loading stage-1, which conforms to the truss analogy. Nevertheless, the strengthened specimen experienced significantly fewer time-dependent transverse deformations when compared with the LN-U-C specimen, since the CFRP wraps increased the stiffness of the beam in the transverse direction and reduced the stresses in the steel stirrups. While for the LN-U-S specimen, the strain pattern varied from the compression deformations during the stage-1 (no shear cracks appeared in the 1st period) to tensile deformations when the torque was applied during the stage-2, in accordance with increasing the principal tensile stresses due to the torsional shear stresses.

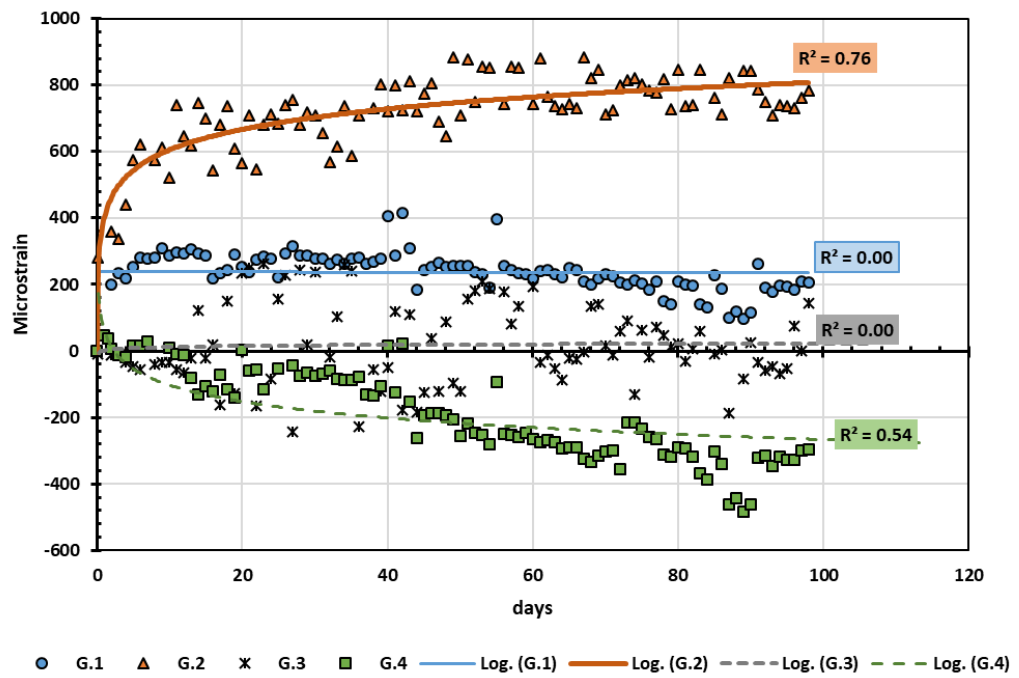


Figure 5.14: Developed strains in the beam's main rebars for the LN-U-C specimen at 125 mm from the column face

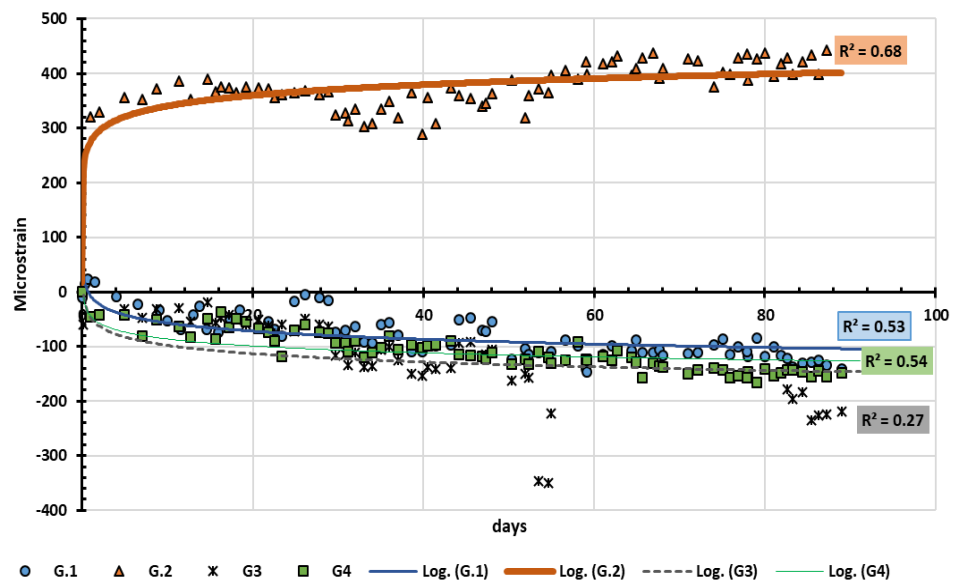


Figure 5.15: Developed strains in the beam's main rebars for the LN-S-C-H specimen at 125 mm from the column face

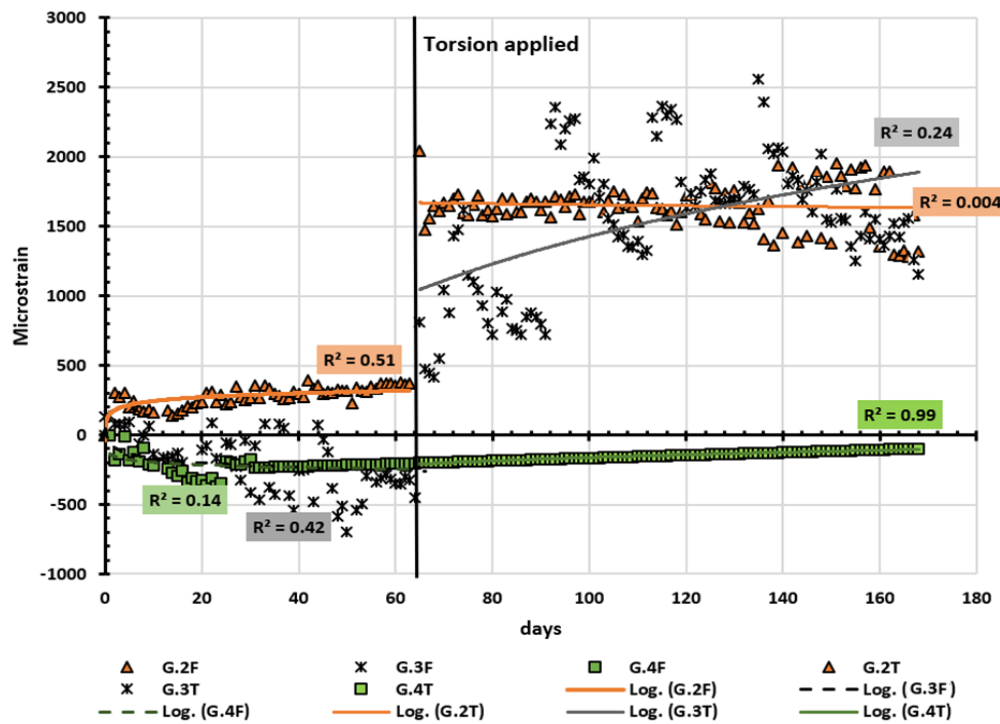


Figure 5.16: Developed strains in the beam's main rebars for the LN-U-S specimen at 125 mm from the column face

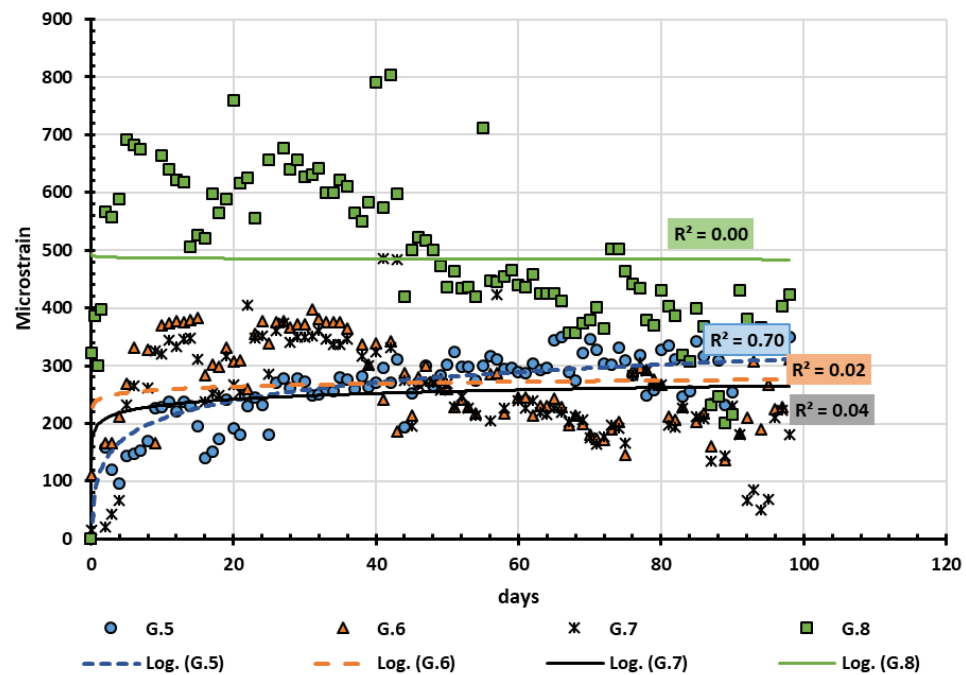


Figure 5.17: Developed strains in the beam's main rebars for the LN-U-C specimen at 350 mm from the column face

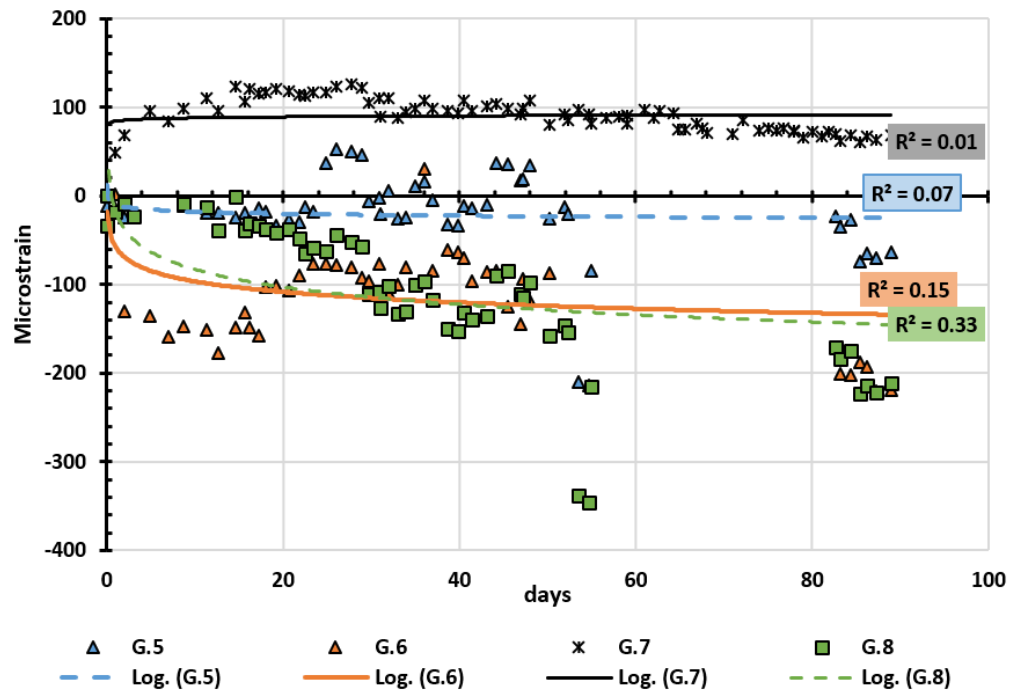


Figure 5.18: Developed strains in the beam's main rebars for the LN-S-C-H specimen at 350 mm from the column face

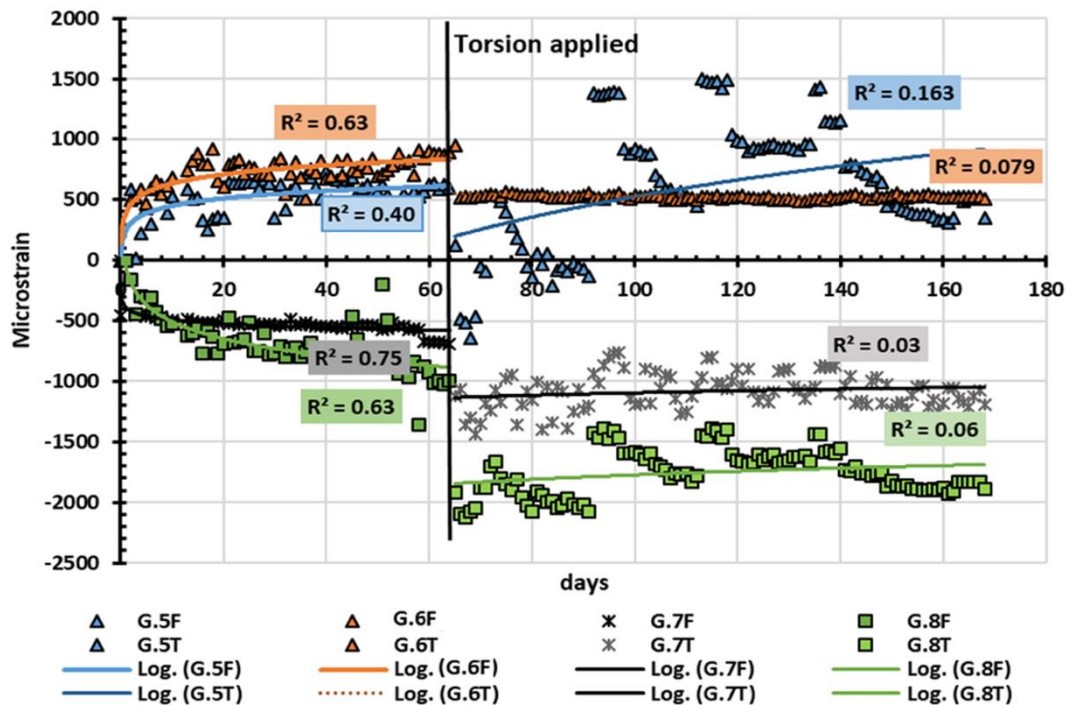


Figure 5.19: Developed strains in the beam's main rebars for the LN-U-S specimen at 350 mm from the column face

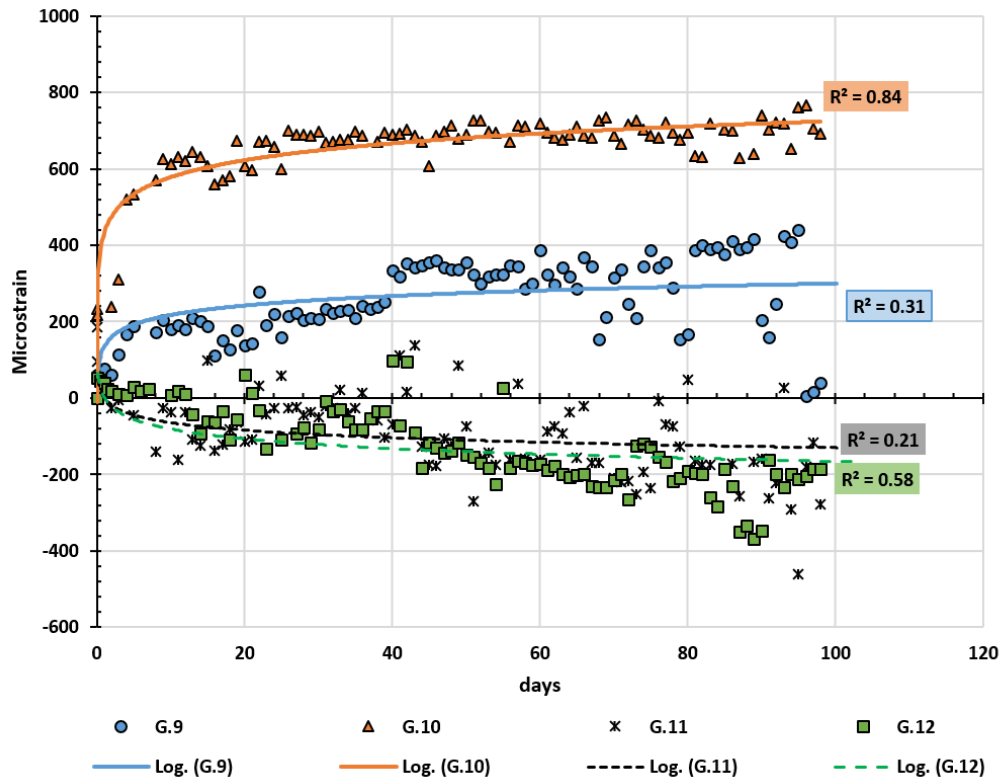


Figure 5.20: Developed strains in the beam's main rebars for the LN-U-C specimen at 620 mm from the column face

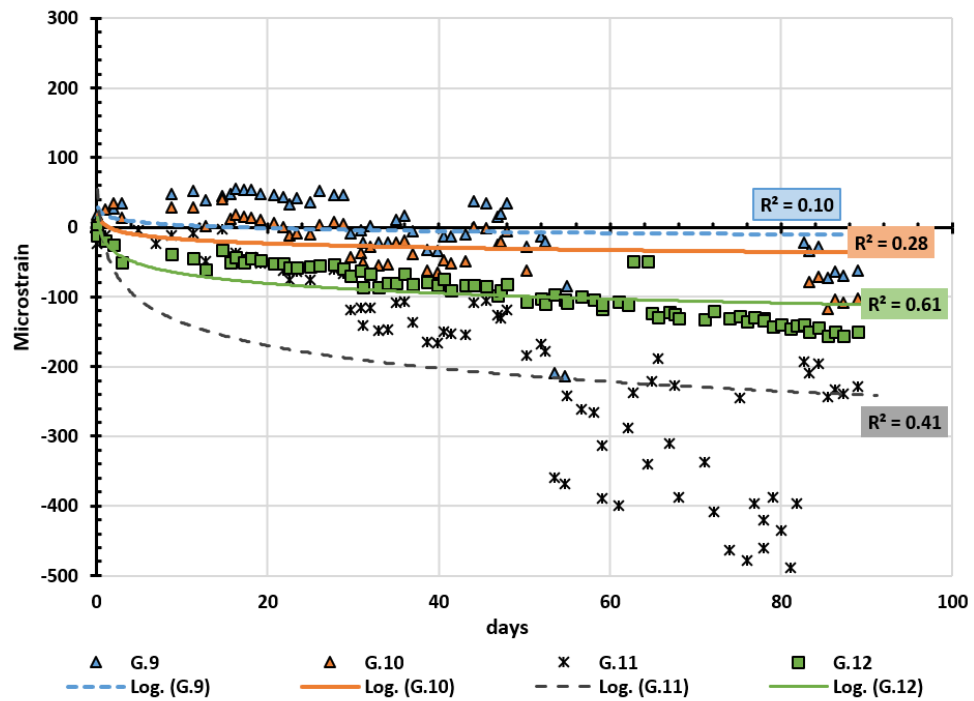


Figure 5.21: Developed strains in the beam's main rebars for the LN-S-C-H specimen at 620 mm from the column face

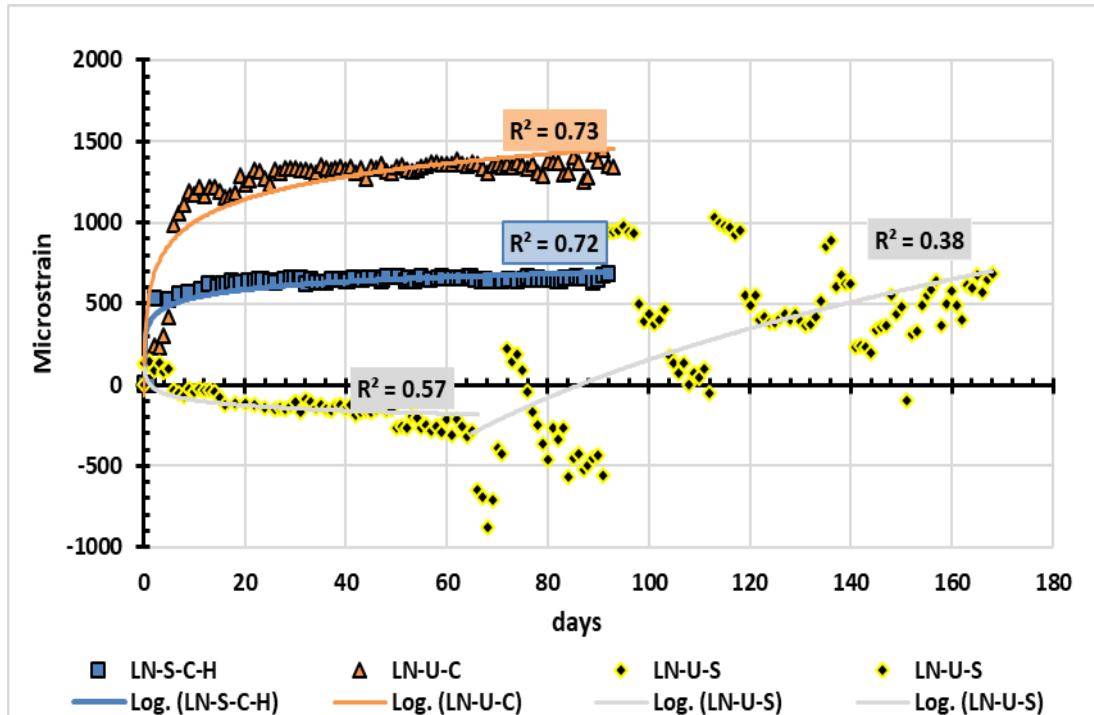


Figure 5.22: Developed strains in the stirrups for all specimen at 310 mm from the column face

5.6 Summary

The long-term behaviour of specimens under sustained torsional loads, combined with flexural and direct shear, have been investigated and discussed in this chapter. The main findings that can be deduced from the experimental results are outlined below:

- 1- In agreement with the extant literature, the test outcomes showed a considerable rise in the beam's rotations due to long-term torsional loads, while the conducted tests revealed that the CFRP wraps significantly enhanced the time-dependent torsional stiffness when compared with the unstrengthened specimen.
- 2- Torsional loads reduced the flexural stiffness, since they increase the beam's curvature and deflection which were corresponded to the level of torsional cracks.
- 3- The level of development of the torsional cracking and twisting angles conformed with the rate of creep and shrinkage deformations in the inclined concrete struts. Further, a very good correlation between the

measured and predicted rotations was obtained, based on the hyperbolic formula.

- 4- Rapid increments in the beams rotations and cracking rates at the early age of loading. However, no new cracks were seen after 30 days and the predicted twist angles at an age of 365 days was only 6%, 18%, and 7% greater than that obtained at 90 days for LN-S-C-H, LN-U-C and LN-U-S, respectively
- 5- Significant growth in the time-dependent torsional cracks was observed for the unstrengthened specimen in relation to creep and shrinkage developments. The CFRP hoops arrested the propagation of cracks, as the observed crack widths were within the code's recommendations.
- 6- Variations in the surface strains between the beam's sides and along the beam's lengths were found. These variations were a result of changes to the applied forces along the beam's length and sides, concrete strut forces due to compression stress fields induced by torque actions, compatibility conditions, cracks locations, and concrete time dependent deformations.
- 7- Different increases in the developed strains were noticed in the specimens at the beam surface in different zones which attributed to levels of compression stress fields (torque action) and time dependent deformations in the inclined concrete struts. The increments in the instantaneous strains were 1.8, 1.81, and 0.47 larger than the bending induced strains for LN-U-C, LN-U-C-H, and LN-U-S specimens, respectively. While the observed time dependent strains were considerably greater (up to 8.6) than the bending induced strains.
- 8- Different strain levels can be developed in the beam's rebars through the beam's regions due to sustained torsional loads, regardless of flexural tension or compression regions. Additional transverse reinforcement using CFRP strips reduced the longitudinal deformations in corresponding to the truss mechanism and torsional compression field. Also, incorporating the torsional load after the sustained bending load altered the rebars strains in relation to levels of combined forces and cracking of concrete.

Chapter 6 Analytical Investigations

6.1 Introduction

This chapter proposes a number of formulas based on the truss mechanism which are intended to be used to quantify the joint forces and which consider the effects of combined loads and different wrapping schemes. With reference to the experimental results (Chapter 4), the joint demands can be considerably affected by the interaction between the combined loads and the type of the strengthening schemes. Significantly, incorporating torsional loads altered the stress and strain levels in the beam rebars that transferred to the joint zones. The recommended design provisions for RC joints (ACI-ASCE 352R-02 Committee, 2002; Eurocode 2, 2004; NZS 3101, 2006; BS8110, 1997) do not provide guidelines to evaluate joint shear forces (demands) in corresponding to levels of induced forces in the beam's main rebars under combined actions. Further, this investigation shows that it is important that codes should consider the influence of FRP reinforcement on the stresses developed in the steel rebars and concrete struts which are consistent with struts inclination angles that varied across the beam's sides. This would allow the proper quantification of the joint demands and the rise in the plastic strains in the main beam rebars that can be produced from the increase in the torsional capacity of the strengthened beam regions and from the interaction between the combined loads and the reduction in the strut inclination angles.

A number of formulas have been developed that can be used to evaluate the forces in the main tension ties and compression struts under the action of torsional, flexural and direct shear forces, depending on the various wrapping schemes. Further, this chapter proposes an iterative model to allow for the prediction of the joints capacities and detorsion levels.

6.2 Shear Demand and Concrete Strut Capacity

6.2.1 Concrete Strut Capacity

The interaction between bending, torsion, and shear produces a variation in strain around the perimeter of the cross-section and over the member length, as identified in previous chapters. In this investigation, the behaviours of the tested beam-column joints specimens under combined forces conforms with the truss analogy. Hence, the beam's regions can be idealised as a space truss model which is formed from the longitudinal and transverse ties and the

concrete struts developed across the beams sides as discussed in Appendix-A. Accordingly, the interaction between flexural, torsion, and shear forces magnified the tension forces in the beam's main rebars and compression forces in the concrete struts (beam's sides). Thus, to prevent any brittle failure in concrete struts, this study attempts to limit the torsional enhancement levels (via the CFRP) and acted vertical shear forces in the beam's sides to the concrete strut capacity (σ_d). These enhancement levels are predicted using the modified fib Bulletin 14 (2001) (Eq. 6.1). The tests results indicate that a close correlation between the predicted and observed CFRP strains was achieved by utilising the effective FRP strain (Eq. 2.8) proposed by Triantafillou and Antonopoulos (2000). This was employed according to the effective fibre ratio (Eq. 6.2a and b) developed by Hii and Al-Mahaidi (2007). The thin-walled truss mechanism is also recommended by the major codes of practices, including ACI Committee 318 (2014) and Eurocode 2 (2004), to evaluate torsional member capacity, as it includes the steel rebar contribution ($T_{u_{steel}}$) where Eq. 3.1 and Eq.3.2 can be used. Then, the overall expected torsional capacity can be computed by the superposition of the contributions from the steel rebars and the CFRP (Eq. 2.4), the validity of the superposition approach is confirmed in the literature.

$$T_{U_{frp}} = 2 \varepsilon_{fd,e} E_f \frac{t_f b_f}{S_f} A_o (\cot(\alpha_d) + \cot(\alpha_f)) \sin(\alpha_f) 10^3 \quad \text{Eq. 6.1}$$

$$\rho_f = \frac{4t_f b_f U_c}{3A_c S_f} \quad [\text{CFRP strips}] \quad \text{Eq. 6.2a}$$

$$\rho_f = \frac{4t_f U_c}{3A_c} \quad [\text{Continuously bonded CFRP wraps}] \quad \text{Eq. 6.2a}$$

Where;

$\varepsilon_{fd,e}$ = design value of effective fibre strain

E_f = the FRP Young's modulus in GPa

S_f = the spacing between CFRP strips in mm

t_f = the FRP thickness in mm

b_f = the FRP strips width in mm

α_d = the angle of the concrete strut in degrees

α_f = the orientation of the fibres measured from the beam longitudinal axis in degrees

ρ_f = the effective FRP ratio

This study considered the reduction in compression concrete strut capacity-vertical component (σ_{dv}) using Eurocode 2 for concrete cracked in shear, as given in Eq. 6.3. This reduction is also stipulated by CEB-FIP (1991) for concrete essentially under compression stresses. The maximum strength (f_{dv}) attained by the diagonal concrete strut in the transverse direction can be evaluated according to Eq. 6.4. As Eq. 6.4 is based on the truss mechanism (Figure 6.1a) which f_{dv} is equivalent to $f_d \sin \alpha_d$ and f_d corresponds to concrete strength (f'_c) and struts area. Also, Figure 6.1a illustrates the acted stresses in the transvers direction of the beam's sides where the maximum shear flow (q_i) resulted from the addition of the torque and vertical shear. The term α_d (angle of inclination) in Eq. 6.4 can be either assumed as per Eurocode 2 (2004) or calculated directly using Eq. 6.7 to 6.10, 6.12, and 6.14 (these are discussed in Section 6.2.2). This investigation identified that wrapping schemes can enhance the confinement degree and reduce the softening of concrete from tensile cracking. This study recommends Eq.6.3 for both strengthened and un-strengthened members to conservatively avoid any failure in the concrete. For a favourable redistribution of shear stresses over the member depth, a root-square summation of direct shear and torsional capacities have been utilised to drive Eq. 6.5 in order to verify the member's capacity; this agrees with ACI Committee 318 (2014) and AASHTO LRFD (2010) recommendations for solid sections. For ultimate torsional member capacity, the approach can directly evaluate (without an iteration process) the shear flow area (A_o) according to ACI Committee 318 (2014), which corresponds to 85% of the section's area that is enclosed by stirrups, as presented in Table A.1 and Figure 6.1b. These analytical calculations correspond with the analogy of the circulatory action of torsional forces (Section 2.2), while the wrapping torsion is not considered since this work investigates the torque influences on RC solid (closed) sections.

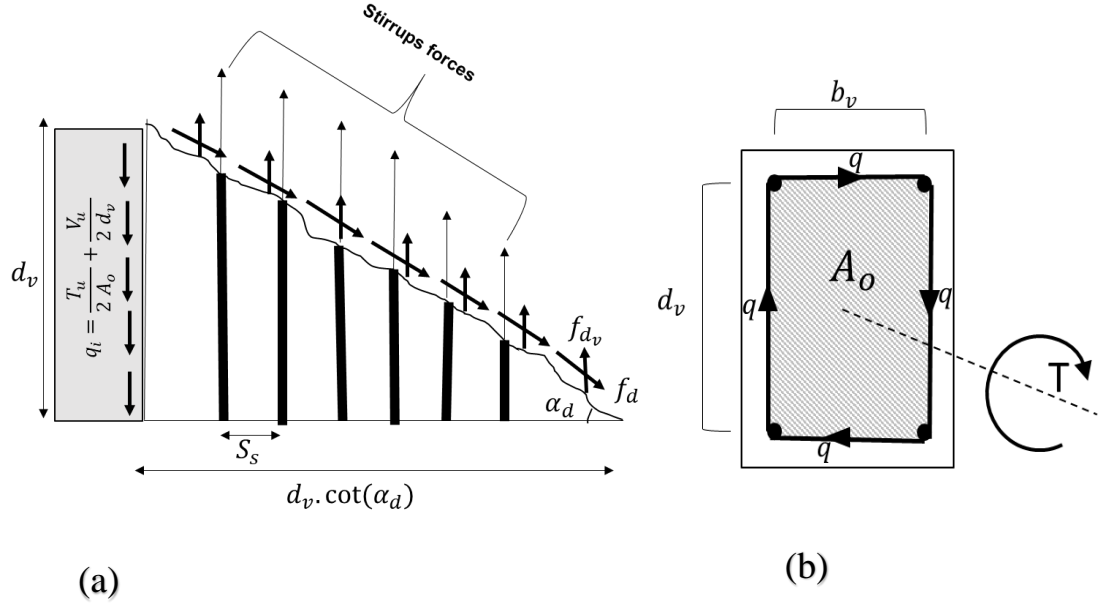


Figure 6.1: (a) Truss mechanism in the beam's sides (b) shear flow and section effective area

$$\sigma_{d_v} = 0.6 \left(1 - \frac{f'_c}{250} \right) f_{d_v} \quad \text{Eq.6.3}$$

$$f_{d_v} = \frac{f'_c}{(\cot(\alpha_d) + \tan(\alpha_d))} \quad \text{Eq.6.4}$$

$$\sqrt{(V_u)^2 + \left(\frac{(T_{ufrp} + T_{usteel}) U_c}{0.85(2A_o)} \right)^2} (A_*)^{-1} \leq \sigma_{d_v} \quad \text{Eq.6.5}$$

Where;

U_c = the outer perimeter of the section in mm

A_c = the section's gross area in mm²

f_{d_v} = the stress in the concrete strut capacity in the transverse direction in MPa

d_v = the effective depth between top and bottom rebars (d-d') in mm

b_v = the effective width of the beam in mm

V_u = the maximum applied vertical shear in N

T_{ufrp} = contribution of FRP for the member torsional capacity in N.mm

T_{usteel} = contribution of steel rebars for the member torsional capacity in N.mm

A_* = the area that is equivalent to A_c for strengthened sections in mm², or the equivalent to a magnitude of (A_o) for unstrengthened sections

6.2.2 Joint Shear Demand

The joint shear demand (joint forces) resulting from the combination of beam forces can be quantified according to the truss mechanism. The interaction between torsion, bending, and direct shear according to the space truss analogy has been discussed in Chapter 2. This study has utilised this method to evaluate the tensile forces in the main rebars in the flexural tension zone of the beam by satisfying the equilibrium conditions. This study considered the effect of various FRP wrapping schemes and subsequently, establishing the relevant formulas which conform to the truss method. Eq. 6.6 satisfies the equilibrium of forces by taking a moment about the top chords (Figure 6.2b) (the bottom side being exposed to tensile stresses induced by flexural and torsional forces). The amount of shear flow (q_i) and the concrete strut angle in each side (wall) of the sections are varied, as given in Eq. 6.8 to Eq. 6.10. These variations depend on the direction of the torsional and vertical shear forces. However, for simplicity, uniform shear distribution has been assumed over the depth of the sides, similar to that adopted by Greene Jr and Belarbi (2009a) and Rahal and Collins 1995.

The relationship between the inclination angle (α_{di}), the shear flow and forces in the transverse reinforcement (stirrups forces- N_t) is depicted in Figure 6.1a, while the shear flow induced by the torque is evaluated according to Bredt's equation (Eq. 6.10). The magnitude of tensile forces in the bottom chords (N_{lb}) for the un-strengthened members can be predicted using Eq. 6.11, which is a rearrangement of Eq. 6.6 (formed by substituting Eq.6.7 into 6.11).

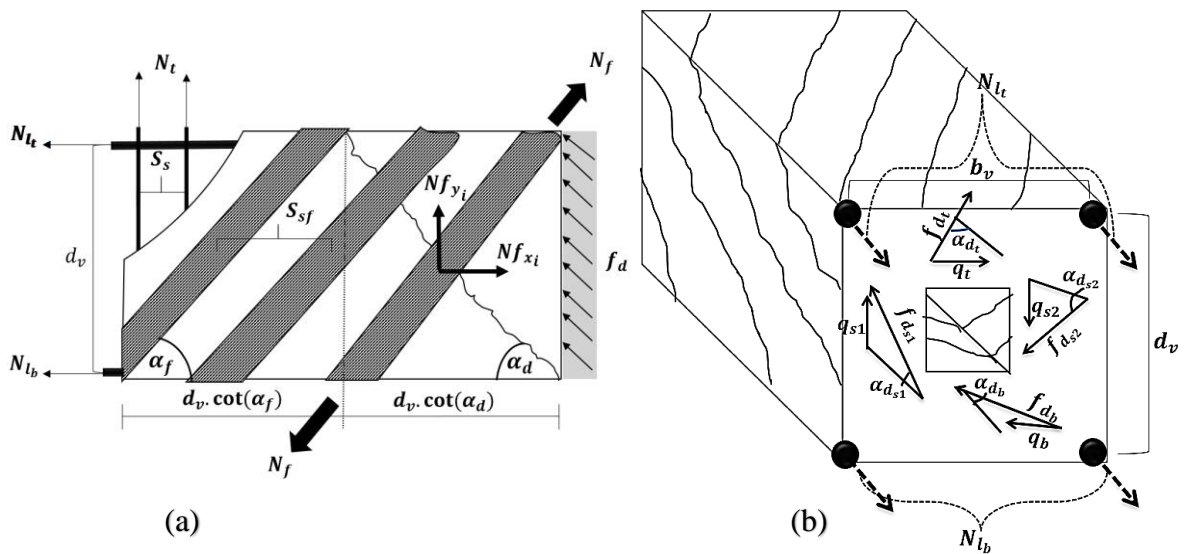


Figure 6.2: (a) Truss mechanism for inclined fibres (b) Space truss mechanism

$$M_u = A_{l_b} F_l (d_v) - 0.5 q_{s1} (d_v) \cot(\alpha_{d_{s1}}) (d_v) - 0.5 q_{s2} (d_v) \cot(\alpha_{d_{s2}}) (d_v) - q_b (b_v) \cot(\alpha_{d_b}) (d_v) \quad \text{Eq.6.6}$$

$$\cot(\alpha_{d_i}) = \frac{q_i S_s}{A_{t_s} f_{t_y}} \quad \text{Eq.6.7}$$

$$q_{s1} = \left(\frac{T_u}{2 A_*} + \frac{V_u}{2 d_v} \right) \quad \text{Eq.6.8}$$

$$q_{s2} = \left(\frac{T_u}{2 A_*} - \frac{V_u}{2 d_v} \right) \quad \text{Eq.6.9}$$

$$q_t = q_b = \left(\frac{T_u}{2 A_*} \right) \quad \text{Eq.6.10}$$

$$N_{l_b} = \frac{M_u}{d_v} + 0.5 \left(\frac{T_u}{2 A_*} + \frac{V_u}{2 d_v} \right)^2 \left(\frac{d_v S_s}{A_{t_s} f_{t_y}} \right) + 0.5 \left(\frac{T_u}{2 A_o} - \frac{V_u}{2 d_v} \right)^2 \left(\frac{d_v S_s}{A_{t_s} f_{t_y}} \right) + \left(\frac{T_u}{2 A_o} \right)^2 \left(\frac{b_v S_s}{A_{t_s} f_{t_y}} \right) \quad \text{Eq.6.11}$$

Where;

q_i = the shear flow in N/mm for section's four sides (q_{s1} , q_{s2} , q_t , and q_b)

A_{l_b} = the area of bottom stingers in mm^2

F_l = the strength in bottom stingers in MPa

F_t = the tensile strength in transverse reinforcements in MPa

N_{l_b} = the tensile force in bottom chords in N

N_{l_t} = the tensile force in top chords in N

N_t = the tensile force of transverse reinforcements in N

N_f = the tensile force in CFRP strips in N

α_{d_i} = the inclination angle of concrete strut for section's four sides ($\alpha_{d_{s1}}$, $\alpha_{d_{s2}}$, α_{d_t} and α_{d_b})

A_{t_s} = the cross-sectional area of transverse reinforcements in mm^2

f_{d_i} = the stress in the inclined concrete struts for section's four sides ($f_{d_{s1}}$, $f_{d_{s2}}$, f_{d_t} , and f_{d_b}), in MPa

M_u = the maximum applied bending moment in N.mm

S_s = the spacing between transverse reinforcements in mm

6.2.2.1 Shear Demand in Concrete Elements with Wrapping Schemes

The evaluation of tensile forces in the main rebars for the strengthened members with vertically oriented wraps needs to consider the influence of the fibre wraps on the inclination angles of the concrete struts of the beam's four sides (left, top, right and bottom). To address the variations in the inclination angles and influence of wrapping fibres orientations, this study has developed a number of formulas that corresponded to warping types and fibres orientations. This can be achieved by accounting for the contribution of the CFRP layer in the vertical direction, as given in Eq. 6.12; where the evaluated angles of inclinations based on Eq. 6.12 should not be more than that obtained from Eq.6.7. Otherwise, the inclination angle is controlled by the yielding of the steel reinforcement before the rupture of CFRP. Following the same steps that were used to develop Eq. 6.11; Eq. 6.13 is introduced to compute the peak tensile forces in the main steel rebars under the combined actions.

Similarly, the CFRP contribution can be adopted for the inclined configuration. However, the relationship between the angle fibre strips and concrete struts (which is illustrated in Figure 6.2a) has to be determined by establishing force equilibrium in the vertical direction for all sides, as given in Eq.6.14. Moreover, to account developed forces in the longitudinal direction (horizontal component - Nf) in the inclined CFRP strips, Eq.6.15 is derived in this study to compute these tensile forces in the CFRP strips. The resultants of CFRP horizontal component was considered at the middle of each wall section. Again, by satisfying equilibrium conditions and substitution of Eq. 6.14 and Eq.6.15 in Eq. 6.6 produces Eq. 6.16, as an expansion of Eq. 6.11. These developed formulas (Eq. 6.14 to 6.16), can be directly utilised to compute the angles of concrete struts (at each beam's side) and tensile force in the main rebars (joint's forces), with different fibre orientations and loads combinations.

The proposed formulas can be modified to account for the different directions of the flexural forces (i.e. negative bending moment), which would induce yielding of the upper chords. This can be performed by equating the applied bending moment to the internal resisting moment about the bottom side and following the same procedure to compute the angles of inclinations, shear flow, and rebar top forces (N_{lt}). However, the proposed formulas have been developed in corresponding to behaviours of fully wrapped sections. While for partial wrapping schemes (e.g. U wraps), further works are recommended to verify the optimal reduction ratio in the wraps contributions in relation to failure

types (i.e. rupture or debonding) and the observed concrete damage in corresponding to Eq. 2.7 and 2.8.

$$\cot(\alpha_{d_i}) = q_i \left(\frac{S_f}{A_f E_f \varepsilon_{fd,e}} \right) \quad \text{Eq.6.12}$$

$$N_{l_b} = \frac{M_u}{d_v} + 0.5 q_{s1} d_v \cot(\alpha_{s1}) + 0.5 q_{s2} d_v \cot(\alpha_{s2}) + q_b b_v \cot(\alpha_b) \quad \text{Eq.6.13}$$

$$\cot(\alpha_{d_i}) = \frac{q_i S_f}{A_f E_f \varepsilon_{fd,e} \sin(\alpha_f)} - \cot(\alpha_f) \quad \text{Eq.6.14}$$

$$N_{f_{xi}} = (A_f \varepsilon_{ef} E_f d_v S_f^{-1}) \cos(\alpha_f) [(\cot(\alpha_f) + \cot(\alpha_{d_i}))] \quad \text{Eq.6.15}$$

$$N_{l_b} = \frac{M_u}{d_v} + 0.5 q_{s1} d_v \cot(\alpha_{s1}) + 0.5 q_{s2} d_v \cot(\alpha_{s2}) + q_b b_v \cot(\alpha_b) - 0.5 \sum_{i=s1}^{i=s2} N_{f_{xi}} - N_{f_{xb}} \quad \text{Eq.6.16}$$

Where;

$N_{f_{xi}}$ = the tensile force in CFRP strips for section's four sides ($N_{f_{xs1}}, N_{f_{xs2}}, N_{f_{xb}}$ and $N_{f_{xt}}$), in N

6.3 Analytical Models of Beam-Column Joint

It is essential to recognise the shear transfer mechanism of the forces that develop at the joint boundaries and which of the failures of RC beam-column connections resulted from inadequate shear strength. Considering the complication of the shear mechanism and the influencing parameters that affect the joint's behaviour, a number of empirical models (Sarsam and Phipps, 1985) and semi-empirical models (Bakir and Boduroğlu, 2002 and Vollum and Newman, 1999a) have been developed to estimate the strength of the joint. Also, several theoretical models were developed, derived using the strut-and-tie theory. These include, the fixed angle softened strut-and-tie model (Hwang and Lee, 1999), the modified rotated angle strut-and-tie model (Wong, 2005), the general multi-strut-and-tie model (Pantelides et al., 2002b), the strut-and-tie models for deteriorated RC half-joints (Desnerck et al., 2018), and the generalized monotonic strut-and-tie model (Parker, 1997). In general, these models require the user to define the strut nodes dimensions which crosspond to the compression zones depths of the beams and columns at the joint boundries; these models are intended to be applied to beam-column joints under flextural loads.

As discussed in Chapter 2, the truss mechanism (compression strut fields - tension ties) for the joint load transfer have been identified (Paulay et al., 1978) and adopted by NZS 3101 (2006). Based on the panel truss mechanism, the Panel Zone Principal Stress-Strain analogy has been adopted by Pantazopoulou and Bonacci (1992) to develop a rational joint model. This model satisfies the equilibrium of forces, compatibility of strain and materials constitutive law. Further, Tsonos (2008) and Tsonos (1996) proposed a joint model which considered the panel truss mechanism and complied with the stress relationships based on Mohr circle. These theoretical models were verified against concentrically loaded members.

In contrast, this study aims to utilise the concepts of the average stress-strain distributions according to the panel zone principal stress-strain method that was developed by (Pantazopoulou and Bonacci, 1992), to predict the joint strength and distortion level when subjected to the set of combined forces. It has been adopted as a more traditional direct strut method, which is based mainly on the equilibrium conditions of the stresses. This means that the strain compatibility, material constitutive conditions, node forces, along with their dimensions, are generally extremely complicated to define under the intricate loading conditions based on the direct strut method found in this investigation. This study re-derives and modifies the panel zone principal stress-strain formulas (Pantazopoulou and Bonacci, 1992) using an iterative approach to satisfy, 1) the equilibrium conditions which correspond to the panel truss and the diagonal strut mechanisms proposed by Tsonos (2008; 2006), and Paulay et al. (1978), 2) the rotating angle theory, and 3) the compatibility conditions according to Mohr's circle. Also, this proposed iterative model accounts for the softening of concrete according to an established constitutive model (Belarbi et al., 1996; Belarbi and Hsu, 1995). This approach will also allow the joint distortion to be determined in combination with the joint shear demands.

6.3.1 Review of Panel Truss Models

Paulay et al. (1978), defined the panel truss mechanism for beam-column joints and suggested that both the truss mechanism and direct strut action transfers shear forces through the joint regions. The authors assumed that a significant part of the joint force can be transferred via the inclined stress field (truss panel action) and the remainder through a direct diagonal strut. These inclined stress fields are induced to balance the vertical and horizontal shear forces that developed into the joint along the rebars resulting via the bond

action. Hence, the panel action to be developed requires a horizontal tie which includes the joint links and the beam rebars in addition to the vertical column rebars.

Tsonos (2008), and Tsonos (1996) proposed a model to evaluate the joint shear capacity in accordance with the panel truss analogy. Similar to Paulay et al. (1978), the model considers the contributions from the panel truss mechanism and the diagonal strut mechanism (Figure 6.3). Both mechanisms were superimposed by adding the force components of the direct strut (D_{cx} and D_{cy}) to the truss model forces (T_{yi} , D_{syi} , and D_{sxi}); in vertical direction, these forces equated to the shear demands in the same direction (Figure 6.3a and b); i.e. $D_{cy} + (T_{y1} + \dots + T_{y4} + D_{sy1} + \dots + D_{syv}) = V_{jy}$. Likewise, the sum of the joint forces in the horizontal direction are equal to the joint demand in the corresponding direction; i.e. $D_{ch} + (D_{sh1} + \dots + D_{shv}) = V_{jh}$. Where, T is the tensile force in truss rebars and D is the compression force in the inclined struts. The joint forces conform with Mohr's circle compressive (σ_{II}) and tensile principal stresses (σ_I). The shear capacity for the joint is assumed to correspond to the biaxial strength relationship between the principal stresses as described below.

- The computation of normal stress in the vertical direction (σ) and the shear stress is as follows:-

$$\tau = \frac{V_{jh}}{h_c b_c} \quad \text{Eq.6.17}$$

$$\sigma = \frac{V_{jv}}{h_c b_c} \quad \text{Eq.6.18}$$

$$\Omega = \frac{V_{jv}}{V_{jh}} \quad \text{Eq.6.19}$$

Where,

τ = shear stresses developed in the joints

σ = normal stress in the joint vertical direction

- The computation of principal stresses (σ_{II} and σ_I) based on Mohr's circle,

$$\sigma_{I,II} = \pm \frac{\sigma}{2} + \frac{\sigma}{2} \sqrt{1 + \frac{4\tau^2}{\sigma^2}} \quad \text{Eq.6.20}$$

- The 5th degree equation based on the biaxial relationship between the principal stresses in concrete (Figure 6.3c) and relating it to the concrete strength f'_c (Eq. 6.21), and equating the joint shear strength (τ) to $\lambda\sqrt{f'_c}$ (Eq. 6.22) is proposed in similar way to that suggested by ACI-ASCE 352R-02 Committee (2002),

$$10 \frac{\sigma_I}{f'_c} + \left(\frac{\sigma_{II}}{f'_c} \right)^5 = 1 \quad \text{Eq.6.21}$$

$$\tau = \lambda \sqrt{f'_c} \quad \text{Eq.6.22}$$

- By substituting Eq. 6.19, Eq. 6.20, and Eq.6.22 into Eq.6.21, the following expression is obtained,

$$(x + \psi)^5 + 10\psi - x = 1 \quad \text{Eq.6.23}$$

where

$$x = \frac{\Omega \lambda}{2\sqrt{f'_c}}$$

$$\psi = \frac{\Omega \lambda}{2\sqrt{f'_c}} \sqrt{1 + \frac{4}{\Omega^2}}$$

The solution of Eq. 6.23 gives the joint strength coefficient (λ). These expressions indicate that the model is based only on the relationships between the joint stresses and the concrete compressive strength, without considering the compatibility of strains. Also, it does not consider the softening of concrete in relation to strain levels.

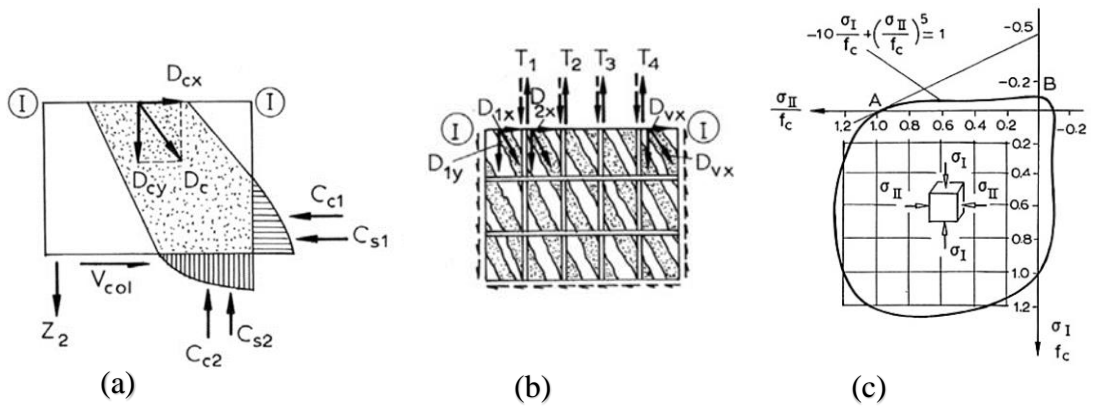


Figure 6.3: (a) Concrete strut mechanism (b) The joint panel truss mechanism (c) Concrete biaxial strength represented by a 5th degree parabola (Tsonos, 2008)

Pantazopoulou and Bonacci (1992) assumed that the stresses and strains were uniformly developed into the joint panels. This assumption is demonstrated in Figure 6.4, where the stresses on the joint panel, which include the shear stress (v_{lt}) and normal stresses in the longitudinal (σ_l) and transverse stress (σ_t) directions of the column are averaged. The total joint normal stresses, σ_l and σ_t are considered to be induced by the column axial load (N_v) and the beam axial load (N_h). As mentioned earlier, this model takes into account the equilibrium and compatibility conditions along with the softening of the concrete struts according to the MCFT stress-strain equations (Section 2.2.3). The model also reflects the influences of the main parameters on the joint strength and deformations (i.e. longitudinal and transverse rebars, axial loads, and compressive concrete strength). As such, it correlates the inclination angle (α) of the joint concrete struts with the ratio of the longitudinal (ρ_l) and transverse (ρ_t) rebars in the joint's area and the levels of axial loads as given in equation Eq. 6.24.

$$\left[\frac{1 + \frac{1}{n\rho_t} - \frac{r}{n\rho_l(n\rho_t + r)}}{1 + \frac{1}{n\rho_t}} \right] \tan^4 \alpha + \left[\frac{\frac{e_v}{\epsilon_t}}{(1 + n\rho_l)(n\rho_t + r)} \right] \tan^2 \alpha - 1 = 0 \quad \text{Eq. 6.24}$$

Where,

$n = E_s/E_c$ (the modular ratio).

$r = e_h/\epsilon_t$.

$e_h = N_h/(E_c b_c h_b)$.

$e_v = N_v/(E_c b_c h_b)$.

- The shear strength (v_{lt}) for the joint panel before the yielding of the joint's links is related to the developed strains (ϵ_t) in the links as given in Eq. 6.25.

$$v_{lt} = \frac{1}{\tan \alpha} \left(\rho_t E_s \epsilon_t + \frac{N_h}{b_c h_b} \right) \quad \text{Eq. 6.25}$$

- This model recognises that the joint deformations are excessively altered after the joint's links yield. Thus, the strain in the transverse direction (ϵ_t) should be calculated according to Eq.6.26. While the joint capacity is the minimum of the shear stresses that are obtained from Eq. 6.27 and Eq. 6.28; in these expressions, the joint capacity is limited to the yielding of

the longitudinal column reinforcement (Eq. 6.27) or the crushing of the concrete struts (Eq. 6.28).

$$\epsilon_t = \left(\frac{1 + \frac{1}{n\rho_l}}{E_c(\rho_t f_y + e_h E_c)^3} \right) v_{lt}^2 - \frac{e_v}{n\rho_l(\rho_t f_y + e_h E_c)^2} - \frac{\rho_t f_y - e_h E_c}{E_c} \quad \text{Eq. 6.26}$$

$$v_{lt} = \sqrt{\left(\rho_t f_y + \frac{N_h}{b_c h_b} \right) \left(\rho_l f_y + \frac{N_v}{b_c h_c} \right)} \quad \text{Eq. 6.27}$$

$$v_{lt} = \sqrt{\left(f_{max} - \rho_t f_y + \frac{N_h}{b_c h_b} \right) \left(\rho_t f_y + \frac{N_h}{b_c h_b} \right)} \quad \text{Eq. 6.28}$$

Where,

f_{max} = The ultimate strength of the softened concrete struts according to the MCFT method that was developed by Vecchio and Collins (1986)

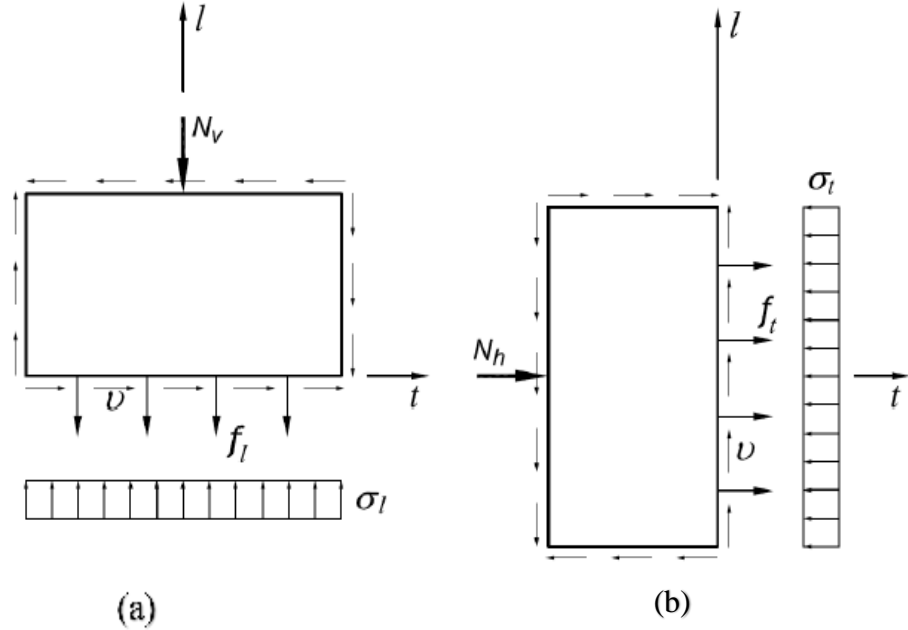


Figure 6.4: Stress equilibrium according to average stress-strain panel zone (a) Equilibrium of vertical force (b) Equilibrium of horizontal forces (Pantazopoulou and Bonacci, 1992)

6.3.2 Model Derivation for Beam-Column Joint

Based on the concept of average stresses proposed by Pantazopoulou and Bonacci (1992), the distribution of the normal stress and shear stress are considered uniform across the joint. The stresses along the main bars of the beam and top face of the joint is illustrated Figure 6.5a, where a significant proportion of the beam stresses was introduced into the joint by bond stresses between the bars and the surrounding concrete (equal and opposite to the rebar forces f_{sl_i} - Figure 6.5c). This study assumed that sufficient bonding and anchorage conditions, to maintain the panel mechanism through the diagonal concrete struts, were developed between cracks (Figure 6.5c). The kinematics of the joint panel due to the beam shear demand is illustrated in Figure 6.5b; this shows the total deformation of the joint as defined by the average angle of distortion (γ) and longitudinal (ϵ_l) and transverse (ϵ_t) strains.

Referring to Figure 6.5c, the equilibrium of forces in the joint horizontal (l) and vertical (t) directions are given in Eq. 6.29 and Eq.6.30, respectively. The total forces acting in the joint core corresponding to the panel truss and diagonal struts mechanisms were equated to the joint shear forces (V_{jh} and V_{jv}) (Tsonos, 2008; Tsonos, 1996; Paulay et al., 1978), where the force components of the concrete strut (fcD_i) are added to the truss model forces (e.g. f_{sl_i} and f_{st_i}) in the horizontal and vertical direction; these forces equate to the shear demands (V_{jh} and V_{jv}) in the same direction; further, the column axial force (P_c) is incorporated in Eq. 6.30 in satisfying the equilibrium of the joint. The vertical shear forces (V_{jv}) can be evaluated according to Eq. 6.31 and Eq.6.32 (Paulay et al., 1978; Priestley and Seible, 1995). Eq. 6.33 and 6.34 restate the equilibrium of forces to comply with the average stresses of the two orthogonal directions (σ_l and σ_t); as the average stresses in concrete are equivalent to the developed forces in concrete divided by the corresponding joint's face. While the average stresses that developed in the embedded steel rebars (σ_{sl} and σ_{st}) need to be adjusted based on the smeared stress concept (continuous materials, i.e. the stress-strain relationship correctly attained) by multiplying σ_{sl} and σ_{st} by the reinforcement ratios in both the longitudinal and transverse direction of the joint.

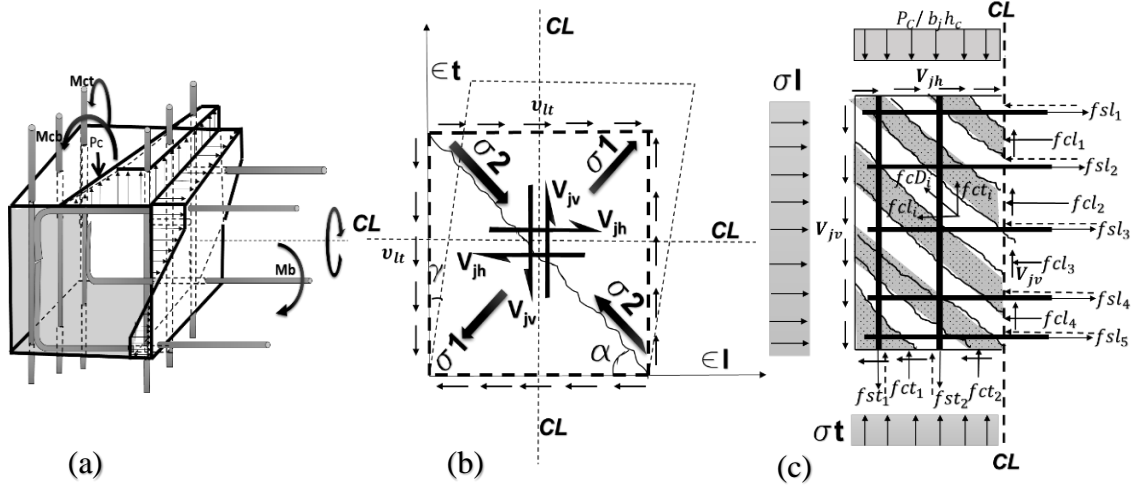


Figure 6.5: (a) Stress variation along steel bars (b) kinematics of joints (c) forces and average stresses in the joint's section

$$\sum_{i=1}^n fcl_i + \sum_{i=1}^n fsl_i = V_{jh} \quad \text{Eq. 6.29}$$

$$\sum_{i=1}^n fct_i + \sum_{i=1}^n fst_i = V_{jv} - P_c \quad \text{Eq. 6.30}$$

$$V_{jv} = \beta V_{jh} \quad \text{Eq. 6.31}$$

$$\beta = \frac{h_b}{h_c} \quad \text{Eq. 6.32}$$

$$\sigma_{cl} + \rho_{sl} \sigma_{sl} = \frac{v_{lt}}{\beta} \quad \text{Eq. 6.33}$$

$$\sigma_{ct} + \rho_{st} \sigma_{st} = \beta v_{lt} - \frac{P_c}{b_j h_c} \quad \text{Eq. 6.34}$$

$$v_{lt} = \frac{V_{jh}}{b_j h_c} \quad \text{Eq. 6.35}$$

Where;

fsl_i and fst_i = the forces in the longitudinal and transverse reinforcements, respectively, in kN

fcl_i and fct_i = the forces in the concrete strut in the longitudinal and vertical directions, respectively, in kN

P_c = the axial compressive force (column's load) in kN

V_{jh} and V_{jv} = the horizontal and vertical joint shear forces, respectively, in kN

σ_{sl} and σ_{st} = the stresses in the longitudinal and transverse reinforcement, respectively, in MPa

σ_{cl} and σ_{ct} = the stresses in the concrete in the longitudinal and transverse directions, respectively, in MPa

ρ_{sl} and ρ_{st} = the reinforcement ratio in the longitudinal and transverse directions, respectively

σ_l and σ_t = total average joint stresses in the longitudinal and transverse directions, respectively, in MPa

v_{lt} = the joint shear stress in MPa

h_c = the column depth in mm

b_j = the joint depth in mm

h_b = the beam depth in mm

To evaluate the angle of inclination (α) of the concrete strut, the rotating angle theory is employed, where the angle coincides with the principal stresses σ_2 – σ_1 as shown in Figure 6.5b. The general transformation matrix for the in-plane stresses in the orthogonal directions ($l - t$) and the principal stress coordinates ($1 - 2$) for the concrete is given by Eq. 6.36. Eq. 6.37 to 6.39 are the equilibrium equations which are compatible with the (Mohr) truss model. An additional equation which associates the maximum principal stresses of the concrete with the normal stresses along the l and t directions is also required and is given as Eq. 6.40. For simplicity, the tensile capacity of the concrete (σ_1) is considered to be negligible and, in any plane the normal stresses are not considered to exceed the concrete compressive capacity.

$$\begin{bmatrix} \sigma_l - \rho_{sl} \sigma_{sl} \\ \sigma_t - \rho_{st} \sigma_{st} \\ v_{lt} \end{bmatrix} = \begin{bmatrix} \sin^2 \alpha & \cos^2 \alpha & -2 \sin \alpha \cos \alpha \\ \cos^2 \alpha & \sin^2 \alpha & 2 \sin \alpha \cos \alpha \\ \sin \alpha \cos \alpha & -\sin \alpha \cos \alpha & (\cos^2 \alpha - \sin^2 \alpha) \end{bmatrix} \begin{bmatrix} \sigma_1 \\ \sigma_2 \\ 0 \end{bmatrix} \quad \text{Eq. 6.36}$$

$$\sigma_2 = -v_{lt} \frac{1}{\sin \alpha \cos \alpha} = -v_{lt} \left(\frac{1}{\tan \alpha} + \tan \alpha \right) \quad \text{Eq. 6.37}$$

$$\sigma_l - \rho_{sl} \sigma_{sl} = -v_{lt} \cot \alpha \quad \text{Eq. 6.38}$$

$$\sigma_t - \rho_{st} \sigma_{st} = -v_{lt} \tan \alpha \quad \text{Eq. 6.39}$$

$$\sigma_2 + \sigma_1 = \sigma_l + \sigma_t \quad \text{Eq. 6.40}$$

Three compatibility equations based on the Mohr circle of strain reported by Vecchio and Collins (1986) were used. The relationship between the strain components (ϵ_l , ϵ_t , ϵ_1 , ϵ_2 , and γ_{lt}) are given by Eq. 6.41 to 6.43. The inclination of the joint concrete compressive strut (Eq.6.43) can be determined according to the compression stress field theory (Vecchio and Collins, 1986). Finally, the reinforcement is assumed to be adequately anchored within the concrete such that strain compatibility exists between the two components. Thus, two constitutive equations (Eq.6.44 and 6.45) which conform to Hook's law and neglect the tension stiffening of concrete are used to evaluate the longitudinal and transverse strains in the bars.

$$\epsilon_2 + \epsilon_1 = \epsilon_l + \epsilon_t \quad \text{Eq. 6.41}$$

$$\frac{\gamma_{lt}}{2} = \frac{(\epsilon_1 - \epsilon_l)}{\tan \alpha} \quad \text{Eq. 6.42}$$

$$\tan^2 \alpha = \frac{\epsilon_l + \epsilon_2}{\epsilon_t + \epsilon_2} \quad \text{Eq. 6.43}$$

$$\epsilon_t = \frac{\rho_{sl} \sigma_{sl}}{E_{sl}} \quad \text{Eq. 6.44}$$

$$\epsilon_l = \frac{\rho_{st} \sigma_{st}}{E_{st}} \quad \text{Eq. 6.45}$$

Where;

ϵ_l and ϵ_t = the average strains in longitudinal and transverse directions, respectively

ϵ_1 and ϵ_2 = the average strains in the principal directions, respectively.

E_{sl} and E_{st} = the modulus of elasticity for the longitudinal and transverse reinforcement, respectively

γ_{lt} = the shear distortion angle in radian and E_c is the modulus of elasticity of concrete

Referring to the previous equations and relationships between the stresses and strains in the concrete and reinforcement, the sum of Eq. 6.33, 6.34, 6.38 and 6.39 produced equations (6.46) and (6.47) in order to evaluate (ϵ_l) and (ϵ_t) before the initiation of yielding in the joint rebars occur. According to Eq. 6.43, the magnitude of the principal strains, (ϵ_1) and (ϵ_2) are related to the angle of inclination as given in Eq. 6.48 and 6.49. The nominal angle of

inclination of the concrete strut before yielding of the steel ties is computed by associating the maximum compressive strain (ϵ_2) to (σ_2/E_c) in Eq. 6.43, where σ_2 is given in Eq. 6.37. This produces a quadratic polynomial equation (Eq. 6.50) in terms of ($\tan \alpha$).

$$\epsilon_l = v_{lt} \frac{\left(\cot \alpha + \frac{1}{\beta}\right)}{E_{sl} \rho_{sl}} \quad \text{Eq. 6.46}$$

$$\epsilon_t = \frac{\frac{-P_c}{b_j h_c} + v_{lt}(\beta + \tan \alpha)}{E_{st} \rho_{st}} \quad \text{Eq. 6.47}$$

$$\epsilon_1 = \frac{(\epsilon_l \tan^2 \alpha - \epsilon_t)}{(\tan^2 \alpha - 1)} \quad \text{Eq. 6.48}$$

$$\epsilon_2 = \frac{(\epsilon_l - \epsilon_t \tan^2 \alpha)}{(1 - \tan^2 \alpha)} \quad \text{Eq. 6.49}$$

$$\left(\frac{v_{lt}}{E_c} + \frac{v_{lt}}{E_{sl} \rho_{sl}}\right) + v_{lt} \frac{\tan \alpha}{\beta E_{sl} \rho_{sl}} - \frac{\tan^3 \alpha}{E_{st} \rho_{st}} \left(\beta v_{lt} - \frac{P_c}{b_j h_c}\right) - \tan^4 \alpha \left(\frac{v_{lt}}{E_{st} \rho_{st}} + \frac{v_{lt}}{E_c}\right) = 0 \quad \text{Eq. 6.50}$$

A rapid decrease in the joint strength after the yielding of the shear links was reported by Bonacci and Pantazoupoulou (1993). Thus, when ϵ_l is equal to $\left(\frac{\sigma_{sly}}{E_{sl}}\right)$, the angle of inclination should be calculated from Eq. 6.51. The vertical strain (ϵ_t) of the reinforcement (ties) is related to the yielding of the horizontal ties by substitution of Eq. 6.51 in Eq. 6.47, as given in Eq. 6.52. Finally, after the yielding of the steel ties, the horizontal and vertical strain (ϵ_l and ϵ_t) in Equations 6.48 and 6.49 should be replaced by ϵ_{ly} and ϵ_{ty} .

$$\cot \alpha = \frac{\sigma_{sly} \rho_{sl} - \frac{v_{lt}}{\beta}}{v_{lt}} \quad \text{Eq. 6.51}$$

$$\epsilon_t = \frac{1}{E_{st} \rho_{st}} \left(\frac{-P_c \sigma_{sly} \rho_{sl} + \frac{P_c v_{lt}}{\beta} + b_j h_c \beta v_{lt} \sigma_{sly} \rho_{sl}}{(\sigma_{sly} \rho_{sl} - v_{lt}) b_j h_c} \right) \quad \text{Eq. 6.52}$$

The capacity of the compression inclined cracked concrete struts is reduced in accordance with the increase of tensile strain (ϵ_1). The softening of

concrete in compression has been evaluated by Vecchio and Collins (1986), (1993), and Belarbi and Hsu (1995), Hsu, (1996). The softened stress-strain relationship is presented in Eq.2.3a, and Eq.2.3b; this study utilises the recent concrete model (Hsu and Belarbi model) to investigate the concrete strut capacity in accordance with the joint major strains (ϵ_l and ϵ_t). The ultimate concrete strut strength (f_{max}) is given in Eq. 6.53a and Eq. 6.53b.

$$f_{max} = \xi_{\sigma 0} f_c' \quad \text{Eq. 6.53a}$$

$$\xi_{\sigma 0} = \frac{0.9}{\sqrt{1 + 400\epsilon_1}} \quad \text{Eq. 6.53b}$$

The formulas of the proposed beam-column joint model (Section 6.3.2) were implemented by using in MATLAB (2013), which is based on algorithm shown in Figure 6.6; an iterative method was used to check the concrete strut capacity and the yielding of the bars through the incrementing of the joint shear (v_{lt}). The joint shear increment is limited to the shear forces were calculated according to Section 6.2.2 of this study.

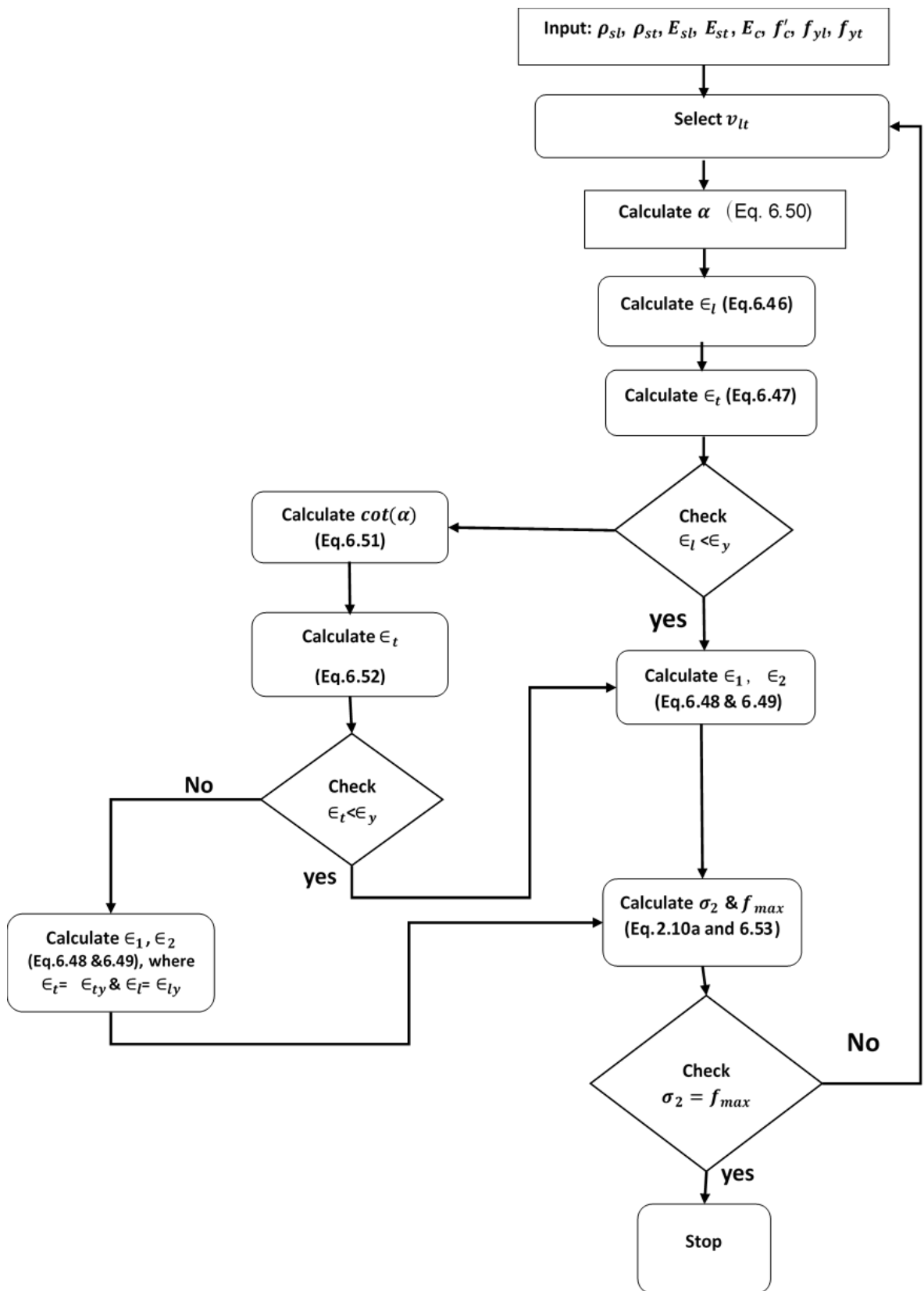


Figure 6.6: Solution flow chart

6.4 Model Validation and Discussion

The peak tensile forces in the beam's bottom steel for all specimens (SH-U-C, SH-S-C-A, SH-S-C-H, and SH-S-C-I) were calculated according to Section 6.2 (i.e. Eq. 6.11, Eq. 6.13, and Eq. 6.16) and compared to the tests results (Figure 6.7). The beam forces (T_B) were quantified based on experimentally obtained data (strain measurements). Figure 6.7 shows a good agreement between the predicted and tests results with a mean value of 0.98 for the ratio of the test to the model results and a corresponding coefficient of variation (COV) of 2% was achieved. Table 6.1 shows the predicted ultimate torsional capacity (i.e. designed capacities-Section 6.2.1) for the specimens along with the computed concrete inclination angle (α_d) in the beam's side walls and designed struts concrete capacity (σ_d). The predicted (σ_{dv}) is based on the lowest (most critical) obtained value in the beam side 1, where the torsion and shear acted in the same direction (i.e. additive). Based on the evaluated percentage differences (Table 6.1), there was no crushing of the concrete before the specimens reached their designed capacities.

In addition, the predictions of the strengthened member behaviour closely followed the actual development of the design load to maximum and then beyond as it deteriorated following the peak load. The differences between the analytically and experimentally obtained torsional peak loads are shown in Figure 6.8. This study has taken the partial factors of safety equal to unity in order to apply direct comparison with tests results; however, incorporation of the material safety factors for concrete and FRP composites are recommended in-line with design code stipulations, as given in (Eurocode 2, 2004; fib Bulletin 14, 2001). For example, Eurocode 2 suggests reducing rebars strength and the concrete struts strength by 1.15 and 1.5, respectively. Wherein the fib bulletin 14 recommends a reduction of the fibres modulus based on the FRP thickness (e.g. multiple layers) and proposed the partial safety factor (i.e. ranged from 1.2 to 1.35 to CFRP).

Table 6.1: Predicted (designed) torsional capacity, strut angles in the beam sides, concrete strut capacity and ultimate strut stress.

Specimen	Tu_{steel} (Eq. 3.1) kN.m	Tu_{frrp} (Eq. 6.1) kN.m	V_u kN	α_d (°) (Eq. 6.7, Eq. 6.12, and Eq. 6.14)			f_{dv} (Eq. 6.4) MPa	σ_{dv} (Eq. 6.3) MPa	strut stress (Eq. 6.5) MPa	% Diff. (σ_d - Struts/ σ_d)
				Side (1)	Side (2)	Top and Bot.				
SH-U-C	14.1	-	9	38	42	40	17.47	9.00	7.68	15%
SH-S-C-A		12.6	17	39	50	44	16.14	7.75	7.07	10%
SH-S-C-I		7.7	13.8	21	34	26	12.25	6.27	5.77	9%
SH-S-C-H		7.5	13.7	25	35	29	12.95	6.72	6.75	17%

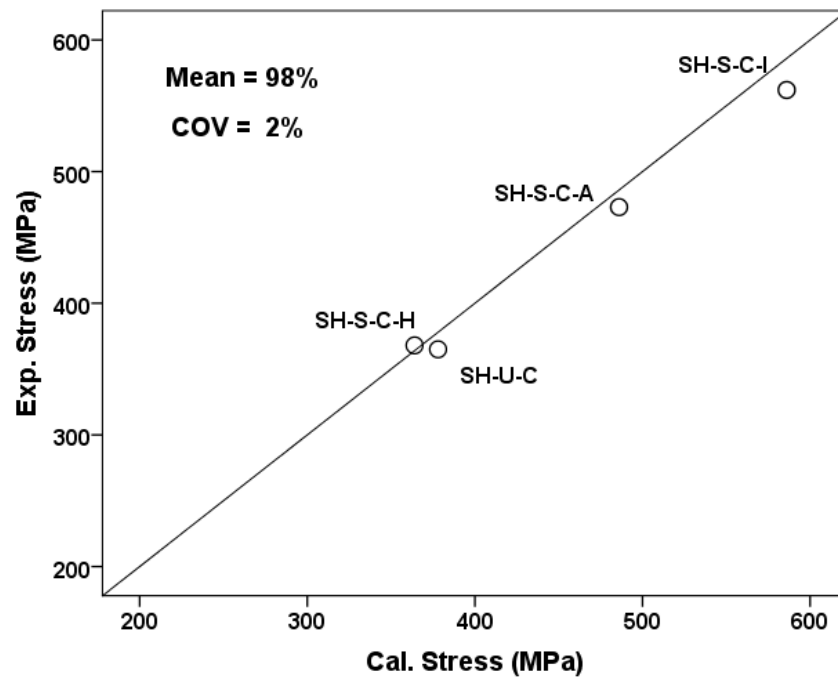


Figure 6.7: Experimental versus predicated tensile stresses in the bottom beam chords by using the proposed method

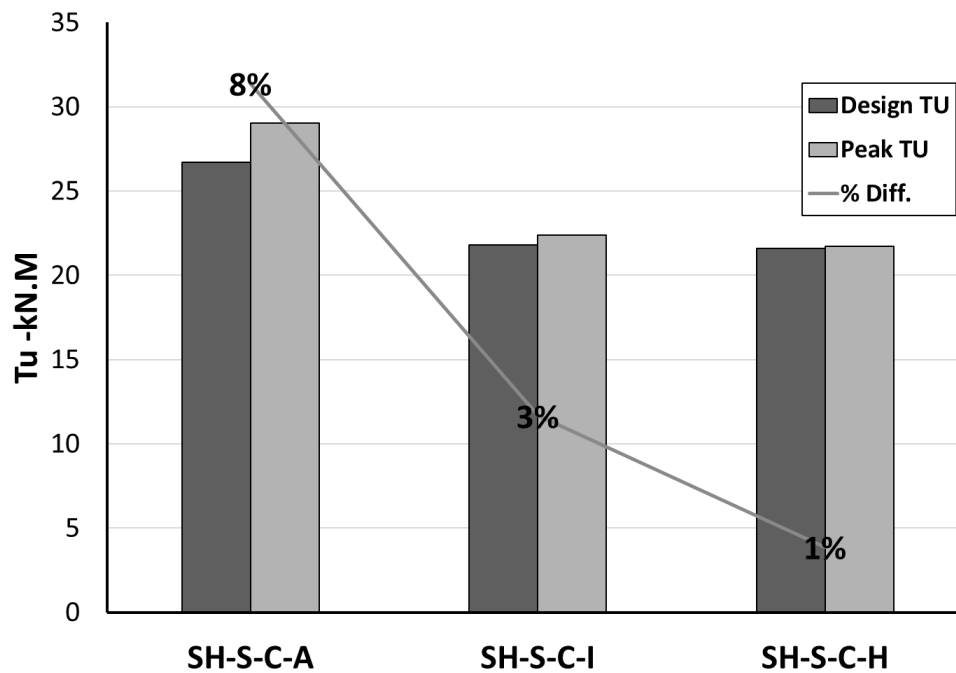


Figure 6.8: A comparison between the design and peak torsional capacity (T_u) for strengthened specimens

The shear distortion angle of the joint zone for each specimen was evaluated according to Eq. 6.42. The comparison between the model and the tests (Section 4.6) in terms of angle of distortion is shown in Figure 6.9. From this figure it can be seen that the model can successfully predict the joint distortion when subjected to different beam forces (shear demands). In addition to the computed joints detorsion levels, the developed model was further tested by validating the predicted joints capacities under different levels of combined loads against independent experimental data. Accordingly, the results of five un-strengthened RC beam-column joints (SP1, SP3, SP4, SP7, and SP8) reported by Elshafiey et al. (2016) were considered as given in Table 6.2. These five specimens failed in the joint zones where the experimental joint forces were calculated according to Section 6.2.2 (Eq. 6.7 to Eq. 6.11). The comparison of the predicted results using the proposed model and the experimental results from Elshafiey et al. (2016) in terms of maximum joint force (V_j) is shown in Figure 6.10. Again, a good correlation is seen with a mean value of 98% for the ratio of the experimental to the predicted V_j ; the COV is equivalent to of 4%.

Table 6.2: Comparison between experimental and predicted results using the developed model.

Study	Specimen	Max. joint shear force (V_j) (kN)		Exp./Cal.
		Exp.	Cal.	
Elshafiey et al. (2016)	Sp1	346	352	0.98
	Sp3	412	423	0.97
	Sp4	487	468	1.04
	Sp7	473	531	0.89
	Sp8	635	608	1.04
Average				0.98
Standard deviation				6%

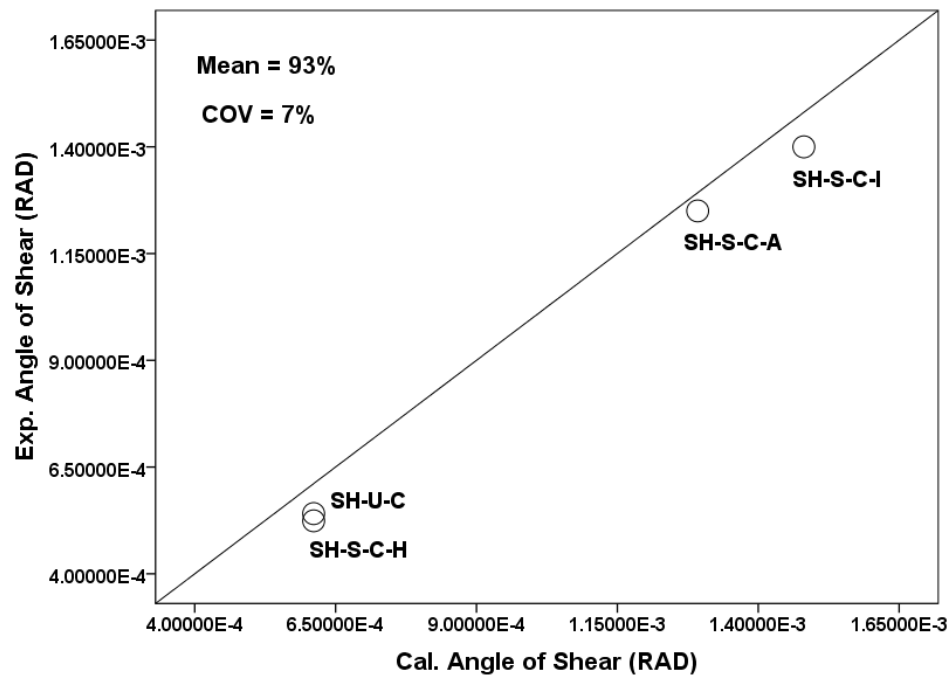


Figure 6.9: Comparison between experimental and predicted maximum joint distortion angles

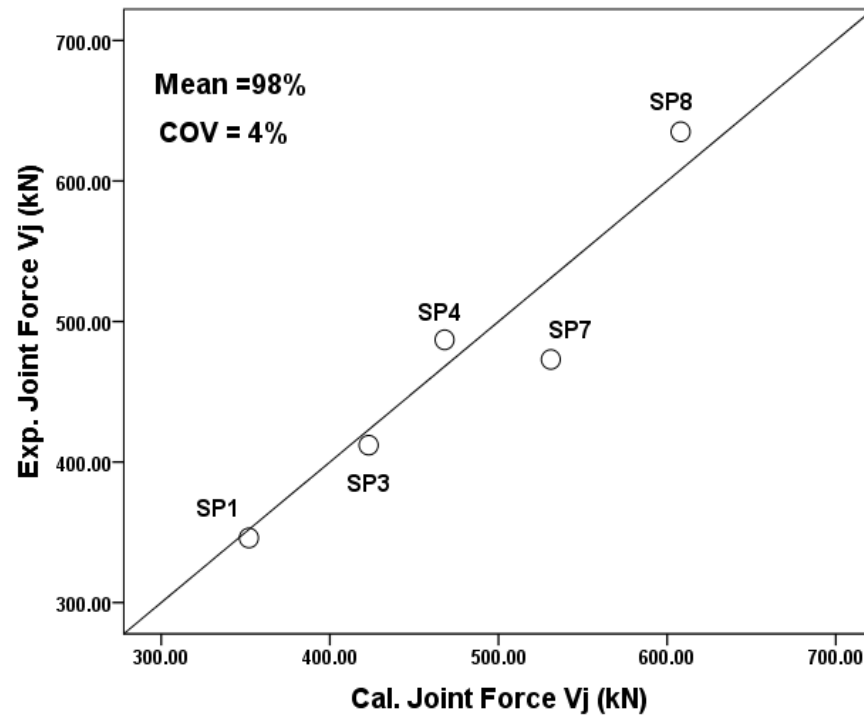


Figure 6.10: Comparison between experimental and predicted maximum joints forces (V_j)

The model developed in this investigation has been formulated to evaluate the influence of an increase in beam load on the joint's integrity resulting from additional torsional forces that are proportional to the beams strengthening schemes. It considers that the beam forces are essentially transferred into the joint zone by the main steel, while the beam flexural compressive forces at the joint boundaries (beam compressive stress block) will be less effective in accordance with the ratio of torque to bending. The magnitude of the main rebar forces corresponds to the level of bending, torsional and shear forces (Eq. 6.11, Eq. 6.13, and Eq. 6.16) that can be carried by the beam. However, the beam carrying capacity is directly influenced by the concrete strut strength (Eq. 6.4); the transverse reinforcement (stirrups and CFRP) are represented in the strut inclination angle (Eq. 6.7, Eq. 6.12, and Eq. 6.14) in which both components have an effect on the strut and steel forces, which is reflected in Eq. 6.4, Eq. 6.11, Eq. 6.13, and Eq. 6.16.

Similarly, the shear resistance capacity of the joint zone through all the solution stages is limited by the peak strength of the softened concrete (Eq. 6.53). The derived expressions in Section 6.3.2 account for the effect of the

reinforcement ratios (ρ_{sl} and ρ_{st}), the column axial load (P_c) and the joint aspect ratio (β) on the joint capacity and its distortion level. It was also noticed that the effectiveness of the joint reinforcement was enhanced by an increase in the concrete strength (f'_c). Furthermore, these joint expressions could be adjusted to consider the joints that were externally bonded with uniaxially FRP systems by including the fibres ratios along the longitudinal and vertical axis (ρ_{frp_l} and ρ_{frp_t}) in a similar manner to the ratio of steel reinforcement in the same directions. In this case, the $\rho_{sl} \sigma_{sl}$ and $\rho_{st} \sigma_{st}$ in the equilibrium equations should be respectively replaced by $(\rho_{sl} \sigma_{sl} + \rho_{frp_l} \sigma_{frp_l})$ and $(\rho_{st} \sigma_{st} + \rho_{frp_t} \sigma_{frp_t})$, as shown in Figure 6.11, as well as following the procedure shown in Section 6.3.2 to formulate the other equations based on this modification. Hence, the reformulation of the corresponding equations is given in Eq. 6.46R, Eq. 6.47R, Eq. 6.50R, Eq. 6.51R, and Eq. 6.52R. Further, future work should be carried out to investigate the sensitivity of this adjustment to the other factors such as multiple FRP layers, bonding length and anchorage systems.

$$\epsilon_l = v_{lt} \frac{\left(\cot \alpha + \frac{1}{\beta} \right)}{E_{sl} \rho_{sl} + E_{fl} \rho_{frp_l}} \quad \text{Eq. 6.46R}$$

$$\epsilon_t = \frac{\frac{-P_c}{b_c h_c} + v_{lt} (\beta + \tan \alpha)}{E_{st} \rho_{st} + E_{ft} \rho_{frp_t}} \quad \text{Eq. 6.47R}$$

$$\left(\frac{v_{lt}}{E_c} + \frac{v_{lt}}{E_{sl} \rho_{sl} + E_{fl} \rho_{frp_l}} \right) + v_{lt} \frac{\tan \alpha}{\beta E_{sl} \rho_{sl} + \beta E_{fl} \rho_{frp_l}} - \frac{\tan^3 \alpha}{E_{st} \rho_{st} + E_{ft} \rho_{frp_t}} \left(\beta v_{lt} - \frac{P_c}{b_c h_c} \right) - \tan^4 \alpha \left(\frac{v_{lt}}{E_{st} \rho_{st} + E_{ft} \rho_{frp_t}} + \frac{v_{lt}}{E_c} \right) = 0 \quad \text{Eq. 6.50R}$$

$$\cot \alpha = \frac{\sigma_{sly} \rho_{sl} + \epsilon_y E_{fl} \rho_{frp_l} - \frac{v_{lt}}{\beta}}{v_{lt}} \quad \text{Eq. 6.51R}$$

$$\epsilon_t = \frac{1}{E_{st} \rho_{st} + E_{ft} \rho_{frp_t}} \left(\frac{-P_c (\sigma_{sly} \rho_{sl} + \epsilon_y E_{fl} \rho_{frp_l}) + \frac{P_c v_{lt}}{\beta} + b_j h_c \beta v_{lt} (\sigma_{sly} \rho_{sl} + \epsilon_y E_{fl} \rho_{frp_l})}{(\sigma_{sly} \rho_{sl} + \epsilon_y E_{fl} \rho_{frp_l} - v_{lt}) b_j h_c} \right) \quad \text{Eq. 6.52R}$$

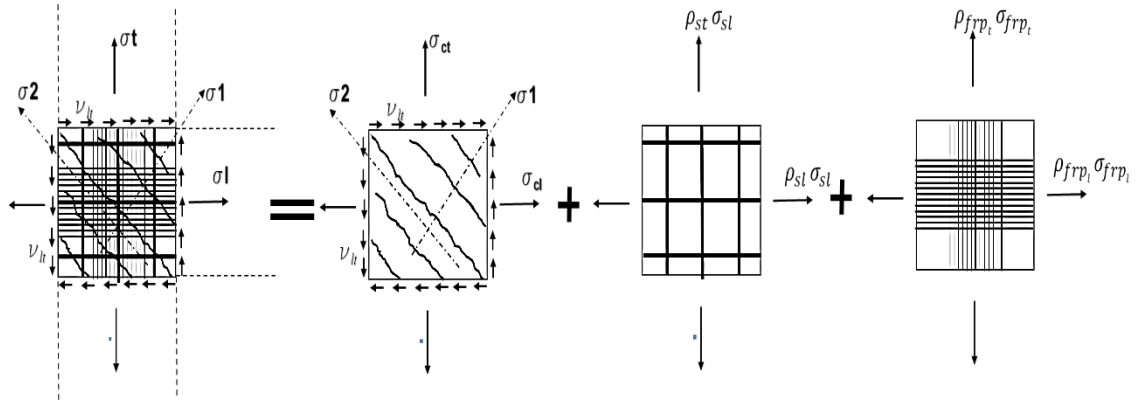


Figure 6.11: Joint stress equilibrium in two orthogonal directions in the presence of steel and FRP reinforcement

6.5 Summary

The aim of this analytical investigation is to quantify the influences of the combined forces and the different wrapping schemes on the joint forces, concrete damage, and joint distortions. The main conclusions drawn from this investigation are summarised as follows:

1. The predicted results using the developed formulas indicated that the interaction of forces in the beam chords were adequately quantified. The mean value of the experimental to prediction ratio was 98% with a coefficient of variation (COV) of 2%.
2. The superposition approach employed to incorporate the CFRP contributions in terms of predicting the member's torsional capacity and the variation in concrete struts inclination angle is suitable. These contributions were evaluated according to the truss analogy.
3. A design approach was introduced in order to account the level of developed compressive forces due to shear-flow levels, and hence prevent the concrete failure. As the level of compressive strut's forces is limited to the concrete strut capacity (σ_d). Further, the reduction in strut strength (σ_d) due to shear induced cracks is evaluated according to Eurocode 2. Meanwhile, the root-square summation of direct shear

and torsional forces is considered to evaluate the shear stress distribution over the section depth.

4. The predicted (designed) torsional peak loads in this investigation were very close to the tests results; the maximum difference between actual and model results did not exceed 8% for the SH-S-C-A specimens. Further, at the ultimate design load, no failure in concrete has been observed which agreed with the computed concrete struts' capacity.
5. It was found that the concept of the average stress-strain distributions, according to the panel zone principal stress-strain, allows the joint deformation to be determined in combination with the joint shear demands. The geometry conditions, softening of concrete, and definition of nodes forces and their dimension within and the joint boundaries are extremely complex and difficult to determine using the traditional direct strut method under combined loads.
6. An iterative model has been developed based on the panel zone principal stress-strain method. This model addresses the softening of the concrete and the truss panel and direct strut mechanisms. Also, it accounts for the joint's most influential parameters, i.e., concrete strength, the main rebar and transverse reinforcement ratios, the column axial load, and the joint aspect ratio (β). This model will allow the joint distortion and capacity to be determined in combination with the joint shear demands.
7. A good agreement between the iterative model and the test results was achieved; mean values of not less 93% with a COV of not more than 7% was obtained in terms of the joint's deformation angle. Further, a strong correlation was seen (i.e. a mean value of 98% and a COV of 4%) for the ratio of the experimental to the predicted V_j .
8. To account for the effect of joint wrappings, modifications of the model expressions were introduced accordingly. However, the sensitivity of these modifications still needs to be verified using different factors (i.e. number of FRP layers, bonding length, and anchorage systems).

Chapter 7 Finite Element Modelling

7.1 Introduction

The experimental program aimed to investigate the influences of multiple actions including torsion with considering several effective beam wraps on the behaviour of beam-column joints. Hence, beside the experimental investigations, a validated Finite Elements (F.E.) model is required for further studies on influence of combined loads on the beam-column joints with various variables. Meanwhile, a reliable model can be effectively utilised as an investigative tool in conjunction with different wrapping schemes, material properties, multiple CFRP layers, and loading conditions to further verify the mechanics and deformation of beam-column joints. The considered variables in this investigation include different ratios of torsion to bending and shear loads in order to investigate- (i) the level of developed strains (plastic strains) in the beam's main rebars and concrete, (ii) joints damage levels, and (iii) failure zones. Further, this study explores the influence of using High Strength Concrete (HSC) on behaviours of the beam-column joints under sustained loads (long-term) and monotonic loads up to failure (short-term).

The finite element models are created by using the Midas FEA and three-dimensional non-linear static analysis were conducted to account the out-of-plane and in-of-plane stresses and strains developed from torque actions. The Midas FEA has powerful tools to generate detailed geometries and meshes, in addition, it provides several material constitutive models. The constitutive condition and nonlinear characteristics of concrete were based on the total strain crack model. The viability of this model to simulate the behaviours of strengthened RC sections under torque actions has been verified in Chapter 2. In this chapter, the methodology and techniques that were utilised for creating the finite element models is presented. The numerical results obtained from the finite element analysis were compared with the computed values from the formulas developed in Chapter 6 to quantify the joint demands and concrete struts damage.

7.2 Modelling of Material

Several constitutive models are incorporated in the Midas FEA in order to realistically simulate the behaviours of different materials. In this study, the beam-column joints were composed from three materials (i.e. concrete, steel rebars, and CFRP wraps). A detailed discussion regarding the utilised constitutive models is provided in this Section.

7.2.1 Concrete Modelling

Total strain cracks model is proposed in Midas FEA for cracked concrete which is based on the Modified Compression Field Theory (MCFT) by Vecchio and Collins (1986). As identified in Chapter 2, this model was formulated on the basis on plain stress constitutive model and it has been extended into three-dimensional model as proposed by Selby and Vecchio (1993; 1991). The total strain crack model conforms to smeared crack concept, where the concrete deterioration over the continuum is intended to be quantified through the constitutive relations which are evaluated in corresponding to the principal directions of the strains. The cracked concrete treated as orthotropic material and the crack initiation follows the principal strains directions. The equilibrium conditions and compatibility relationships corresponded to average stresses and strains. The total strain crack model allows to define nonlinear behaviour of concrete in more practical way by considering one stress-strain condition for tensile response and one for compressive response. Further, based on the smeared cracks concept, the concrete cracking levels only can be identified using the total strain crack model in the Midas FEA.

Midas FEA propose two methods (rotating and fixed crack methods) to model the cracked concrete behaviour in accordance with the total strain crack model. The rotating crack method assumes the directions of cracks coincide with the axes of principal strains and the directions of cracks continuously rotate in relation to the changes of principal strain's axis, where no shear produced in the direction of cracks as shown in Figure 7.1. This method ignores the cracks developed at the previous loading stages. In contrast, once the crack direction is identified, the fixed cracks method assume that the crack's axis remains constant.

In this numerical investigation, the total strain crack model was employed by considering constitutive relationships for modelling the tensile, compressive, and shear behaviour of concrete. The fixed crack method was used to model

the concrete cracking behaviour to be compared with the visible cracks that were noticed in the tests. Since, the fixed crack model can reflect the physical characteristics of the formed cracks. The compressive strength and modulus of elasticity of concrete that experimentally obtained (Chapter 3) were used to define concrete properties in the Midas FEA. While, for high strength concrete, the modulus of elasticity was evaluated according to Eurocode 2 (2004).

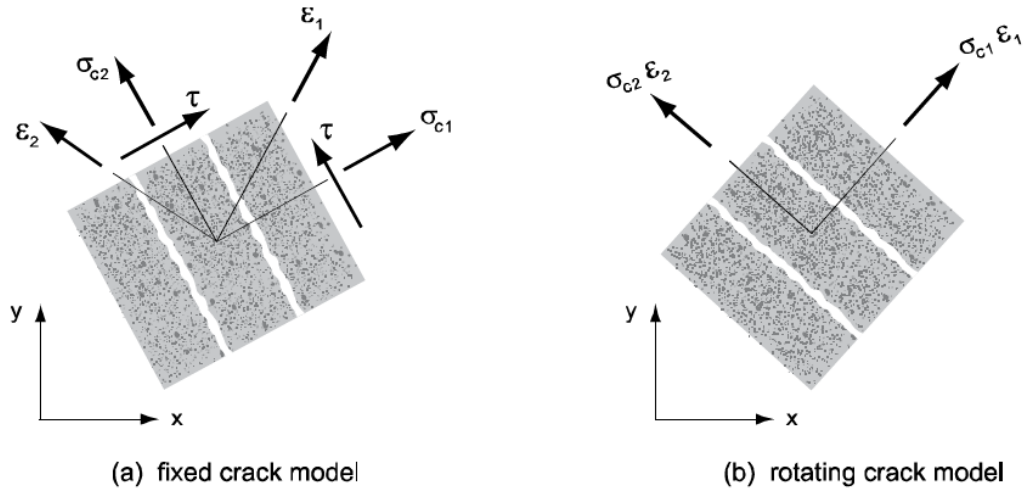


Figure 7.1: Fixed and rotating crack models

(Midas FEA Manual, 2015)

7.2.1.1 Concrete in Tension

At pre-cracking stage, the behaviour of concrete is linear elastic up to the ultimate tensile strength (f_t). However, when the concrete stress exceeds the ultimate tensile strength, the reinforced concrete exhibits strain decrements in accordance with a softening model that relates to the fracture energy (G_F) through a crack band width (h). Midas FEA provides several models to represent the concrete behaviour in tension that involved several softening functions -i.e. decrements when the peak load reached. These models include linear, exponential, Hordijk, and Multilinear (user defined stress-strain curve). In the present study, the Hordijk (1991) model (see Figure 7.2) was employed; as it introduces a nonlinear softening expression that realistically reflects the behaviour of concrete at post-cracking stage. It assumes that the concrete capacity (stress) gradually decreases; while at the ultimate strain value (ϵ_{ult}), the concrete tensile capacity drops to zero (fully opened cracks). The ultimate strain (ϵ_{ult}), for concrete based on the Hordijk (1991) work is equivalent to $5.136 (G_f/h_e f_t)$.

The fracture energy (G_F) of concrete was evaluated from Eq. 7.1 which it is proposed by the fib Model Code (2010a). The Model Code indicates that the concrete fracture energy mainly depends on the maximum aggregate size, water/cement ratio, and age of concrete. A crack band width is assumed to be equivalent the characteristic element length (h_e) according to Bažant and Oh (1983), and they suggested h_e as length of element (e) projection along the direction of the crack. By using trial and error approach, Rots (1988) proposed optimal values of h_e as function of element length (e) and type as shown in Figure 7.3. The chosen h_e in this study is the same of element length (e) of hexahedron solid elements that used for modelling the concrete behaviour. The tensile strength input (f_t) was based on the experimental direct tensile tests results (Table 3.9) which were close to the level of principal tensile stresses that induce shear cracking ($0.33\sqrt{f'_c}$); as identified by testing reinforced concrete panels that conducted by Vecchio and Collins (1986) and recommended by ACI Committee 318 (2014). Further, for higher grade of concrete (i.e. 65 MPa), f_t was estimated according $0.33\sqrt{f'_c}$ as given in ACI Committee 318 (2014).

$$G_F = 73 (f_{cm})^{0.18} \quad \text{Eq. 7.1}$$

Where

f_{cm} = the mean compressive strength of concrete

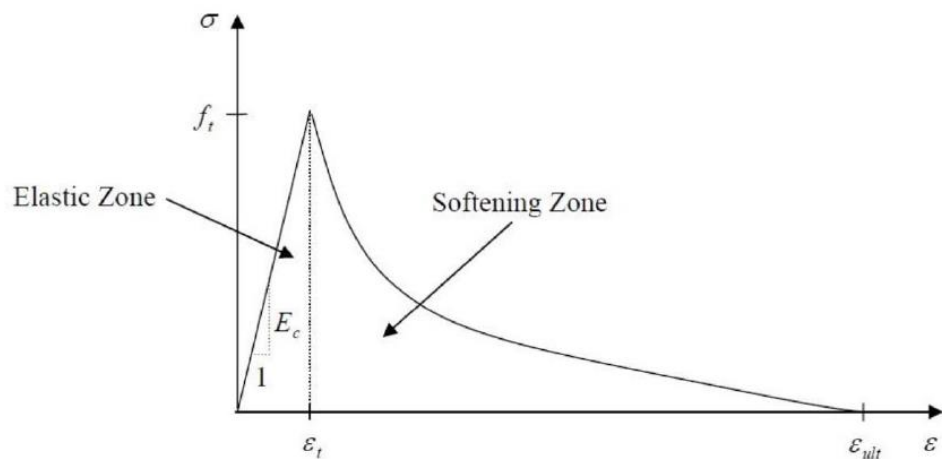


Figure 7.2: Tensile behaviour of concrete based on Hordijk Model
(Hordijk, 1991)

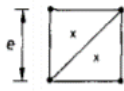
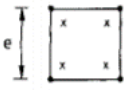
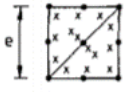

element type and integration	effective band width h for zig-zag fracture propagation through regular mesh (found by trial-and-error for present problem)
	e
	$e\sqrt{2}$
	$\frac{1}{2}e\sqrt{2}$
	e

Figure 7.3: Recommended crack band width according to element size (e) and type

(Rots, 1988)

7.2.1.2 Concrete in Compression

As presented in Chapter 2, the MCFT theory identifies the influence of transverse tensile strains on softening levels of the concrete compressive strength. Further, the rise in the concrete strength with increasing isotropic stress due lateral confinement is accounted in the Midas FEA as suggested by Vecchio and Selby (1993; 1991). The compressive behaviour curve (base curve) is iteratively modified by the software at each load step in relation to levels of softening and confinement, accordingly. Vecchio and Collins (1993) found that the base curve introduced by Thorenfeldt (1987) well represented the concrete softening behaviour better than the parabola curve. This was performed by modifying the Thorenfeldt curve according to the softening factor (β) as shown in Figure 7.4. β is presented as function of principal tensile (ϵ_1) and compressive strains (ϵ_2) as given in Eq. 7.2. Hence, a predefined Thorenfeldt curve with the softening function (Eq. 7.2) was used to model the behaviour of concrete according to the total strain crack model. The compressive strength results obtained from concrete cylinder samples (Table 3.8) were used as input to define the peak stress value f'_c of the base curve in the model.

$$\beta = \frac{1}{1 + k_c} \quad \text{Eq. 7.2}$$

Where,

$$k_c = 0.27 \left(\frac{\epsilon_1}{\epsilon_o} - 0.37 \right)$$

ϵ_o = The maximum compressive strain that corresponds to ultimate compressive stress obtained from the uniaxial test

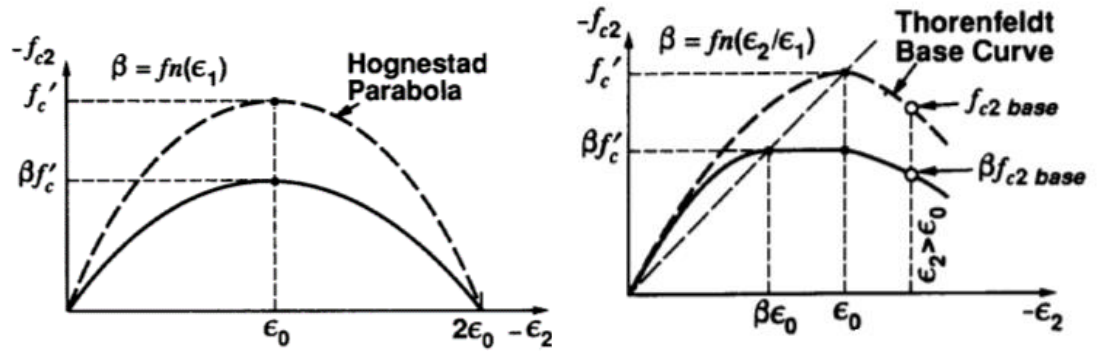


Figure 7.4: Proposed softening models for concrete in compression
(Vecchio and Collins, 1993)

7.2.1.3 Shear in Concrete

Based on the fixed crack method, the cracked concrete is capable of transmitting shear stresses; while the reduction in shear stiffness corresponds to the value of shear retention factor (Rots, 1988). Further, Vecchio and Collins (1986) indicated at rough crack surfaces the concrete can transfer shear via aggregate interlock; wherein the shear occurred along the cracks was considered by the MCFT theory. Hence, the modelling of the shear behaviour is required in the fixed crack method, where the shear stiffness is decreased after cracks initiations. The Midas FEA utilised Eq. 7.3 to compute the reduction in shear stiffness (reduced shear modulus- G^r).

$$G^r = RG \quad \text{Eq. 7.3}$$

Where, R is the shear retention factor. The R value for cracked concrete varies from 0.1 to 0.25 as identified by Rots (1988); while the Midas FEA allows to be ranged from 0 to 1. Nevertheless, a value of 0.25 was chosen in the present study based on the recommendation by Vollum et al. (2010) and Hii and Al-Mahaidi (2005).

7.2.2 Steel Rebars Modelling

The steel rebars (longitudinal and transverse) were modelled in the analysis using the Von Mises yield criteria. The steel rebars were assumed to follow the bilinear behaviour, elastic-plastic. The magnitude of yield stress for different reinforcing rebars (16, 12, and 8 mm) that identified from the tests were used to define the rebars strength. Further, the elastic modulus, Poisson's ratio, expansion coefficient, and weight density were obtained from the experimental results and the data provided by the manufacturer.

7.2.3 CFRP Modelling

The carbon fibres behave as an orthotropic linear elastic material. The Vinson and Sierakowski (2006) introduced the rule of mixture method. This method proposes that the FRP's composite materials (fibres and matrix) are transversely isotropic; hence, the elastic properties are same in the 2-3 plane while are differed in the normal direction 1 (i.e. fibres direction) as shown in Figure 7.5. Correspondingly, the elastic constants can be reduced to only five constants corresponded to longitudinal/fibres direction (1) and transverse direction, including: E_{11} , E_{22} , ν_{12} , ν_{23} , and G_{12} ; where, E_{11} and E_{22} are the longitudinal and transverse modulus of elasticity for the CFRP composites, respectively; ν_{12} and ν_{23} are the Poisson's ratio in 1-2 and 2-3 planes, respectively, and G_{12} is the shear modulus in 1-2 plane. The CFRP composites properties correspond to mechanical properties of the CFRP constituents – i.e. fibres and matrix. Nevertheless, for in-situ impregnated wraps, fib Bulletin 14 (2001) recommends to evaluate the properties and dimension of the FRP composites based on the fibres properties; hence, the modulus of elasticity (E_{11}) in fibres direction was assumed equivalent to fibres modulus as given in Chapter 2. Based on the previously published studies on the FRP composites; Sayed et al. (2014) stated that Poisson's values of $\nu_{12} = 0.22$ and $\nu_{23} = 0.30$ which these values corresponded to Poisson's ratios for fibres and matrix (epoxy), respectively. Owing to the unidirectional property of the wraps used where the contribution in transverse and shear stiffness is insignificant, Hii and Al-Mahaidi (2006; 2005) proposed the transverse modulus of elasticity (E_{22}) and shear modulus (G_{12}) to be taken as 10% and 5% of the longitudinal modulus of elasticity. Further, the Poisson's ratio was assumed of 0.3.

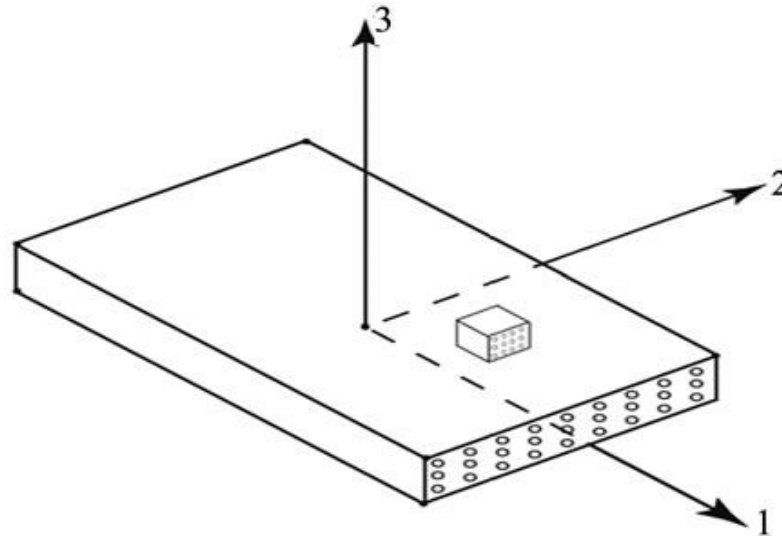


Figure 7.5 : Arrangement of fibres direction for transversely isotropic composite

(Bhaskar and Mohamed, 2012)

7.3 Elements Types and Mesh Generation

Full-size (three-dimension) beam-column joints models with the same geometries and details of the tested specimens (Chapter 3) were created. It is important to correctly discretize the model's parts in order to obtain realistic behaviour and avoiding numerical problems related with the element's distortion. For this case, Midas FEA is provided with different element types including 3-D solid elements, 2-D plan elements, and 1-D line elements (see Figure 7.6). Twenty-noded 3-D quadratic (2nd) hexahedron solid elements were used for modelling the concrete; as tetrahedral elements are stiffer than hexahedral elements, hence, a model with hexahedral elements generally provide more accurate results (MIDAS FEA Manual, 2015). Further, the 1st order elements produce less accurate results comparing to 2nd order elements; this corresponds to the shear-locking effect which results in an inaccurate displacement evaluation induced by ignoring the curvature (Thaker, 2016). Mesh generation for the concrete was performed with the map mesh function (internal nodes have a valence of four); as the map mesh is more appropriate to be used for regular shaped members.

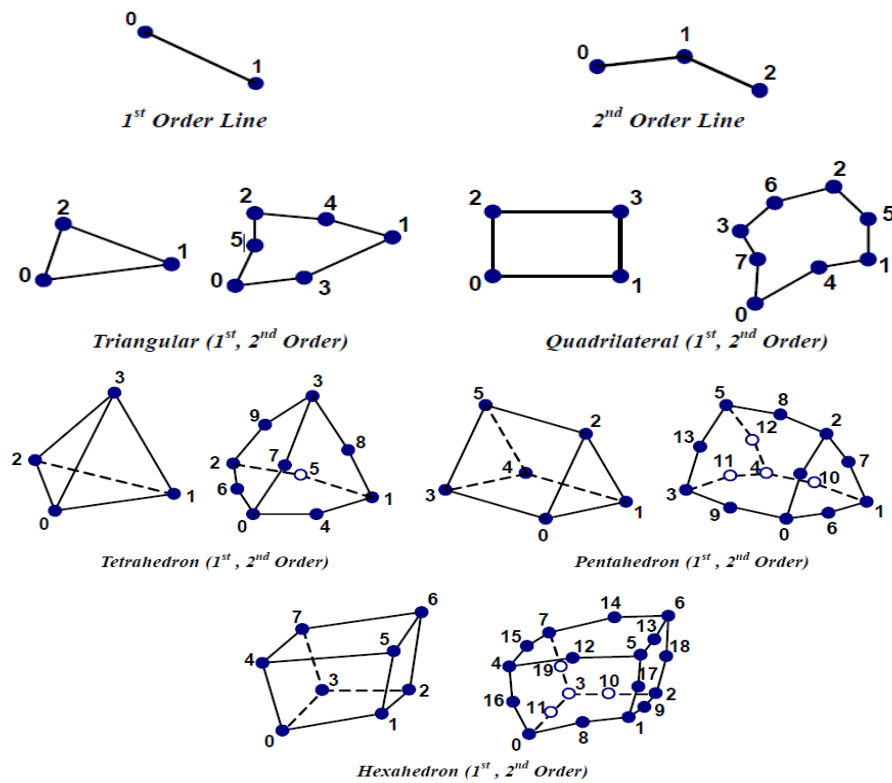


Figure 7.6: Midas FEA elements types

All embedded reinforcements were modelled by using bar reinforcement element in concrete solid element. The bar was defined as a geometrical line and the auto mesh function was utilised to divide the bar into sections in corresponding to the size of the solid concrete elements. The concept of embedded reinforcement modelling was performed by incorporating the stiffness of the bar within the continuum element stiffness where the rebar is located in the solid element. Through the pre-processing stage, the bar elements are divided and meshed by utilising auto mesh function in order to correspond with the continuum elements sizes (concrete solid element). Further, the interaction between the rebars and the concrete elements is assumed to be perfectly bonded in accordance with the embedded rebars concept. However, the interface properties between concrete and rebars can be defined using interface elements for the concrete-rebars contact regions. Nevertheless, this numerical investigation intends to model full scale, three-dimensional beam-column joints that involved a considerable amount of steel bars and subjected to combined forces inducing cracks at early age of loading, which they increased the computation time and the numbers of alterations.

Meanwhile, in the case of modelling the bond behaviour using interface elements, it enormously increases the number of elements (i.e. computational time) and introducing numerical convergence problems.

The CFRP wraps are modelled using a plane stress element that is available in the Midas FEA. The thickness of CFRP wraps was equivalent to 0.22 mm (CFRP sheet thickness), while the CFRP elements were connected to the concrete solid elements via common nodes. Due to minimal thickness of CFRP sheets, it was practical to model the wraps as 2D plane stress elements that had negligible out-of-plane (bending) stiffness. However, to simulate the out-of-plane behaviour of CFRP wraps using 3D elements requires to limit the aspect ratio of the element, which should be corresponded to the element thickness (0.22 mm). This in turn produces considerable number of elements (extremely fine mesh); hence, the model size and computational time can be tremendously increased. This approach of modelling the FRP strips with plane stress elements was also employed by Tao (2013); Hii and Al-Mahaidi (2006; 2005).

Here, extra attention was paid in defining the material local coordinate to be matched with the element's local coordinates. Correspondingly, the element major axis (1-1) was oriented according to the fibres direction as they aligned to the beam transverse direction (i.e. full and hoops wraps) or inclined at 45° from the beam longitudinal axis (i.e. inclined wraps). Similar to concrete elements, the map mesh function was used to generate the mesh for CFRP wraps with same elements size for concrete (25 mm). While for the inclined wraps, the locations of a number of nodes were adjusted to joint with the concrete element's nodes. Hence, this modelling approach assumes full bond between CFRP wraps and concrete in which the wraps can only fail by rupturing, since this types of failure corresponds with the experimental observations (Chapter 4); wherein no premature failure due to wraps debonding (peeling-off) were seen before the rupture of the wraps.

Nevertheless, an approach is suggested to simulate the bond-slip behaviour of FRP's wraps and predict premature (debonding) failure in the interface zone by using the Midas FEA package. The debonding/interfacial failure is likely to occur before the rupture of FRP's wraps in the partially strengthened sections (i.e. using U wraps, a single FRP's sheet or plate), which corresponds to wraps bonding length, concrete strength, and wrapping schemes (ACI Committee 440.2R-08, 2008). The interface between concrete-FRPS wraps

is subjected to both peeling (normal) and shearing forces. The peeling stresses that normal to the bond (adhesive) interface can be assumed to induce failure in concrete; hence, the interfacial normal stiffness (K_n) corresponds to the elastic modulus (E_c) of concrete, $K_n = E_c/h_i$ (kN/mm³), where h_i is thickness of interface and can be taken as unit thickness in the FE models (Midas FEA Manual, 2015). The nonlinear behaviour of wraps-concrete interface due shear traction (Figure 7.7) can be idealised as bilinear bond-slip relationships based on Lu et al. (2005) model. This model was successfully utilised by Sayed et al. (2014), Chen et al. (2012), and Baky et al. (2007) for modelling simply supported RC beams with FRP's wraps. The following equations (Eq.7.4 to 7.8) have been introduced to evaluate shear-tangential stress (τ) and slip (S) values. Hence, the behaviour of interface elements can be simulated in terms of τ and S with zero-thickness elements (springs).

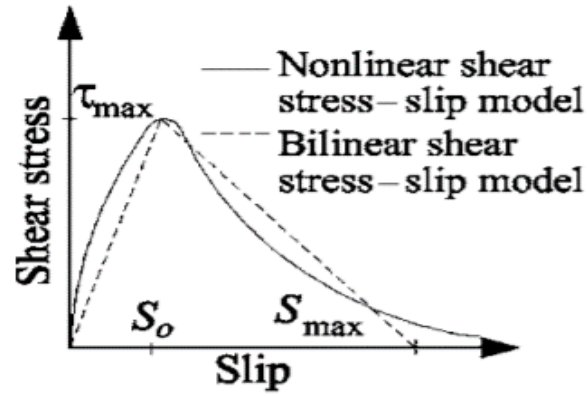


Figure 7.7: Slip-bond models for FRP's-concrete interface

(Baky et al., 2007)

$$\tau_{max} = 1.5\beta_w f_t \quad \text{Eq.7.4}$$

$$S_o = 0.019\beta_w f_t \quad \text{Eq.7.5}$$

$$\beta_w = \sqrt{\frac{2 - b_f/s_f}{1 + b_f/s_f}} \quad \text{Eq.7.6}$$

$$S_{max} = \frac{2G_{Fi}}{\tau_{max}} \quad \text{Eq.7.7}$$

$$G_{Fi} = 0.308\beta_w^2 \sqrt{f_t} \quad \text{Eq.7.8}$$

Where;

τ_{max} = the maximum interfacial shear stress

S_o = the relative slip at τ_{max}

S_{max} = the maximum relative slip

f_t = The tensile strength for concrete ($0.33\sqrt{f'_c}$)

b_f = the width of CFRP sheet

S_f = the spacing between of CFRP sheet (centre to centre)

G_{Fi} = the interfacial fracture energy

7.4 Loads and Boundary Conditions

The Midas FEA enables to apply different types of loads including forces (i.e. concentrated, pressure, and body force), displacement, and temperature. As presented in Chapter 3, the tests were conducted by either applying a displacement control load (short-term group) or a constant sustained load (long-term group) on the loading arm attached to the beam end tip via rigid steel box. Also, the column was subjected to a constant axial load on the column's top using a thick plate to distribute the load uniformly. The column load was remained constant throughout the analysis stages (i.e. simulating the constant column's load effect in the tests). The beam displacements were applied in the created models (short-term group) as small steps 0.2 mm; while for sustained loaded models (long-term group), a constant load was applied. To replicate the testing condition and to apply combined loads including torsion, a steel rigid arm was created with using rigid link elements (see Figure 7.8). The self-weight of the beam-column joints was imposed as body force based on the weight density of the modelled material. The column's bottom end was constrained from translation in all directions in the FE models, while the top side of the columns was released in the direction of the column axial load.

For nonlinear static analysis, the concrete time-dependent deformations induced by creep and shrinkage need to be incorporated in the models subjected to sustained loads. While the Midas FEA only allows to directly define the creep coefficients and shrinkage strains into the concrete constitutive relationships by using the elastic model (i.e. neglect cracking behaviours). This poses a challenge to model a cracked section and predicting the time-dependent inelastic response under sustained loads. However, in this numerical investigation, the concrete creep was incorporated into the total strain crack constitutive model by iteratively modifying the modulus of elasticity of concrete based on the age-adjusted effective modulus method (Eq. 7.9) in corresponding to the loading periods. As the creep coefficients for

concrete were evaluated from the concrete creep samples (Figure 3.17) while the age adjusted coefficient is assumed equivalent to 0.8 as identified in Chapter 2. This proposed approach accounts the aging of concrete and allows the predicting of elastic and inelastic concrete deformations due to creep.

$$E_{adj(t,t_0)} = \frac{E_{t_0}}{1 + \chi \phi_{(t,t_0)}} \quad \text{Eq. 7.9}$$

Where,

$E_{adj(t,t_0)}$ = the age adjusted modulus of the elasticity of concrete

E_{t_0} = the modulus of elasticity of concrete at time (t_0)

$\phi_{(t,t_0)} = \frac{\varepsilon_{cr}}{\varepsilon_e}$ [the creep coefficient at time (t)]

t_0 = the initial time of loading

χ = the adjusted ageing coefficient

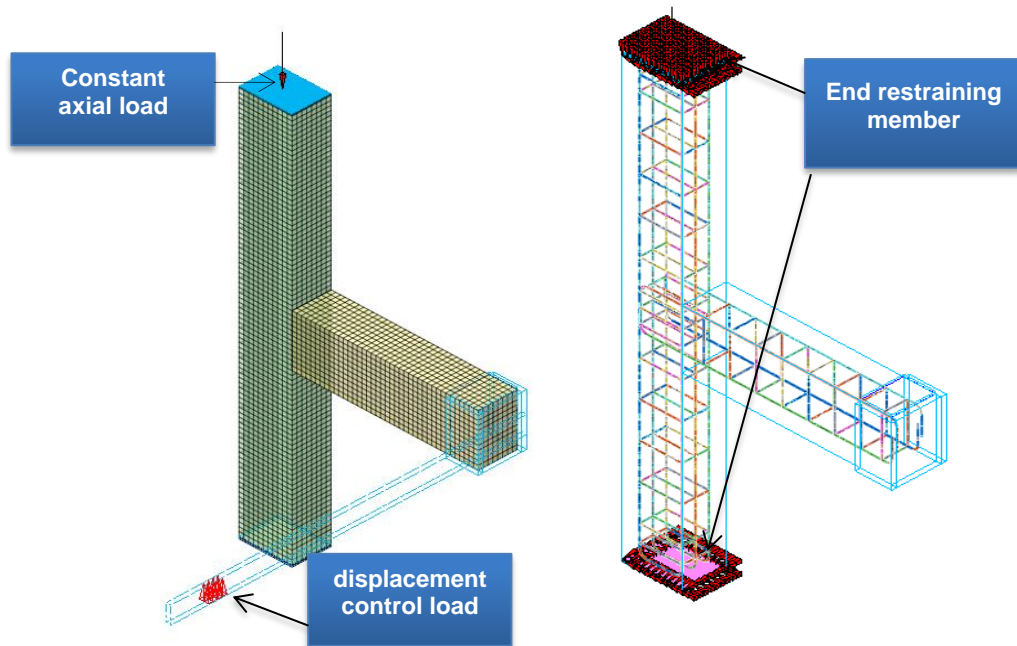


Figure 7.8: loads and support conditions in the F.E. models

The free shrinkage strains (ε_{sh}) that experimentally obtained from the concrete prisms (Figure 3.18) were imposed to the concrete elements as a thermal drop. The equivalent thermal drop loads (ΔT_{eq}) were calculated by converting the shrinkage strains according to Eq.7.10; as the shrinkage strains divided by the coefficient of thermal expansion (α_{th}). Similar approach for defining shrinkage strains was utilised by Shehzad et al. (2019) to model RC walls restrained at their base. The thermal expansion coefficient for concrete (α_{th}) was taken as the value of $\alpha_{th} = 10 \mu\varepsilon/^{\circ}\text{C}$. This value based on BS EN 1992-1-1 (2004) Bamforth (2007) in CIRIA 660 recommendations for concrete with siliceous limestone aggregate.

$$\Delta T_{eq(t)} = \frac{\varepsilon_{sh(t)}}{\alpha_{th}} \quad \text{Eq. 7.10}$$

7.5 Verification of the Numerical Model

This section compares the results of the created F.E. models with the experimentally obtained results of the beam-column joints. Comparisons between the results of short and long-term twist angles and deflections were made; also, the rebars strains readings at flexural tension zones near to the column face (joints demand) and developed cracks were given. Wherein, the geometric dimensions, reinforcements and wrapping details of the beam-column joints were the same as investigated in the experimental programme (Chapter 3). The predicted data were collected from the same locations that considered in the testes in order to apply direct comparison.

7.5.1 Short-Term Behaviour

The beams end-span deflections, twist angles, rebars strains, and cracks that obtained from F.E. models are compared with the experiments results of the beam-column joints subjected to monotonic loads up to failure (short-term group). Figure 7.9 and Figure 7.10 compare the measured end-span deflections and twist angles, respectively, for the tested specimens with the predicted values from the F.E. models. Also, Figure 7.11 and Figure 7.12 show the developed strains in the beam main rebars and concrete cracks, respectively. The extracted strain readings were compared with the measurements were taken during the experiments to quantify the escalating

in the joints demands under combined loads. These figures show that the proposed models are capable to predict the behaviour of both the strengthened and un-strengthened beam-column joints through all loading stages. For all models, it can be seen that the ultimate load, torque, and developed strains were accurately predicted with a deviation of less than 5%. However, for SH-S-C-I model with the inclined CFRP wrapping scheme, the analysis exhibited convergence problem shortly after the peak (the solution was terminated); at this stage the tested specimen experienced sharp decrease in the carrying capacity resulted by excessive plastic deformation in the stirrups followed by a damage in concrete and rupture of wraps. These significant local failures induced numerical instabilities, hence, the failure stage (decline stage) was not identified. Further, the solution for the SH-U-F model diverged when the members experienced considerable plastic strains in rebars near the column face (the flexural plastic zone) with severe open cracks (tension zone) and crushing of concrete at the flexural compression zone. Also, it found that the F.E. models' response for SH-S-U-A at post cracking stage was stiffer than those observed during the test. This can be resulted from the approximation introduced during modelling the specimen (i.e. perfect bond between the rebars and the concrete and between the concrete and the wraps).

Figure 7.12 shows the developed cracks and corresponded principal tensile strains in concrete for all models at the end of loadings. The analysis outcomes showed the viability of the F.E. models by using Midas FEA to predict the damaged zones corresponded to those identified in the experiments as presented in Chapter 4. It can be seen that the excessive cracks and tensile strains through the beams region due to incorporating torsional forces were predicted. Further, these graphs (Figure 7.12) clearly show the influence of the combined loads and the different CFRP wraps on the joint damage; for instance, the full wraps (SH-S-C-A) induced the damage and cracks to be extended to the column (joint region). While insignificant strain levels were observed in the column (joint area) for SH-S-C-H (hoops wraps) and SH-U-C models along with excessive cracks at the beam region which conforms with the tests results.

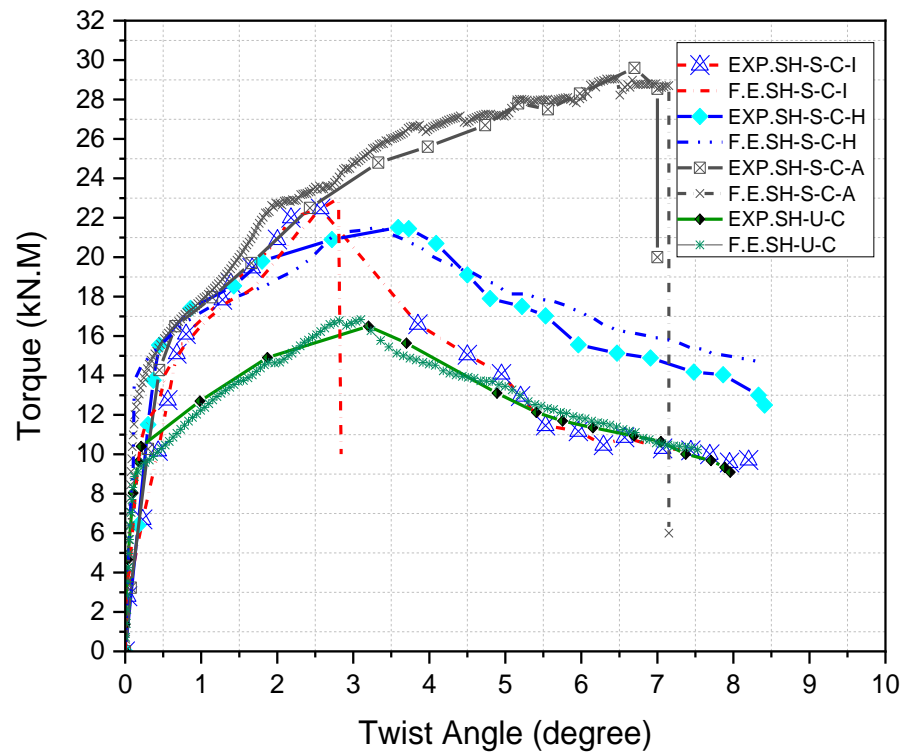
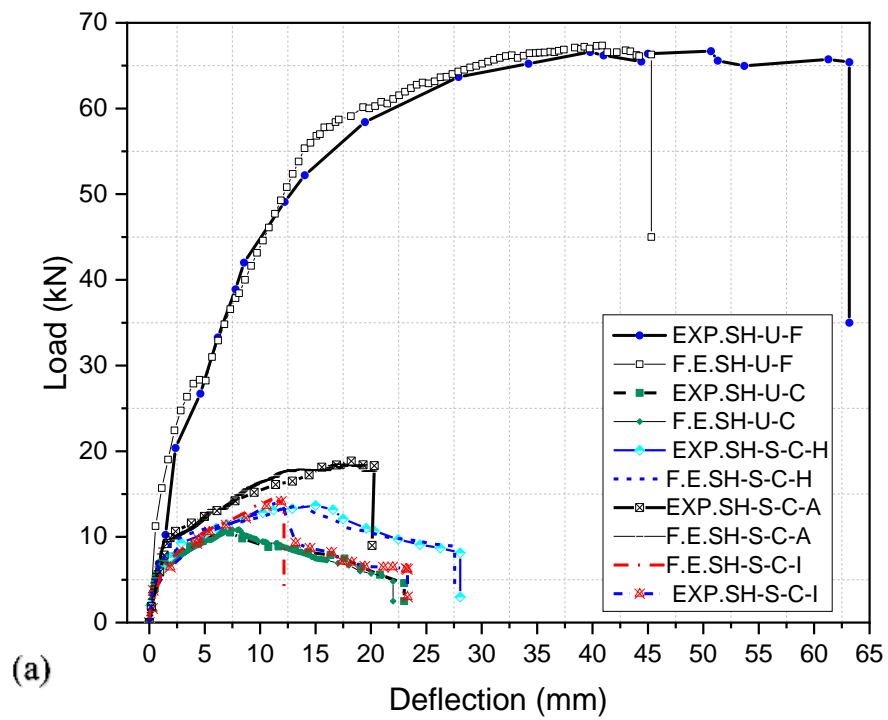


Figure 7.9: Comparison between the experimental and F.E. results for twist angles due to torque action



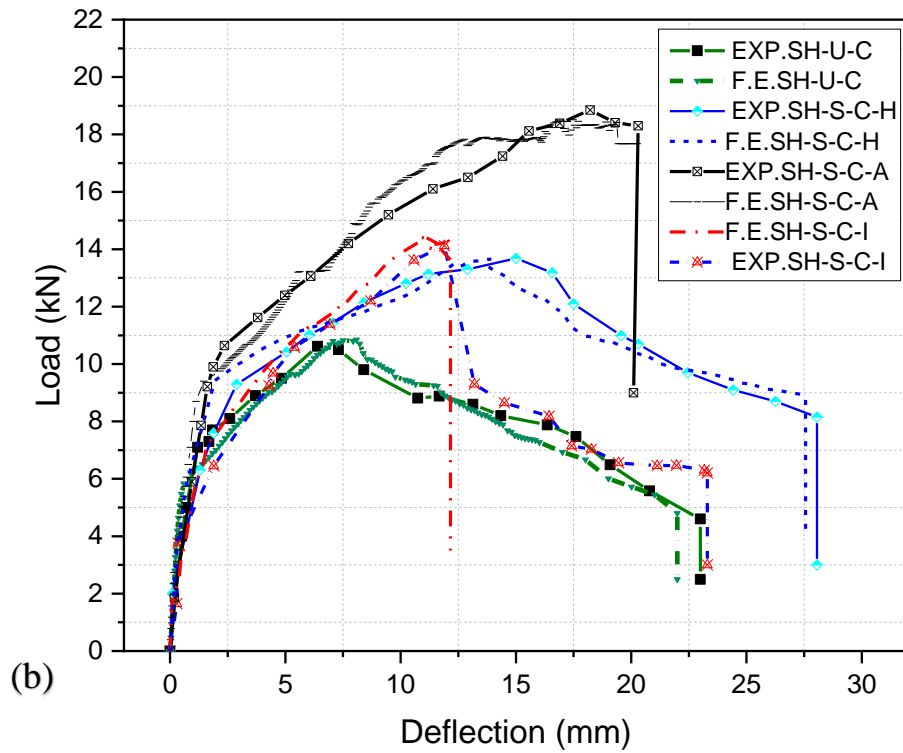


Figure 7.10: Comparison between the experimental and F.E. results for end-span deflection of the beams (a) all specimens (b) specimens under combined loads

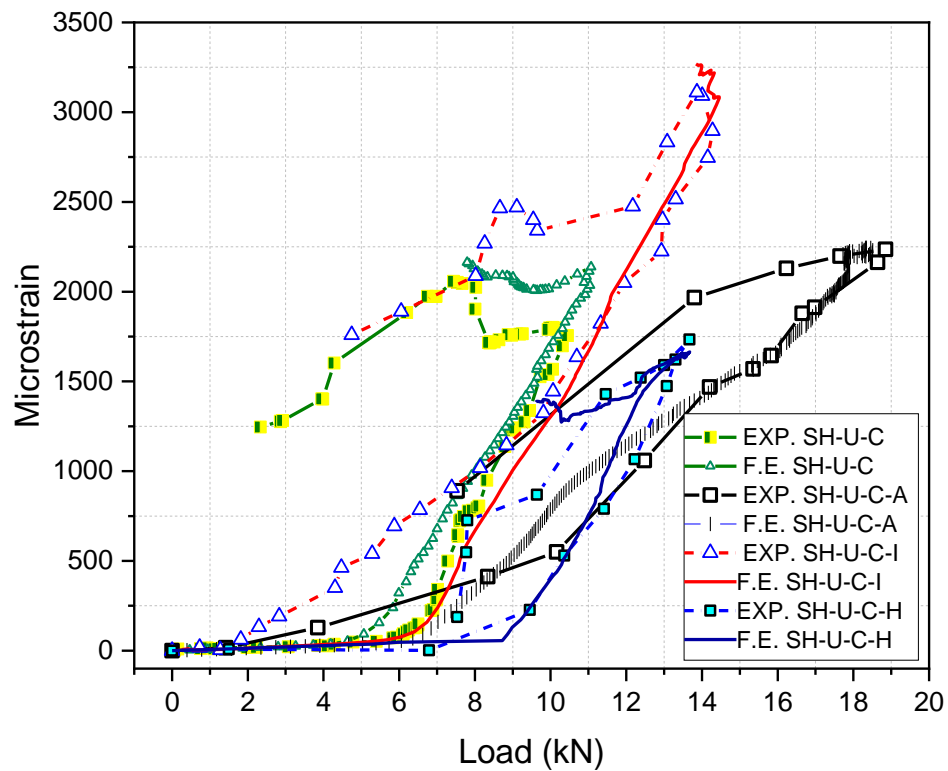
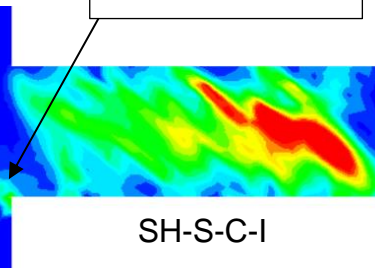
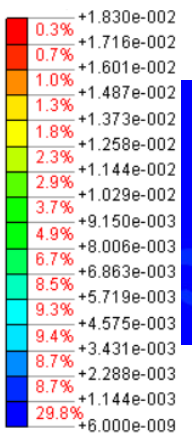
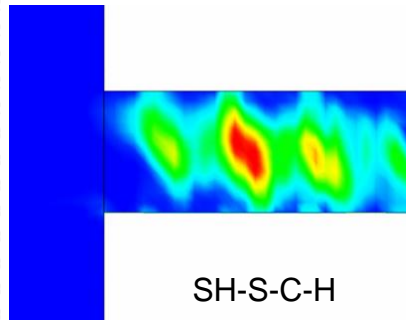
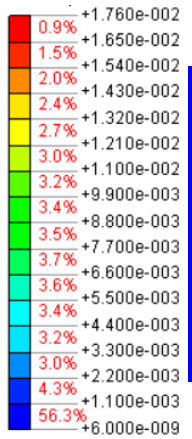
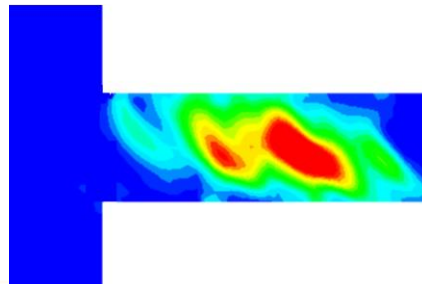
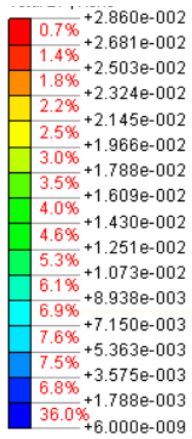
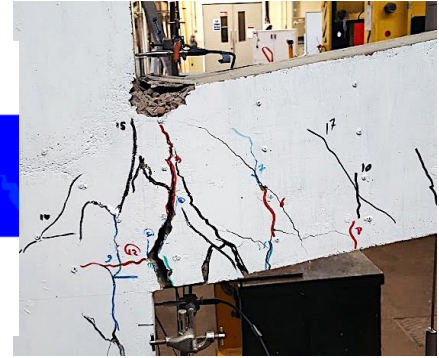
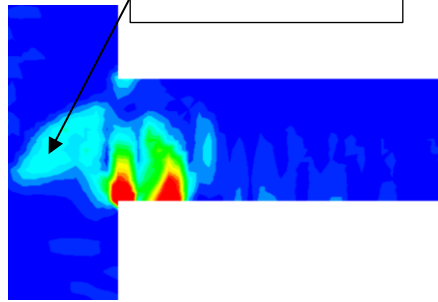
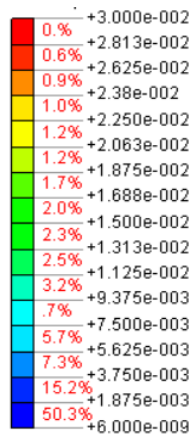


Figure 7.11: Comparison between the experimental and F.E. result for the beams main rebar strains at 100 mm from the column face



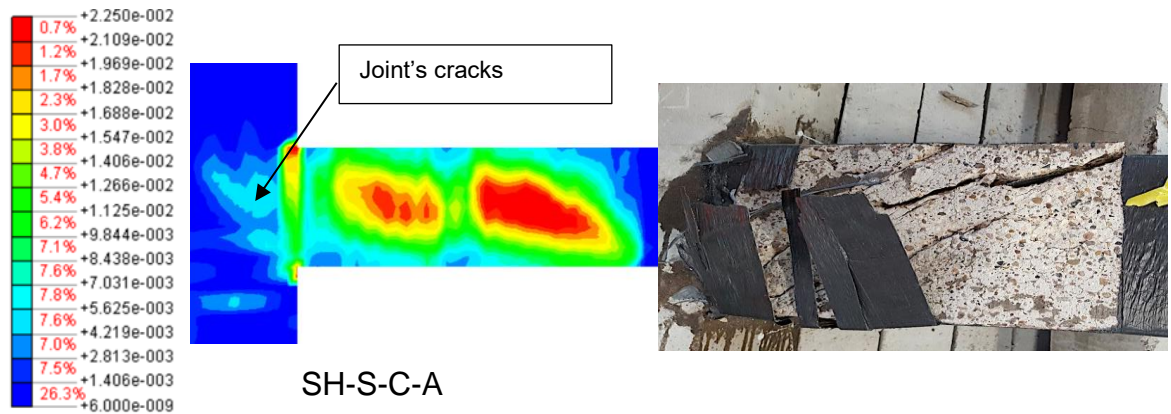


Figure 7.12: Comparisons between the strains profiles obtained from F.E. models (short-term group) and observed damage from tests

7.5.2 Long-Term Behaviour

This section compares the predicted twist angles and concrete cracks induced by sustained combined loads to the corresponding tests results that given in Chapter 5. Figure 7.13 compares the long-term twist angles through the loading period for the LN-U-C and LN-S-C-H F.E. models and the tested specimens. There is good agreement between the results for both specimens as can be seen in the figure. This confirms that the presented F.E. approach can predict the time-dependent twist angles. However, for the unstrengthened specimen (LN-U-C), the Midas FEA underestimated the twist level at early age of loading (10 days) which can be attributed to the value used of creep coefficient that corresponded to 20% of the concrete compressive strength. While the levels of stresses induced in the concrete struts can be higher than those applied to the creep samples.

Figure 7.14 and Figure 7.15 show the developed cracks and corresponded principal tensile strains in the concrete for LN-U-C and LN-S-C-H F.E. models, respectively. These figures demonstrate the reliability of the numerical analysis results compared with the tests results (Chapter 5) to predict the developed cracks and damaged zones under sustained combined loads. It can be seen (Figure 7.14) that the LN-U-C model exhibited considerable time-dependent strains levels (more than 4000 micro-strain) and diagonal-shear cracks concentrated in the beam region around the beam four sides due to time-dependent deformations (creep and shrinkage) in the inclined concrete struts. While the column region including the joint area experienced less strain levels (lower than 700 micro-strain) through all the loading period. On the

other hand, the maximum observed (Figure 7.15) time-dependent strains in concrete for the LN-S-C-H model with CFRP hoops was in line with those observed in the test results. Also, insignificant strains of not more than 160 micro-strain were observed in the column (i.e. at the joint area). The predicted cracks for the LN-S-C-H model were partially open and no fully open crack was developed; this indicates that Midas overestimates the corresponded strains that initiate fully open cracks.

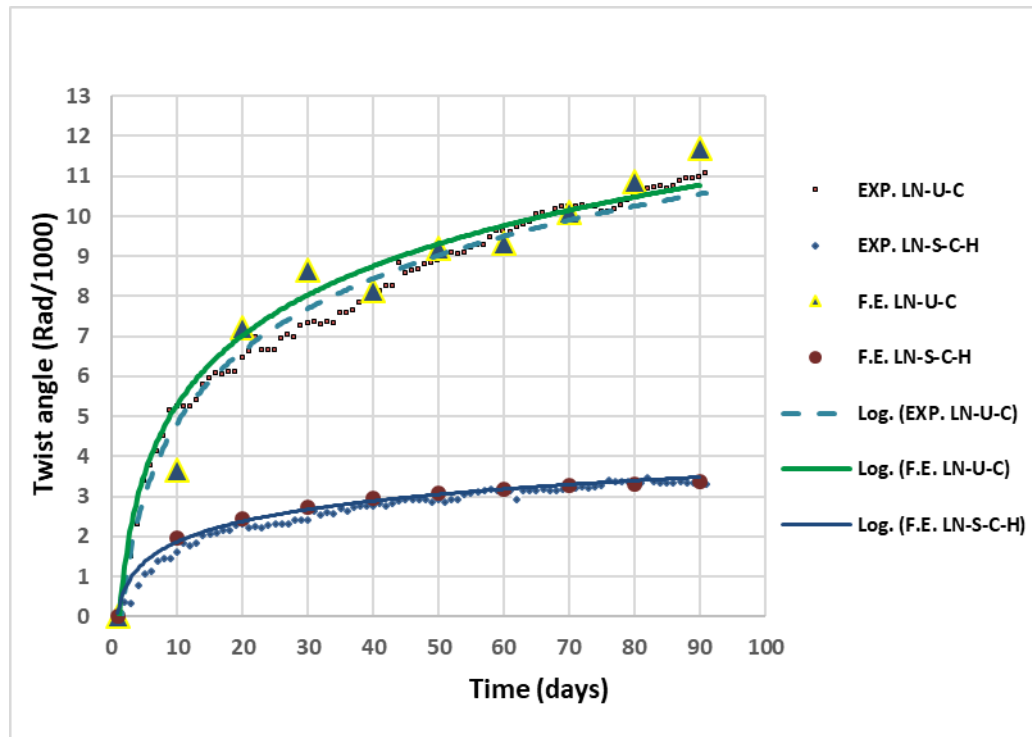
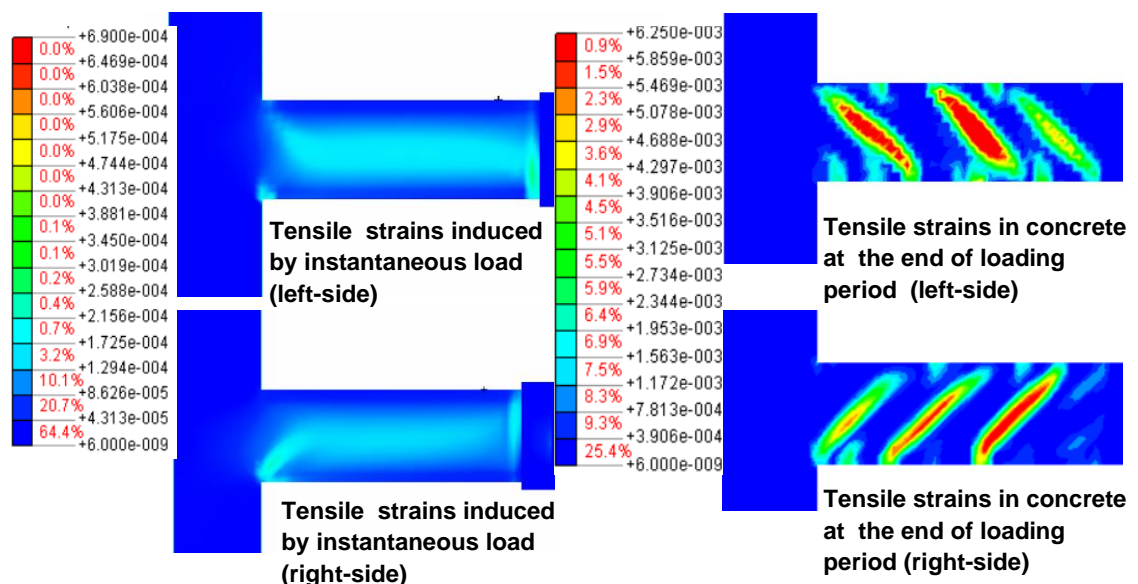


Figure 7.13: Comparison between the experimental and F.E. results for long-term twist angles due to sustained loads



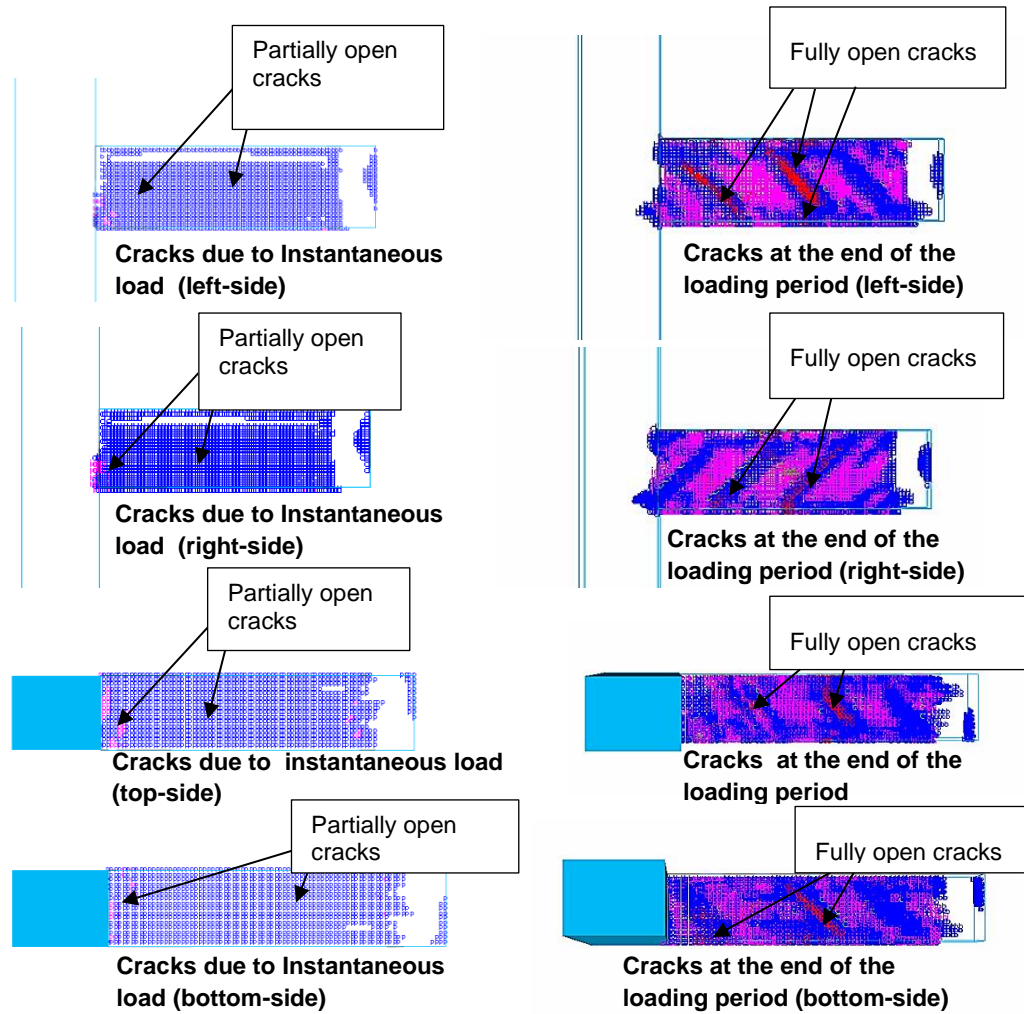
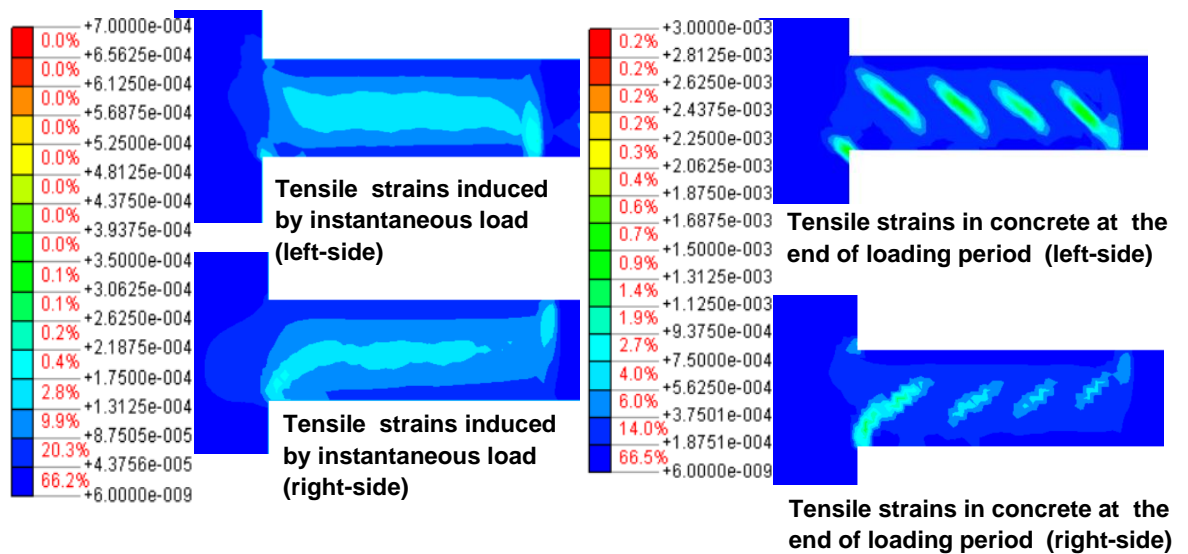


Figure 7.14: Time-dependent strains and cracks profiles for the LN-U-C model



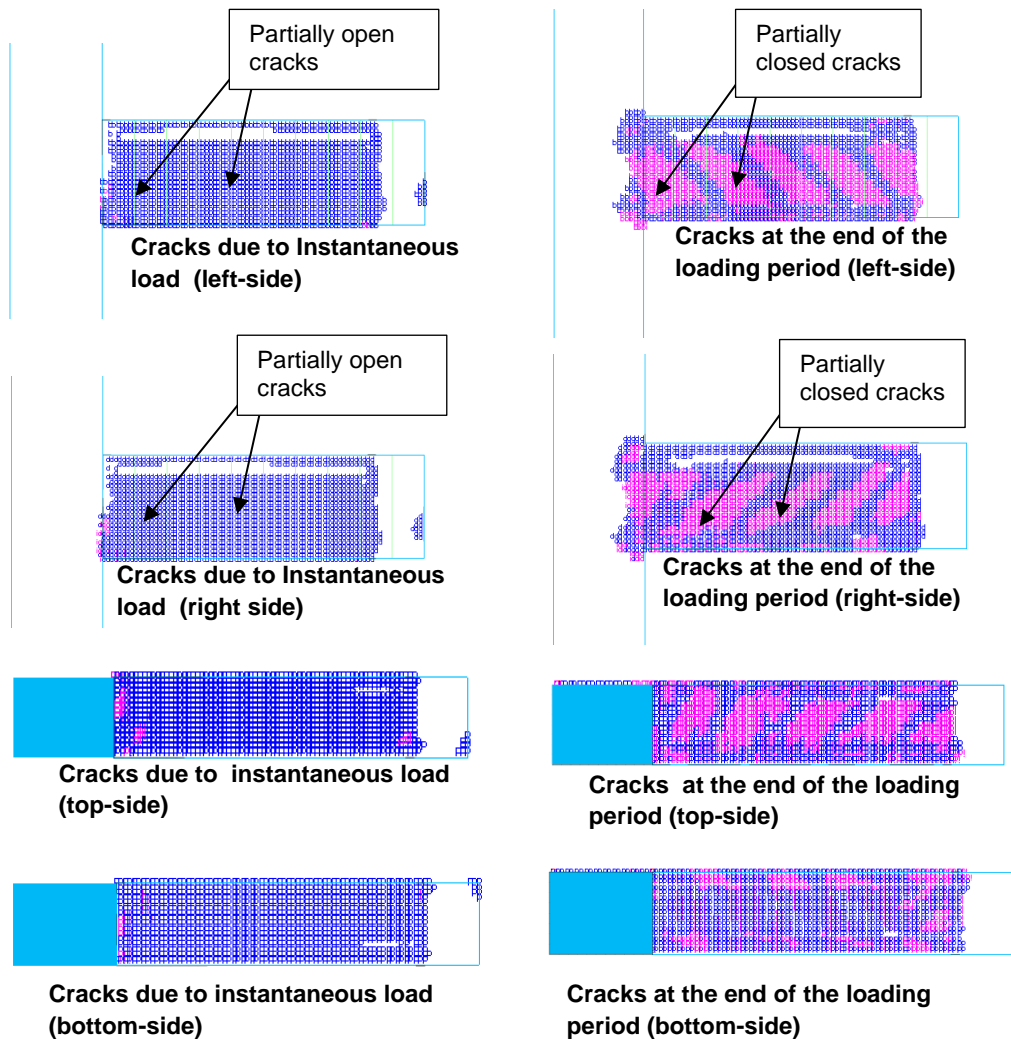


Figure 7.15: Time-dependent strains and cracks profiles for the LN-S-C-H model

7.6 Influence of Different Ratios of Torsion to Bending-Shear Loads

As discussed in Chapter 2, the loads combination including torsional forces cause variation of strains around the beam's perimeter. Further, the presence of torsional forces reduces the shear and flexural strength of RC members. It is evident from the test results that the shear stresses resulted from torsion and direct shear that increases the strains in both transverse and longitudinal reinforcement as well as significantly degrades the cracking stiffness. Also, the effect of beam torsional forces was identified; these escalated the strain levels in the main beam rebars with relation to the magnitude of the applied torque to the bending-shear force and external fibres wrapping schemes. This section aims to numerically (F.E. analysis) investigate the influences of various beam torque ratios on the behaviour of exterior RC beam-column joints.

The F.E. models subjected to different torque to bending-shear ratios. The ratios of torsion (T) to bending moment (M) and vertical shear (S) were 1.57, 1, and 0.5. The 1.57 T/M-S ratio has been verified with experimentally tested RC beam-column as presented in the previous section (7.5). The model's details and material properties were matched with the tested beam-column joints specimen. Further, all models were also under a constant axial load of magnitude equal to $0.1 A_g f'_c$ which was applied to the column's top.

Figures 7.16a and 7.16c show the load-deflection curves of for unstrengthened and strengthened models, respectively. These curves demonstrate reductions in loading carrying capacities in relation to the increase in the torsion ratios which the lowest capacities were observed with the 1.57 T/M-S ratio. While the maximum carrying load levels were induced by 0.5 T/M-S ratio. These reflect the significant effect of torsional forces of reducing the flexural capacity of the RC members; this influence was also confirmed by Hsu and Liang (2003) and Hsu and Wang (2000). The reductions in the section's capacities can arise from large increments in the concrete struts forces (i.e. concrete softening and failure) and yielding of transverse and main reinforcements due to combined loads including torsion, as identified in the previous chapters.

The beam twist graphs of the models under torsional actions are given in Figure 7.16b and 7.16d, respectively. Figure 7.16b reveals increments in the torsional load capacity by 33% and 25% for models subjected to 1 and 0.5

T/M-S ratios, respectively, compared with those induced by 1.57 T/M-S ratio of loads. These increments correspond with the increase of the bending moments; since the increase of the flexural compressive stresses induced by low T/M-S (0.5 and 1) alleviated the tensile forces from torque in the beam weaker chords (top rebars). Further, it can be seen (Figure 7.16b), the induced compressive forces tend to enhance torsional cracking loads (pre-cracking stage for 0.5 T/M-S ratio), reducing cracks propagations (post-cracking stage for 0.5 and 1 T/M-S ratios) and the beam torsional cracks, up to the peak load as shown in Figure 7.16 and 7.17. Also, it can be seen that lower inclined cracks levels were occurred in the beam right side (1 T/M-S ratio) as the direct shear counteracted the torsional shear flow. While for 0.5 T/M-S loads ratio, no inclined cracks were observed in the beam region. However, insignificant influence of the load's ratios on the beam torque capacity with a difference less than 3% can be observed for the strengthened models (SH-S-C-A and SH-S-C-H). This is thought to be due to the levels of induced stresses in the concrete struts and the corresponded maximum strength (σ_d) that can be attained by the diagonal concrete strut. Hence, the solutions diverged for all models with different loads ratios when the stresses in the concrete struts were close to those induced by maximum torsional force of 1.57 T/M-S ratio. While the increase in the direct shear forces combined with torsion that corresponded with Eq. 6.5 tend to increase the struts forces at the beam's left side (the induced shear-flows in the same direction) and reducing the torsional capacity due to the failure of concrete; as can be seen (Figure 7.16d) for SH-S-C-I models with ratios of 0.5 and 1 T/M-S. Further, it can be deduced from the curves that decrements in the torque-twist ($T-\psi$) deformations (i.e. ductility levels) with loads ratios 0.5 and 1 T/M-S compared with 1.57 T/M-S loads ratio. This was corresponded to the level of damage in compression struts.

Figures 7.18a and 7.18b show the developed strain levels in the beams main rebars near to the joint's zones (i.e. 100 mm from the column face) for unstrengthened and strengthened models, respectively. These levels influence joint's cracks and distortion degrees as identified in Chapter 4. Figure 7.18a graphs indicate the inclusion of torsion with flexural and shear forces can largely increase the strain levels under lower loads levels than caused by flexural and direct shear loads. Interestingly, the loads ratio of 0.5 T/M-S produced significant plastic strains (exceeded 2800 micro-strain) than those induced by 1 M/S loads ratio which the model was predominantly subjected to flexural force. Accordingly, these large plastic strain levels in the

beam main rebars were extended to the column region (joint's area) and caused excessive damage and cracks as shown in Figure 7.17. Similarly, the lower T/M-S loads ratios (0.5 and 1) produced larger strain levels than was 1.57 T/M-S load ratio for strengthened models. Also, the strengthened models subjected to 0.5 T/M-S load ratio exhibited significant plastic strains in the bottom main rebars of the beams near to column face. This indicate that with large flexural load ratios, the beam plastic hinge initiated near to the column's face with significant plastic strains, where can be extended to the column in the joint's area (see Figure 7.17).

Table 7.1 compares the ratio of predicted rebars strain to yield strain based on the FE results with the computed stress to yield stress ratio according to Section 6.2.2-the truss mechanism. These results confirmed that the levels of plastic stresses and strains can be produced under 0.5 and 1 T/M-S ratios which these influenced the joint forces (i.e. joint demands), and can be transferred through the beams main rebars. Again, the given results demonstrate that the increase in the imposed levels as observed under 0.5 T/M-S load ratio was severely escalated the levels of plastic deformations.

Table 7.1: Predicted rebars strains to yield strains ratios and computed stresses to yield stresses ratios for the created models

Model	Loads Ratio	Strain ¹	Strain/yield strain ²	Computed stress ³	Stress/yield stress ⁴	%Diff ⁵
SH-U-C	1 T/M-S	2970	1.06	633	1.13	7%
	0.5 T/M-S	5200 ⁶	1.86	960	1.71	8%
SH-S-C-A	1 T/M-S	3012	1.08	567	1.01	6%
	0.5 T/M-S	5064	1.81	869	1.55	14%
SH-S-C-I	1 T/M-S	2563	0.92	520	0.93	1%
	0.5 T/M-S	4404	1.57	914	1.63	4%
SH-S-C-H	1 T/M-S	2171	0.78	440	0.79	1%
	0.5 T/M-S	4408	1.57	844	1.46	7%
Standard deviation						4%

¹ Measured strain from FE model at the maximum load in micro-strain (μ).

² Yield strain for the steel main rebars (16 mm) as obtained from rebars tests (2800 μ).

³ Computed stress induced by combined load according to Section 6.2.2.

⁴ Yield stress for the steel main rebars (16 mm) as obtained from rebars tests (560 MPa).

⁵ % difference between predicted strain ratio and computed stress ratio.

⁶ The maximum observed rebar strain measured before the rupture of the rebars in the tests.

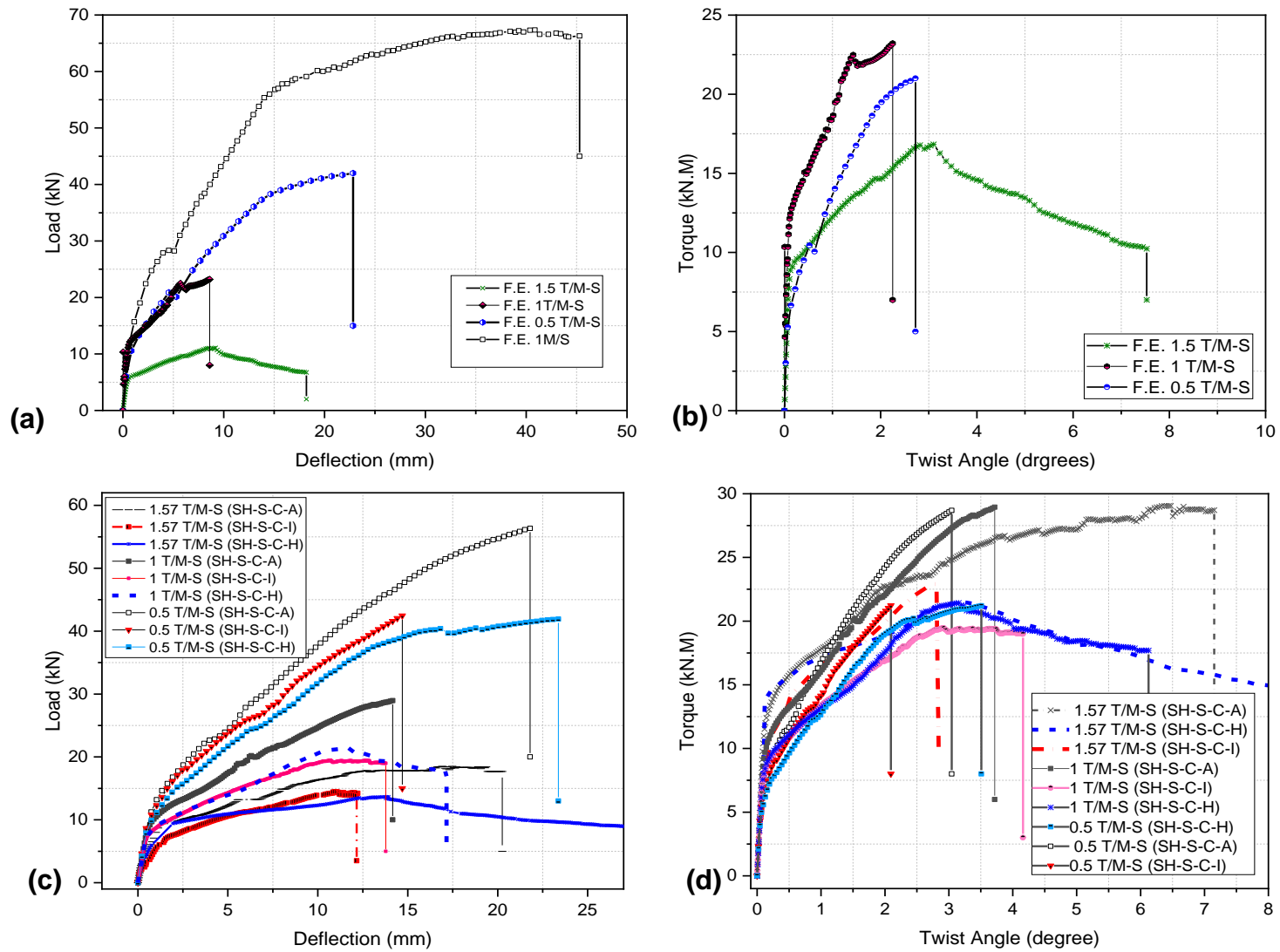


Figure 7.16: (a) Load-deflection curves for unstrengthened models (b) Twist-angle curves for unstrengthened models (c) Load-deflection curves for strengthened models (d) Twist-angle curves for strengthened models

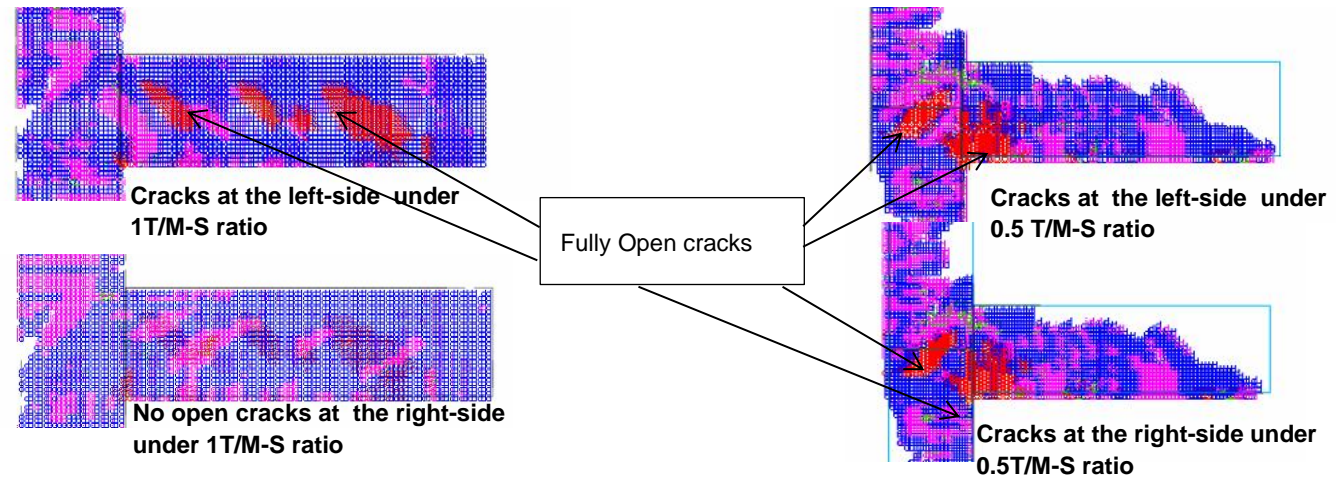


Figure 7.17: Cracks profile for the unstrengthened models subjected to 1 and 0.5 T/M-S loads ratios

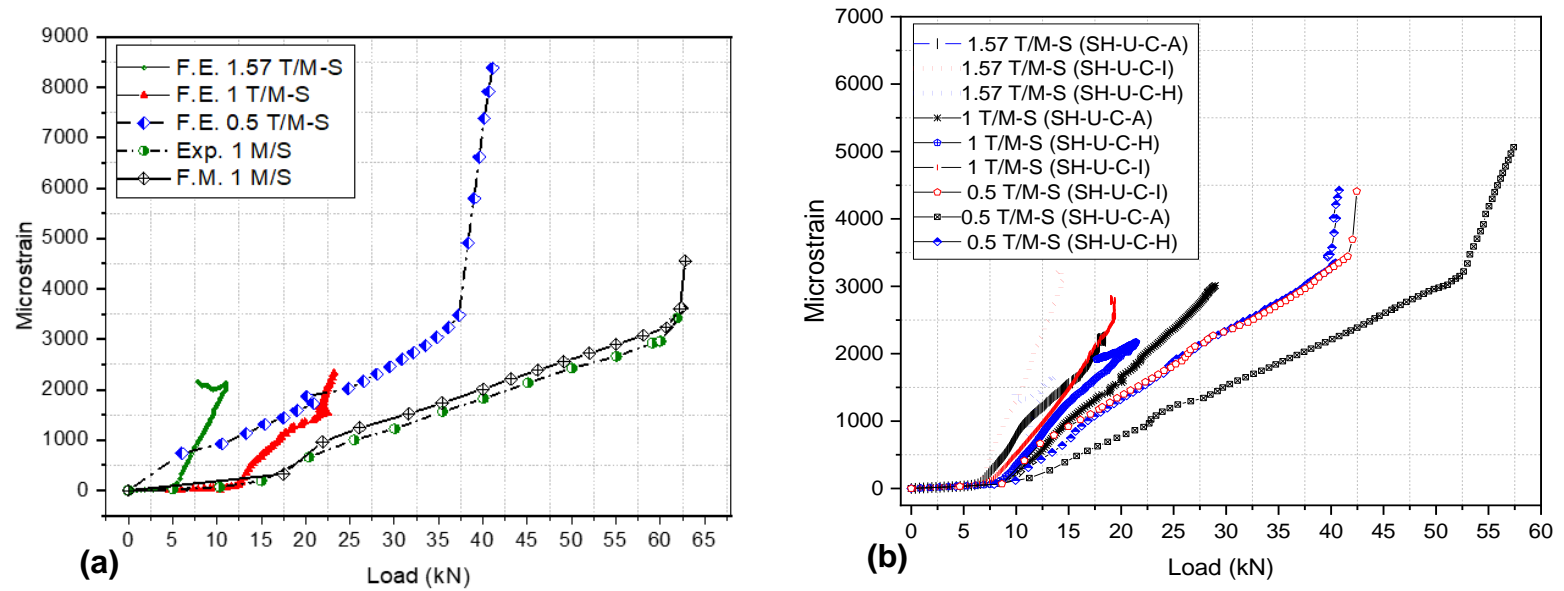


Figure 7.18: Predicted the beam rebars strains developments (a) for the unstrengthened models (b) the strengthened models

7.7 Influence of Different CFRP Layers

The level of strengthening beam's region on the models behaviours were investigated by increasing the wraps layers (two and three layers). All models (SH-S-C-H, SH-S-C-A, and SH-S-C-I) subjected to 1.57 torque to bending-shear ratio in order to examine the effectiveness of the considered beam's torsional schemes (different layers) under high torque loads. To apply direct comparison with specimens that created with different CFRP layers, the models geometry, material properties, and loading conditions were same as those of the short-term models.

Figure 7.19 compares the load-deflection and torque-twist behaviours for each model with different strengthening levels (1, 2, and 3 CFRP's layers). It can be seen that the models with three CFRP layers were exhibited the highest loads capacities. However, the increase in the observed loads levels were varied in corresponding to the scheme types. The CFRP Hoops (SH-S-C-H) and Full wraps (SH-S-C-A) showed about 8% of an improvement in the loads attained using three CFRP layers in comparison with a single layer of CFRP wraps. This marginal improvement can be related to a damage of concrete between CFRP hoops (un-wrapped regions) or crushing of the concrete struts (reaching struts capacity- σ_d) in the case of the fully strengthened beams (SH-S-C-A). Again, this confirms that the effectiveness of strengthening schemes is limited to the concrete struts capacity (σ_d), which is in line with the outcomes obtained from the experimental and analytical investigations.

In comparison with the model strengthened with a single layer of inclined CFRP wraps, the models (SH-S-C-I) with multiple layers showed 12% and 23% increments in the loads capacities when using two and three CFRP layers, respectively. These increments correspond to the increase in the CFRP wraps stiffness (wraps thickness), and these wraps could potentially reduce the principal tensile stresses that induced in beam's sides and, hence, the concrete damage. From Figure 7.19, all models (different schemes) with multi-CFRP layers exhibited higher stiffness levels (i.e. less deformation levels) than those observed from the models strengthened with a single CFRP layer. However, the increase in the level of strengthening beam's region with using multi-CFRP layers reduced members ductility levels (deformation after the peak load) that were corresponded to levels of induced stresses in the concrete struts and σ_d . On the other hand, for each strengthening scheme,

the created models (two and three layers) showed similar joint's cracks to those seen from the models with a single layer as shown in Figure 7.12.

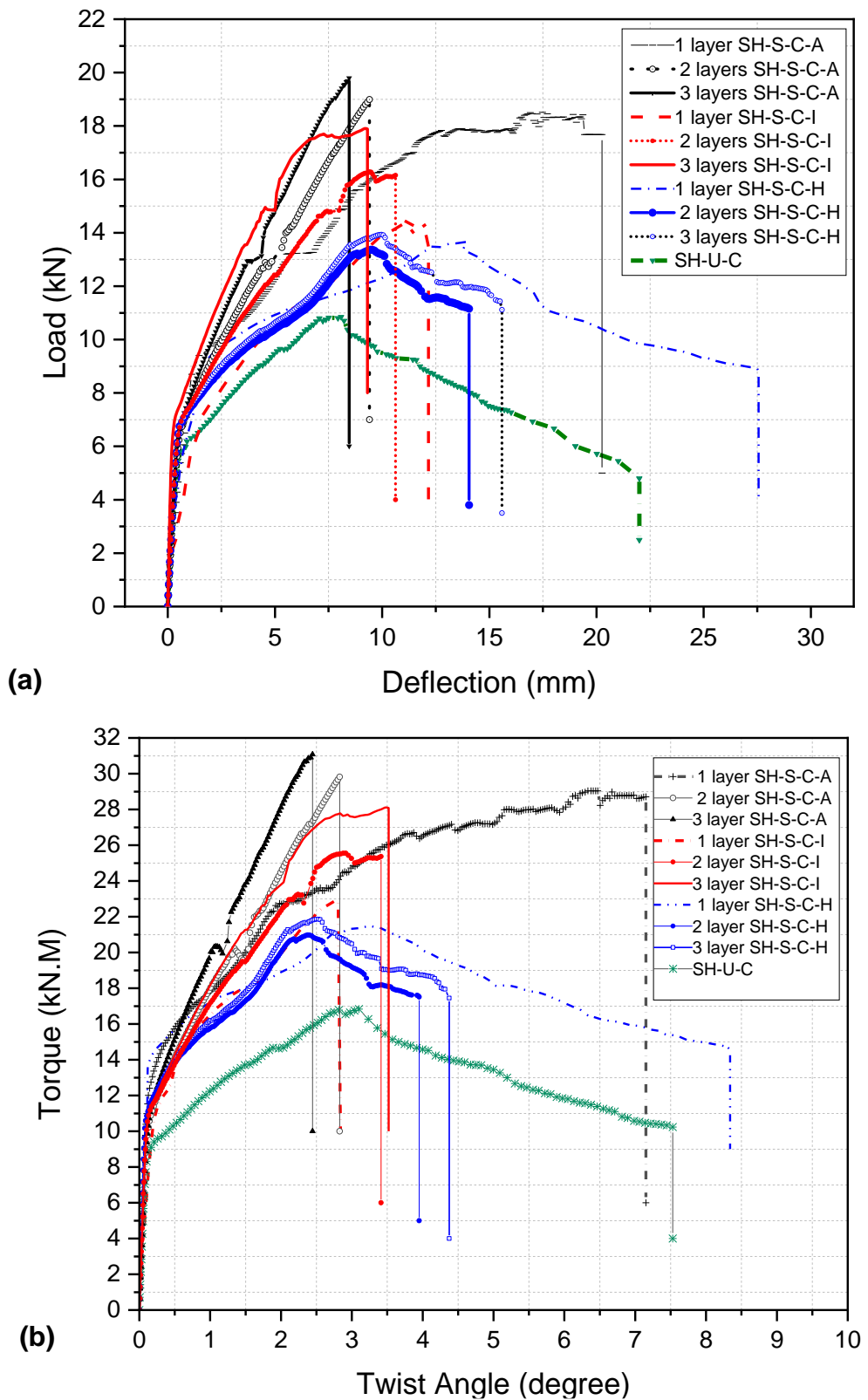


Figure 7.19: (a) Load-deflection curves for models with different CFRP layers (b) Twist-angle curves for models with different CFRP layers

7.8 Influence of High Compressive Strength of Concrete

In this section, 12 beam-column joint models were investigated with using High Strength Concrete (HSC) of 65 MPa compressive strength. As identified in Chapters 2, 4, and 6, the inclined concrete struts capacities (σ_d) in the beam and the joint area with the column correspond to the compressive strength of concrete. The created models subjected to different loading ratios (i.e. 1.57, 1, and 0.5 T/M-S) with a constant axial load - equivalent to $0.1 A_g f'_c$. The wrapping schemes, geometry, and details were same as those presented in the previous sections to be comparable with the validated models of Normal Strength Concrete (NSC).

Table 7.2 summarise the results obtained from the models in terms of maximum carrying loads, torque, the beams main rebars strains, and the observed damage. Comparisons between results extracted from the models with NSC are also presented in Table 7.2; along with the computed struts stresses and their capacities based on Section 6.2.1 (Eq. 6.3 to 6.5) in order to quantify the level that induced crushing of concrete in corresponding with the various ratios of loads.

In general, the models created with HSC exhibited higher loads capacities than the NSC models ranged from 5% to 41%. As the using of HSC can potentially enhance the concrete cracking loads and struts capacities as well as allowing to fully mobilise the truss mechanism (yielding of stirrups and main rebars) before crushing of concrete. Wherein, the cracking torque for the HSC model (SH-U-C) was increased to 14.03 kN.M (evaluated based on Eq. 3.5) compared with NSC model (11.4 kN.m). Nevertheless, the HSC models showed less differences in the carrying loads with those obtained from NSC models under 0.5 T/M-S loads ratio. Since the failure mainly caused by rupture of the beam bottom rebars near to the column face due to considerable tensile stresses induced by bending and torsional forces. On the other hand, the improvements in the loading capacities due to using CFRP wraps with HSC were followed the same trend that observed from the experiments and F.E. analysis for NSC models (see Figure 7.20); as the highest carrying capacities produced with using full wrapping schemes (SH-S-C-A). However, It can be noticed from Figure 7.20 that the HSC models showed less twisting deformations than those obtained from NSC models (Figure 7.16d). These increases in the models stiffness influenced the post-peak load behaviour (failure stage) and hence, the ductility levels.

The increases in the beams bottom rebars strains (Table 7.2) were affected by the level of the loads attained, the loads ratios, and the wrapping type. Hence, due to escalation of the rebars forces in relation to the increase in the combined forces, significant increments in the developed strains were observed. However, SH-U-C model under 0.5 T/M-S loads ratio experienced lower strain value than observed from the NSC model; whilst this value is still larger than the maximum measured strain prior of the rupture of the rebars during the tensile tests. Hence, it can be deduced from Table 7.2 that substantial plastic strains (larger than 2800 microstrain) can be developed in the beam main rebars near to the column face caused by the interaction between the combined loads. Accordingly, cracks of concrete were occurred in the column at the joint region for all models subjected to 0.5T/M-S loads ratios due to significant increase in the joints demands (forces) that transferred via the beams main rebars. Likewise, several cracks were also extended to the column at the joint region for wrapped models that subjected 1.57 and 1 T/M-S loads ratios. However, the level of concrete cracking in the column at the joint area for the HSC models were less than those observed in the NSC models. This attributed to the enhancement in concrete tensile strength and the column cracking load due to increase of the applied column axial load as confirmed by Hamil (2000b).

In consistent with the tests results (Chapter 4), the inclined wrapping schemes (SH-S-C-I) produce larger strains levels than other schemes, as the inclined wraps tend to reduce the concrete strut angles and this also reflected in the computed angles according to Eq. 6.14. Also, it can be noticed that the developed strains in the beam bottom rebars with 1 and 0.5 T/M-S loads ratios induced ruptures of the rebars. Further, the computed struts stresses in the beams to the corresponded capacities (σ_d) showed a damage in the beams struts due to the increase in the shear stresses (i.e. torsion and direct shear forces). According to the truss mechanism, the level of the increase in the applied struts stress corresponded to the peak loads attained and the inclination angles of concrete struts. As confirmed in the previous chapters (Chapters 4 and 6), the inclination angle is mainly related to the ratio of the induced shear flow (q) to the transverse reinforcement's ratio and the angle of the warps (α_f).

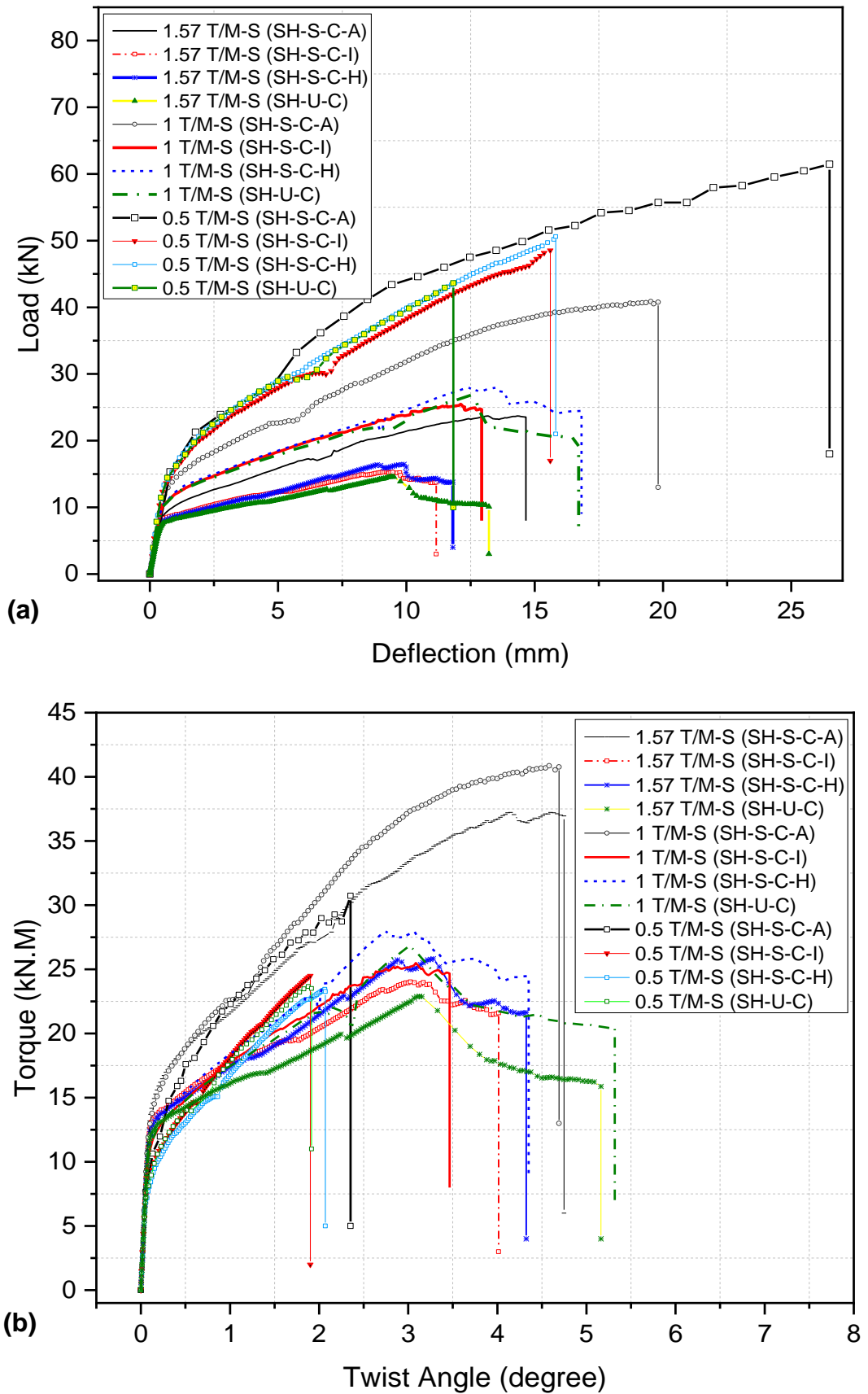


Figure 7.20: (a) Load-deflection curves for HSC models (b) Twist-angle curves for HSC models

Table 7.2 Comparison between HSC and NSC models results and observed damage for HSC models.

Model	Load Ratio	HSC			NSC			% Diff. ¹		Comp. Struts stress ²				Observed damage
		Load (kN)	Torque (kN-M)	Strain ($\mu\epsilon$)	Load (kN)	Torque (kN-M)	Strain ($\mu\epsilon$)	Load	Strain ($\mu\epsilon$)	σ_d (MPa)	α_d ³ (°)	Struts - SD (MPa)	SD/ σ_d	
SH-U-C	1.57 T/M-S	14.6	22.9	3043	11.0	17.3	1754	32%	73%	11.7	27	12.7	109%	C ⁴ , R ⁵ _s , Y ⁶ _b
	1 T/M-S	26.8	26.8	3195	23.2	23.2	2970	15%	8%	10.4	23	14.8	142%	C, R _s , Y _b
	0.5 T/M-S	43.8	21.9	6840	41.9	20.9	8385	5%	18%	11	25	12.1	110%	R ⁷ _b , J ⁸ _F , C ⁹ _f , Bc ¹⁰
SH-S-C-A	1.57 T/M-S	23.7	37.2	3406	18.5	28.9	2241	29%	52%	10.7	24	10.8	101%	C, R _s , Y _b , J _F
	1 T/M-S	40.9	40.9	3657	28.9	28.9	3012	41%	21%	11.7	27	11.9	102%	C, R _s , Y _b , J _F
	0.5 T/M-S	61.5	30.7	5560	56.3	28.2	4408	9%	21%	12.5	30	8.9	72%	R _b , J _F , C _f
SH-S-C-I	1.57 T/M-S	16.3	25.6	2988	13.8	21.7	2654	18%	13%	6.8	14	7.4	109%	C, R _s , Y _b , J _f
	1 T/M-S	25.5	25.5	6610	19.5	19.5	2798	31%	136%	7.2	15	7.4	103%	C, R _b , R _s , Y _b , J _F
	0.5 T/M-S	48.9	24.5	7682	41.9	20.9	4404	17%	74%	6.3	13	7.1	113%	R _b , J _f , C _f , Bc
SH-S-C-H	1.57 T/M-S	17.2	27.0	2126	13.7	21.4	1593	26%	33%	7.6	16	7.8	101%	C, R _s , J _F
	1 T/M-S	28.0	28.0	4570	21.4	21.4	2171	31%	111%	7.7	16	8.1	105%	C, C _f , R _s , J _F
	0.5 T/M-S	51.2	25.6	6164	41.9	20.9	4425	22%	39%	7.2	15	7.4	103%	R _b , J _F , C _f , Bc

¹ % difference between predicted load and the beam bottom rebars strains at 100 mm from the column faces from NSC models to those obtained from HSC models.

² Computed induced stress in the concrete beam struts at the peak load and struts capacity (σ_d) based on Section 6.2.1.

³ Computed struts angle at the beam left side as based on the lowest (most critical) obtained value where the torsion and shear are additive according to Section 6.2.2.

⁴ C is donated for a crushing in the beam concrete struts accompanied with severe inclined beam cracking.

⁵ R_s is donated for a severe plastic strain in the beam stirrups.

⁶ Y_b is donated for yielding in the beam bottom rebars close to the column face.

⁷ R_b is donated for rupture of the beam bottom rebars close to the column face.

⁸ J_F is donated for cracks in the column at the joint region.

⁹ C_f is donated for severe flexural cracks at the beam flexural plastic hinge near to column face.

¹⁰ B_c fully open inclined cracks in the beam region.

7.9 Long-Term Behaviour for HSC and NSC under Various Loads Ratios

As presented in Chapter 2, the extant literature did not show the effects of sustained torsional loads combined with flexural and direct shear on the beams deformations with considering different loads ratios. Hence, to investigate the influence of different loads ratios (1.57, 1, and 0.5 T/M-S) on the long-term behaviour of the beam-column joints, several models were created with NSC (Normal Strength Concrete) and HSC (High Strength Concrete). The same material properties (NSC) and geometries of LN-U-C specimen were modelled. The applied constant loads for the three loads ratios were maintained to be equivalent to 90% of the torsional cracking capacity as used in the tests; i.e. cracking loads were 14.03 kN.M and 11.4 kN.M for HSC and NSC, respectively. Hence, for NSC models, the applied loads were 6.5, 10.3, and 20.5 kN for 1.57, 1, and 0.5 T/M-S loads ratios, respectively. For HSC models, the applied loads were 8, 12.6, and 25.2 kN for 1.57, 1, and 0.5 T/M-S loads ratios.

The creep coefficients and free shrinkage strains for the NSC models were obtained from concrete samples (Chapter 3). Also, for the HSC concrete samples, the concrete time-dependent deformations (creep and shrinkage) were obtained from concrete samples tested by Mohammed (2020), which were under same environmental conditions in the laboratory-controlled room where the NSC were kept as given in Table 7.3. Further, the Eurocode 2 (2004) model was employed to predict the concrete shrinkage and creep coefficients for HSC based on the compressive strength of the concrete, relative humidity, and type of cement used. A good agreement can be observed from Table 7.3 between the experimental data and the predicted results. Nevertheless, the rate of creep and shrinkage of the experimentally obtained data at early age were lower than those predicted according to the code model. This overestimation in the predicted values could be from the missing reading in the test for a period when the samples moved from the curing room to the controlled room and the measuring started.

Table 7.3: Creep coefficients and free shrinkage induced strain for HSC samples.

Time (days)	Creep Coeff.	Shrinkage (Micro-strains)	EC2 Creep Coef.	EC2 Shrinkage (Micro-strains)	%Diff	
					creep	Shr.
0	0	0	0	0	0	0
10	0.46	114.24	0.567	136.74	18.84%	16.5%
20	0.63	165.24	0.719	187.27	12.38%	11.8%
30	0.75	188.7	0.804	209.21	6.68%	9.8%
40	0.84	205.02	0.867	222.24	3.15%	7.7%
50	0.91	220.32	0.918	230.86	0.92%	4.6%
60	0.96	229.5	0.961	236.99	0.10%	3.2%
70	1.01	238.68	0.997	241.57	1.27%	1.2%
80	1.048	245.82	1.029	245.13	1.85%	0.3%
90	1.087	251.87	1.057	247.96	2.86%	1.6%
Standard deviation					6%	5.2%

Figures 7.21a and 7.21b show the time-dependent twist angles of the beams induced by torque actions for NSC and HSC models, respectively. As the twist deformations increased in a high rate in the early stages of loading and decreased at various decreasing rates over time which is in line with the observation from the tests (Chapter 5). It can be seen from Figure 7.21a that the maximum twist deformations induced by high torsion loads ratio (1.57 T/M-S) as the beam region exhibited significant strain levels in the concrete at the beam's sides as presented in Section 7.5.2 and Section 5.4, with severe inclined cracks that were affected the beam's rigidity. While these strains were corresponded to the imposed compressive stresses levels and the induced time-dependent deformations (creep and shrinkage) in the concrete struts as discussed in Chapter 5. However, for the load's ratios of 1 and 0.5 T/M-S, less twist time-dependent deformations were occurred. As the analysis results showed that the increase of the direct shear loads reduced the strains levels and cracks propagation in the beam right side in compare with those occurred in the left side (see Figure 7.22), which in turn enhanced the beam's rigidity. This was because the torque induced shear flow was counteracted by those from the direct shear. Further, the increment in the flexural forces reduced the

tensile stresses in the flexural compression zone that could be produced from the torque action. Where the numerical analysis results showed no crack in the beam's top as shown in Figure 7.22a. Also, the developed creep deformations in the uncracked flexural compression zone can reduce the tensile strains caused by torsional forces, which is consistent with the outcomes of the tests as discussed in Chapter 5. Nevertheless, the results of this numerical investigation agree well with the test results of LN-C-U, where significant strains levels were developed at the beam left and the bottom sides (greater than 5000 microstrain) as shown in Figure 7.22. Figures 7.22 and 7.23 compare the principal tensile strains that developed due to instantaneous loads and time-dependent deformations for the NSC and HSC models, respectively. It can be seen that large tensile strains which were accompanied with severe cracks have been developed; these corresponded to the interaction of combined loads and concrete time-dependent deformations.

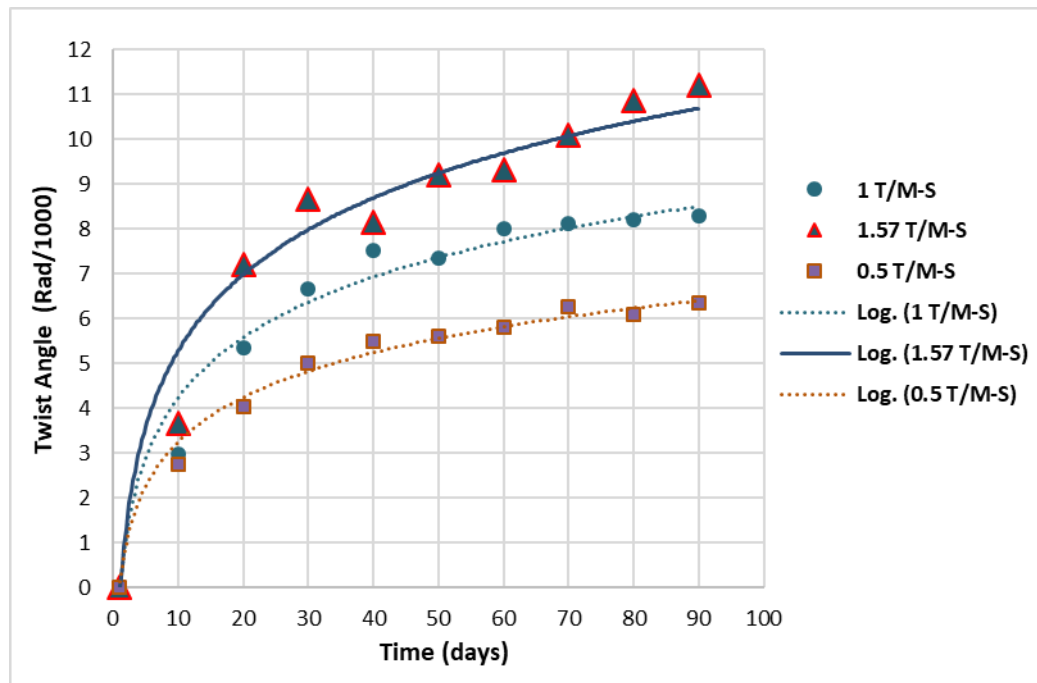
Figure 7.21b indicates that the using of HSC can enhance the models twisting stiffness compared with the NSC samples, as less twist angles can be observed during the loading periods. Interestingly, the developed maximum twisting deformations for the model under 1.57 T/M-S loads ratio were 212% and 273% less than those induced by 1 T/M-S and 0.5 T/M-S loads ratios. This corresponds to the level of the developed time-dependent strains in the beam region, as the average principal tensile strains that observed in the model under 1.57 T/M-S loads ratio at the end of load duration was less than 700 microstrain (Figure 7.23a). Meanwhile, a single transverse crack formed near the column face at the bottom of the beams (maximum flexural stresses) and extended to the beam right side. Wherein, in the case of excluding the crack formed at the bottom and right face, no other cracks were formed at the end of the analysis which would reduce the beam stiffness and increase the twist deformations as occurred in the NSC model. Further, the increase in the cracking load (larger tensile strength of concrete) and decrease in the creep and shrinkage strains by using HSC in compare with the NSC samples (Chapter 5) were impaired the formation of cracks. In contrast, for the other two models (1 and 0.5 T/M-S), significant time-dependent strains (larger than 5000 microstrain at the end of analysis) accompanied with inclined shear cracks and transverse flexural cracks were developed in the beam region (Figures 7.23b and 7.23c). This increase in the developed strains were resulted from the increase in the flexural and direct shear forces. As the increase in flexural stress prompted flexural cracks at the beam region which

were more significant in the model under 0.5 T/M-S loads ratio (Figure 7.23c), as the bending moment (20.3 kN. M) was higher than the predicted cracking bending moment (16.2 kN.M) based on Eurocode 2 (2004). Also, the direct shear forces increase the principal stresses in the concrete struts at the beam left side where the direct shear and torsion were additive, hence, the levels of strains were larger. These increments of the imposed stresses increased the development of the time-dependent deformation in concrete, and the formed cracks reduced the beam stiffness accordingly, as well as increased the twist deformations. On the other hand, this numerical investigation showed that the developed tensile strains in the column at the joint regions during the analysis duration were less than occurred in the beams regions and no cracks were noticed in the columns for all models.

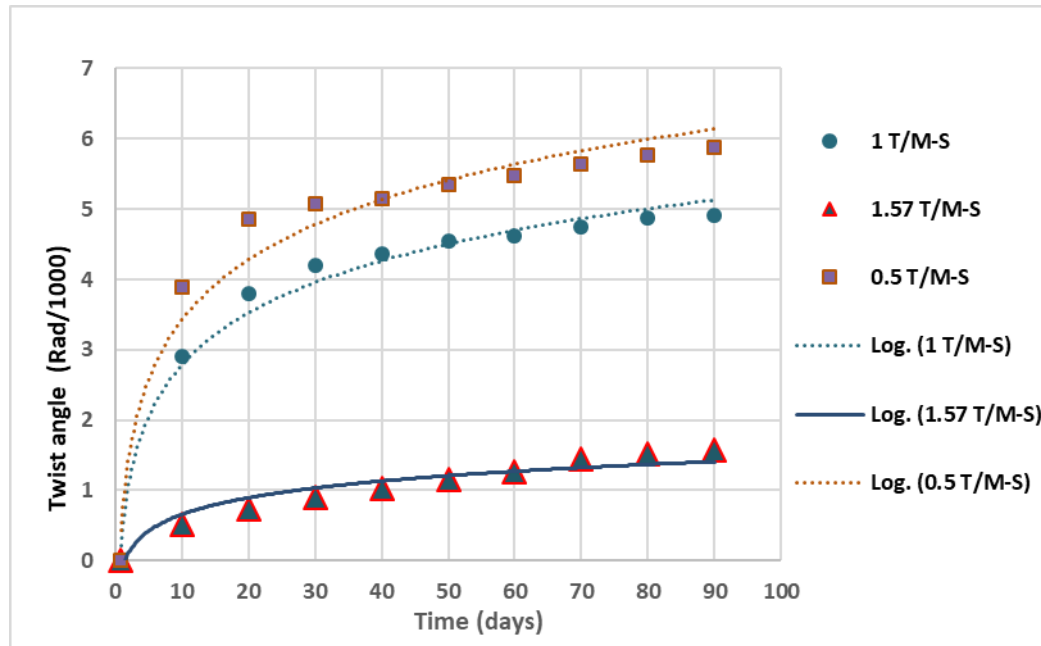
Figures 7.24a and 7.24b compares the predicted end-beam deflection (instantaneous and long-term) for the NSC and HSC models under combined loads with those evaluated according to Eurocode 2 (2004). These predictions are based on the beams curvatures due to bending moments as presented in Section 5.4.1. For the NSC models under 1.57 and 1 T/M-S loads ratios, a significant increase in the beam deflection (see Figure 7.24a) which is ranged from 4.7 to 5.5 times compared with those subjected to flexural forces according to the code model. Since, the imposed flexural forces were less than the threshold cracking moment (M_{cr}) that based on Eurocode code model. Thereby, the deflection values were under predicted due to an overestimating of the models stiffness's – i.e. they were considered uncracked sections. While, for the model subjected 0.5 T/M-S, a less difference (1.5 times flexural induced deflection) with the code model was observed in comparison with the other load's ratios. The beam's deflection was evaluated based on the cracked section approach, which was conformed with the increase in the flexural load that was beyond the flexural cracking loads (10.7 kN). The rise in the beam's deflections mainly because the torsional induced cracks reduced the beam's stiffness and potentially increase the loss of tension stiffening in the flexural tension zone. In addition, the high shear stresses and the developed time-dependent deformation can produce a shorting in the compression struts (Neville et al., 1983).

For HSC models, Figure 7.24b showed the influence of the combined loads and cracking levels on the increase in the deflection levels in comparison with Eurocode code model. These increases in the predicted deflections at the end of analysis (90 days) were 1.47, 4.78, and 1.62 times than those based on the

code model subjected to loads ratios of 1.57 T/M-S, 1 T/M-S, and 0.5 T/M-S, respectively. For the models under 1 T/M, the code model was considerably underestimated the beam's deflection, i.e. based on the uncracked section assumption. While less difference was obtained from the model under 1.57 T/M-S loads ratio compared with 1 T/M-S model, as the model did not experience high strains levels or significant torsional cracks (inclined cracks). This figure demonstrates that the time-dependent deflection was affected by the level of combined forces and the induced cracks (i.e. transverse and inclined cracks). Hence, for the model under high level of combined loads (0.5 T/M-S) which exhibited large tensile strains (Figure 17.23c) and cracks levels in the beam region was attained the highest deflection values compared with the other models created with HSC. While 1.57 T/M-S loads ratio was produced the lowest deflections values, since the developed strains and crack levels were insignificant. These observations are consistent with the tests results (Chapter 5) about the role of the level of combined loads and the developed time-dependent cracks of reducing the members' stiffness and affecting the twisting levels and hence, the deflection values.

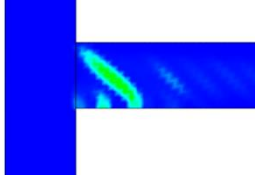
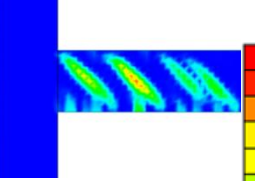
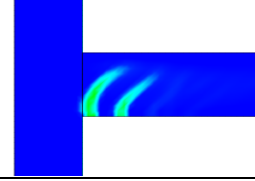
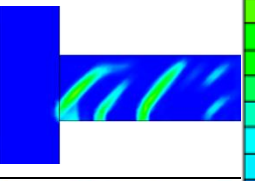

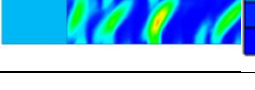

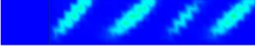


(a)

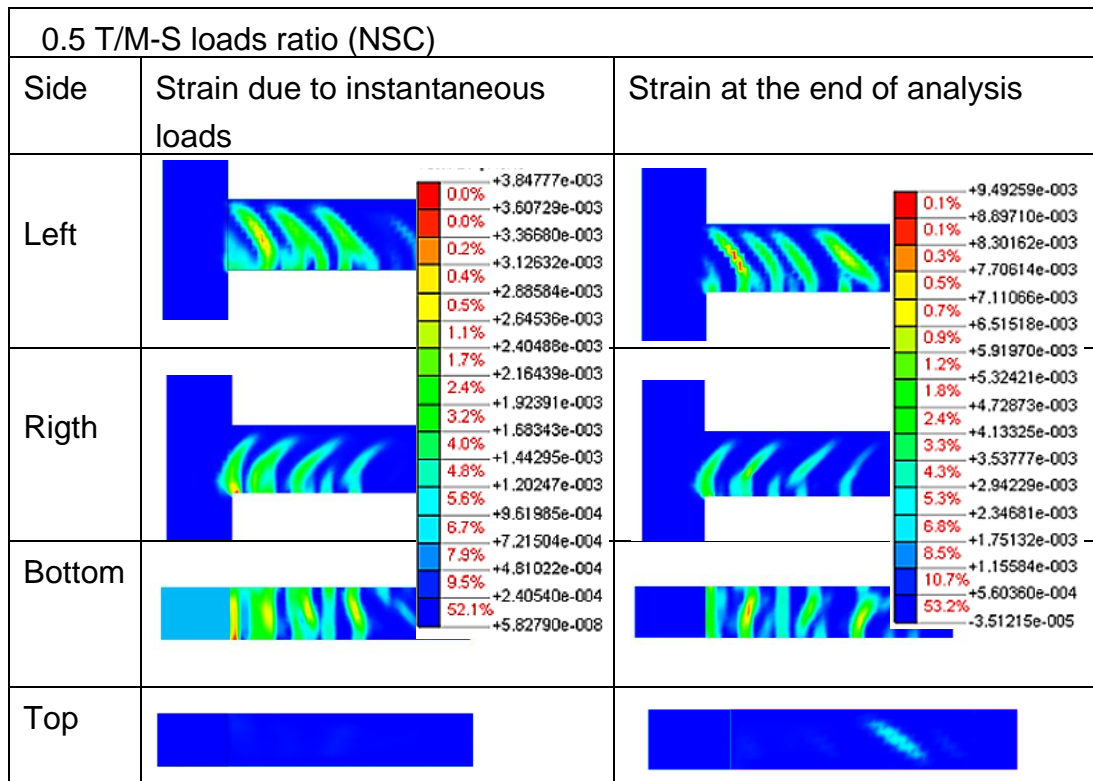


(b)

Figure 7.21: Developed end-beam twist angle with time under different ratios of sustained loads (a) Models created with NSC (b) Models created with HSC

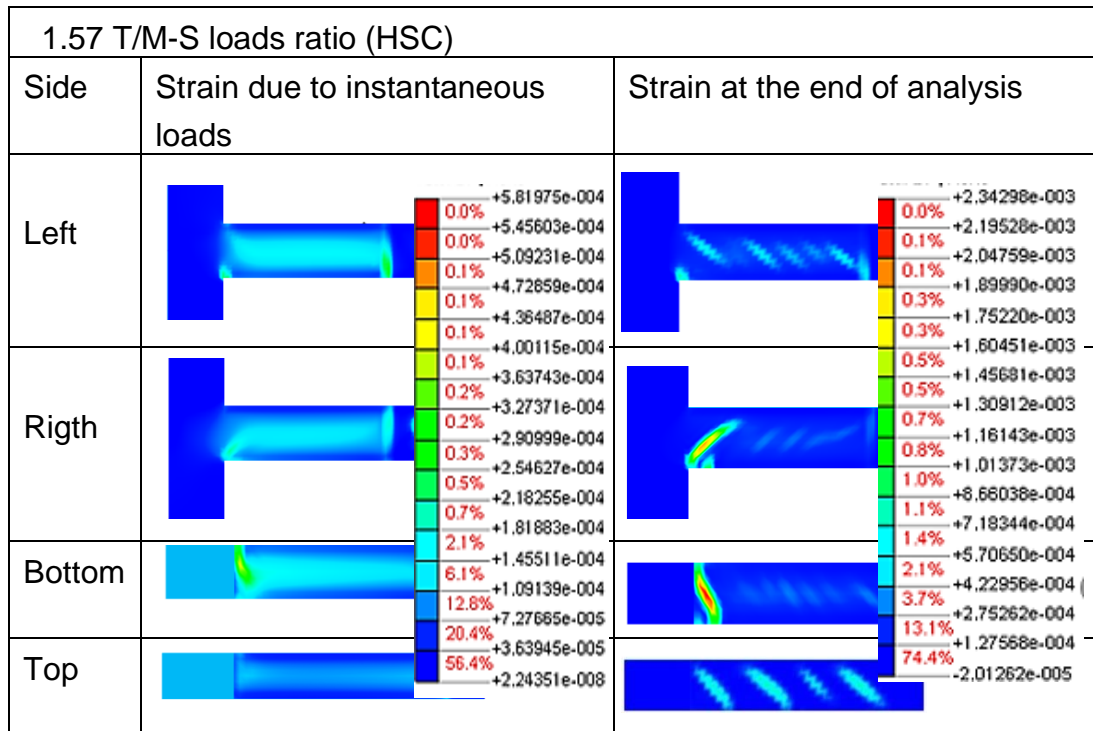
1 T/M-S loads ratio (NSC)		
Side	Strain due to instantaneous loads	Strain at the end of analysis
Left	 <div> <div>0.1%</div><div>+1.86409e-003</div> <div>0.2%</div><div>+1.74758e-003</div> <div>0.3%</div><div>+1.63108e-003</div> <div>0.4%</div><div>+1.51457e-003</div> <div>0.7%</div><div>+1.39807e-003</div> <div>0.9%</div><div>+1.28156e-003</div> </div>	 <div> <div>0.1%</div><div>+7.92532e-003</div> <div>0.2%</div><div>+7.42784e-003</div> <div>0.3%</div><div>+6.93036e-003</div> <div>0.5%</div><div>+6.43288e-003</div> <div>0.7%</div><div>+5.93541e-003</div> <div>1.0%</div><div>+5.43793e-003</div> </div>
Righth	 <div> <div>1.2%</div><div>+1.16506e-003</div> <div>1.5%</div><div>+1.04855e-003</div> <div>1.8%</div><div>+9.32046e-004</div> <div>2.1%</div><div>+8.15541e-004</div> <div>2.4%</div><div>+6.99035e-004</div> <div>3.0%</div><div>+5.82530e-004</div> <div>3.6%</div><div>+4.66024e-004</div> <div>5.4%</div><div>+3.49519e-004</div> <div>11.8%</div><div>+2.33013e-004</div> <div>64.6%</div><div>+1.16508e-004</div> <div></div><div>+2.63676e-009</div> </div>	 <div> <div>1.5%</div><div>+4.94045e-003</div> <div>2.0%</div><div>+4.44297e-003</div> <div>2.8%</div><div>+3.94549e-003</div> <div>3.6%</div><div>+3.44801e-003</div> <div>4.5%</div><div>+2.95053e-003</div> <div>5.6%</div><div>+2.45305e-003</div> <div>7.1%</div><div>+1.95557e-003</div> <div>8.5%</div><div>+1.45809e-003</div> <div>10.6%</div><div>+9.60611e-004</div> <div>51.0%</div><div>+4.63132e-004</div> <div></div><div>-3.43478e-005</div> </div>
Bottom	 <div> <div>11.8%</div><div>+2.33013e-004</div> <div>64.6%</div><div>+1.16508e-004</div> </div>	 <div> <div>10.6%</div><div>+9.60611e-004</div> <div>51.0%</div><div>+4.63132e-004</div> </div>
Top		

(a)

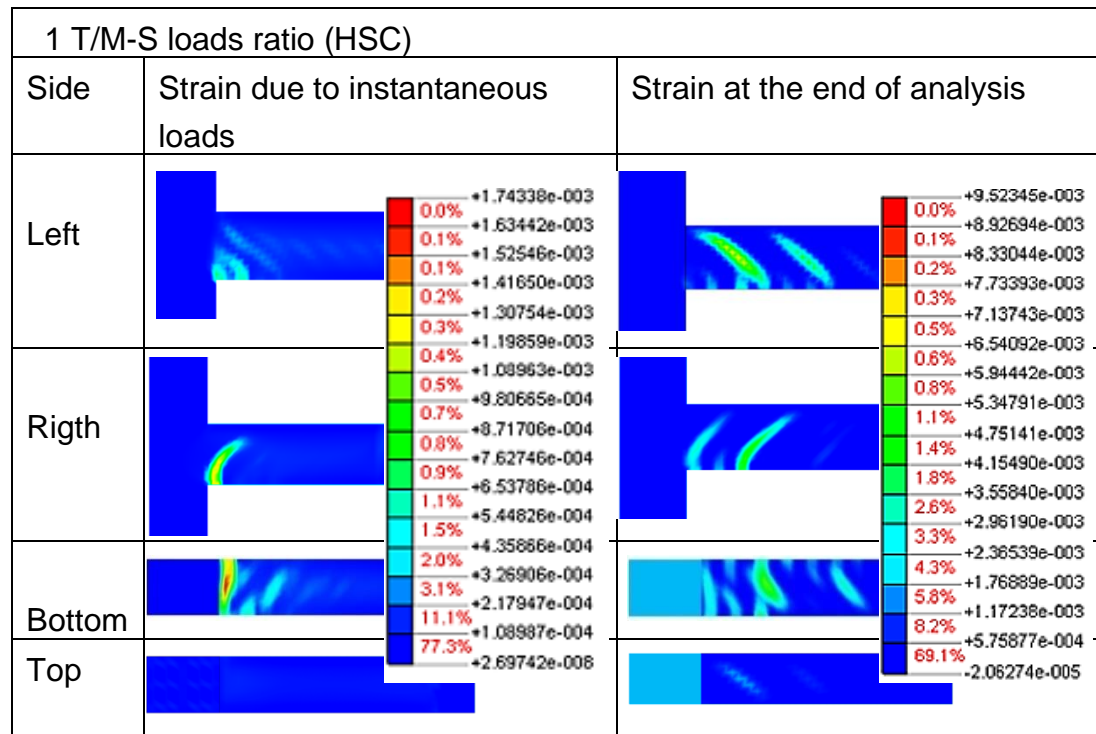


(b)

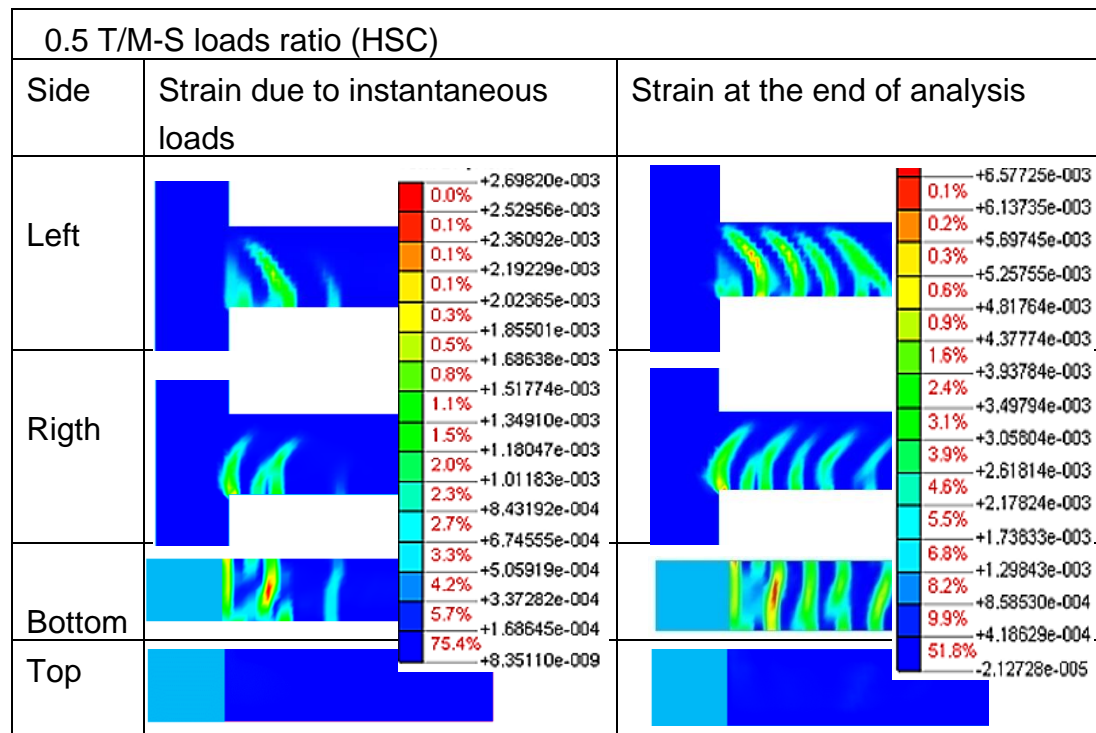
Figure 7.22: Instantaneous and time-dependent principal tensile developed for the models created with NSC (a) under 1 T/M-S sustained loads ratio (b) under 0.5 T/M-S sustained loads ratio



(a)

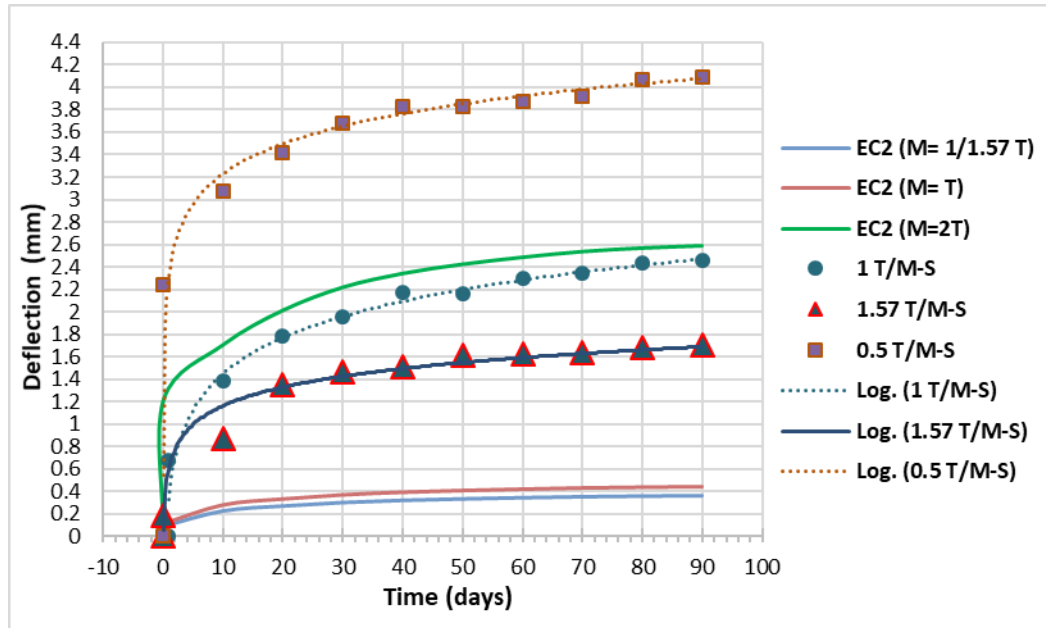


(b)

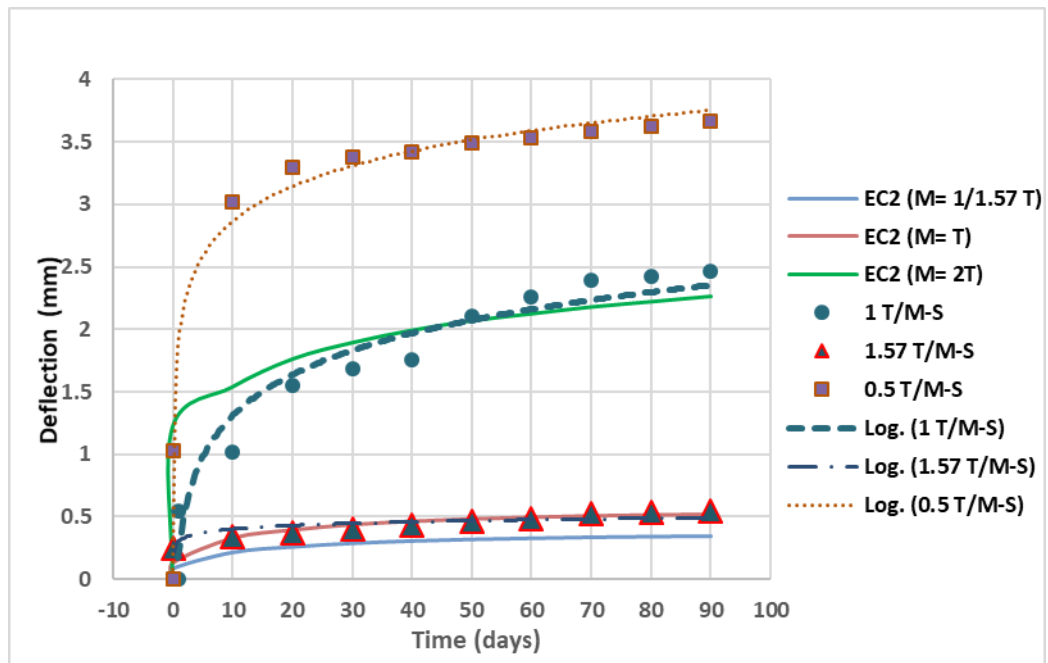


(c)

Figure 7.23: Instantaneous and time-dependent principal tensile developed for the models created with HSC (a) under 1.57 T/M-S sustained loads ratio (b) under 1 T/M-S sustained loads ratio (c) under 0.5 T/M-S sustained loads ratio



(a)



(b)

Figure 7.24: Developed end-beam deflection with time under different ratios of sustained loads (a) Models created with NSC (b) Models created with HSC

7.10 Summary

In this chapter, a nonlinear finite element approach based on the total strain crack model was utilised. The aim of this investigation is to predict the short-term and long-term behaviours of RC beam-column joints subjected to combined loads including torsion, bending, and direct shear. The created beam-column joints were modelled with using NSC and HSC; also, three wrapping schemes by using multiple CFRP layers and different loads ratios (i.e. 1.57, 1, and 0.5 T/M-S) were considered. The following are the main outcomes that can be drawn from the numerical investigations:

1. The details of the constitutive models that considered for the materials used (concrete, CFRP, and steel), simulation of the beam-column joints under monotonic and sustained loads, and the analysis approach were provided.
2. The employment of the total strain crack constitutive model was very well presented the cracking behaviour of concrete under combined loads compared with tests results.
3. The proposed approach by modifying the modulus of elasticity of concrete to consider the creep deformations with incorporating the shrinkage strains as thermal strains was capable to simulate the long-term behaviour of the beam-column joints.
4. Based on the comparisons between the results obtained from the models and experiments under monotonically increased loads (short-term groups), close results were obtained in terms of beam's twist angles, deflection, and developed strains in the beam's main rebars and concrete, and level of cracks.
5. The numerical models showed significant rise in the plastic strains (up to 1.86 times yield induced strain) that can be developed in the beam main rebars near to column face due to different loads ratios. These strain influenced the damage and cracks levels in the column at the joints area. The increase in the rebars strains were related to the level of the combined loads in corresponding to the load ratios and the type of wrapping used.
6. The increase of the torque to bending ratio reduced the flexural capacity, while the increase in bending load levels enhanced the beams torsion resistance. These results are consistent with those deduced from the tests and the literature. However, for strengthened

models, the enhancement levels in torsional capacities that corresponded to the increase in the bending loads were insignificant, due to concrete struts damage which in turn a non-convergence occurred.

7. The enhancement in carrying capacity of strengthened models using multiple CFRP wraps was limited to the concrete struts capacity; as a marginal increase (8%) in the load capacities for models with full and hoops wraps when three CFRP used. However, models with inclined wraps -multiple layers showed up to 23% increment of the attained loads than using a single layer.
8. The models created with HSC showed higher enhancements levels in their carrying loads capacities under different loads ratios than those observed from NSC models with enhancements ranging from 5% to 41%. The observed high loads levels were accompanied with considerable rise in the steel rebars strains which exceeded the strain induced a rupture of the beam's main rebars for the models under 0.5T/M-S load's ratio. The rise in the rebars strains were influenced by the level of loads attained, loads ratios, and wrapping types.
9. The increase in the loads attained via using CFRP wraps with HSC followed the same trend that observed from the experiments and F.E. analysis for NSC models; as the highest carrying capacities produced with using full wrapping schemes. Further, the wraps used prompted the damage and cracks to be extended to the column at the joint's area.
10. The influence of different ratio of the combined sustained loads on beam-column joints deformations agreed with the tests observations. As the models exhibited considerable time-dependent strains levels (can be greater than 5000 micro-strain) and diagonal-shear cracks concentrated in the beam region. While the column region including the joint area experienced less tensile strain levels, with no crack was observed.
11. The models created with NSC, the maximum time-dependent twist deformations was induced by high torsion loads ratio (1.57 T/M-S); where severe time-dependent torsional cracks around the beam's sides were developed in which affected the model stiffness.
12. The NSC models subjected to 1T/M-S and 0.5T/M-S load's ratios were experienced less time-dependent twist than the 1.57 T/M-S model. This decrement can be related to (i) the increase of the direct shear loads which reduced the strains levels and cracks propagation in the

beam right side (i.e. direct shear acted against torsion induced shear-flow), (ii) the high level of flexural forces reduced the tensile stresses in the flexural compression zone (the beam's top) produced from torsion, and (iii) the developed creep and shrinkage deformations in the uncracked flexural compression zone can alleviate the tensile strains occurred normal to the inclined compression struts.

13. The using of HSC improved the models time-dependent twisting stiffness in comparison with the NSC models, as less twist angles were obtained. Nevertheless, for the model under 1.57 T/M-S load ratio exhibited small twist deformations, which were about 212% and 273% lesser than the models under 1T/M-S and 0.5T/M-S, respectively.
14. Considerable differences in the model's end-beam's deflections up to 5 times larger than those predicted according to Eurocode 2 model. These differences were found more significant when torsional cracks severely developed along with high strains levels due to interaction between the combined loads and the developed time-dependent deformations in concrete.

Chapter 8 Conclusions and recommendations

8.1 Conclusions

The experimental outcomes, along with the adopted analytical methods and numerical analysis reflect the consistent influence of the fibre ratio, interaction between the combined forces, concrete strut capacity, and fibre orientation on the joint forces, failure mode, and distortion levels. A large rise in the strut force resulting from shear stresses led to sudden-brittle failure. Likewise, increases in the beams main steel rebars strains have been identified at the column face, again influenced by the load interactions and the wraps used. Conclusions from the experimental investigation, analytical approaches, and numerical F.E. analysis are accordingly described as four main sections that corresponding to the study phases as given in the following sections.

8.1.1 Findings from the Experimental Investigation (Short-Term Tests)

The tested beam-column joints were subjected to monotonically increased loads. Theses testes included three different wrapping schemes (i.e. full, hoops, and inclined strips wraps) that have been presented in the previous research to enhance the torsional behaviours of RC beams. The conclusions from the tests series are described as follows:

- The presence of torsional forces is adversely affected the specimens capacities, which produced significant increments in the beam's chords (main rebars) forces and caused severe damage to the beam's concrete struts.
- The failure mode and the location of the plastic hinge corresponded with the level of combined loads attained and the type of wraps. As the rise in the flexural forces level interacted with torque for the fully wrapped specimen, this increased the stresses in the beams' chords near the column face (flexural plastic hinge).
- The wrapped specimens had showed different enhancement levels in both pre-cracking (around 3%) and post-cracking stiffness, ranging from 35% to 114% with respect to fibre ratio and confinement degree. Correspondingly, the specimen with full wraps showed the highest loads levels.

- The key factors that can influence the beams brittle failure mechanisms have been identified. These are: level of shear stresses and corresponding compression struts forces, softening level due to concrete cracking, the angle degree of the compression struts, and longitudinal to transverse reinforcements ratios.
- Escalations in the developed strains in the beams' main chords under multiple loads were identified in relation to the fibres' orientations. The maximum measured strain was found in the specimen with the inclined CFRP strips, where the inclined wraps intended to reduce the concrete struts angle and produced larger longitudinal strains compared with other 90° oriented schemes.
- In relation to the truss mechanism, the increments in the transverse reinforcement (CFRP wraps' contributions) increased the inclination angle of the concrete struts, such that they became steeper, thus reducing the amount of stress in the longitudinal main rebars. This phenomenon was found in the behaviour of the specimens with full and hoops wraps, where, under the same load levels, they produced lower strain values than the unstrengthened control specimen.
- A comparison between the maximum observed capacity from the tests and those predicted according to the modified interactions formula (mode-1) showed deviations of 16% and 14% for specimens with the inclined and hoops wraps, respectively, due to concrete damage and large stirrup deformations.
- The decrements in the ductility indices ($P-\Delta$ and $Tu-\psi$) for the tested specimens were related to the degradation levels of the concrete struts, which were in turn affected by the value of shear-flow induced from torsional and shear forces and the corresponding wrapping degree.
- The observed distortion levels and cracks in the joint zone were related to the joint's demands induced by the beam's loads. Where these forces were mainly transferred into the joint's region through the beam's chords.
- The tests indicated that the joint's demands corresponded with the level of the interacted loads and wrapping arrangements.
- The strengthened specimens with the 45° inclined wraps and full wraps experienced joint shear deformations of 71% and 63% of those measured from the specimen under flexural forces, respectively. Meanwhile, the observed peak loads were only 22% and 29% for the

specimens with the 45° inclined wraps and full wraps, respectively, when compared with the specimen under flexural forces (SH-U-F).

8.1.2 Findings from the Experimental Investigation (Long-Term Tests)

The long-term tests series were set to investigate the influences of sustained torsional forces on the beam-column joints. The conclusions from the long-term tests series under sustained loads are described as follows:

- Significant increases in the time-dependent beam's twisting were observed from the tests, which agreed with the results deduced from the previous research. These increases were ranged from 2.1 to 5.47 of the initial angles.
- The results obtained from the strengthened specimens revealed that the CFRP wraps considerably improved the long-term stiffness of the specimen. Lower time-dependent twisting and cracking levels were found in comparison with the unstrengthened specimens.
- Incorporating of the torque loads caused a reduction in the flexural stiffness in the beam's region, which resulted in increases in the beam's curvature and deflection.
- The tests outcomes showed a rapid increase in the beams' twist deformations and cracking rates at the early age of loading for all specimens. Meanwhile, the rates slowed down during the later ages of loading in relation to creep and shrinkage developments.
- No new torsional cracks were noticed in the specimens after 30 days, when the loads applied. Further, the predicted twist angles at an age of 365 days was ranged from 6% to 18% greater than those measured at 90 days.
- The unstrengthened specimen under the single loading stage exhibited significant growth in the time-dependent torsional cracks (up to 7 times larger than the initial width). However, the use of the CFRP hoops had arrested the propagation of cracks, as the observed cracks widths were within the code's recommendations, i.e. equal or less than 0.3 mm.
- The measured surface strains varied across the beam's sides, beam's levels, and beam's lengths. These were due to variations in the imposed loads through the beam's sides and lengths, directions and levels of compressive stress fields in the concrete struts, compatibility

conditions, cracks locations, and concrete creep and shrinkage deformations.

- Time-dependent surface strains were developed in different beam's sides and zones. For the unstrengthened specimens, the surface strains exceeded 5000 micro-strain in some zones. These zones were located at the beam's left side, where torque and shear acted in same direction, and the beam's bottom side, due to combined tensile stresses induced from torque and bending actions.
- Increases in the instantaneous surface strains ranged from 0.47 to 1.81 larger than the flexural induced strains that were predicted according to Eurocode 2 (2004) model. Meanwhile, the observed time dependent strains were considerably greater than the bending induced strains, i.e. up to 8.6 times the flexural strains.
- The tests results indicated that the strains in the rebars were developed with time and varied throughout the beam's faces and sides.
- Using CFRP strips as additional transverse reinforcements reduced the longitudinal deformations in corresponding to the truss mechanism and torsional compressive field.
- For the specimen under two loading stages, most of the obtained readings became more scattered after the application of the torsional load and the development of torsional cracks. These indicated that the rebar strains can be substantially altered in relation to the level of torsional forces and cracking of concrete.
- The strengthened specimen experienced significantly fewer time-dependent deformations in the beam's stirrups - about 1.2 times less than the unstrengthened specimens. This was because the CFRP wraps increased the stiffness of the beam in the transverse direction and reduced the stresses in the steel stirrups.

8.1.3 Conclusions Based on the Developed Analytical Approaches

The following are the main conclusions that can be drawn from the proposed approaches and the validation process.

- To include the CFRP contributions in terms of predicting the member's torsional capacity and the variation in concrete struts inclination angle, the superposition approach is utilised. It is recommended that the

prediction of CFRP wraps and steel rebars' contributions is should be based on the truss mechanism.

- A design approach is introduced to avoid sudden-brittle damage to the concrete struts. This is achieved by limiting the compressive strut's forces due to combined actions to the concrete strut capacity (σ_d). The reduction in the struts' strength (σ_d) is accounted according to Eurocode 2 (2004).
- In comparison to the tests' results, the predicted torsional peak loads according to the developed design approach were very close. The difference between the actual and predicted results did not exceed 10%. Correspondingly, at the ultimate design load, no failure in concrete was observed during the tests, which confirms the adequacy of the predicted concrete struts' capacity.
- The proposed formulas to predict the joint's demands under multiple loads adequately quantified the interacted beam's chords forces in corresponding to different wrapping schemes used. A strong agreement was obtained, where the mean value of the ratio of the tests' results to the predicted values was 98%, with a corresponding coefficient of variation (COV) of only 2%.
- An iterative joint's model has been developed based on the panel zone principal stress-strain method, proposed by Pantazopoulou and Bonacci (1992). This model addresses the softening of the concrete, the truss panel, and the direct strut mechanisms, according to Tsonos (2008; 2006). The developed model considers the joint's key factors; i.e. concrete strength, the main rebars and transverse reinforcement ratios, the column axial load, and the joint aspect ratio.
- A good agreement was observed between the predicted values according to the joints' developed model and those from the tests' results with a mean values of no less 93% for the ratio of the experimental to the predicted results and COV of no more than 7%, in terms of joint's deformation angles and shear strength.
- Modifications to the joints model expressions is proposed to address the effects of the joint's wraps.

8.1.4 Conclusions Based on the Developed Numerical F.E. Approach

Conclusions from the numerical investigations under different parameters, modelling details, and the analysis results are described below:

- The cracking behaviour of concrete for the F.E. models in both short and long term groups in comparison with the tests results was very well predicted based on the total strain crack model - the smeared crack concept by considering the softening of concrete in both tension and compression.
- To account for the time-dependent deformation of concrete, an approach is introduced by modifying the modulus of the elasticity of concrete according to the age-adjusted effective modulus method to incorporate the creep deformations and further the shrinkage strains imposed as thermal strains.
- Under different loads ratios, the numerical models showed a significant increase in the plastic strains which was up to 1.86 times of the yield strain. The strains levels were considerably exceeded those obtained from the specimen that was subjected to the bending moment. These were developed in the beam main rebars near the column face and influenced the damage and cracking levels in the column at the joints area.
- Different enhancement levels were attained from the model created with HSC (high strength concrete). Further, the HSC models showed larger loads capacities than the NSC (normal strength concrete) models, which were ranged from 5% to 46%. Nevertheless, these levels followed the same trend that was observed from the experiments and F.E. analysis for the NSC models.
- The largest carrying capacities were produced when using the full wrapping schemes. Correspondingly, the wraps used prompted the damage and cracks to be extended to the column at the joint's area, where this was more pronounced with full and inclined wraps.
- The decrements in the flexural capacity related to the increment of the torque to bending-shear (T/M-S) loads ratio, while the increase in the bending load levels improved the beams torsion resistance by 33% and 25% for models subjected to 0.5 and 1 T/M-S ratios, respectively, compared with those induced by 1.57 T/M-S ratio of loads. These results are consistent with those deduced from the testes and the

literature. However, the increases in the bending capacities for the strengthened models were insignificant due to the damage to the compression struts.

- The effects of the sustained loads with various T/M-S ratios on the beam-column joints deformations were found to be in line with the tests observations. Nevertheless, the column region including the joint area experienced low tensile strain levels and no cracks were observed.
- The highest time-dependent twist levels for the NSC models were produced by a high torsion loads' ratio (1.57 T/M-S), since the model exhibited severe time-dependent torsional cracks around the beam's sides, which mainly affected the model's stiffness. Meanwhile, for the models that were under 1T/M-S and 0.5T/M-S load ratios, less time-dependent twist angles were obtained.
- The observed time-dependent twist deformations were corresponded with the induced level of flexural forces, which reduced the torsional tensile stresses in the flexural compression zone. In addition, the developed creep and shrinkage deformations in the uncracked flexural compression zone can alleviate the tensile strains that occurred normal to the inclined compression struts.
- In comparison to the NSC models, the HSC models showed less time-dependent twist angles. In the case of the model under 1.57 T/M-S load ratio, small twist deformations were induced, which were about 212% and 273% lesser than the models under 1T/M-S and 0.5T/M-S (exhibited flexural cracks), respectively. These time-dependent deformations were influenced by the level of inclined cracks and developed tensile strains that corresponded with the quality of concrete strength and reduction in the creep and shrinkage levels.
- Differences in the model's beams' deflections were up to 5 times larger than those predicted according to Eurocode 2 (2004) model. These differences were found to be more significant where severe torsional cracks occurred. These were accompanied by high strains levels due to interaction with combined loads and the developed time-dependent deformations of concrete.

8.2 Recommendations for Future Research

Based on the experimental, analytical, and numerical investigation outcomes, the following are recommended areas for further research:

- Further experimental investigations can be carried out to address the effects of material properties, such as fibre reinforced concrete, FRP bars, and high strength concrete on the short and long-term behaviours of beam-column joints under torque actions.
- Additional testes are recommended to fully validate the outcomes obtained from the developed numerical approach under different loads ratios and loading durations.
- It is recommended that additional levels of sustained torsional loads (different from the used 90% of cracking load), combined with bending and direct shear should be taken into consideration. Furthermore, these loads should be altered by adopting different loading stages during the tests.
- The effectiveness of the torsional beam's wraps for the beam-column joints can be investigated under cyclic combined loads, with a consideration for an escalation in the beam's chords forces, joint damage level, and location of the plastic hinge.
- This research has presented an analytical model to predict the joint's capacity. It is recommended that future studies should conduct more experimental investigations in order to further validate the model outcomes regarding the presence of joints' wraps, different concrete strengths, and a slab.
- The influence of time-dependent torsional deformations and cracks on the stiffness of the beams and corresponding deflection levels has been identified. Further research is required to address the influence of torsional loads combined with bending and shear on the beam's deflection, along with the loss of tension stiffening during the member's working life.

Bibliography

- AASHTO LRFD. 2010. *Bridge Design Specifications (5th Edition) with 2010 Interim Revisions*. American Association of State Highway and Transportation Officials (AASHTO).
- ABAQUS, H. 2008. Documentation: Version 6.8. *Dassault Systèmes*.
- ACI-ASCE 352R-02 Committee. 2002. Recommendations for design of beam-column joints in monolithic reinforced concrete structures. In: American Concrete Institute.
- ACI 209.1R-05. 2005. *Report on factors affecting shrinkage and creep of hardened concrete*. United States.
- ACI 209.2R-08. 2008. *Guide for modeling and calculating shrinkage and creep in hardened concrete*. American Concrete Institute Farmington Hills, MI.
- ACI 209.R-92. 1992. Prediction of creep, shrinkage, and temperature effects in concrete structures. In: American Concrete Institute.
- ACI 224R-01. 2001. Control of Cracking in Concrete Structures (Reapproved 2008). *Technical Documents*.
- ACI 440R-07. 2007. *Report on fiber-reinforced polymer (FRP) reinforcement for concrete structures*.
- ACI Committee 214R. 2011. Evaluation of Strength Test Results of Concrete. *American Concrete Institute, Farmington Hills, MI, USA*.
- ACI Committee 318. 2014. Building code requirements for structural concrete and commentary. In: American Concrete Institute.
- ACI Committee 440.2R-08. 2008. *Guide for the Design and Construction of Externally Bonded FRP Systems for Strengthening Concrete Structures*. American Concrete Institute.
- Al-Bayati, G., Al-Mahaidi, R., Hashemi, M.J. and Kalfat, R. 2018. Torsional strengthening of RC beams using NSM CFRP rope and innovative adhesives. *Composite Structures*. **187**, pp.190-202.
- Alavi-Dehkordi, S., Mostofinejad, D. and Alaei, P. 2019. Effects of high-strength reinforcing bars and concrete on seismic behavior of RC beam-column joints.(Report). *Engineering Structures*. **183**, p702.
- Allawi, A.A., Chai, H.K. and Majeed, A.A. 2015. Torsional Analysis of Multicell Concrete Box Girders Strengthened with CFRP Using a Modified Softened Truss Model. *Journal of Bridge Engineering*. **20**(8), pB4014001.
- Allos, A.E. and Rashid, A.H. 1989. Prestressed Concrete Rectangular Beams Subjected to Sustained Torque. *Structural Journal*. **86**(4).
- Almusallam, T.H. and Al-Salloum, Y.A. 2007. Seismic Response of Interior RC Beam-Column Joints Upgraded with FRP Sheets. II: Analysis and Parametric Study. *Journal of Composites for Construction*. **11**(6), pp.590-600.
- Altoubat, S.A. and Lange, D.A. 2001. Creep, shrinkage, and cracking of restrained concrete at early age. *ACI Materials Journal*. **98**(4), pp.323-331.

- Ameli, M., Ronagh, H.R. and Dux, P.F. 2007. Behavior of FRP Strengthened Reinforced Concrete Beams under Torsion. *Journal of Composites for Construction*. **11**(2), pp.192-200.
- Anil, K.S. and Pandit, G.S. 1980. Sustained Load Tests in Torsion. *Journal Proceedings*. **77**(2).
- Antonopoulos, C.P. and Triantafillou, T.C. 2003. Experimental Investigation of FRP-Strengthened RC Beam-Column Joints. *Journal of Composites for Construction*. **7**(1), pp.39-49.
- ASCE/SEI 7-10. 2013. Minimum Design Loads for Buildings and Other Structures. In: American Society of Civil Engineers.
- Atta, A.M. and El-Shafiey, T.F. 2014. Strengthening of RC dapped-end beams under torsional moment. *Magazine of Concrete Research*. **66**(20), pp.1065-1072.
- Attaalla, S.A. 2004. General analytical model for nominal shear stress of type 2 normal-and high-strength concrete beam-column joints. *Structural Journal*. **101**(1), pp.65-75.
- Baggio, D., Soudki, K. and Noël, M. 2014. Strengthening of shear critical RC beams with various FRP systems. *Construction and Building Materials*. **66**, pp.634-644.
- Bakir, P.G. and Boduroğlu, H.M. 2002. A new design equation for predicting the joint shear strength of monotonically loaded exterior beam-column joints. *Engineering Structures*. **24**(8), pp.1105-1117.
- Baky, H.A., Ebead, U.A. and Neale, K.W. 2007. Flexural and Interfacial Behavior of FRP-Strengthened Reinforced Concrete Beams. *Journal of Composites for Construction*. **11**(6), pp.629-639.
- Bamforth, P. 2007. *Early-age thermal crack control in concrete*. Ciria London.
- Bazant, Z.P. 1972. Prediction of concrete creep effects using age-adjusted effective. *J. Am. Concr. Inst.* **69**(4), pp.212-217.
- Bazant, Z.P. and Baweja, S. 2000. Creep and Shrinkage Prediction Model for Analysis and Design of Concrete Structures: Model B3-Short Form. *Special Publication*. **194**.
- Bazant, Z.P. and Oh, B.H. 1983. Crack band theory for fracture of concrete. *Matériaux et construction*. **16**(3), pp.155-177.
- Beeby, W. and Forth, J. 2005. Control of cracking in walls restrained along their base against early thermal movements. In: *Concrete for Transportation Infrastructure: Proceedings of the International Conference held at the University of Dundee, Scotland, UK on 5–7 July 2005*: Thomas Telford Publishing, pp.123-132.
- Belarbi, A. and Hsu, T.T. 1995. Constitutive laws of softened concrete in biaxial tension compression. *Structural Journal*. **92**(5), pp.562-573.
- Belarbi, A., Zhang, L. and Hsu, T.T. 1996. Constitutive Laws of Reinforced Concrete Membrane Elements. In:
- Bentz, E.C., Vecchio, F.J. and Collins, M.P. 2006. Simplified Modified Compression Field Theory for Calculating Shear Strength of Reinforced Concrete Elements. *ACI Structural Journal*. **103**(4), p614.

- Bernardo LFA and Lopes SMR. (2009) Torsion in High-Strength Concrete Hollow Beams: Strength and Ductility Analysis. *ACI Structural Journal* 106.
- Bhaskar, P. and Mohamed, R.H. 2012. Analytical estimation of elastic properties of polypropylene fiber matrix composite by finite element analysis. *Advances in Materials Physics and Chemistry*. 2012.
- Bonacci, J. and Pantazoupoulou, S. 1993. Parametric Investigation of Joint Mechanics. *Structural Journal*. **90**(1).
- Borst, R.d., Remmers, J.J., Needleman, A. and Abellan, M.A. 2004. Discrete vs smeared crack models for concrete fracture: bridging the gap. *International journal for numerical and analytical methods in geomechanics*. **28**(7-8), pp.583-607.
- BS8110. 1997. Structural Use of Concrete, Part 1: Code of Practice for Design and Construction. *British Standards Institution, UK*.
- BS 882. 1992. *Specification for aggregates from natural sources for concrete*. British Standards Institution London.
- BS EN 1992-1-1. 2004. *Eurocode 2: Design of concrete structures. General rules and rules for buildings*.
- BS EN 12350-2. 2000. Testing fresh concrete: slump test. *London: British Standards Institution*.
- CEB-FIP, C. 1991. model code 1990. *Comite Euro-International Du Beton, Paris*. pp.87-109.
- Chalioris, C.E. 2007. Analytical model for the torsional behaviour of reinforced concrete beams retrofitted with FRP materials. *Engineering Structures*. **29**(12), pp.3263-3276.
- Chalioris, C.E. 2008. Torsional strengthening of rectangular and flanged beams using carbon fibre-reinforced-polymers – Experimental study. *Construction and Building Materials*. **22**(1), pp.21-29.
- Chen, G., Chen, J. and Teng, J. 2012. On the finite element modelling of RC beams shear-strengthened with FRP. *Construction and Building Materials*. **32**, pp.13-26.
- Chiu H-J, Fang IK, Young W-T, et al. (2007) Behavior of reinforced concrete beams with minimum torsional reinforcement. *Engineering Structures* 29: 2193-2205
- Chun, S.-C. and Shin, Y.-S. 2014. Cyclic Testing of Exterior Beam-Column Joints with Varying Joint Aspect Ratio. *ACI Structural Journal*. **111**(3), p693.
- Cocchi, G.M. and Volpi, M. 1996. Inelastic analysis of reinforced concrete beams subjected to combined torsion, flexural and axial loads. *Computers and Structures*. **61**(3), pp.479-494.
- Collins, M.P. and Mitchell, D. 1980. Shear and torsion design of prestressed and non-prestressed concrete beams. *PCI journal*. **25**(5), pp.32-100.
- Cotsovos, D.M., Zeris, C.A. and Abbas, A.A. 2009. Finite element modelling of structural concrete. *COMPdyn 2009*.
- Davood, M. and Alireza, A. 2017. Flexural Strengthening of Reinforced Concrete Beam- Column Joints Using Innovative Anchorage System. *ACI Structural Journal*. **114**(6).

- Deifalla, A., Awad, A., Seleem, H. and Abdelrahman, A. 2020. Investigating the behavior of lightweight foamed concrete T-beams under torsion, shear, and flexure. *Engineering Structures*. **219**, p110741.
- Deifalla, A., Awad, A. and Elgarhy, M. 2013. Effectiveness of externally bonded CFRP strips for strengthening flanged beams under torsion: An experimental study. *Engineering Structures*. **56**, pp.2065-2075.
- Deifalla, A. and Ghobarah, A. 2010a. Full Torsional Behavior of RC Beams Wrapped with FRP: Analytical Model. *Journal of Composites for Construction*. **14**(3), pp.289-300.
- Deifalla, A. and Ghobarah, A. 2010b. Strengthening RC T-Beams Subjected to Combined Torsion and Shear Using FRP Fabrics: Experimental Study. *Journal of Composites for Construction*. **14**(3), pp.301-311.
- Desnerck, P., Lees, J.M. and Morley, C.T. 2018. Strut-and-tie models for deteriorated reinforced concrete half-joints. *Engineering Structures*. **161**(C), pp.41-54.
- Elfgrén, L. 1972. *Reinforced concrete beams loaded in combined torsion, bending and shear: a study of the ultimate load-carrying capacity*. thesis, Division of Concrete Structures, Chalmers University of Technology.
- Elfgrén, L., Karlsson, I. and Losberg, A. 1974. Torsion-bending-shear interaction for reinforced concrete beams. *Journal of the Structural division (1956-1982)*. **100**(ST 8, Proc. Paper 10749), pp.1657-1676.
- Elshafiey, T.M., Atta, A.M., Afefy, H.M. and Ellithy, M.E. 2016. Structural performance of reinforced concrete exterior beam–column joint subjected to combined shear and torsion. *Advances in Structural Engineering*. **19**(2), pp.327-340.
- EN BS 1008. 2002. 1008 Mixing Water for Concrete. *British Standards Institution: London, UK*.
- EN BS 10002-1. 2001. Tensile testing of metallic materials. Method of test at ambient temperature. *British Standards Institution*.
- Engindeniz, M. 2008. *Repair and strengthening of pre-1970 reinforced concrete corner beam-column joints using CFRP composites*. Dissertation/Thesis thesis, Georgia Institute of Technology.
- Eurocode 2, B. 2004. 1-2: 2004 Eurocode 2: Design of concrete structures- Part 1-2: General rules-Structural fire design. *European Standards, London*.
- Ewida, A.A. and McMullen, A.E. 1981. TORSION-SHEAR-FLEXURE INTERACTION IN REINFORCED CONCRETE MEMBERS. *Magazine of Concrete Research*. **33**(115), pp.113-122.
- Fédération Internationale Du Béton. 1999. *Structural Concrete: Textbook on Behaviour, Design and Performance: Updated Knowledge of the CEB/FIP Model Code 1990*. fib.
- fib Bulletin 14. 2001. *Externally bonded FRP reinforcement for RC structures*. Lausanne, Switzerland.: fib - International Federation for Structural Concrete.
- fib Model Code. 2010a. First complete draft—vol 1, CEB–FIB. *Bulletin d'Information*. **55**.
- fib Model Code, F.I.d.B.f. 2010b. final draft,. *Bulletin 66*. **vol.2**.

- Forth, J. 2015. Predicting the tensile creep of concrete. *Cement and Concrete Composites*. **55**, pp.70-80.
- Forth, J., Mu, R., Scott, R., Jones, A. and Beeby, A. 2014. Verification of cracked section shrinkage curvature models. *Proceedings of the Institution of Civil Engineers*. **167**(5), pp.274-284.
- Forth, J.P., Brooks, J.J. and Bingel, P.R. 2003. Movement in a seven storey reinforced concrete frame. *Proceedings of the Institution of Civil Engineers-Structures and Buildings*. **156**(2), pp.131-140.
- GangaRao, H.V.S., Taly, N. and Vijay, P.V. 2007. *Reinforced concrete design with FRP composites*. Boca Raton: CRC Press.
- Gao, B., Leung, C.K.Y. and Kim, J.-K. 2007. Failure diagrams of FRP strengthened RC beams. *Composite Structures*. **77**(4), pp.493-508.
- Ghali, A., El-Badry, M. and Favre, R. 2002. *Concrete structures: stresses and deformations*. 3rd ed. London: Spon.
- Ghali, A. and Favre, R. 1986. *Concrete structures: stresses and deformations*. London: Chapman and Hall.
- Ghobarah, A., Chidiac, S.E. and Ghorbel, M.N. 2002. Upgrading Torsional Resistance of Reinforced Concrete Beams Using Fiber-Reinforced Polymer. *Journal of Composites for Construction*. **6**(4), pp.257-263.
- Gilbert, R. 2002. Creep and shrinkage models for high strength concrete—proposals for inclusion in AS3600. *Australian Journal of Structural Engineering*. **4**(2), pp.95-106.
- Gilbert, R.I. 1988. *Time effects in concrete structures*. Amsterdam;Oxford;: Elsevier.
- Gilbert, R.I. and Ranzi, G. 2010. *Time-Dependent Behaviour of Concrete Structures*. GB: CRC Press.
- Goode, C. 1975. Reinforced concrete beams subjected to a sustained torque. *The Structural Engineer*. **53**(5), pp.215-220.
- Greene Jr, G. and Belarbi, A. 2009a. Model for Reinforced Concrete Members under Torsion, Bending, and Shear. I: Theory. *Journal of Engineering Mechanics*. **135**(9), pp.961-969.
- Greene Jr, G. and Belarbi, A. 2009b. Model for Reinforced Concrete Members under Torsion, Bending, and Shear. II: Model Application and Validation. *Journal of Engineering Mechanics*. **135**(9), pp.970-977.
- Gribniak, V., Kaklauskas, G. and Bacinskas, D. 2008. Shrinkage in reinforced concrete structures: a computational aspect. *Journal of Civil Engineering and Management*. **14**(1), pp.49-60.
- Gvozdev, A., Lessig, N. and Rulle, L. 1968. Research on reinforced concrete beams under combined bending and torsion in the Soviet Union. *Special Publication*. **18**, pp.307-336.
- Hamil, S.J. 2000b. *Reinforced concrete beam-column connection behaviour (BL)*. Dissertation/Thesis thesis, ProQuest Dissertations Publishing
- Hasan, N.M. 2016. *Time dependent flexural analysis of reinforced concrete members*. thesis.
- Helal, Y. 2012. *Seismic strengthening of deficient exterior RC beam-column sub-assemblages using post-tensioned metal strips*. Dissertation/Thesis thesis, University of Sheffield

- Hii, A.K.Y. and Al-Mahaidi, R. 2006. An experimental and numerical investigation on torsional strengthening of solid and box-section RC beams using CFRP laminates. *Composite Structures*. **75**(1), pp.213-221.
- Hii, A.K.Y. and Al-Mahaidi, R. 2007. Torsional Capacity of CFRP Strengthened Reinforced Concrete Beams. *Journal of Composites for Construction*. **11**(1), pp.71-80.
- Hii, K. and Al-Mahaidi, R. 2005. Torsional strengthening of reinforced concrete beams using CFRP composites - an experimental and numerical investigation. In: 2005: Institute of Materials Engineering Australasia -Conference Proceeding.
- Hordijk, P. 1991. Local approach to fatigue of concrete. *TU Delft, Delft University*.
- Hsu, H.L. and Liang, L.L. 2003. Performance of hollow composite members subjected to cyclic eccentric loading. *Earthquake Engineering & Structural Dynamics*. **32**(3), pp.443-461.
- Hsu, H.L. and Wang, C.L. 2000. Flexural-torsional behaviour of steel reinforced concrete members subjected to repeated loading. *Earthquake Engineering & Structural Dynamics*. **29**(5), pp.667-682.
- Hsu, T.T. 1968a. Torsion of structural concrete-behavior of reinforced concrete rectangular members. *Special Publication*. **18**, pp.261-306.
- Hsu, T.T. 1968b. Ultimate torque of reinforced rectangular beams. *Journal of the Structural Division*. **94**(2), pp.485-510.
- Hsu, T.T. 1997. ACI shear and torsion provisions for prestressed hollow girders. *Structural Journal*. **94**(6), pp.787-799.
- Hsu, T.T. and Mo, Y. 1985a. Softening of concrete in torsional members-design recommendations. In: *Journal Proceedings*, pp.443-452.
- Hsu, T.T. and Mo, Y. 1985b. Softening of Concrete in Torsional Members-Theroy and Tests. In: *Journal Proceedings*, pp.290-303.
- Hsu, T.T.C. 1990. Shear Flow Zone in Torsion of Reinforced Concrete. *Journal of Structural Engineering*. **116**(11), pp.3206-3226.
- Hsu, T.T.C. 1993. *Unified theory of reinforced concrete*. London;Boca Raton;; CRC Press.
- Hsu, T.T.C. 1996. Toward A Unified Nomenclature for Reinforced-Concrete Theory. *Journal of Structural Engineering*. **122**(3), pp.275-283.
- Hwang, S.-J. and Lee, H.-J. 1999. Analytical Model for Predicting Shear Strengths of Exterior Reinforced Concrete Beam-Column Joints for Sesimic Resistance. *ACI Structural Journal*. **96**, pp.846-857.
- Inge Karlsson, L.E. and Anderson, L. 1974. Long-time Behavior of Reinforced Concrete Beams Subjected to Pure Torsion. *Journal Proceedings*. **71**(6).
- Institution, B.S. 1992. *Specification for aggregates from natural sources for concrete*. British Standards Institution London.
- Ishai, O. 1964. Elastic and inelastic behaviour of hardened mortar in torsion. In: *Symp. on Creep of Concrete, 1964*.
- Jariwala, V.H., Patel, P.V. and Purohit, S.P. 2013. Strengthening of RC beams subjected to combined torsion and bending with GFRP composites. In: 2013, pp.282-289.

- Kassem, W. 2016. Strut-and-tie modelling for the analysis and design of RC beam-column joints. *Materials and Structures*. **49**(8), pp.3459-3476.
- Khaldoun, N.R. and Michael, P.C. 1995. Effect of Thickness of Concrete Cover on Shear-Torsion Interaction-An Experimental Investigation. *Structural Journal*. **92**(3).
- Kim, J., LaFave, J.M. and Song, J. 2009. Joint shear behaviour of reinforced concrete beam-column connections. *Magazine of concrete research*. **61**(2), pp.119-132.
- Kusuhara, F., Azukawa, K., Shiohara, H. and Otani, S. 2004. Tests of reinforced concrete interior beam-column joint subassembly with eccentric beams. In: *13th World Conference on Earthquake Engineering, Vancouver, BC, Canada*.
- Kurt H. Gerstle, D.L.L.P.B.M.D. 1978. Strength of Concrete under Multiaxial Stress States. *ACI Symposium Publication*. **55**
- Lampert, P. and Collins, M.P. 1972. Torsion, bending, and confusion-An attempt to establish the facts. In: *Journal Proceedings*, pp.500-504.
- Lee, J. and Fenves, G.L. 1998. Plastic-damage model for cyclic loading of concrete structures. *Journal of engineering mechanics*. **124**(8), pp.892-900.
- Leung, M.B. and Schnobrich, W.C. 1987. Reinforced Concrete Beams Subjected to Bending and Torsion. *Journal of Structural Engineering*. **113**(2), pp.307-321.
- Li, Q. 2012. *Performance of RC Bridge Columns under Cyclic Combined Loading including Torsion*. Doctor of Philosophy thesis, University of Houston.
- Li, Q., Belarbi, A. and Prakash, S.S. 2010. Seismic Performance of Square RC Bridge Columns under Combined Loading Including Torsion with Low Shear. *Earth and Space 2010*. pp.3011-3018.
- Lopes SMR and Bernardo LFA. (2009) Twist behavior of high-strength concrete hollow beams-Formation of plastic hinges along the length. *Engineering Structures* 31: 138-149.
- Lubliner, J., Oliver, J., Oller, S. and Oñate, E. 1989. A plastic-damage model for concrete. *International Journal of solids and structures*. **25**(3), pp.299-326.
- Lu, X.Z., Teng, J.G., Ye, L.P. and Jiang, J.J. 2005. Bond-slip models for FRP sheets/plates bonded to concrete. *Engineering Structures*. **27**(6), pp.920-937.
- Ma, S., Bunnori, N.M. and Choong, K.K. 2018. Prediction of Ultimate Torque of Reinforced Concrete Box Beam Bonded with CFRP Strips. *KSCE Journal of Civil Engineering*. **22**(11), pp.4353-4363.
- MATLAB, M. 2013. *MATLAB and Simulink, 8.1. 0.604 (R2013a)*. The MathWorks Inc. Natick, MA.
- MIDAS FEA Manual. 2015. detail FE analysis system for Advanced Nonlinear and Detail Analysis System. *FEA analysis and algorithm manual*.
- Mitchell, D. and Collins, M.P. 1974. Diagonal compression field theory-a rational model for structural concrete in pure torsion. In: *Journal Proceedings*, pp.396-408.

- Mohammad, M. 2020. *Time-dependent flextural performance and loss of tension stiffening of corroded reinforced concrete beams*. Doctor of Philosophy thesis, University of Leeds.
- Mondal, T.G. and Prakash, S.S. 2015. Improved softened truss model for RC circular columns under combined torsion and axial compression. *Magazine of Concrete Research*. **67**(16), pp.855-866.
- Mostofinejad, D., Akhlaghi, A. and Eslami, A. 2018. Estimating the Seismic Performance of CFRP-Retrofitted RC Beam-Column Connections Using Fiber-Section Analysis. *Journal of Earthquake Engineering*. **22**(6), pp.1092-1110.
- Mostofinejad, D. and Hajrasouliha, M. 2019. 3D beam--column corner joints retrofitted with X-shaped FRP sheets attached via the EBROG technique.(Report). *Engineering Structures*. **183**, p987.
- Mostofinejad, D. and Talaeitaba, S.B. 2011. Nonlinear Modeling of RC Beams Subjected to Torsion using the Smeared Crack Model. *Procedia engineering*. **14**, pp.1447-1454.
- Mu, R., Forth, J., Beeby, A. and Scott, R. 2008. Modelling of shrinkage induced curvature of cracked concrete beams. *Taylor Made Concrete Solutions (Walraven JC and Steelhurst D (eds))*. Taylor & Francis, Abingdon, UK. pp.573-578.
- Neville, A.M. 2011. *Properties of concrete*. 5th ed. Harlow: Prentice Hall.
- Neville, A.M. and Brooks, J.J. 2010. *Concrete technology*. 2nd ed. London;Harlow;: Prentice Hall.
- Neville, A.M., Dilger, W.H. and Brooks, J.J. 1983. *Creep of plain and structural concrete*. London;New York;: Construction Press.
- Ngo, D. and Scordelis, A.C. 1967. Finite Element Analysis of Reinforced Concrete Beams. *ACI Journal Proceedings*. **64**(3).
- Nie, J. and Cai, C.S. 2000. Deflection of Cracked RC Beams under Sustained Loading. *Journal of Structural Engineering*. **126**(6), pp.708-716.
- NZS 3101. 2006. *Concrete structure standard-the design of concrete structures incorporating amendment No. 1 & 2 (NZS 3101: Part 1: 2006-A1&A2)*. SNZ Wellington, New Zealand.
- Obaidat, Y.T., Ashteyat, A.M. and Obaidat, A.T. 2020. Performance of RC Beam Strengthened with NSM-CFRP Strip Under Pure Torsion: Experimental and Numerical Study. *International Journal of Civil Engineering*. **18**(5), pp.585-593.
- Panchacharam, S. and Belarbi, A. 2002. Torsional behavior of reinforced concrete beams strengthened with FRP composites. In: *First FIB Congress, Osaka, Japan*, pp.01-110.
- Pantazopoulou, S. and Bonacci, J. 1992. Consideration of questions about beam-column joints. *ACI Structural Journal*. **89**(1), pp.27-36.
- Pantelides, C., Hansen, J., Nadauld, J. and Reaveley, L.D. 2002a. Assessment of Reinforced Concrete Building Exterior Joints with Substandard Details, PEER Report, No. 2002/18, Pacific Earthquake Engineering Research Center. *University of California, Berkeley, USA*.

- Pantelides, C.P., Hansen, J., Nadauld, J. and Reaveley, L.D. 2002b. Assessment of reinforced concrete building exterior joints with substandard details. *PEER report*. **18**.
- Park, R. 1988. Ductility evaluation from laboratory and analytical testing. In: *Proceedings of the 9th world conference on earthquake engineering, Tokyo-Kyoto, Japan*, pp.605-616.
- Park, S. and Mosalam, K.M. 2012. Parameters for shear strength prediction of exterior beam–column joints without transverse reinforcement. *Engineering Structures*. **36**, pp.198-209.
- Parker, D.E. 1997. *Shear strength within reinforced concrete beam-column joints*. Dissertation/Thesis thesis, ProQuest Dissertations Publishing
- Parvin, A., Altay, S., Yalcin, C. and Kaya, O. 2010. CFRP Rehabilitation of Concrete Frame Joints with Inadequate Shear and Anchorage Details. *Journal of Composites for Construction*. **14**(1), pp.72-82.
- Patel, P.V., Jariwala, V.H. and Purohit, S.P. 2016. Torsional Strengthening of RC Beams Using GFRP Composites. *Journal of The Institution of Engineers (India): Series A*. **97**(3), pp.313-322.
- Paulay, T., Park, R. and Priestley, M. 1978. Reinforced concrete beam-column joints under seismic actions. In: *Journal Proceedings*, pp.585-593.
- Paulay, T. and Priestley, M.J.N. 1992. Seismic design of reinforced concrete and masonry buildings.
- Peng, X.-N. and Wong, Y.-L. 2011. Experimental study on reinforced concrete walls under combined flexure, shear and torsion. *Magazine of Concrete Research*. **63**(6), pp.459-471.
- Pham AT, Pham XD and Tan KH. (2019) Slab corner effect on torsional behaviour of perimeter beams under missing column scenario. *Magazine of Concrete Research* 71: 611-623.
- Prakash, S., Belarbi, A. and You, Y.-M. 2010. Seismic performance of circular RC columns subjected to axial force, bending, and torsion with low and moderate shear. *Engineering Structures*. **32**(1), pp.46-59.
- Priestley, M.J.N. and Seible, F. 1995. Design of seismic retrofit measures for concrete and masonry structures. *Construction and Building Materials*. **9**(6), pp.365-377.
- Rabbat, B.G. and Collins, M.P. 1978. A variable angle space truss model for structural concrete members subjected to complex loading. *Special Publication*. **55**, pp.547-588.
- Raffaella, G., Gentry, T. and Wight, J. 1992. Earthquake loading on R/C beam-column connections. In: *10th World Conference on Earthquake Engineering, Balkema, Rotterdam*, pp.3185-3190.
- Rahal, K. and Collins, M.P. 1995. Analysis of sections subjected to combined shear and torsion-a theoretical model. *ACI Structural Journal*. **92**, pp.459-459.
- Rahal, K.N. 2007. Combined torsion and bending in reinforced and prestressed concrete beams using simplified method for combined stress-resultants. *ACI Structural Journal*. **104**(4), p402.

- Ranaivomanana, N., Multon, S. and Turatsinze, A. 2013. Tensile, compressive and flexural basic creep of concrete at different stress levels. *Cement and Concrete Research*. **52**, pp.1-10.
- Raphael, M.J. 1984. Tensile Strength of Concrete. *ACI Journal Proceedings*. **81**(2).
- Rashid, Y.R. 1968. Ultimate strength analysis of prestressed concrete pressure vessels. *Nuclear engineering and design*. **7**(4), pp.334-344.
- Robert, R. and Manfred, C. 2015. Material Behavior of Ultra-High-Strength Concrete under Multiaxial Stress States. *ACI Materials Journal*. **112**(5).
- Ronagh, H.R. and Baji, H. 2014. On the FE Modeling of FRP-Retrofitted Beam–Column Subassemblies. *International Journal of Concrete Structures and Materials*. **8**(2), pp.141-155.
- Rots, J.G. 1988. Computational modeling of concrete fracture.
- Sakata, K. and Shimomura, T. 2004. Recent progress in research on and code evaluation of concrete creep and shrinkage in Japan. *Journal of Advanced Concrete Technology*. **2**(2), pp.133-140.
- Salom, P.R., Gergely, J. and Young, D.T. 2004. Torsional Strengthening of Spandrel Beams with Fiber-Reinforced Polymer Laminates. *Journal of Composites for Construction*. **8**(2), pp.157-162.
- Santhakumar, R., Dhanaraj, R. and Chandrasekaran, E. 2007. Behaviour of retrofitted reinforced concrete beams under combined bending and torsion: A numerical study. *Electronic Journal of Structural Engineering*. **7**, pp.1-7.
- Sarsam, K. and Phipps, M. 1985. The shear design of in situ reinforced concrete beam–column joints subjected to monotonic loading. *Magazine of Concrete Research*. **37**(130), pp.16-28.
- Sasmal, S. 2009. *Performance evaluation and strengthening of deficient beam-column sub-assemblages under cyclic loading*. Dissertation/Thesis thesis, University of Stuttgart.
- Sayed, A.M., Wang, X. and Wu, Z. 2014. Finite element modeling of the shear capacity of RC beams strengthened with FRP sheets by considering different failure modes.(reinforced concrete)(fiber reinforced polymer). *Construction and Building Materials*. **59**, p169.
- Scott, H.R. and Beeby, W.A. 2005. Long-Term Tension-Stiffening Effects in Concrete. *ACI Structural Journal*. **102**(1).
- Scott, R. 1992. The effects of detailing on RC beam/column connection behaviour. *Structural Engineer*. **70**(18).
- Selby, R.G. and Vecchio, F.J. 1997. A constitutive model for analysis of reinforced concrete solids. *Canadian Journal of Civil Engineering*. **24**(3), pp.460-470.
- Selby, R. and Vecchio, F. 1993. *Three-dimensional constitutive relations for reinforced concrete*, Pub. No. 93–02, technical report, University of Toronto, Dept. of Civil Engineering.
- Selby, R.G. and Vecchio, F.J. 1991. Toward Compression-Field Analysis of Reinforced Concrete Solids. *Journal of Structural Engineering*. **117**(6), pp.1740-1758.

- Shannag, M.J. and Alhassan, M.A. 2005. Seismic Upgrade of Interior Beam-Column Subassemblages with High-Performance Fiber-Reinforced Concrete Jackets. *ACI Structural Journal*. **102**(1).
- Shehzad, M.K., Forth, J.P. and Bradshaw, A. 2019. Imposed loading effects on reinforced concrete walls restrained at their base. *Proceedings of the Institution of Civil Engineers - Structures and Buildings*. **0**(0), pp.1-17.
- Shigeru Hakuto, R.P. and Hitoshi, T. 2000. Seismic Load Tests on Interior and Exterior Beam-Column Joints with Substandard Reinforcing Details. *ACI Structural Journal*. **97**(1).
- Täljsten, B. 1997. Strengthening of beams by plate bonding. *Journal of materials in civil engineering*. **9**(4), pp.206-212.
- Täljsten, B. and Elfgren, L. 2000. Strengthening concrete beams for shear using CFRP-materials: evaluation of different application methods. *Composites Part B: Engineering*. **31**(2), pp.87-96.
- Tao, Y. 2013. Fibre reinforced polymer (FRP) strengthened masonry arch structures.
- Teixeira MM and Bernardo LFA. (2018) Ductility of RC beams under torsion. *Engineering Structures* 168: 759-769.
- Thaker, T.A. 2016. *Experimental and Nonlinear Finite Element Analysis of Double Skin Beam-Column Joints*. thesis, University of Leeds.
- Thorenfeldt, E. 1987. Mechanical properties of high-strength concrete and applications in design. In: *Symposium Proceedings, Utilization of High-Strength Concrete, Norway, 1987*.
- Thurlimann, B. 1979. Torsional strength of reinforced and prestressed concrete beams-CEB approach. *Special Publication*. **59**, pp.117-144.
- Timoshenko, S. 1940. *Strength of materials Part 1*. D. Van Nostrand Co., Inc.
- Tirasit, P. and Kawashima, K. 2007. Seismic Performance of Square Reinforced Concrete Columns under Combined Cyclic Flexural and Torsional Loadings. *Journal of Earthquake Engineering*. **11**(3), pp.425-452.
- Triantafillou, T.C. 1998. Shear strengthening of reinforced concrete beams using epoxy-bonded FRP composites. *ACI structural journal*. **95**, pp.107-115.
- Triantafillou, T.C. and Antonopoulos, C.P. 2000. Design of Concrete Flexural Members Strengthened in Shear with FRP. *Journal of Composites for Construction*. **4**(4), pp.198-205.
- Triantafillou, T.C. and Antonopoulos, C.P. 2003. Experimental Investigation of FRP-Strengthened RC Beam-Column Joints. *Journal of Composites for Construction*. **7**(1), pp.39-49.
- Troxell, G. 1958. Log-time creep and shrinkage tests of plain and reinforced concrete. In: *ASTM*, pp.1101-1120.
- Tsonos, A. 1996. Influence of p-delta effect and axial force variations on seismic performance of R/C beam-column joints. In: *11 th World Conference on Earthquake Engineering*.
- Tsonos, A.G. 2008. Effectiveness of CFRP-jackets and RC-jackets in post-earthquake and pre-earthquake retrofitting of beam-column subassemblages. *Engineering Structures*. **30**(3), pp.777-793.

- Vecchio, F. and Collins, M.P. 1981. *Stress-strain characteristics of reinforced concrete in pure shear*.
- Vecchio, F.J. and Collins, M.P. 1986. The modified compression-field theory for reinforced concrete elements subjected to shear. *ACI J.* **83**(2), pp.219-231.
- Vecchio, F.J. and Collins, M.P. 1993. Compression Response of Cracked Reinforced Concrete. *Journal of Structural Engineering.* **119**(12), pp.3590-3610.
- Vinson, J.R. and Sierakowski, R.L. 2006. *The behavior of structures composed of composite materials*. Springer Science & Business Media.
- Vollum, R. and Newman, J. 1999a. Strut and tie models for analysis/design of external beam-column joints. *Magazine of Concrete Research.* **51**(6), pp.415-426.
- Vollum, R. and Parker, D. 2008. External beam–column joints: design to Eurocode 2. *Magazine of Concrete Research.* **60**(7), pp.511-521.
- Vollum, R.L., Eder, M.A., Elghazouli, A.Y. and Abdel-Fattah, T. 2010. Modelling and experimental assessment of punching shear in flat slabs with shearheads. *Engineering Structures.* **32**(12), pp.3911-3924.
- Vollum, R.L. and Newman, J.B. 1999b. Towards the design of reinforced concrete eccentric beam—column joints. *Magazine of Concrete Research.* **51**(6), pp.397-407.
- Warwaruk, J. 1981. Torsion in Reinforced Concrete. *Special Publication.* **72**.
- Wight, J.K. and MacGregor, J.G. 2012. *Reinforced concrete: mechanics and design*. Boston, Mass;London,: Pearson Education.
- William, K.J. and Warnke, E.P. 1974. Constitutive model for the triaxial behaviour of concrete. *IABSE Seminar on “Concrete Structures Subjected to Triaxial Stresses”, ISMES, 1974.Bergamo.* **19**, p1.
- Wong, H.F. 2005. *Shear strength and seismic performance of non-seismically designed reinforced concrete beam-column joints*. thesis.
- Zhang, H. and Smith, S.T. 2013. Fibre-reinforced polymer (FRP)-to-concrete joints anchored with FRP anchors: tests and experimental trends1. *Canadian Journal of Civil Engineering.* **40**(11), pp.1103-1116.
- Zhang, J., Lu, Z. and Zhu, H. 2001. Experimental study on the behaviour of RC torsional members externally bonded with CFRP. In: *FRP Composites in Civil Engineering. Proceedings of the International Conference on FRP composites in Civil Engineering*.

Appendix A Torsional Shear Flow and Truss Model

The Area of Shear Flow (A_o)

The circulatory torsion stresses (τ) induce a shear flow (q) around the section's periphery, which results in diagonal concrete struts in the RC members. A large number of researchers (e.g. Mondal and Prakash, 2015; Allawi et al., 2015; Deifalla and Ghobarah, 2010a; Rahal, 2007; Hsu, 1997; Rahal and Collins, 1995; Hsu, 1990; Hsu and Mo, 1985a; Collins and Mitchell, 1980; Mitchell and Collins, 1974) have used Bredt's formula of thin-tube analogy to evaluate a shear flow (q) in concrete sections, where the torsional shear stress (τ) is equivalent to the shear flow (q) multiplied by twice the area (A_o) bounded by the path of the shear flow.

The area (A_o) corresponds to the thickness of the shear flow region (wall thickness). In general, the major codes of practice, which include Eurocode 2 (2004) and CEB-FIP (1991) recommend that the shear flow zone thickness (t) for solid sections can be determined by dividing the cross sectional area by its perimeter, while FIB Model Code (2010b) suggests (t) equivalent of twice the distance between the outer member's surface and the centre of the longitudinal rebars. The ACI Committee 318 (2014) permits using the area (A_{oh}) enclosed by the centreline of the transverse shear reinforcement, as given in Table A.1. Collins and Mitchell (1980) proposed an approach to compute the area of the shear flow by eliminating the concrete cover contribution and reducing the hoops area (A_{oh}) according to the depth of the compression zone (a_o). However, they did not consider the decrease in concrete strength after cracking (softening phenomenon) on the a_o depth.

Hsu (1990) introduced a rational approach to determining shear zone thickness (t) by incorporating the compatibility conditions, curvature, and softening (ξ) of the concrete strut, to determine the thickness of the shear flow zone. However, this approach employs a trial and error method to solve the set of equations. Furthermore, it was derived from a member under pure torsion and not one under combined loads. Further discussion of the application of torsional shear stress combined with flexural and direct shear stresses is given in Section 2.2.2, along with a summary of the methods developed to analyse and design concrete structures under combined actions.

Table A.1: Area of shear flow calculation formulas

Code or Author	Shear flow Area
Eurocode 2 (2004)	$A_o = (h - t)(b - t)$ $t = \frac{A_c}{P_c}$
ACI Committee 318 (2014)	$A_o = 0.85 A_{oh}$
Collin's and Mitchel (1980)	$A_o = A_{oh} - \frac{a_o}{2} p_h$ $a_o = \frac{A_{oh}}{p_h} \left[1 - \sqrt{1 - \frac{T_n p_h}{0.85 f_c A_{oh}^2} \left(\tan \alpha + \frac{1}{\tan \alpha} \right)} \right]$
Hsu (1990)	$A_o = A_c - \frac{t}{2} p_c + \partial t^2$ $p_o = p_c - 4\partial t^2$ $\xi = \frac{\frac{A_l f_{yl}}{p_o} + \frac{A_t f_{yt}}{S}}{0.8 f_c t}$ $\cos^2 \alpha = \frac{\frac{A_l f_{yl}}{p_o}}{\frac{A_l f_{yl}}{p_o} + \frac{A_t f_{yt}}{S}}$ $t = \frac{A_o \xi^2}{p_o \sin^2 \alpha \cos^2 \alpha}$

Where;

h = section depth

b= section width

α = inclination of concrete struts

∂ = coefficient can be taken equivalent to unity

S= stirrup spacing centre to centre

p_o = perimeter of the shear flow area

A_l and A_t = area of rebars in longitudinal and transverse directions, respectively

f_{yl} and f_{yt} = yielding strength of rebars in the longitudinal and transverse directions, respectively

Truss Model Analogy and Angle of Inclination (α)

During the post-cracking stage, the RC members resist the shear stresses via a mechanism that depends on the structural characteristics of the reinforcement and the concrete as a composite material. The propagation of inclined cracks starts when the applied torsional shear stresses increase the level of the principal tensile stresses that normally act on diagonal struts beyond the tensile strength of the concrete. One early approach of predicting the torsional capacity of RC structures is known as the space truss model, which was introduced by Rausch in 1929 (Hsu and Mo, 1985a; Collins and Mitchell, 1980). The space truss model was formed from longitudinal and transverse tension ties with diagonal compression concrete struts to equilibrate the circulatory torsional shear flow (q), as shown in Figure A.1, where each of the section's sides has upper and lower chords, vertical ties, and diagonal struts.

The space truss model was first formulated with the assumptions that the tangential struts developed with at a 45° angle and that the area of shear flow (A_o) matched the gross cross-sectional area (A_c). Hsu and Mo (1985a) indicate that this can lead to overestimations in the member's strength. In many cases, the constant 45° angle model does not reflect the actual behaviour of the RC sections. An overview of previous studies of torsion was conducted by Warwaruk (1981), who reported that the inclination angle (α) is affected by the ratio of longitudinal to transverse reinforcement. Corresponding to the equilibrium conditions of forces in each side (wall) of the truss model, Elfgrén (1972), along with Rabbat and Collins (1978) determined the inclination angle (α) of each wall by equating the force in the diagonal concrete struts induced by the shear flow (q) to the tie force in the vertical direction, as given in Eq.A.1 to A.3. They neglected the tensile strength of concrete and assumed that the transverse reinforcement yielded (f_{ty}). This approach can be effectively used to predict the ultimate carrying capacity of structures. Similarly, by using an equilibrium of stresses, Hsu (1996) suggested a special formula (Eq.A.4) to calculate the angle (α) of a member under only pure shear stresses, where both longitudinal (f_{ly}) and transverse reinforcement (f_{ty}) reached their yielding limits (plastic truss model).

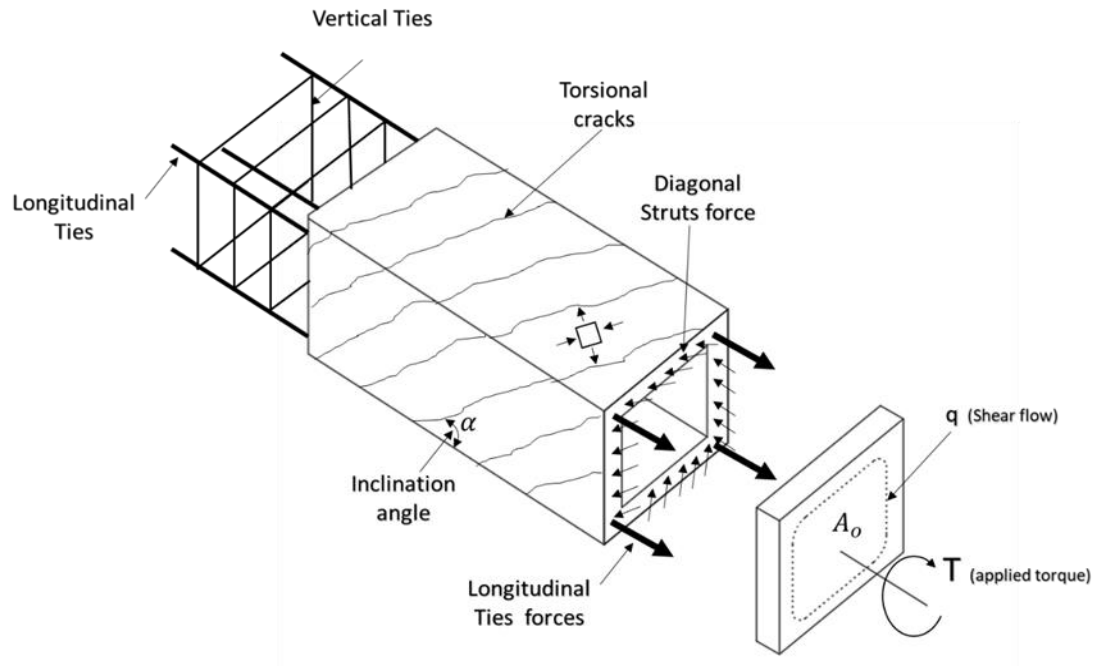


Figure A. 1: Space truss model

A general approach presented in (Vecchio and Collins, 1981; Collins and Mitchell, 1980), utilised the Compression Field Theory (CFT) in order to comply with the compatibility conditions of the Mohr circle of strain (Fig. A.3) and evaluate the strut's angle (α), as given Eq.A.5. This approach was also adopted in the Modified Compression Field Method (Vecchio and Collins, 1986) and the Softened Truss Model (Hsu and Mo, 1985b). Although, these methods are proposed to predict the behaviour of a member through all loading stages, they require a coded programme to iteratively solve the sets of equations (which are reviewed in Section 2.2.4). Bentz et al. (2006), introduced a simplified approach of the Modified Compression Field Method (MCFT) to estimate the angle (α) (Eq. A.6) and concrete softening factor. However, the use of this simplified approach also required an iterative process, where the analyses began with an estimation of the magnitude of the average longitudinal steel strain (ϵ_{sl}) in the tension zone.

The fIB Model Code (2010b) and the AASHTO LRFD (2010) proposed the simplified MCFT without an iteration process to calculate the shear resistances of RC structures under direct shear (v), bending (M), and axial forces (N) actions. This assumes the expected shear action to equilibrate the strut force that occurs at a constant angle ($0.5 \cot \alpha = 1$) in order to evaluate

the steel strain at the mid depth of the member (Eq.2.7). Eurocode 2 (2004) recommends that the design of the concrete strut angle should be taken between 22 to 45 degrees. Furthermore, the ACI Committee 318 (2014) permits the space truss model approach with a 45-degree strut angle in order to design members under torque actions.

Truss model :

$$\sigma_d = \frac{q}{t \cos \alpha \sin \alpha} \quad \text{Eq. A.1}$$

$$\frac{A_{st} f_{ty}}{s} = \frac{\sigma_d t \sin \alpha \cos \alpha}{\cot \alpha} \quad \text{Eq. A.2}$$

$$\cot(\alpha_l) = \frac{q s}{A_{st} f_{ty}} \quad \text{Eq. A.3}$$

Plastic Truss model :

$$\tan(\alpha) = \sqrt{\frac{\rho_t f_{ty}}{\rho_l f_{ly}}} \quad \text{Eq. A.4}$$

CFT, MCFT and STM :

$$\tan^2 \alpha = \frac{\epsilon_l + \epsilon_2}{\epsilon_t + \epsilon_2} \quad \text{Eq. A.5}$$

Simplified MCFT :

$$\alpha = 29^\circ + 7000 \epsilon_l \quad \text{Eq. A.6}$$

$$\epsilon_l = \frac{\frac{M}{dv} + V(0.5 \cot \alpha) + 0.5N}{2 E_s A_s} \quad \text{Eq. A.7}$$

Where;

σ_d = concrete strut stress

t = thickness of the shear flow zone

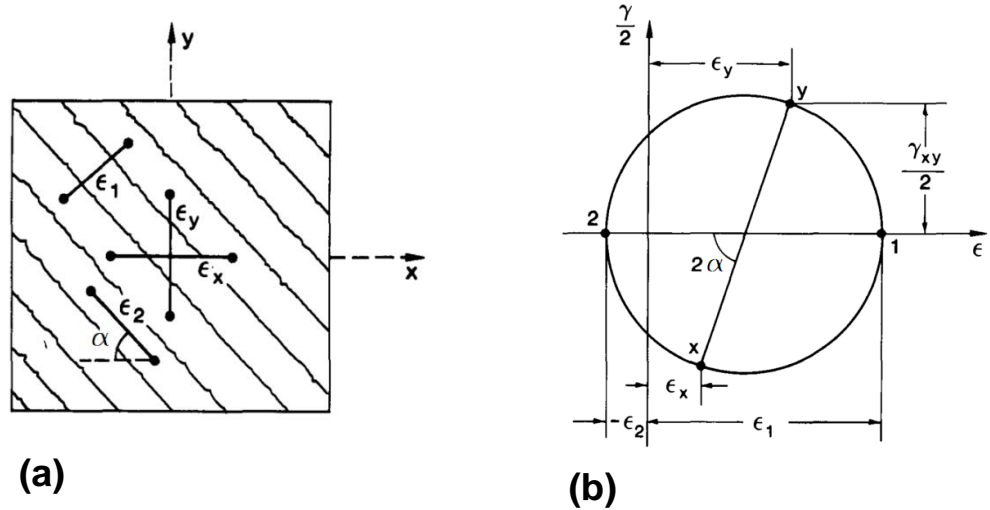
ρ_l and ρ_t = reinforcement ratios in longitudinal and transverse directions, respectively

ϵ_l and ϵ_t = strains in longitudinal and transverse directions, respectively

ϵ_1 and ϵ_2 = principal strains

E_s = modulus of elasticity for steel rebars

A_s = area of steel rebars in the tension zone



(ϵ_i and γ_{ij} corresponding normal and shear strains)

Figure A. 2: (a) Average strains in a cracked element (b) Mohr's Circle for Average Strains

(Vecchio and Collins, 1986)

Truss Model for RC Beams under Sustained Torsional Loads

Inge Karlsson and Anderson (1974) utilised the truss model in order to theoretically evaluate the torsional stiffness of the cracked beams. The total stress of each section's side (e.g. right, left, top, and bottom sides for a rectangular section) was assumed as the sum of the developed stresses in the longitudinal bars, transverse reinforcement, and inclined concrete struts (Eq. A.8 to A.11). The inclination angle and wall's thickness has been assumed to be constant, where it is taken to be the equivalent of 45° and $1/5$ of the shortest link leg, respectively. However, these assumptions may not necessarily hold true, as discussed in the previous section.

The truss stresses (e.g. longitudinal, transverse, and concrete) have been transformed in terms of elastic strain energy per unit length (Eq. A.12), where the strain expression of each side (ϵ_i) is formulated by adding the sum of the stresses (Eq. A.13). Again, the total strain of all the section sides should be superimposed. The torsional stiffness (K_t) of the cracked section is computed by using the general equation of the strain energy for members under torque ($\epsilon = T^2/2K_t$). Furthermore, creep coefficients were incorporated in the stiffness expression by using the effective modulus of elasticity approach (Eq. A.14). In addition, an adjustment (linear interpolation) to the torsional stiffness (K_t)

was adopted (Eq. A.15) for a member that was loaded between the cracking limit (T_{cr}) and the yield limits (T_y).

The twist angles (θ) that were obtained analytically (Eq. A.16) and experimentally were compared; the model to test ratio varied from 0.84 to 1.30. Nevertheless, this model neglects the compatibility conditions between the shear and normal strains, and is based on the longitudinal forces in the top and bottom reinforcement that are assumed to be equal. This is not applicable for members that are subjected to flexural forces in addition to torsional loads. Moreover, the shrinkage effects on the concrete struts are not considered.

$$\sigma_c = \frac{T}{2 A_o t \sin \alpha \cos \alpha} \quad \text{Eq. A.8}$$

$$\sigma_{l1} = \frac{T y}{4 A_o A_{l1} \tan \alpha} \quad \text{Eq. A.9}$$

$$\sigma_{l2} = \frac{T y}{4 A_o A_{l2} \tan \alpha} \quad \text{Eq. A.10}$$

$$\sigma_t = \frac{T S}{2 A_o A_t \cot \alpha} \quad \text{Eq. A.11}$$

$$\varepsilon = \frac{1}{2} \frac{\sigma^2 A_e}{E} \quad \text{Eq. A.12}$$

$$\varepsilon_i = \frac{1}{2} \sum \frac{\sigma_c^2 y t}{E_c} + \frac{\sigma_{l1}^2 A_{l1}}{E_s} + \frac{\sigma_{l2}^2 A_{l2}}{E_s} + \frac{\sigma_t^2 A_t}{E_s} \quad \text{Eq. A.13}$$

$$K_t = \frac{E_c x y^3}{\frac{\left(1 + \frac{y}{x}\right)^2}{\rho_l n} + 10 \frac{y}{x} \left(1 + \frac{y}{x}\right) (1 + \phi_{(t,t_0)}) + \frac{\left(1 + \frac{y}{x}\right)^2}{\rho_l n}} \quad \text{Eq. A.14}$$

$$J = \frac{T - T_{cr}}{T_y - T_{cr}} \quad \text{Eq. A.15}$$

$$\theta = J \frac{T_y}{K_t} \quad \text{Eq. A.16}$$

Where;

T= applied torque

σ_c = the compressive stress in inclined concrete struts

t = thickness of the shear flow

y= the section depth (centre to centre of stirrups legs)

σ_{l1}, σ_{l2} = the longitudinal stresses in top and bottom bars, respectively

A_{l1}, A_{l2} = the areas for bottom and top reinforcements, respectively

σ_t = stresses in the transverse reinforcements (stirrups)

ε_i = the strain energy per unit length for each of the member's sides

σ = elements stresses (e.g. the rebars, stirrups and concrete)

A_e = the area of each element

E = the modulus of elasticity of each element

X = the shortest length of the stirrup's leg (centre to centre)

$$\frac{1}{\rho_l} = 0.25 \left(\frac{1}{\rho_t} + \frac{1}{\rho_b} \right)$$

$$\rho_t = \frac{A_{l1}}{xy} \text{ and } \rho_t = \frac{A_{l2}}{xy}$$

$$n = \frac{E_s}{E_c}$$

Appendix B The Frame Model Details

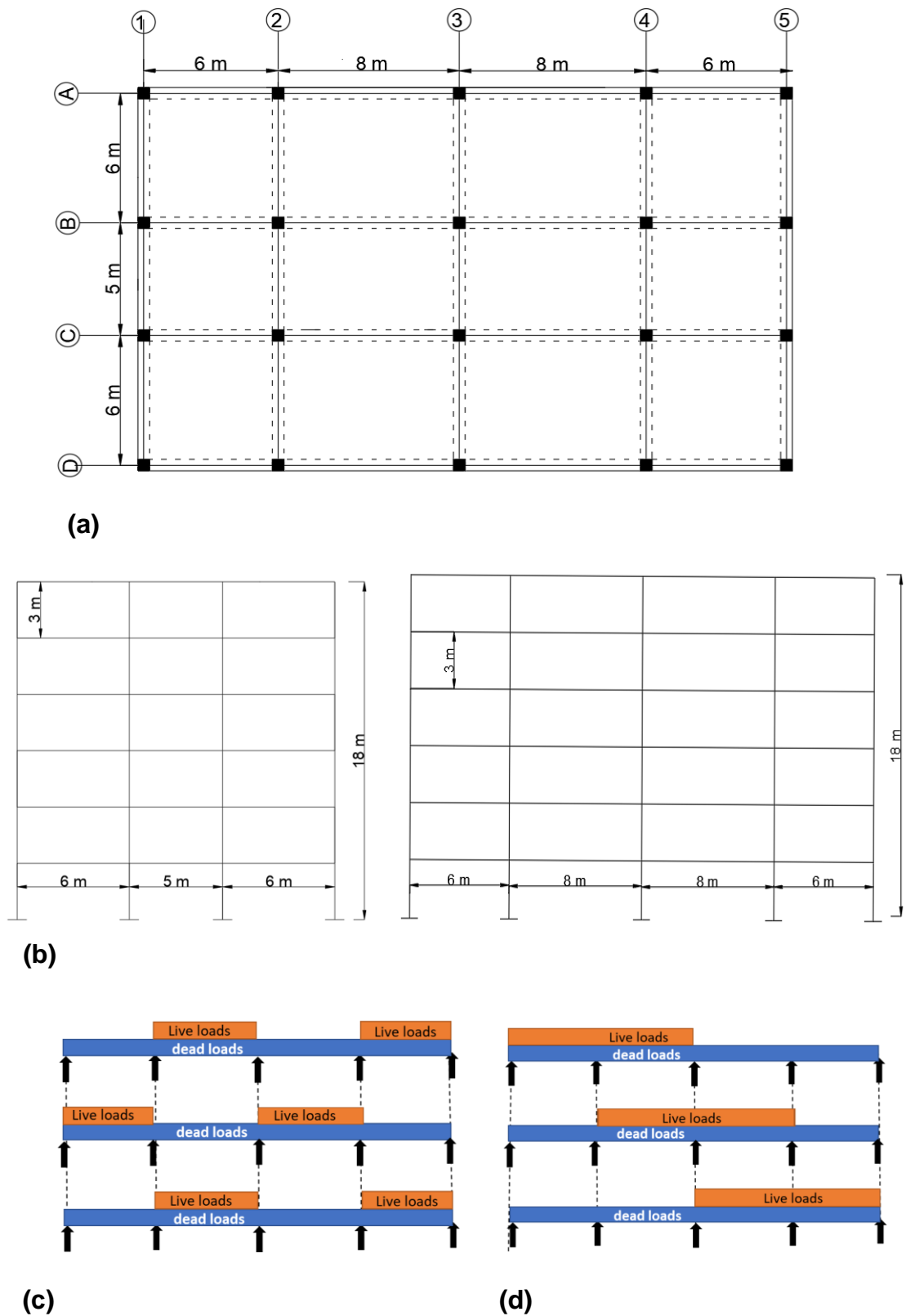


Figure B. 1: (a) Plan details of the frame model (b) Side and front views for the frame model (c) Gravity Loads arrangement-type 1 (d) Gravity Loads arrangement-type 2

1- Load Details

1.1 Dead load:

1.1.1 Floor load, according to Table (C3-1), ASCE/SEI 7-10 (2013) :

- i- Self-weight (0.15 m thickness) was calculated by SAP2000 package.
- ii- Floor Tiles + Subflooring + Plastering $\approx 2 \text{ kN/m}^2$

1.1.2 Beam loads; dead load imposed to the beam consists of:

- i- Self-weight was calculated by SAP2000 software.
- ii- Wall load on the beam, according to Table (C3-1) ASCE7-05 code = 3.78 kN/m^2 (bricks walls-partitions)
 $3.78 \times (\text{floor height c/c} - \text{beam's depth}) \approx 9.8 \text{ kN/m}$

1.2 Live load, According to Table (4.1), ASCE/SEI 7-10 (2013).

- i- Floors = 1.92 kN/m^2 (residential)
- ii- Roofs = 0.96 kN/m^2 (ordinary flat, pitched and curved roofs).

1.3 Wind loads, calculated according to BS6399 code,

$$\text{Total calculated wind pressure (P)} = 1.32 \text{ kN/m}^2$$

2- Loads Combinations

According to Section 2.32, ASCE/SEI 7-10 (2013), the considered loads combinations are listed as follows:-

$$2.1 \quad 1.4D$$

$$2.2 \quad 1.2D + 1.6L + 0.5L_r$$

$$2.3 \quad 1.2D + 1W + 1L + 0.5L_r$$

$$2.4 \quad 0.9D + 1W$$

Where; D is dead load, L is live load, W is wind load, and L_r is roof live load.

3- Modelling Details Using Sap 2000

- 3.1 Three-dimensional model has been created (Figures 3.1) and the gravity loads (i.e. dead and live loads) were applied in vertical direction-normal to the floors plane (out-of-plane forces).
- 3.2 Linear static analysis were performed to compute members forces. However, to replicate the cracking effects in corresponding to the ultimate design state, the beams and columns flexural stiffnesses were reduced by decreasing the sections moment of inertia (I_g) to $0.35 I_g$ for beams and $0.7 I_g$ for columns; these reductions are suggested by ACI Committee 318 (2014), Table 6.6.3.1.1(a).
- 3.3. As presented in Figure B.1, live loads were alternated between the floor spans. The loads arrangements include, (1) alternate the variable (live) loads between adjacent spans (see Figure B.1c), (2) any two adjacent spans loaded with the live and dead loads, while other spans loaded with only dead loads (see Figure B.1d). As the loads arrangement (1) induces ultimate sagging moments in alternate spans and ultimate potential hogging moment in the adjacent spans. While, the loads arrangement provides the ultimate hogging moment at the intermediate support between two adjacent spans.
- 3.4. The lateral loads (wind loads) were applied in both longitudinal and transverse directions of the each floor (in-of-plane forces).
- 3.5. Floors (slab) were modelled as area sections in which in-of- plane and out-of-plane stiffnesses were considered.
- 3.6. Diaphragm constraints were assigned to the floor slabs in order simulates the floors in-plane stiffness.
- 3.7. The column's ends at the building base (foundation) were fixed, where no transitions and rotations in all directions were assumed.
- 3.8. To account the overlap length between the joined column and beam by forcing the models to use the clear beam's length (instead of c/c length), the end-length offsets command was utilised.

4- Torsional reinforcements check

4.1 Ultimate imposed torsion (T_u) that obtained from Sap2000 analysis results is 2.24 kN.m.

4.2 Threshold torsion according to ACI Committee 318 (2014),

Section 22.7.4.1a) is equivalent to $0.083\phi\lambda\sqrt{f_c'}\left(\frac{A_{CP}^2}{P_{CP}}\right)$

→ 3.04 kN.m

→ 3.04 > 2.24 (no torsional reinforcements are required)

Where; ϕ is strength reduction factor (0.75), λ is modification factor (1), f_c' is the design concrete compressive strength (28 MPa), A_{CP} is the area enclosed by outside perimeter of the beam cross section (400mm x 280mm), P_{CP} is the outside perimeter of the beam cross section (2x(400mm+280mm)).

5- Joint design details (scaled specimens)

5.1 The joint design details for the scaled specimens are corresponded to Joint type -1, for members without significant deformation (non –seismic requirements) - ACI-ASCE 352R-02 Committee (2002).

5.2 Shear reduction factor (ϕ) is 0.85 (ACI-ASCE 352R-02 Committee, 2002).

5.3 Critical section for development length of the beam longitudinal reinforcement was calculated from the beam-column face (Type-1).

5.4 The design steel rebars strength (f_y) was equivalent to 563 MPa. Two rebars (16 mm) at the beam flexural tensile zone developed into column at the joint zone using 90° hooked rebars in corresponding to ACI Committee 318 (2014), Sections 25.3 and 25.4.

5.5 Joint Shear forces (V_j) were computed as follows:

$V_j = T_B - V_{col}$, where $T_B = \alpha A_s f_y$ and $\alpha = 1$ (neglect strain hardening).

$$\rightarrow T_B = 226.4 \text{ kN}$$

$$\rightarrow M_n = A_s f_y (d - a/2), \text{ where } a = 44 \text{ mm } \left(\frac{A_s f_y}{0.85 f_c' b} \right), d = 258 \text{ mm}, \\ b = 210 \text{ mm}.$$

$$\rightarrow M_n = 53.4 \text{ kN.m and } V_{col} = \frac{M_n}{L_c} \rightarrow 23.7 \text{ kN (ignore } V_{col}, \text{ small value)}$$

$$\rightarrow V_j = 226.4 \text{ kN}$$

5.6 Nominal joint shear strength (V_n) according to Section 4.7, ASCE 352R-02 Committee (2002).

$$V_n = 0.083 \gamma^2 \sqrt{f_c'} b_j h_c \text{ where } \gamma = 15 \text{ (Table-1, ACI-ASCE 352R-02 Committee (2002))}$$

$$\rightarrow \phi V_n = 335 \text{ kN} > 226.4 \text{ kN} \rightarrow \text{ok}$$

5.7 According to Section 4.21.3, ASCE 352R-02 Committee (2002), at least two joint ties should be provided within the top and bottom of the beam main reinforcement into the joint zone; in addition, for the beam-column joint is part of the primary system for resisting non-seismic lateral loads, the centre-to-centre spacing of the ties should not exceed 150 mm. Correspondingly, three joint's ties were used at 75mm centre-to-centre to confine the joint zone.

6- Shear Reinforcements details for the beam

6.1 Shear reduction factor (ϕ) is 0.75, Table 21.2.1— ACI Committee 318 (2014).

6.2 The design steel rebars strength (f_y) was equivalent to 571 MPa for 8 mm stirrups diameter.

6.3 According ACI Committee 318 (2014), the maximum spacing between stirrups is the small of following: -

a) $\frac{d}{2} \approx 125 \text{ mm c/c}$ (Section 9.7.6.2, ACI Committee 318 (2014))

b) 600 mm (Section 9.7.6.2, ACI Committee 318 (2014))

$$c) S = \frac{A_v f_y}{0.35 b_w} = 780 \text{ mm (Section 9.6.3.3 , ACI Committee 318 (2014))}$$

$$d) S = \frac{A_v f_y}{0.062 \sqrt{f_c'} b_w} = 265 \text{ mm (Section 9.6.3.3 , ACI Committee 318 (2014))}$$

Use $\phi 8 @ 125 \text{ mm centre-to-centre (c/c)}$

6.4 Maximum flexural (direct) shear capacity for the beam were computed as follows:

$$a) V_c = 0.17 \lambda^2 \sqrt{f_c'} b_w d \rightarrow 48.7 \text{ kN (Section 22.5.51, ACI Committee 318 (2014))}$$

$$b) V_s = (A_v f_y d)/S \rightarrow 118 \text{ kN}$$

$$c) V_u = \phi(V_s + V_c) \rightarrow 125 \text{ kN}$$

Where, A_v is the area of stirrups (2 legs), V_s is the stirrups shear contribution, V_c is the concrete shear contribution, λ is modification factor (1), f_c' is the design concrete compressive strength (28 MPa), b_w is the beam width (210 mm).

Table B.1: Predicted (designed) maximum applied beam's loads

Specimen	Bending kN.m (ACI 318)	Shear kN (ACI 318)	Torsion_steel (Eq. 3.1) kN.m	Torsion_CFRP (Eq. 6.1) kN.m	Max. Load (p) kN
SH-U-F	54 ¹	125	N.A	N.A	63.5 ²
SH-U-C			14.1	N.A	9 ³⁴
SH-C-S-A				12.6	17 ³⁴
SH-C-S-H				7.5	13.6 ³⁴
SH-C-S-I				7.7	13.9 ³⁴

¹ $f_c' = 34 \text{ MPa}$ (Table 3.8 -Chapter3).

² Load = bending moment /bending lever arm.

³ Load = total torsion / torque lever arm.

⁴ Total torsion = Torsion_steel + Torsion_CFRP.

Appendix C Concentric Loading Test Setup

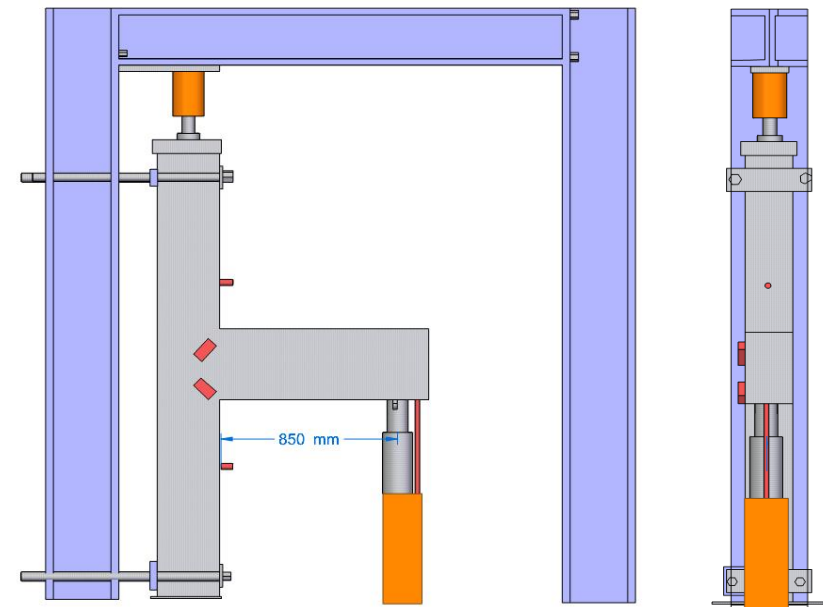
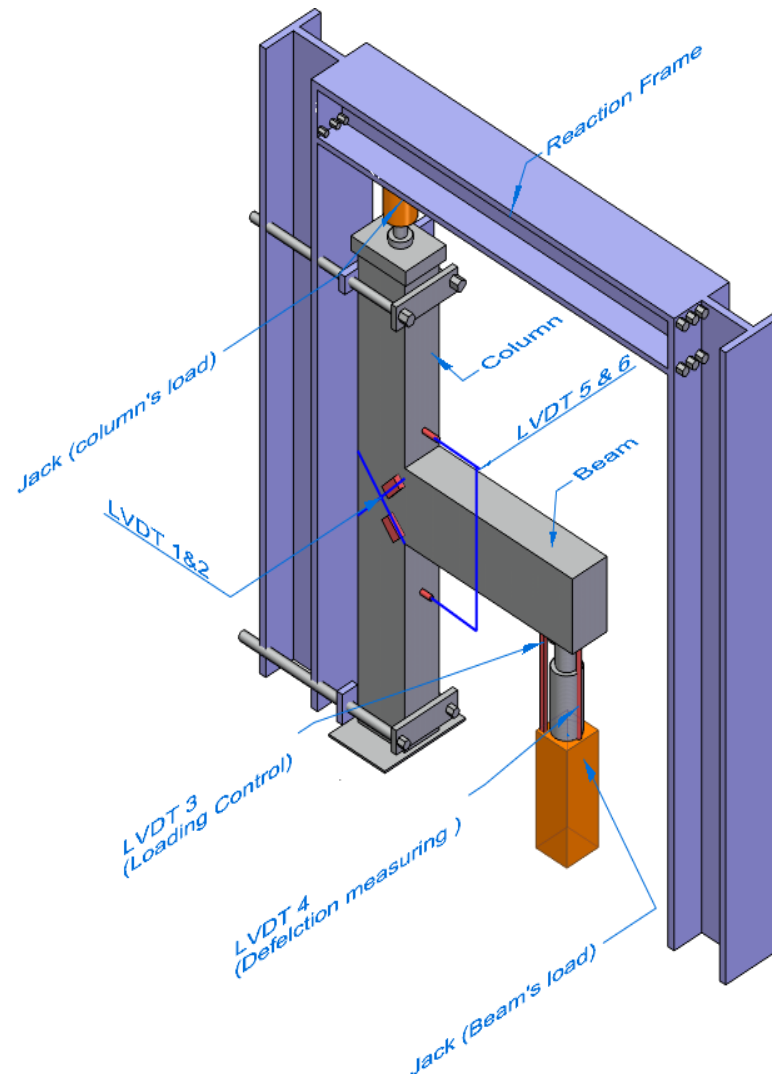


Figure C. 1: Concentric test schematic diagrams